

REPORT DOCUMENTATION PAGEForm Approved
OMB NO. 0704-0188

Public Reporting burden for this collection of information is estimated to average 1 hour per response, including the time for reviewing instructions, searching existing data sources, gathering and maintaining the data needed, and completing and reviewing the collection of information. Send comment regarding this burden estimates or any other aspect of this collection of information, including suggestions for reducing this burden, to Washington Headquarters Services, Directorate for Information Operations and Reports, 1215 Jefferson Davis Highway, Suite 1204, Arlington, VA 22202-4302, and to the Office of Management and Budget, Paperwork Reduction Project (0704-0188,) Washington, DC 20503.

1. AGENCY USE ONLY (Leave Blank)		2. REPORT DATE	3. REPORT TYPE AND DATES COVERED Final Report
4. TITLE AND SUBTITLE Plasma Actuators for Separation Control on Stationary and Oscillating Airfoils		5. FUNDING NUMBERS DAAD19-00-1-0447	
6. AUTHOR(S) See reprint			
7. PERFORMING ORGANIZATION NAME(S) AND ADDRESS(ES) Univ. of Notre Dame 511 Main Bldg. Notre Dame, IN 46556		8. PERFORMING ORGANIZATION REPORT NUMBER	
9. SPONSORING / MONITORING AGENCY NAME(S) AND ADDRESS(ES) U. S. Army Research Office P.O. Box 12211 Research Triangle Park, NC 27709-2211		10. SPONSORING / MONITORING AGENCY REPORT NUMBER 41077.2-EG	
11. SUPPLEMENTARY NOTES The views, opinions and/or findings contained in this report are those of the author(s) and should not be construed as an official Department of the Army position, policy or decision, unless so designated by other documentation.			
12 a. DISTRIBUTION / AVAILABILITY STATEMENT Approved for public release; distribution unlimited.		12 b. DISTRIBUTION CODE	
13. ABSTRACT (Maximum 200 words) see attached report			
14. SUBJECT TERMS		15. NUMBER OF PAGES	
		16. PRICE CODE	
17. SECURITY CLASSIFICATION OR REPORT UNCLASSIFIED	18. SECURITY CLASSIFICATION ON THIS PAGE UNCLASSIFIED	19. SECURITY CLASSIFICATION OF ABSTRACT UNCLASSIFIED	20. LIMITATION OF ABSTRACT UL

NSN 7540-01-280-5500

Standard Form 298 (Rev.2-89)
Prescribed by ANSI Std. Z39-18
298-102**BEST AVAILABLE COPY**

20040709 081

FINAL REPORT
under program
DAAD19-00-1-0447

PLASMA ACTUATORS FOR SEPARATION CONTROL
ON STATIONARY AND OSCILLATING AIRFOILS
by
M. Post and T. Corke

DISTRIBUTION STATEMENT A
Approved for Public Release
Distribution Unlimited

May 2004

PLASMA ACTUATORS FOR SEPARATION CONTROL ON STATIONARY AND OSCILLATING AIRFOILS

Abstract

by

Martiqua L. Post

Given the importance of separation control associated with retreating blade stall on helicopters, the primary objective of this work was to develop a plasma actuator flow control device for its use in controlling leading-edge separation on stationary and oscillating airfoils. The plasma actuator consists of two copper electrodes separated by a dielectric insulator. When the voltage supplied to the electrodes is sufficiently high, the surrounding air ionizes forms plasma in the regions of high electrical field potential. The ionized air, in the presence of an electric field gradient, results in a body force on the flow.

The effect of plasma actuator was experimentally investigated and characterized through a systematic set of experiments. It was then applied to NACA 66₃018 and NACA 0015 airfoils for the purpose of leading-edge separation control. The effectiveness of the actuator was documented through surface pressure measurements on the airfoil, mean wake velocity profiles, and flow visualization records. For the stationary airfoil, the actuator prevented flow separation for angles of attack up to 22°, which was 8° past the static stall angle. This resulted in as much as a 300% improvement in the lift-to-drag ratio.

For the oscillating airfoil, the measurements were phase-conditioned to the oscillation motion. Three cases with the plasma actuator were investigated: steady

actuation, unsteady plasma actuation, and so-called "smart" actuation in which the actuator is activated during portions of the oscillatory cycle. All of the cases exhibited a higher cycle-integrated lift and an improvement in the lift cycle hysteresis.

The steady plasma actuation increased the lift over most of the cycle, except at the peak angle of attack where it was found to suppress the dynamic stall vortex. Because of this, the sharp drop in the lift coefficient past the maximum angle of attack was eliminated. The unsteady plasma actuation produced significant improvements in the lift coefficient during the pitch-down portion of the cycle, especially near the minimum angle of attack. A "smart" actuator approach produced the best improvement in the lift cycle with the highest integrated lift, and elimination of the sharp stall past the maximum angle of attack. It is possible that the "smart" actuation could be optimized further. However, these results are extremely promising for improving helicopter rotor performance.

CONTENTS

TABLES	iv
FIGURES	v
SYMBOLS	v
CHAPTER 1: INTRODUCTION	1
1.1 Motivation	1
1.2 Background	2
1.2.1 Separation Control Techniques	3
1.2.2 Airfoil Aerodynamics	10
1.2.3 Helicopter Aerodynamics	14
1.2.3.1 Dynamic Stall	18
1.2.3.2 Controlling Retreating Blade Stall	20
1.3 Research Overview and Objectives	21
CHAPTER 2: THE PLASMA ACTUATOR: THEORY & OPTIMIZATION	23
2.1 Background	23
2.1.1 Electronics	29
2.1.2 Operation	30
2.1.2.1 Steady Actuation	34
2.1.2.2 Unsteady Actuation	34
2.1.2.3 Phased Actuation	36
2.2 Plasma Actuator Measurements	38
2.2.1 Actuator Optimization Set-up	38
2.2.2 Steady Actuator Measurements	41
2.2.2.1 Effect of Amplitude Input	43
2.2.2.2 Effect of Waveform Input	45
2.2.2.3 Effect of Operating Frequency	47
2.2.2.4 Effect of Width of Lower Electrode	49
2.2.2.5 Effect of Multiple Steady Actuators	51
2.2.3 Unsteady Actuator Measurements	53
2.2.4 Phased Actuator Measurements	57

CHAPTER 3: EXPERIMENTAL SETUP	63
3.1 Experimental Facility	63
3.2 Flow Visualization	65
3.3 Stationary Airfoil Setup	67
3.3.1 Pressure Data Acquisition	73
3.4 Oscillating Airfoil	76
3.4.1 Servo Motor	77
3.4.2 Servo Motor Position and Direction Circuit	80
3.4.3 Angle of Attack Indicator Circuit	84
3.4.4 "Smart" Actuation Circuit	87
3.4.5 Pressure Data Acquisition	90
 CHAPTER 4: SEPARATION CONTROL ON STATIONARY AIRFOILS . . .	98
4.1 NACA 66 ₃ - 018 Experiments	98
4.1.1 Baseline Measurements	98
4.1.2 Vortex Generators	101
4.1.3 Steady Actuation	103
4.1.4 Sensitivity to Actuator Amplitude	108
4.2 NACA 0015 Experiments	115
4.2.1 Steady Actuation	115
4.2.2 Unsteady Actuation	121
 CHAPTER 5: SEPARATION CONTROL ON OSCILLATING AIRFOIL . . .	125
5.1 Baseline Measurements	126
5.2 Effects of Different Oscillation Conditions on Dynamic Stall	128
5.2.1 Effect of Mean Angle of Attack	128
5.2.2 Effect of Freestream Velocity	131
5.2.3 Effect of Reduced Frequency	133
5.3 Steady Actuation	136
5.3.1 Effect of Different Oscillation Conditions	144
5.4 Unsteady Plasma Actuation	169
5.5 "Smart" Plasma Actuation	175
5.6 Comparison Between Plasma Actuation Approaches	180
5.6.1 Comparison of C_p Distributions	185
 CHAPTER 6: CONCLUSIONS & RECOMMENDATIONS	197
6.1 Conclusions	197
6.1.1 Plasma Actuator Optimization	197
6.1.2 Separation Control on Stationary Airfoils	199
6.1.3 Separation Control on Oscillating Airfoil	203
6.2 Recommendations	206
 APPENDIX A: SMARTMOTOR PROGRAM	208

APPENDIX B: MATLAB PROGRAMS	210
APPENDIX C: ERROR ANALYSIS	217
BIBLIOGRAPHY	230

TABLES

3.1	STATIC PRESSURE PORT LOCATIONS ON THE SURFACE OF THE AIRFOIL.	74
4.1	COMPARISON OF L/D WITH PLASMA ACTUATORS ON THE NACA 66 ₃ - 018 AIRFOIL FOR $Re_c = 79K$	106
C.1	SUMMARY OF THE UNCERTAINTY IN THE EXPERIMENT.	229

FIGURES

1.1	Schematic of types of passive vortex generators.	4
1.2	Methods to add high momentum fluid to the near-wall flow.	7
1.3	Unsteady periodic excitation concept for flow control.	8
1.4	Concept of the directed synthetic jet (DSJ).	10
1.5	Pressure and shear forces acting on an element of the airfoil surface. . . .	11
1.6	Schematic of the decomposition of resultant forces on and airfoil. Adapted from Leishman [37].	11
1.7	Qualitative comparison of the pressure distribution over an airfoil. Adapted from Anderson [2].	13
1.8	Schematic of why the retreating blade moves slower than the advancing blade.	14
1.9	Hovering lift pattern of a helicopter.	16
1.10	Normal cruise lift pattern of a helicopter.	16
1.11	Lift pattern of a helicopter at speeds where retreating blade stall occurs. .	17
1.12	Schematic of dynamic stall process. Adapted from Leishmann [37].	19
2.1	Schematic of asymmetric plasma actuator arrangement.	25
2.2	Photograph of the plasma actuator where plasma forms at and near the edge of the upper, exposed electrode over the insulated, lower electrode. From Enloe et al. [11].	25
2.3	Electrons emitted from the exposed electrode collect on the dielectric surface (left) and are returned on the subsequent half-cycle of the discharge (right). From Enloe et al. [11].	26
2.4	Block diagram of the electronic system.	31
2.5	Schematic of the circuit used to generate the plasma.	31
2.6	Schematic of the low-power amplifier circuit (1 channel).	32
2.7	Photograph of the low-power amplifier (12 channels).	32

2.8	Schematic of the high-power amplifier circuit (1 channel).	33
2.9	Illustration of plasma actuator time series used for unsteady actuation. . .	35
2.10	Schematic of circuit to generate the signal for the unsteady plasma actuation.	35
2.11	Two-frequency phased excitation to produce a uni-direction moving plasma wave for the phased plasma actuation.	37
2.12	Photograph of the setup used for plasma actuator optimization.	40
2.13	Ensemble average of 100 PIV images showing the average velocity vectors in the velocity field induced by a single plasma actuator under steady operation. Actuator is located at $x = 0$ mm.	42
2.14	$U \propto V^{7/2}$ relationship between actuator voltage amplitude input and induced velocity output for a single steady actuator (Triangle Waveform, Operating frequency: 5 kHz).	44
2.15	Comparison of maximum velocity output for various waveforms of the a.c. operating frequency.	46
2.16	Comparison of velocity output (square symbols) and power (triangle symbols) for different a.c. input operating frequencies.	48
2.17	Maximum velocity versus width of lower electrode for two a.c. input voltages of 12 kV _{p-p} and 16 kV _{p-p}	50
2.18	Relationship between actuator input amplitude voltage and velocity output for one and two steady actuators (Triangle Waveform, Operating frequency: 5 kHz).	52
2.19	Phase-averaged velocity vectors at different phases of the 0.5 Hz unsteady plasma actuator cycle.	54
2.20	Top: Velocity time response due to a step input of the actuator voltage for different amplitudes of a single, unsteady plasma actuator. Bottom: Time constants for different input voltage amplitudes for a single, unsteady plasma actuator (Triangle Waveform, Operating frequency: 5 kHz).	56
2.21	Box diagram of the method used to generate the PIV trigger signal. . . .	59
2.22	Schematic of the circuit used to generate a reference signal to trigger the PIV system at any time in the phased plasma cycle.	59
2.23	Phase-averaged velocity vectors at different time delays for an actuator difference frequency of 1 Hz.	60
2.24	Phase-averaged velocity vectors at the same phase trigger, at different frequencies of the plasma actuator.	62

3.1	Schematic of the open-return wind tunnel at the Center for Flow Physics and Control.	64
3.2	Photograph of the experimental facility.	64
3.3	Photograph of the smoke generator and close-up of the smoke rake. . . .	66
3.4	Sample flow visualization image for the NACA 66 ₃ – 018 airfoil at 16° angle of attack and a freestream velocity of 20 m/s (65.9 ft/s).	66
3.5	Aluminum mold used to cast the NACA 0015 airfoil.	68
3.6	Schematic drawing and photograph the NACA 66 ₃ – 018 airfoil with end plates. Dimensions are in inches.	70
3.7	Schematic drawing showing the locations and orientations of plasma actuators used for separation control on the NACA 66 ₃ – 018 and NACA 0015.	71
3.8	Photographs of the NACA 66 ₃ – 018 airfoil with plasma actuators at the leading edge and mid-chord locations (top) and lines of plasma when viewed in a darkened lab (bottom).	72
3.9	Static calibration curve for the Validyne pressure transducer.	74
3.10	Schematic drawing and photograph of the NACA 0015 airfoil with circular end plates. Dimensions are in inches.	78
3.11	Photograph of the motor on the back wall of the test section.	79
3.12	Schematic of the circuit that uses the motor encoder to determine the instantaneous airfoil position and direction.	82
3.13	Photograph of the servo motor position and direction circuit.	83
3.14	Oscilloscope trace of the sine input to the motor (top) and the actual position of the motor (bottom).	83
3.15	Schematic of the circuits that comprise the angle of attack indicator circuit.	85
3.16	Photograph of the angle of attack indicator circuit.	86
3.17	Schematic of the circuit that generates a signal for the “smart” actuation operation.	88
3.18	Photograph of the “smart” actuation circuit.	88
3.19	Oscilloscope trace of the 5 kHz used to generate the plasma (top) and the “smart” actuation trace (bottom).	89
3.20	Schematic of the circuit used to condition the output signal from the Scanivalve pressure transducer.	92
3.21	Photograph of the circuit used to condition the output signal from the Scanivalve pressure transducer.	92

3.22	Static calibration curve for the Scanivalve PDCR24 pressure transducer. .	93
3.23	Dynamic calibration of the Scanivalve PDCR24 pressure transducer. . . .	95
3.24	Phase lag of the Scanivalve PDCR24 pressure transducer.	95
4.1	Sample C_p distribution around the NACA 66 ₃ – 018 airfoil for $\alpha = 8^\circ$ and $Re_c = 75K$	99
4.2	Comparison between calculated lift coefficient values for a NACA 66 ₃ – 018 airfoil found by integrating C_p distribution, and those of Jansen [25] using a lift-balance at $Re_c = 75K$	100
4.3	Comparison between calculate lift coefficient values for a NACA 66 ₃ – 018 airfoil found by integrating C_p distribution, and those of Jansen [25] using a lift-balance at $Re_c = 200K$	100
4.4	Photograph of vortex generators used as a baseline flow reattachment device on the NACA 66 ₃ – 018 airfoil.	102
4.5	Comparison of C_p distributions on the NACA 66 ₃ – 018 airfoil at $Re_c = 79K$, without and with vortex generator tabs.	102
4.6	Photographs of visualized flow around the NACA 66 ₃ – 018 airfoil with plasma actuators off (top) and on (bottom) for $\alpha = 16^\circ$ and $Re_c = 79K$. .	105
4.7	Suction-side C_p distribution on the NACA 66 ₃ – 018 airfoil with plasma actuator off and on and comparison to vortex generator for $\alpha = 16^\circ$ and $Re_c = 79K$	105
4.8	Wake mean velocity distribution of the NACA 66 ₃ – 018 airfoil with the plasma actuator off and on for $\alpha = 16^\circ$ and $Re_c = 79K$	106
4.9	Photographs of visualized flow around the NACA 66 ₃ – 018 airfoil with plasma actuators off (top) and on (bottom) for $\alpha = 16^\circ$ and $Re_c = 158K$. .	109
4.10	Suction-side C_p distribution on the NACA 66 ₃ – 018 airfoil with plasma actuator off and on, and comparison to vortex generator for $\alpha = 16^\circ$ and $Re_c = 158K$	109
4.11	Comparison of lift coefficient versus angle of attack on the NACA 66 ₃ – 018 airfoil with the plasma actuator off and on at $Re_c = 158K$	110
4.12	Wake mean velocity distribution of the NACA 66 ₃ – 018 airfoil with the plasma actuator off and on for $\alpha = 16^\circ$ and $Re_c = 158K$	110
4.13	Comparison of drag coefficient versus angle of attack on the NACA 66 ₃ – 018 airfoil with the plasma actuator off and on at $Re_c = 158K$	111
4.14	Comparison of drag polars of the NACA 66 ₃ – 018 airfoil with the plasma actuator off and on at $Re_c = 158K$	111

4.15	Suction-side C_p distributions for different plasma actuator amplitudes at $\alpha = 16^\circ$ and $Re_c = 158K$	113
4.16	Wake mean velocity profiles for different plasma actuator amplitudes at $\alpha = 16^\circ$ and $Re_c = 158K$	113
4.17	Lift and drag coefficients for different plasma actuator amplitudes at $\alpha = 16^\circ$ and $Re_c = 158K$	114
4.18	Photographs of visualized flow around the airfoil with the plasma actuator off (top) and on (bottom) for $\alpha = 16^\circ$ and $Re_c = 158K$	116
4.19	Coefficient of pressure distribution on the NACA 0015 airfoil with the plasma actuator off and on for $\alpha = 16^\circ$ and $Re_c = 158K$	117
4.20	Comparison of lift coefficient versus angle of attack for the NACA 0015 airfoil with the steady plasma actuator off and on for $Re_c = 158K$	117
4.21	Wake mean velocity profiles for the NACA 0015 airfoil with the plasma actuator off and on at $\alpha = 16^\circ$ and $Re_c = 158K$	119
4.22	Comparison of drag coefficient versus angle of attack for the NACA 0015 airfoil with the plasma actuator off and on at $Re_c = 158K$	119
4.23	Photographs of visualized flow around the NACA 0015 airfoil with plasma actuators off (left) and on (right) at $Re_c = 158K$	120
4.24	Comparison of lift coefficient versus angle of attack for the NACA 0015 airfoil with the actuator off, steady actuator, and 160 Hz unsteady actuator for $Re_c = 158K$	123
4.25	Comparison of drag coefficient versus angle of attack for the NACA 0015 airfoil with the actuator off, steady actuator, and 160 Hz unsteady actuator for $Re_c = 158K$	123
4.26	Comparison of drag polars for the NACA 0015 airfoil with the actuator off, steady actuator, and 160 Hz unsteady actuator at $Re_c = 158K$	124
5.1	Baseline lift and moment coefficients for the NACA 0015 oscillatory airfoil where $\alpha(t) = 15^\circ + 10^\circ \sin \omega t$ and $k = 0.08$	127
5.2	Effect of varying the mean angle of attack on the lift coefficient (left) and moment coefficient (right), while the amplitude of oscillation is 10 degrees and $k = 0.08$	130
5.3	Effect of varying the freestream velocity on the lift coefficient (left) and moment coefficient (right) for $\alpha(t) = 15^\circ + 10^\circ \sin \omega t$ and $k = 0.08$	132
5.4	Effect of varying the reduced frequency on the lift coefficient (left) and moment coefficient (right) for $\alpha(t) = 15^\circ + 10^\circ \sin \omega t$ and $U_\infty = 10\text{m/s}$	134

5.5	Effect of varying the reduced frequency on the lift coefficient (left) and moment coefficient (right) for $\alpha(t) = 15^\circ + 10^\circ \sin \omega t$ and $U_\infty = 5\text{m/s}$. . .	135
5.6	Coefficient of pressures with the plasma actuator off (left) and on (right) for the upper surface of the airfoil during the pitch-up part of the cycle for $\alpha = 7^\circ$ to 25° in 2° increments for $\alpha(t) = 15^\circ + 10^\circ \sin \omega t$ and $k = 0.08$. . .	137
5.7	Flow visualization and pressure coefficient records for angles of attack near and at the peak of the oscillatory cycle for $\alpha(t) = 15^\circ + 10^\circ \sin \omega t$ and $k = 0.08$.	137
5.8	Flow visualization records with the plasma actuator off at $\alpha(t) = 15^\circ + 10^\circ \sin \omega t$ and $k = 0.08$	141
5.9	Flow visualization records with the steady plasma actuator on at $\alpha(t) = 15^\circ + 10^\circ \sin \omega t$ and $k = 0.08$	142
5.10	Comparison of lift coefficient (left) and moment coefficient (right) versus angle of attack with the plasma actuator off and on for the case of steady actuation at $\alpha(t) = 15^\circ + 10^\circ \sin \omega t$ and $k = 0.08$	143
5.11	Comparison of coefficient of lift versus angle of attack with the plasma actuator off and on for the case of steady actuation at $\alpha(t) = 10^\circ + 5^\circ \sin \omega t$ and $k = 0.08$	146
5.12	Flow visualization records with the plasma actuator off for the case of $\alpha(t) = 10^\circ + 5^\circ \sin \omega t$ and $k = 0.08$	147
5.13	Flow visualization records with the plasma actuator on for the case of steady actuation at $\alpha(t) = 10^\circ + 5^\circ \sin \omega t$ and $k = 0.08$	148
5.14	Comparison of coefficient of lift versus angle of attack with the plasma actuator off and on for the case of steady actuation at $\alpha(t) = 10^\circ + 10^\circ \sin \omega t$ and $k = 0.08$	150
5.15	Flow visualization records with the plasma actuator off for the case of steady actuation at $\alpha(t) = 10^\circ + 10^\circ \sin \omega t$ and $k = 0.08$	151
5.16	Flow visualization records with the plasma actuator on for the case of steady actuation at $\alpha(t) = 10^\circ + 10^\circ \sin \omega t$ and $k = 0.08$	152
5.17	Comparison of coefficient of lift versus angle of attack with the plasma actuator off and on for the case of steady actuation at $\alpha(t) = 12^\circ + 8^\circ \sin \omega t$ and $k = 0.08$	154
5.18	Flow visualization records with the plasma actuator off for the case of steady actuation at $\alpha(t) = 12^\circ + 8^\circ \sin \omega t$ and $k = 0.08$	155
5.19	Flow visualization records with the plasma actuator on for the case of steady actuation at $\alpha(t) = 12^\circ + 8^\circ \sin \omega t$ and $k = 0.08$	156
5.20	Comparison of coefficient of lift versus angle of attack with the plasma actuator off and on for the case of steady actuation at $\alpha(t) = 15^\circ + 5^\circ \sin \omega t$ and $k = 0.08$	158

5.21	Flow visualization records with the plasma actuator off for the case of steady actuation at $\alpha(t) = 15^\circ + 5^\circ \sin \omega t$ and $k = 0.08$	159
5.22	Flow visualization records with the plasma actuator on for the case of steady actuation at $\alpha(t) = 15^\circ + 5^\circ \sin \omega t$ and $k = 0.08$	160
5.23	Comparison of coefficient of lift versus angle of attack with the plasma actuator off and on for the case of steady actuation at $\alpha(t) = 18^\circ + 10^\circ \sin \omega t$ and $k = 0.08$	162
5.24	Flow visualization records with the plasma actuator off for the case of steady actuation at $\alpha(t) = 18^\circ + 10^\circ \sin \omega t$ and $k = 0.08$	163
5.25	Flow visualization records with the plasma actuator on for the case of steady actuation at $\alpha(t) = 18^\circ + 10^\circ \sin \omega t$ and $k = 0.08$	164
5.26	Comparison of coefficient of lift versus angle of attack with the plasma actuator off and on for the case of steady actuation at $\alpha(t) = 20^\circ + 10^\circ \sin \omega t$ and $k = 0.08$	166
5.27	Flow visualization records with the plasma actuator off for the case of steady actuation at $\alpha(t) = 20^\circ + 10^\circ \sin \omega t$ and $k = 0.08$	167
5.28	Flow visualization records with the plasma actuator on for the case of steady actuation at $\alpha(t) = 20^\circ + 10^\circ \sin \omega t$ and $k = 0.08$	168
5.29	Comparison of lift coefficient (left) and moment coefficient (right) versus angle of attack with the plasma actuator off and on for the case of 80 Hz unsteady plasma actuation at $\alpha(t) = 15^\circ + 10^\circ \sin \omega t$ and $k = 0.08$	171
5.30	Comparison of lift coefficient (left) and moment coefficient (right) versus angle of attack with the plasma actuator off and on for the case of 20 Hz unsteady plasma actuation at $\alpha(t) = 15^\circ \pm 10^\circ \sin \omega t$ and $k = 0.08$	171
5.31	Flow visualization records for the unsteady plasma actuator at 20 Hz.	172
5.32	Flow visualization records with the unsteady plasma actuator at 20 Hz. for the airfoil with $\alpha(t) = 15^\circ + 10^\circ \sin \omega t$ and $k = 0.08$	174
5.33	Comparison of lift coefficient (left) and moment coefficient (right) versus angle of attack with the plasma actuator off and on for the case of "smart" plasma actuation at $\alpha = 15^\circ + 10^\circ \sin \omega t$ and $k = 0.08$	177
5.34	Flow visualization records with the "smart" plasma actuator on at $\alpha(t) = 15^\circ + 10^\circ \sin \omega t$ and $k = 0.08$	179
5.35	Flow visualization records at $\alpha = 15^\circ$, $\alpha = 11^\circ$, and $\alpha = 7^\circ$ while the airfoil is pitching down for no actuation, steady plasma actuation, unsteady plasma actuation, and "smart" actuation.	181
5.36	Effect of steady, unsteady, and "smart" actuation on the lift coefficient (left) and moment coefficient (right) for $\alpha(t) = 15^\circ + 10^\circ \sin \omega t$ and $k = 0.08$	182

5.37	Percent lift improvement for plasma controlled cases.	184
5.38	Comparing the coefficient of pressure on the suction-side of the airfoil for the no actuation and steady actuation cases.	187
5.39	Difference between the coefficient of pressure for the no actuation and steady actuation cases.	188
5.40	Comparing the coefficient of pressure on the suction-side of the airfoil for the no actuation, 20 Hz unsteady, and 80 Hz unsteady actuation cases. . .	190
5.41	Difference between the coefficient of pressure for the no actuation and unsteady actuation cases.	191
5.42	Comparing the coefficient of pressure on the suction-side of the airfoil for the no actuation and "smart" actuation cases.	194
5.43	Difference between the coefficient of pressure for the no actuation and "smart" actuation cases.	195
5.44	Difference between the coefficient of pressure for the no actuation, 20 Hz unsteady actuation, and "smart" actuation cases.	196
C.1	Sources of error and their propagation.	218
C.2	Geometric relationship between airfoil and the test section floor.	222

SYMBOLS

English symbols

a	rotor blade aspect ratio (defined Equation 1.10)
$a.c.$	alternating current
c	chord
C	capacitor
C_a	axial force coefficient (defined Equation 3.4)
C_n	normal force coefficient (defined Equation 3.3)
C_d	coefficient of drag (defined Equation 3.5)
C_l	coefficient of lift (defined Equation 3.2)
C_p	coefficient of pressure (defined Equation 3.1)
$C_{m_{LE}}$	moment coefficient about airfoil leading edge (defined Equation 3.11)
$C_{m_{1/4}}$	moment coefficient about airfoil quarter-chord (defined Equation 3.12)
$d.c.$	direct current
DSJ	directed synthetic jet
DSV	dynamic stall vortex
e	electronic charge
E	electric field strength
f	frequency of the imposed disturbance
f_c	filter cut-off frequency (defined Equation 3.7)
f_1	frequency to lower electrodes for phased operation
f_2	frequency to upper electrodes for phased operation
$F+$	dimensionless frequency (defined Equation 1.3)
F_B	body force vector (defined Equation 2.10)

h	height
H	total test section height
I	current
k	reduced frequency (defined Equation 1.9)
k	Boltmann's constant
L	length from 1st to N th actuator for phased actuation operation
n_e	electron density (defined Equation 2.2)
n_i	ion density (defined Equation 2.1)
n_o	background plasma density
N	number of electrodes for phased actuation operation
P	local pressure
P_∞	freestream pressure
PIV	particle image velocimetry
R	radius of the rotor
R	resistor
Re_c	chord Reynolds number
RF	ratio-frequency
RBS	Retreating Blade Stall
s	arc length
t	time
T	temperature
U	local velocity
U_∞	freestream velocity
U_p	phase velocity for phased actuation (defined Equation 2.13)
V	voltage
V_{p-p}	peak-to-peak voltage
V_{rms}	root-mean-square voltage
VG	vortex generators

x	distance in the x-direction
x_s	streamwise length of the separated region
y	distance in the y-direction
z	distance in the z-direction

Greek symbols

α	angle of attack
α_0	mean angle of attack
α_1	alternating angle of attack
δ	boundary layer thickness
Δ	change in
ϵ_o	permittivity of free space
λ_D	Debye length (defined Equation 2.6)
ξ	damping factor (defined Equation 3.9)
ρ	net charge density (defined Equations 2.3 and 2.8)
ρ	local fluid density
ρ_∞	freestream fluid density
τ	period
τ	shear stress force
ϕ	local electric potential
Ω	ohms
ω	physical pitch oscillating frequency

CHAPTER 1

INTRODUCTION

1.1 Motivation

The maximum lift and stall characteristics of a wing affect many performance aspects of aircraft. These include take-off and landing distance, maximum and sustained turn rates, climb and glide rates, and flight ceiling [6]. In a 2-D wing, the maximum achievable lift is ultimately limited by the ability of the flow to follow the curvature of the airfoil. When it cannot, the flow separates. In some cases, this first occurs at the leading edge.

One solution to prevent leading-edge separation is to increase the leading-edge radius. This is the principle effect of a leading-edge flap. An example is a Krueger flap, which consists of a hinged surface on the lower side of the wing leading edge that can extend out and ahead of the wing leading edge. A slotted leading-edge flap (slat) is the leading edge equivalent of the trailing-edge slotted flap. It works by allowing air from the high pressure lower surface to flow to the upper surface to add momentum to the boundary layer, thus preventing flow separation.

Although these leading-edge devices are effective, they have some drawbacks. In particular they are complicated, add weight to the wing, take volume from inside

the wing when not in use, and can be major sources of airframe noise and vibration. Therefore, if they can be replaced by other flow control devices, there could be a number of benefits.

Helicopter rotors are wing sections which have the added complication that they need to cycle in angle of attack to control the lift vector for translational flight. During portions of the retreating phase of the rotor, the rotor flow separates (stalls) due to a combination of high angles of attack and a lower effective velocity. This ultimately limits the payload capability and flight performance of the helicopter and adds large cyclic loads to the helicopter structure.

The passive devices typically effective on fixed wings are impractical on helicopter rotors because they would have to be deployed in a rapid, time-dependent manner in the rotor cycle. In addition, the helicopter rotor is a finely engineered composite structure that has to be able to withstand high centrifugal loading. Any moving or deployable elements on the rotor would be subjected to the same high loading levels. Even the addition of slots or internal cavities in the rotor could present a significant compromise in the structural integrity of the rotor.

1.2 Background

This section provides background information on separation control techniques, airfoil aerodynamics, and rotor aerodynamics.

1.2.1 Separation Control Techniques

Attempted solutions to flow separation include prevention, reduction, or elimination. Several flow control techniques that have been investigated for leading-edge separation include (but are not limited to) boundary layer mixing [4, 65], removal of low-momentum from near-wall flow [14, 60], and momentum addition to near-wall flow [44, 61].

Separation of flow from a surface is governed by the adverse pressure gradient and viscosity. To remain attached to the surface, the flow must have sufficient momentum to overcome the adverse pressure gradient. When it does not, the flow *separates* from the surface. Techniques for separation control are designed to augment the momentum level by a device or actuator at the appropriate position along the flow path. This section introduces the following approaches:

1. Boundary Layer Mixing (ie. vortex generators)
2. Removal of Low-Momentum from Near-Wall Flow (ie. wall suction)
3. Momentum Addition to Near-Wall Flow (ie. a tangential wall jet)

Boundary Layer Mixing

The purpose of boundary layer mixing is to transport momentum from the freestream to the boundary layer. One technique to induce boundary layer mixing is vortex generators (VG). These devices are small plates or airfoils mounted normal the surface and set at an angle of incidence with respect to the local flow direction. The

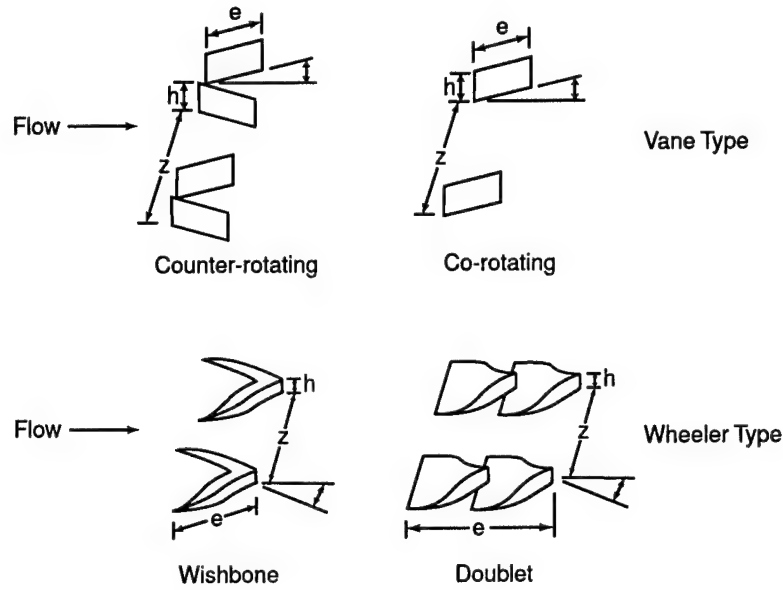


Figure 1.1. Schematic of types of passive vortex generators.

result is an array of near-wall, streamwise vortices embedded within the boundary layer. These streamwise vortices bring high momentum fluid from the freestream into the boundary layer to prevent flow separation.

Passive vortex generators have been in use since the 1940's [67]. A schematic of the various types of vortex generators is shown in Figure 1.1. The VG height, h , is typically on the order of the boundary layer thickness, δ . The spacing between individual generators is important. Too closely spaced co-rotating vortices combine to form one large vortex. Large counter-rotating vortices force regions of vorticity to rise above the surface reducing the effectiveness of the VG.

Schubauer and Spangenberg investigated the effect of fixed, vortex generators on the boundary layer on a flat plate [65]. They found that mixing on a coarse scale by relatively large, widely-spaced devices was far more effective than fine-scale mixing

and that multiple rows were less effective than a single row of devices properly-spaced and stationed. It was concluded that forced mixing (with VG devices) had “basically” the same effect on the boundary layer as a general reduction in pressure gradient.

Low-profile vortex generators are defined as those with a device height, h , between 10% and 50% of the boundary layer thickness. These devices are most useful where flow separation locations are reasonably fixed. When placed just upstream of the point of separation, they can produce streamwise vortices that are strong enough to overcome the separation, but that do not persist downstream in the boundary layer once separation control has been achieved.

The device-induced streamwise vortices can last up to $100h$ [38, 39], with most effective range of low-profile VGs to be about $5h - 30h$ upstream of the point of separation. Due to the simplicity of the vortex generators, they have been frequently applied, but the effectiveness of this method can be limited because of their parasitic drag.

Removal of Low-Momentum from Near-Wall Flow

Boundary layer suction is used to prevent laminar or turbulent separation by removing the low momentum flow from the boundary layer. The principle is to remove the decelerated fluid before it can separate from the surface. Removing the fluid in the near-wall region increases the velocity gradient and curvature of the velocity profile near the surface. This leads to a fuller profile that can withstand the adverse pressure gradient so the flow can remain attached.

There are two techniques for suction; discrete (slot) suction and continuous suction. Discrete suction abruptly decreases the pressure at the location of the slot. Continuous suction is done through a porous surface, which allows for a gradual decrease in pressure along the surface.

One major concern with the suction technique on an operational wing is surface contamination. Contamination caused by ice, rain, dust, pollen, and insects may block suction slots or holes, and therefore reduce their effectiveness. Another concern is that the development of a boundary layer suction system is quite complicated. It involves considerations on the power required, the optimum slot placement, and structural modifications to include suction chambers [16]. These issues have generally discouraged the suction technique as a flow control device on the wings of aircraft.

Momentum Addition to Near-Wall Flow

High momentum flow supplied to the boundary layer is another method for controlling flow separation. This can be done actively by discharging fluid from the body by blowing, or passively by providing a passage from a higher pressure portion of the body, such as the approach of a leading-edge slat. These two methods are illustrated schematically in Figure 1.2.

Leading-edge Slat

A slotted leading-edge flap (slat) works by allowing air from the high-pressure lower surface to flow to the upper surface to add momentum to the boundary layer and prevent flow separation. Unfortunately, the leading-edge slat, under certain flight

Momentum Addition to Near-Wall

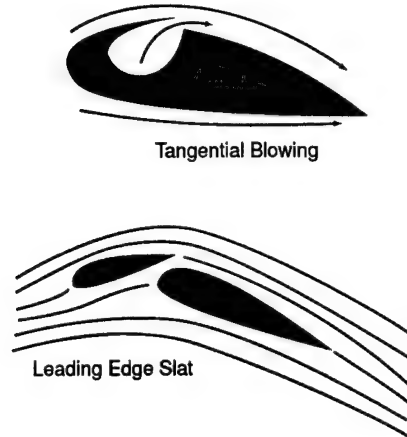


Figure 1.2. Methods to add high momentum fluid to the near-wall flow.

conditions, can be a major source of airframe noise. Broadband noise has been attributed to the interaction of the reattached shear layer in the slat cusp with the slat trailing edge. Tonal noise sources associated with the leading-edge slat are due to trailing edge vortex shedding [48]. Much effort is underway to determine the physics behind the sources of noise and to apply this knowledge to developing noise reduction technologies [33, 45, 48].

Tangential Steady Blowing

The blowing of a thin jet upstream or in the region of separation increases the momentum in the boundary layer and can be an effective method of controlling flow separation. The momentum lost in the boundary layer caused by the adverse pressure gradient is replaced with the momentum of fluid blowing tangentially from the wall.

In general, blowing techniques are very effective in controlling separation; however, to obtain this degree of control requires the complexity and cost of internal piping from a pressure source. Compressed air from a jet engine compressor may be used with the high pressure air bled through a choked blowing slot [5]. Such high pressure air allows the use of relatively small interior piping. Suction control, on the other hand, while more efficient than blowing usually requires more piping [17].

Unsteady Forcing

Both tangential blowing and the generation of vortices through vortex generators have separately been proved to be successful approaches for controlling the boundary layer [5, 65]. Unsteady forcing is intended to combine these effects. It involves pulsing the wall-jet at a discrete frequency in a way that will produce coherent vortices. The frequency sets the streamwise spacing of the vortices. Figure 1.3 illustrates this concept. In some cases, the method can act on a natural stability of the separated shear layer and thereby amplify the unsteady disturbance. This method can be further enhanced by a small amount of steady blowing in addition to the unsteady forcing [61].



Figure 1.3. Unsteady periodic excitation concept for flow control.

Periodic excitation by oscillatory blowing has been documented extensively by Seifert et al. [61, 62, 63, 64] and in the review by Greenblatt and Wygnanski [22]. The effectiveness of this method is largely determined by the response of the flow to the imposed disturbances. There is generally an optimum location and frequency for this approach. The optimum location to introduce the unsteady disturbances is generally near the point of flow separation.

The optimum frequency was found to scale with the length of the separation region and the freestream speed [44]. This is defined as the dimensionless frequency, F^+ , given as

$$F^+ = \frac{f x_s}{U_\infty}, \quad (1.1)$$

where f is the frequency of the imposed disturbance, x_s is the streamwise length of the separated region, and U_∞ is the freestream velocity. The reduced frequency of $F^+ = 1$ has been found to be optimal to control separation [44, 62]. This nominally results in nominally 2-3 coherent structures in the length of the separated region.

Directed synthetic jets (DSJ) [20, 44, 66] use the same concept of unsteady forcing to control separation, except the frequency is chosen to give a “synthetic jet effect,” that enhances entrainment of ambient air. The DSJ is illustrated schematically in Figure 1.4. The “synthetic jet effect” occurs when over the period of the acoustic sound cycle a fluid element moves the complete length of the orifice neck. This leads to a resonance that amplifies the motion of the fluid and produces a large amplitude response. The orifice orients the directed jet along the surface like a tangential jet. The effect is similar to an unsteady wall-jet.

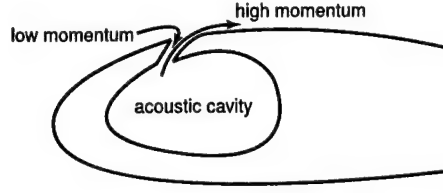


Figure 1.4. Concept of the directed synthetic jet (DSJ).

1.2.2 Airfoil Aerodynamics

Airfoils are two-dimensional wing sections or “lifting-surfaces.” The resultant forces and moments acting on an airfoil are the net result of the action of the distributed pressure around the airfoil surface and viscous shear forces at the surface. Figure 1.5 shows the pressure and shear forces acting on an element of the airfoil surface. The resultant force and moment are obtained by integrating the elemental pressure and shear forces around the airfoil. These forces can be resolved into a chord-axis system, with normal and axial forces, or a wind-axis system, with lift and drag forces. A schematic of the decomposition of these forces on an airfoil is shown in Figure 1.6.

For the normal and lift forces, the pressure force dominates, and the surface shear force contribution is negligible. For the axial and drag forces, the shear stress contribution has a measurable effect and must be taken into account. The surface pressure is typically presented in terms of a pressure coefficient, C_p . In compressible flow, the definition of the coefficient of pressure comes from Bernoulli’s equation,

$$p_\infty + \frac{1}{2}\rho_\infty U_\infty^2 = p + \frac{1}{2}\rho_\infty U^2 \quad (1.2)$$

where p and U are the local pressure and velocity and p_∞ , ρ_∞ , and U_∞ refer to

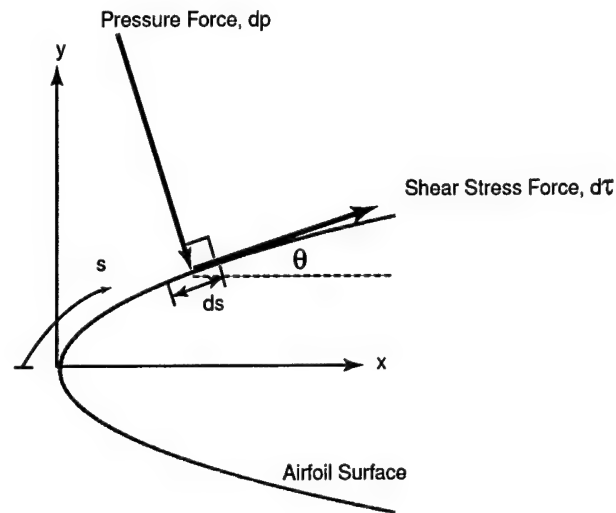


Figure 1.5. Pressure and shear forces acting on an element of the airfoil surface.

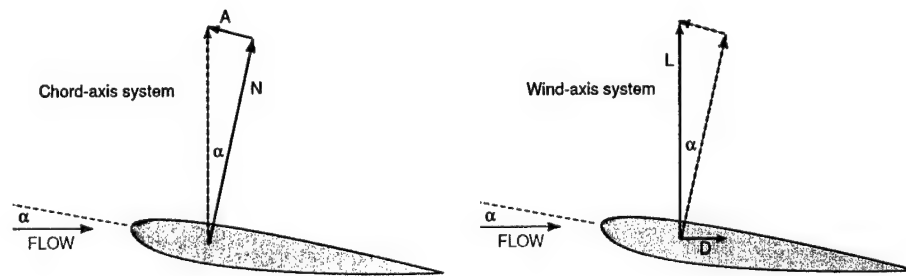


Figure 1.6. Schematic of the decomposition of resultant forces on and airfoil. Adapted from Leishman [37].

the pressure, fluid density, and velocity in the freestream. The pressure coefficient is defined as the difference between local and freestream pressure divided by the dynamic pressure in the freestream,

$$C_p = \frac{p - p_\infty}{\frac{1}{2}\rho_\infty U_\infty^2}. \quad (1.3)$$

For an airfoil, the normal, axial, and moment force coefficients can be expressed in terms of the coefficient of pressure, as

$$C_n = \int_0^1 (C_p^L - C_p^U) d\left(\frac{x}{c}\right), \quad (1.4)$$

$$C_a = \int_0^1 \left(C_p^U \left(\frac{dy_U}{dx} \right) - C_p^L \left(\frac{dy_L}{dx} \right) \right) d\left(\frac{x}{c}\right), \quad (1.5)$$

and

$$C_{m_{LE}} = -\frac{1}{c^2} \int_0^1 (C_p^L - C_p^U) \frac{x}{c} d\left(\frac{x}{c}\right). \quad (1.6)$$

where the superscripts L and U refer to the lower and upper airfoil surfaces, respectively. $C_{m_{LE}}$ represents the moment about the airfoil leading edge.

The normal force coefficient can be used interchangeably with the lift coefficient at small angles of attack. However, it is most accurate to calculate the lift coefficient from both the normal and axial forces and the angle of attack as

$$C_l = C_n \cos \alpha - C_a \sin \alpha. \quad (1.7)$$

The total drag coefficient on the airfoil can be determined by a mean velocity profile taken in the wake. This is given as

$$C_d = \frac{4}{U_\infty^2} \int_0^1 U(y)(U_\infty - U(y)) d\left(\frac{y}{H}\right) \quad (1.8)$$

where $U(y)$ is the local mean streamwise velocity, and H is a distance which encompasses the full wake.

Figure 1.7 illustrates a qualitative comparison of the pressure distribution over an airfoil at a high angle of attack with and without the flow separating at the leading edge. When the flow separates, the pressure distribution on the bottom surface does not change. However on the upper surface, the separated flow results in a higher absolute pressure so that the difference between the upper and lower surface is less. Therefore, the lift is lower when the flow separates. In addition to the loss of lift, there is an increase in drag caused by flow separation, so the lift-to-drag ratio decreases significantly. A summary of airfoil characteristics are compiled by Abbott and von Doenoff [1]. These include lift coefficients and drag polars versus angle of attack up to and past where separation occurs.

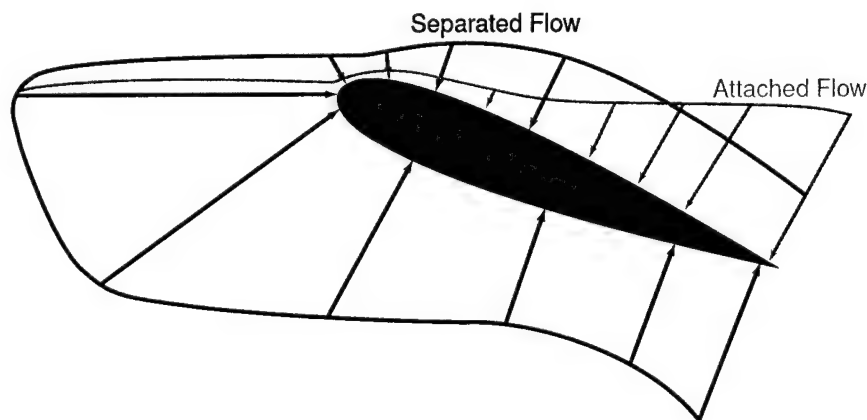


Figure 1.7. Qualitative comparison of the pressure distribution over an airfoil. Adapted from Anderson [2].

1.2.3 Helicopter Aerodynamics

Current rotorcraft designs require significant improvements to accommodate the demands for high performance. In helicopters and other rotorcraft, retreating blade stall (RBS) is the problem that establishes the limits on rotor load and flight speed and subsequently maneuverability and undesirable acoustics.

The retreating blade is the rotor blade that is moving in the opposite direction compared to the flight. This is illustrated in Figure 1.8. The airspeed of the retreating blade decreases as forward speed increases. As the airspeed of the retreating blade decreases, the blade angle of attack must be increased in order to equalize the lift throughout the blade rotation cycle. Increasing the angle of attack of the retreating blade can eventually cause the flow to separate (stall). This ultimately limits the forward flight speed.

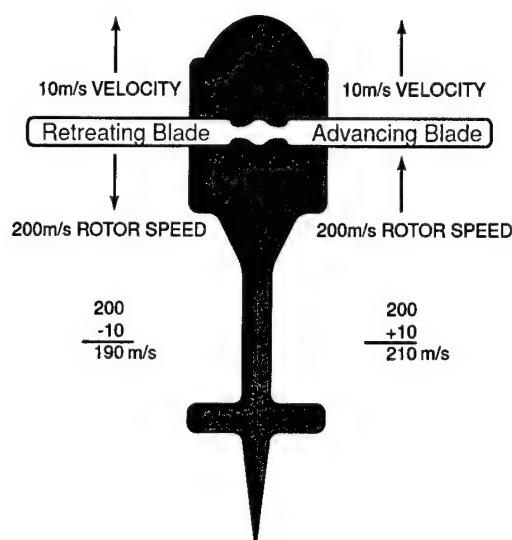


Figure 1.8. Schematic of why the retreating blade moves slower than the advancing blade.

The hovering lift pattern for a helicopter is shown in Figure 1.9. A small, no-lift area surrounds the blade root area. As the forward speed of the rotorcraft increases to a normal cruise speed, the no-lift area moves from the center toward the retreating side. This is illustrated in Figure 1.10. In order to compensate for the loss of lift of the inboard retreating sections, more lift is required on outbound sections. This is achieved by increasing the angle of attack of the retreating blade.

The mechanism for the lift distribution on the retreating blade involves a reverse flow region and areas of negative stall and negative lift. In the area of reversed flow, the rotational velocity of this blade section is slower than the airspeed, so that the air flows in the reverse direction from the trailing edge to the leading edge. In the areas of negative stall and negative lift, the local velocity of this blade section is faster than the airspeed; however, other issues inhibit having a positive angle of attack. Therefore, a negative lift force is generated. As a result, the remaining area of the retreating blade must produce all of the positive lift needed to match the entire advancing blade. The retreating blade must operate at much higher angles of attack compared to the advancing blade. To accomplish this, the rotor angle of attack will pitch up in the retreating part and down in the advancing part.

The lift pattern at airspeeds where retreating blade stall occurs is shown in Figure 1.11. The no-lift area stretches further from the blade root to the retreating blade, and also extends to cover large portions of the blade tip region. When the area near the tip of the blade stalls, vibration and noise begin. At even greater angles of attack, the stall area spreads inward, causing the helicopter to pitch up and roll left.

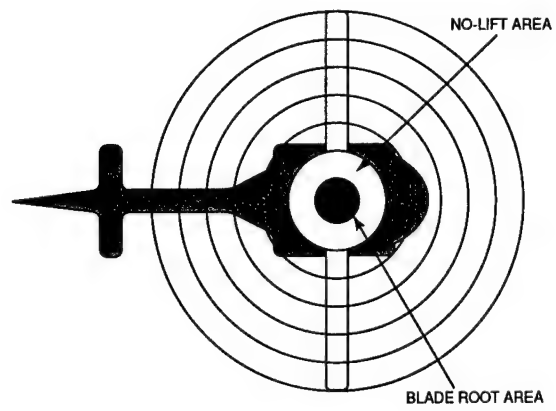


Figure 1.9. Hovering lift pattern of a helicopter.

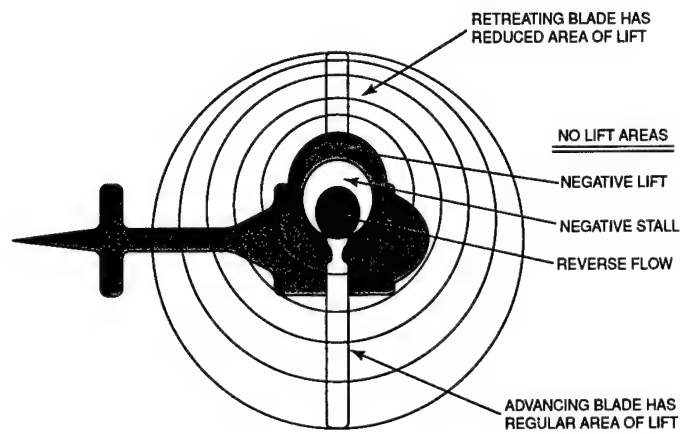


Figure 1.10. Normal cruise lift pattern of a helicopter.

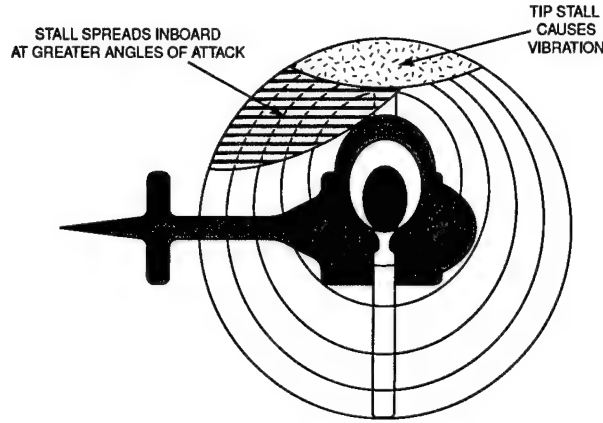


Figure 1.11. Lift pattern of a helicopter at speeds where retreating blade stall occurs.

One important non-dimensional parameter used in rotor aerodynamics is the reduced frequency. This parameter is used to characterize the degree of unsteadiness that occurs in the pitching rotor flowfield. The reduced frequency, k , is normally defined as

$$k = \frac{\omega c}{2U_{\infty}}, \quad (1.9)$$

where ω is the physical pitch oscillating frequency, c is the airfoil chord, and U_{∞} is the freestream velocity. For $k = 0$ the flow is steady. For $0 \leq k \leq 0.05$ the flow is quasi-steady, meaning the unsteady effects are small and for some problems can be negligible. Flow with $k > 0.05$ are considered unsteady. The blade aspect ratio, a , is defined as

$$a = \frac{R}{c} \quad (1.10)$$

where R is the radius of the rotor and c is the chord. For a typical helicopter rotor with blade aspect ratio $R/c \approx 10$, the reduced frequency is 0.07, which is in the unsteady range.

1.2.3.1 Dynamic Stall

Dynamic stall will occur on any airfoil when it is subjected to time-dependent unsteady motion that takes the effective angle of attack above its normal static stall angle [37]. The dynamic stall physics of flow separation are fundamentally different from static stall. Dynamic stall is characterized by the shedding of a concentrated vortical disturbance from the leading edge of the airfoil, namely the dynamic stall vortex (DSV). While the vortical disturbance remains over the suction surface of the airfoil, it acts to enhance the lift being produced. Once the disturbance is convected off the airfoil, a drastic drop in lift results.

A schematic detailing several stages of the dynamic stall process is shown in Figure 1.12. During stage 1, the airfoil exceeds the static stall angle and flow reversals take place in the boundary layer. Stage 2 involves the flow separation and the formation of a vortex at the leading edge of the airfoil. The onset of dynamic stall is indicated by the rapid drop in the moment coefficient. In stage 3, the vortex convects over the airfoil. This provides additional lift as long as it stays over the airfoil. During stage 4, the flow progresses to a state of full leading-edge separation, which is accompanied by a sudden loss of lift and increase in drag. Flow reattachment occurs once the angle of attack of the airfoil is low enough. This defines stage 5. Full flow reattachment may not occur until well below the normal static stall angle because there is a general lag in reorganization of the flow following the fully separated state.

The knowledge of the effects of unsteady motion on unsteady airfoils and dynamic flow separation are mainly based on research on oscillating airfoils in wind tunnel experiments [26, 27, 28, 30, 31, 34, 35, 40, 47, 68]. This simulates the quasi-periodic first harmonic angle of attack vibrations that are found on helicopter rotors during forward flight.

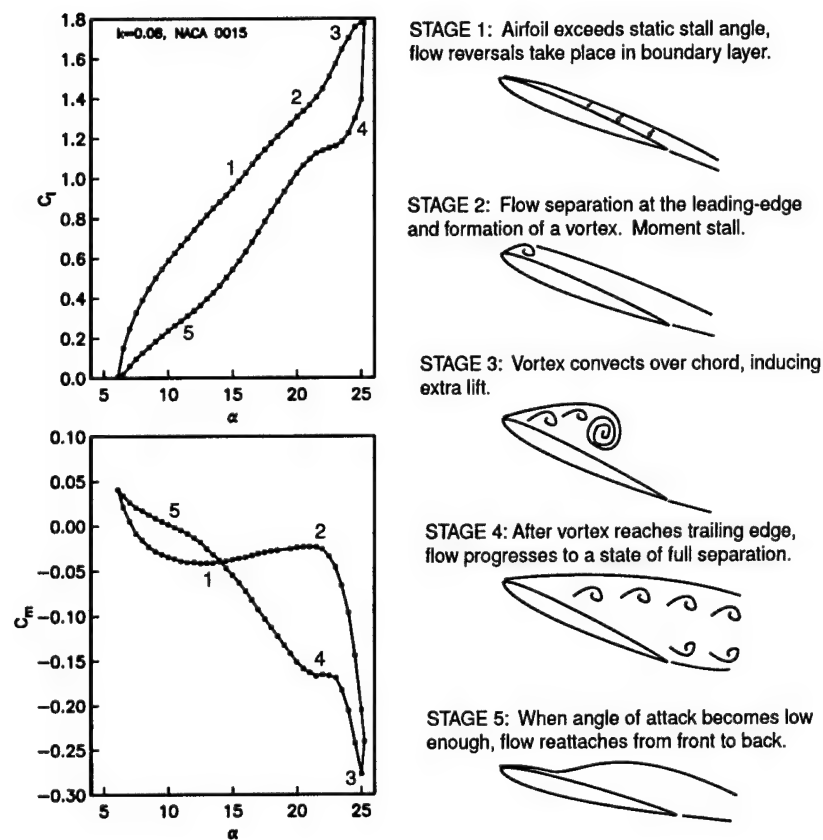


Figure 1.12. Schematic of dynamic stall process. Adapted from Leishmann [37].

1.2.3.2 Controlling Retreating Blade Stall

Flow control on a helicopter rotor is complicated. Rotors operate under unsteady, compressible, high Reynolds number flow conditions. Therefore, to be effective, retreating blade stall must be controlled in unsteady, compressible, high Reynolds number flow. At the same time, the control must not create a significant drag penalty on the advancing blade.

Mechanical high lift devices, such as leading-edge slats, have been investigated and found able to delay dynamic stall [40]. The disadvantages of these devices is that they create drag on the advancing blade, and deploying and retracting them each rotor revolution is impractical. Steady blowing [68] and suction [30] have also been investigated as retreating blade stall control techniques. Acharya et al. demonstrated that suction could be used to completely suppress the dynamic stall vortex [30, 31, 34, 35]. However, using either blowing or suction techniques on a helicopter presents significant difficulties. For example, transferring sufficient fluid to or from the fixed system to the rotating system is challenging.

Unsteady forcing has been shown to be an effective method for controlling incompressible dynamic stall [22, 61, 62, 63, 64]. Nagib et al. demonstrated effective control on lift, moment, and drag coefficients on an oscillating VR-7 airfoil using unsteady forcing [47]. The authors found that the efficiency of forcing diminished with increasing Mach number. Therefore, this technique is limited by the ability to generate adequate forcing conditions at helicopter operating conditions.

1.3 Research Overview and Objectives

Given the importance of separation control associated with retreating blade stall on helicopters, the primary objective of this work was to develop a plasma actuator flow control device for its use in controlling leading-edge separation on stationary and oscillating airfoils.

The approach to separation control used in this work is with the plasma actuator [9, 52]. The idea behind developing any new and innovative technology, including a new flow control device, is first to understand the important parameters behind its performance. At the onset of this research, little was known about the physics or effects of the plasma actuator. Therefore, it was necessary to first experimentally investigate and characterize the effects of a single-dielectric barrier discharge plasma actuator through a systematic set of experiments. The physical actuator configuration, input versus output relations, and different types of operation (steady and unsteady) were investigated. The results were extremely important to optimizing the actuator.

With this knowledge, the plasma actuator was used in controlling leading-edge separation control for the direct application of controlling retreating blade stall. The separation control effectiveness was documented on both stationary and oscillating airfoils. This was based on flow visualization, pressure coefficient measurements on the surface of the airfoil, and mean velocity measurements in the wake of the airfoil.

Chapter 2 presents the theory and optimization of the plasma actuator. It describes the physical configuration, electronics used to generate the plasma, and operation of the actuator, as well as the fluid response to the actuator. Chapter 3 documents the experimental facilities and instrumentation used for this study. Chapter 4 embodies the results of the separation control using the plasma actuator on a stationary airfoil. Chapter 5 presents the results of the plasma actuator for separation control on the oscillating airfoil. Conclusions from this work and recommendations for future work are in Chapter 6.

CHAPTER 2

THE PLASMA ACTUATOR: THEORY & OPTIMIZATION

This chapter describes the theory behind and the optimization of the plasma actuator that was used throughout the experimental study for separation control. It builds on extensive experimental development and numerical modeling of weakly-ionized plasma actuators for flow control applications by the Notre Dame group. The applications include leading-edge separation control related to helicopter retreating-blade stall (Post, 2001 [52]; Post and Corke, 2003 [54, 55]); trailing-edge separation control on turbine blades in the low-pressure turbine stage of turbo-jet engines (Huang, Corke and Thomas, 2003 [24]); active lift enhancement on wings (Corke et al., 2002 [8]); control of boundary layer instabilities at Mach 3.5 (Corke and Matlis, 2002 [9]); and turbulence-transition control in 3-D boundary layers on highly swept wings (Saric, 2002).

2.1 Background

The plasma actuator consists of two metal electrodes separated by a dielectric insulator, as illustrated in Figure 2.1. The upper electrode is exposed to the surrounding

air and the lower electrode is completely insulated. The geometry of the electrodes used most often is asymmetric with a small amount (order of a mm) of overlap.

In this work, the electrodes were made from 0.025 mm thick copper tape. The dielectric insulator was Kapton film tape. Kapton was selected for its electrical properties, which are a high volume resistivity of $10^{17}\Omega\text{-cm}$, high dielectric constant of 2.8, and dielectric strength of 3900 V/mil [15]. Different thicknesses of Kapton film were used. These ranged from 2-mil to 5-mil.

A high voltage a.c. potential is supplied to the electrodes. When the input amplitude is sufficiently high, the air ionizes and forms plasma in the region of largest electric field potential. The plasma forms from the overlapped edge of the upper (exposed) to the area that is over the lower insulated electrode. A photograph of the plasma as it appears in the asymmetric electrode arrangement is shown in Figure 2.2.

The plasma discharge from the actuator is a single dielectric barrier discharge. It has the property that it is self-limiting and therefore stable at atmospheric pressures [11, 12]. During the a.c. cycle, the electrons and ions move according to the electric potential, as shown in Figure 2.3. In one-half of the cycle, electrons move from the exposed electrode to the surface of the dielectric. The buildup of charge on the dielectric will eventually balance the a.c. potential so the plasma generation will stop. This is the self-limiting aspect of the dielectric barrier that prevents a cascade of charges that would cause an electric arc.

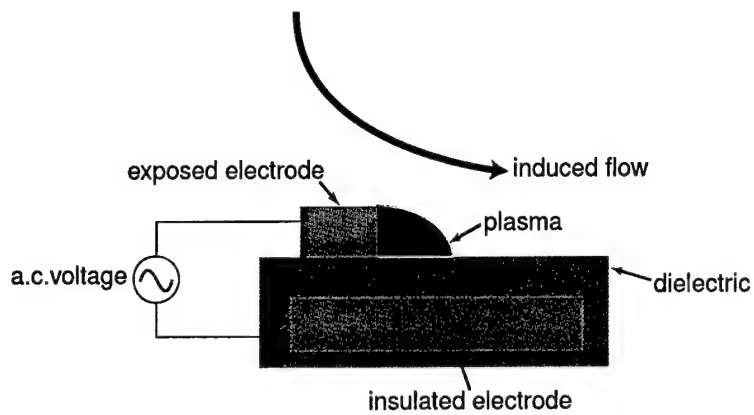


Figure 2.1. Schematic of asymmetric plasma actuator arrangement.

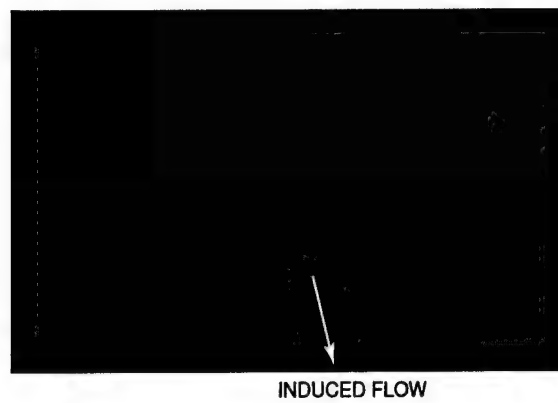


Figure 2.2. Photograph of the plasma actuator where plasma forms at and near the edge of the upper, exposed electrode over the insulated, lower electrode. From Enloe et al. [11].

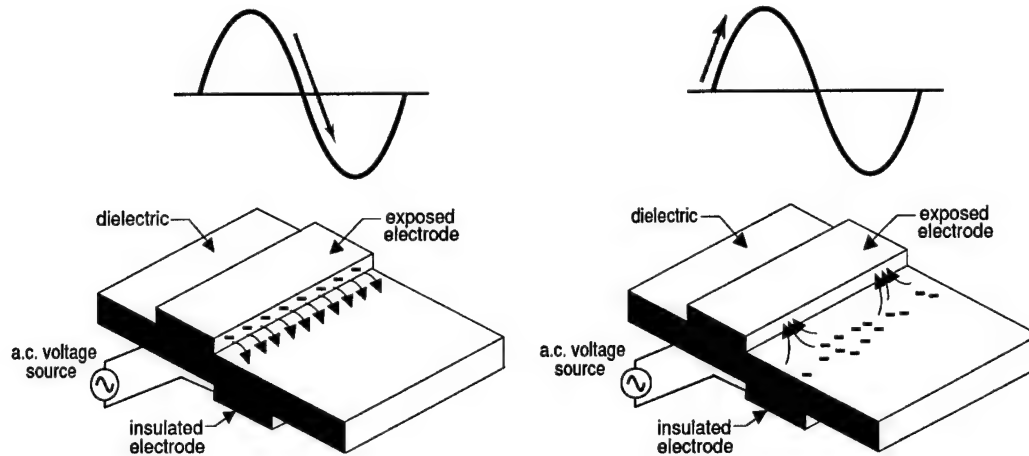


Figure 2.3. Electrons emitted from the exposed electrode collect on the dielectric surface (left) and are returned on the subsequent half-cycle of the discharge (right). From Enloe et al. [11].

In the other half of the a.c. cycle, the plasma reforms and electrons that were deposited on the dielectric travel back to the exposed electrode. The electrons do not leave the dielectric as readily as they do the exposed electrode, so that the plasma generation is not as efficient in this half of the cycle. The basis of the actuator is that the ionized air, in the presence of the electric field, results in a body force that is exerted on the external flow [11, 12]. The body force is proportional to the a.c. voltage amplitude and the volume of plasma. It is a vector that follows the electric field gradient. Thus the asymmetric electrode arrangement shown in Figure 2.1 is designed to produce a body force that draws ambient air toward the wall and from left to right according to the electric field produced.

A relation for the body force vector produced by the actuator was developed by Enloe et al. [11, 12]. The following summarizes that analysis. During the formation

of the plasma, the charged particles (electrons and ions) arrange themselves so as to cancel as much of the electric field as possible. This occurs everywhere except near the boundary region of the plasma. The extent of this region corresponds to the Debye length, λ_D .

The timescale for the charges to redistribute themselves is very short, especially compared to the a.c. period. At equilibrium, the electron density, n_e , and the ion density, n_i , in the plasma can be related to the local electric potential, ϕ , by the Boltzmann relation

$$n_i = n_o \exp\left(-\frac{e\phi}{kT_e}\right) \approx n_o \left(1 - \frac{e\phi}{kT_e}\right) \quad (2.1)$$

$$n_e = n_o \exp\left(\frac{e\phi}{kT_i}\right) \approx n_o \left(1 + \frac{e\phi}{kT_i}\right), \quad (2.2)$$

where n_o is the background plasma density, e is the elemental charge value, k is the Boltzmann's constant, and T is the temperature. The net charge density, ρ , at any point in the plasma is

$$\rho = e(n_i - n_e) \approx -en_o \left(\frac{e\phi}{kT_i} + \frac{e\phi}{kT_e}\right). \quad (2.3)$$

The electric potential, ϕ , and electric field vector, \vec{E} , are related through

$$\vec{E} = -\vec{\nabla}\phi. \quad (2.4)$$

From Maxwell's equations and Equation 2.4

$$-\nabla^2\phi = \frac{\rho}{\epsilon_o}, \quad (2.5)$$

where ϵ_o is the permittivity of the free space. The Debye length, λ_D , is the characteristic length for electrostatic shielding in a plasma and is given as

$$\frac{1}{\lambda_D^2} = \frac{e^2 n_o}{\epsilon_o} \left(\frac{1}{kT_i} + \frac{1}{kT_e} \right). \quad (2.6)$$

Using Equations 2.3, 2.5, and 2.6 gives

$$\nabla^2 \phi = \frac{e^2 n_o}{\epsilon_o} \left(\frac{1}{kT_i} + \frac{1}{kT_e} \right) \phi = \frac{1}{\lambda_D^2} \phi. \quad (2.7)$$

From Equations 2.5 and 2.7,

$$\rho = -\frac{\epsilon_o}{\lambda_D^2} \phi, \quad (2.8)$$

which says that the net charge density at any point in the plasma is proportional to the potential at that point.

Because there is an electric field in the plasma in regions where there is also a net charge density, there is a force on the plasma. The force density, or body force or force per unit volume, $\frac{\vec{F}_B}{V}$, can be calculated directly by taking the charge density times the electric field strength,

$$\frac{\vec{F}_B}{V} = \rho \vec{E}. \quad (2.9)$$

Since the charge density is proportional to the potential from Equation 2.8,

$$\frac{\vec{F}_B}{V} = -\left(\frac{\epsilon_o}{\lambda_D^2} \right) \phi \vec{E}. \quad (2.10)$$

This body force is a vector that can be tailored for a given application through the orientation and design of the electrode geometry that ultimately defines the electric field. This is the motivation for the asymmetric electrode arrangement indicated in Figure 2.1.

In one dimension, Equation 2.10 reduces to

$$\frac{\vec{F}_B}{V} = -\frac{\epsilon_0}{2} (\vec{\nabla} E^2) \quad (2.11)$$

which has been used in the past to obtain an estimate of the body force vector for use in the design of actuator electrode arrangements [12, 49, 50, 51].

2.1.1 Electronics

The main electronic components necessary to generate the plasma were a function generator, variable-gain amplifiers, and step-up transformers. High-voltage probes, inductive current meters, and oscilloscopes were used to monitor the signals associated with the electronics and the plasma itself. A block diagram of the set-up is shown in Figure 2.4.

A schematic of the circuit used to generate the plasma is shown in Figure 2.5. The first amplifier has variable gain. It was built using low-power operational amplifiers. The circuit was also designed to be able to produce a 180 degree phase shift of the input signal. A schematic of the circuit (for 1 channel) is shown in Figure 2.6, and photograph of the circuit (for 12 channels) is shown in Figure 2.7.

The next amplifier stage is designed to increase the output power to a sufficient level to drive the step-up transformers. This is a solid-state, push-pull amplifier that consists of discrete transistors. The circuit has an output amplitude of up to $\pm 100 V_{p-p}$ and a power rating of approximately 150 W per channel. A detailed schematic of the high-power amplifier circuit is shown in Figure 2.8.

The final stage of the plasma generation circuit is a 120:1 step-up transformer. These transformers were specially designed by Corona Magnetics, Inc. for a maximum output voltage of 20 kV, with a center frequency of 8 kHz.

The plasma was most typically driven by a 5 kHz triangle wave. As was shown by Enloe et al. [11], the triangle wave was an efficient waveform to generate the plasma. The choice of the frequency was based on the circuit response, which included the actuator that could be modeled as a inductor-resistor-capacitor network. A Stanford Research Systems 3.1 MHz function generator was used to supply the 5 kHz triangle wave that was used to generate the plasma.

A LeCroy PPE-20kV high-voltage probe was used to monitor the voltage supplied to the electrodes, while a Pearson Model 2100 coil inductance current meter monitored the current. A LeCroy Waverunner LT342 and LT264 was used to monitor the signals to the amplifiers and to the electrodes.

2.1.2 Operation

The actuators could be operated either in a steady, unsteady, or phased manner. This section explains how each of these was achieved. In any operation, the frequency of the a.c. voltage supplied to the electrodes was typically 5 kHz, and the a.c. voltage supplied to the electrodes was on the order of $3 - 11 \text{ kV}_{p-p}$. The power used by the actuator varied and depended on the mode of operation.

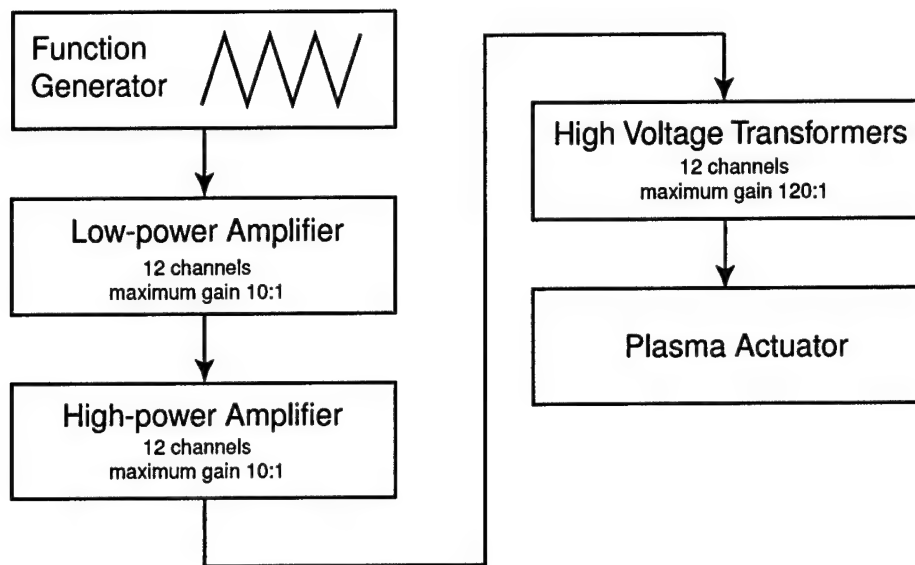


Figure 2.4. Block diagram of the electronic system.

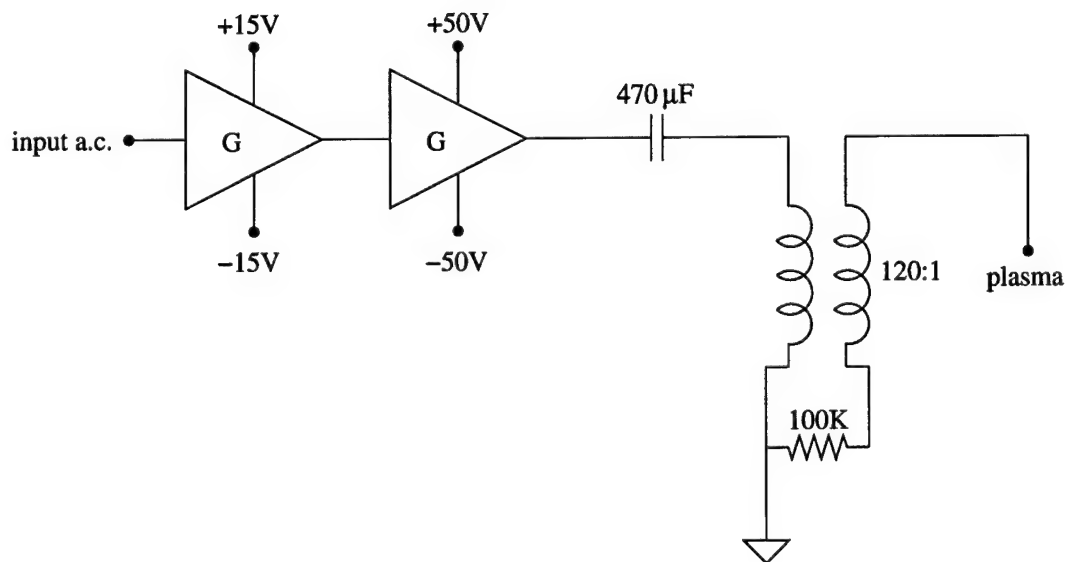


Figure 2.5. Schematic of the circuit used to generate the plasma.

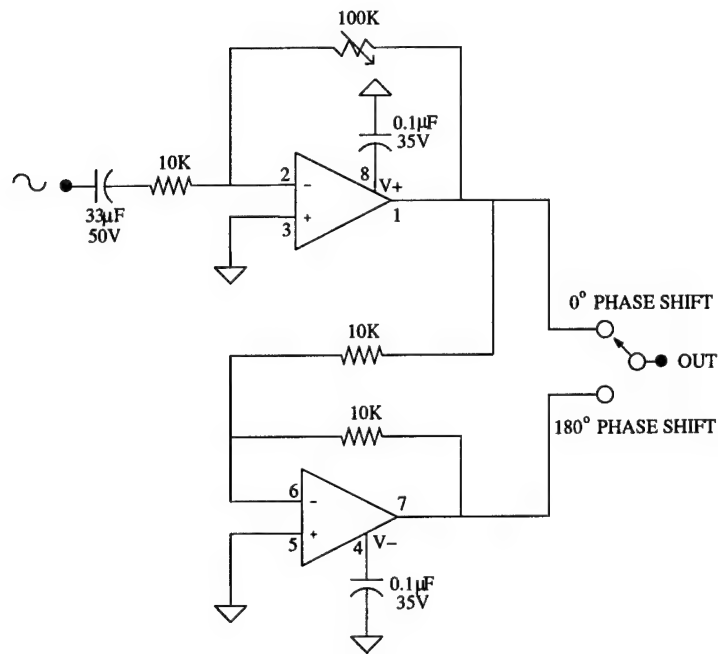


Figure 2.6. Schematic of the low-power amplifier circuit (1 channel).

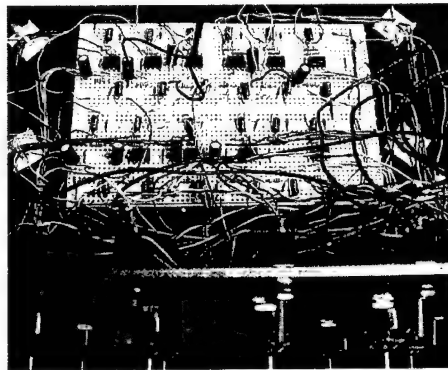


Figure 2.7. Photograph of the low-power amplifier (12 channels).

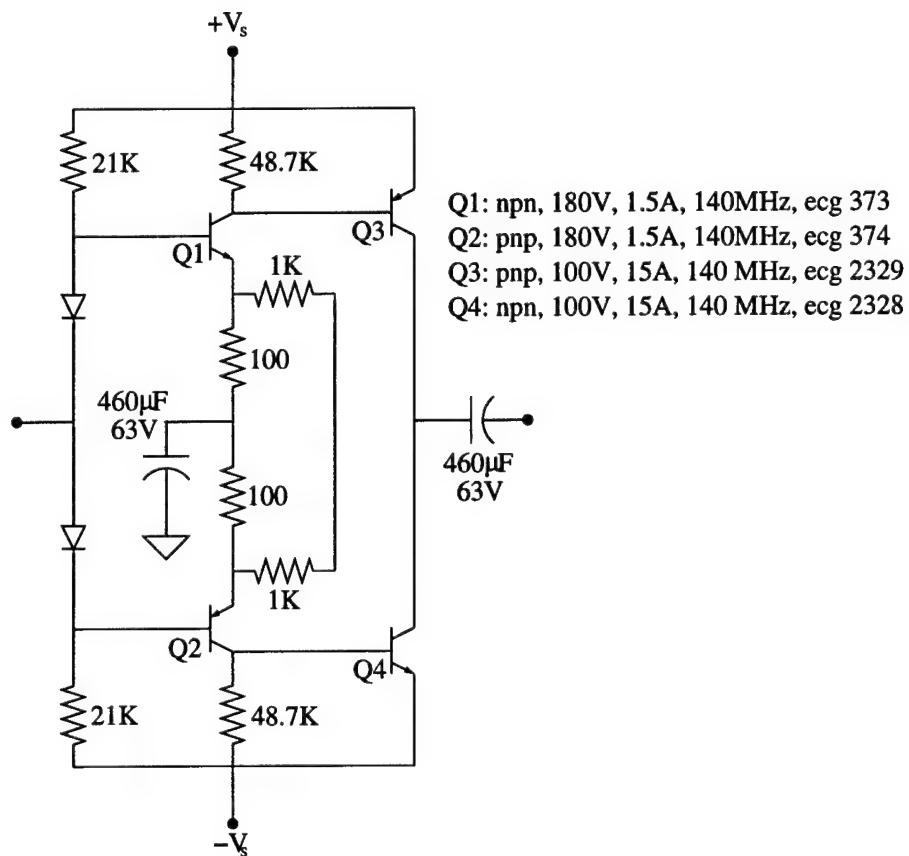


Figure 2.8. Schematic of the high-power amplifier circuit (1 channel).

2.1.2.1 Steady Actuation

In the steady operation, the actuator was powered continuously by the a.c. signal input. Although the plasma is being generated and extinguished twice during the a.c. cycle, the 5 kHz frequency is well above the response frequency of the mean flow, so its effect is quasi-steady.

For steady operation, the maximum power required to reattach the flow in all the applications was approximately 20 Watts per foot span. This was based on the power going into the transformers.

2.1.2.2 Unsteady Actuation

For unsteady operation of the plasma actuator, the a.c. operating frequency (5 kHz) was switched on and off at a lower frequency (order Hz). In addition, the duty cycle of the on-off period could be adjusted. A representation of this is shown in Figure 2.9.

A schematic of the circuit used to generate the low frequency on-off operation with variable duty cycle is shown in Figure 2.10. The LM322 is a precision timer that is used to set the duty cycle. The duty cycle can be precisely adjusted using the variable resistor. The CD4066 is a quad, bilateral switch (only one switch was used) that connected the a.c. operating frequency to the amplifier circuits.

In this operation, different duty cycles were possible. For example, results indicated that the unsteady actuation was effective with a duty cycle of only 10%. This reduced the power by 90% compared to the steady operation.

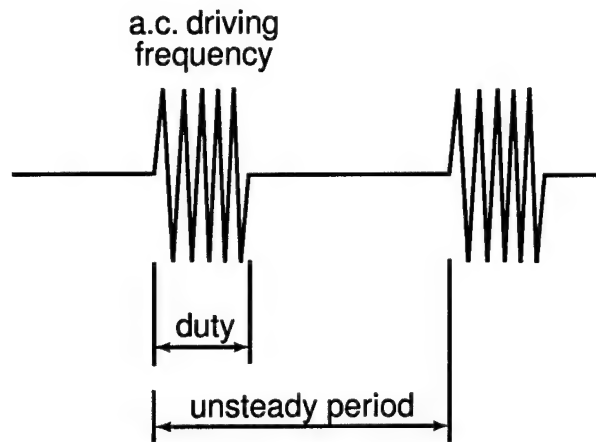


Figure 2.9. Illustration of plasma actuator time series used for unsteady actuation.

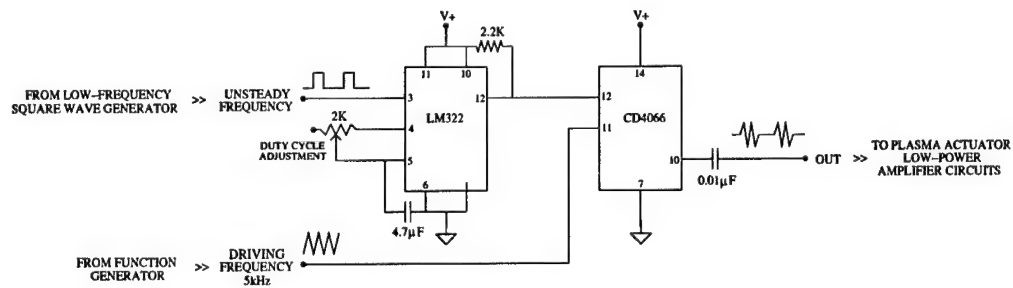


Figure 2.10. Schematic of circuit to generate the signal for the unsteady plasma actuation.

2.1.2.3 Phased Actuation

In the phased operation, multiple actuators in an array were operated with the a.c. input *phase-shifted* with respect to neighboring actuators. This resulted in imparting a traveling wave speed to the actuator effect.

The concept of phased plasma actuators is illustrated in Figure 2.11. This is simply an array of asymmetric electrode arrangements like that in Figure 2.1. The upper electrodes, labeled with (1)'s, are exposed to the air and have a common a.c. supply. The phased electrodes, labeled (2)-(6), are under each of the corresponding upper electrodes. The time traces below the electrode pattern depict one complete cycle to each of the lower electrodes (2-6), where the number on the left refers to the particular electrode.

The upper electrodes operate on short duty-cycle time series with one full period corresponding to τ_2 , at a frequency of f_2 . This frequency is close to the optimum frequency for the system of electronics (typically 5 kHz).

For N number of lower electrodes, the time series is a short duty-cycle pulse shifted by an equal amount

$$\text{Phase shift} = \frac{2\pi}{N}. \quad (2.12)$$

In this case, $N=5$ so the electrodes are phase shifted by 72° with respect to each neighboring electrode. The period of that time series is τ_1 , where $\tau_1 \neq \tau_2$, at a frequency of f_1 . The frequencies f_1 and f_2 are intended to be in the range of the optimum for the electronics.

The plasma forms near the upper electrode exposed to air where the potential is large enough. In Figure 2.11 this occurs where the high and low states of a particular electrode overlap, namely at electrodes (3) and (6). If the frequencies are different between the time series to the upper and lower electrodes, the location of the plasma moves at the difference between the frequencies, $(f_2 - f_1)$. The phase velocity, U_p , that the plasma moves at is then

$$U_p = (f_2 - f_1)(N - 1)L, \quad (2.13)$$

where L is the length from the first actuator to the N th actuator.

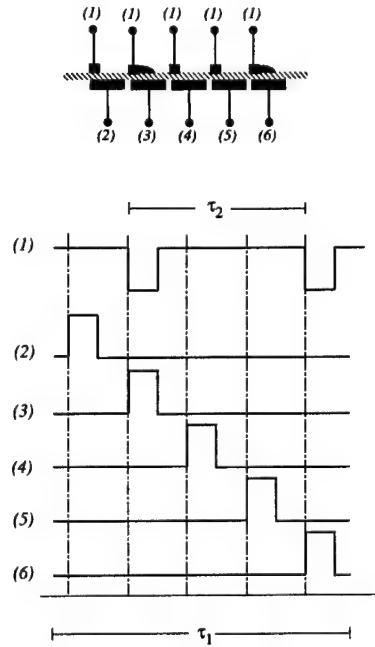


Figure 2.11. Two-frequency phased excitation to produce a uni-direction moving plasma wave for the phased plasma actuation.

2.2 Plasma Actuator Measurements

The purpose of this part of the research was to fully characterize the operation of the plasma actuator through a systematic set of experiments. The focus was on

1. different physical actuator configurations,
2. determining the amplitude and frequency response input/output relations,
3. comparing steady versus unsteady operation, and
4. determining the important time scales associated with the fluid response to the actuator.

These experiments were fundamental in optimizing the actuator for the separation control experiments that were to follow.

2.2.1 Actuator Optimization Set-up

The principle measurement tool used in this part of the work was Particle Image Velocimetry (PIV). Since PIV is a non-intrusive technique, it worked well to measure the flow field in the vicinity of the plasma. Other techniques, such as hot-wires have difficulties measuring within the large electric field and charged air. Matlis (2004) has made such measurements using a specially designed hot-wire anemometer [43]. In addition, pitot probes have been used, but their isolated metal surfaces can be covered by the plasma, affecting the measurement. Even if these techniques were used, they still provide single velocity components at a single spatial point. The PIV

has the advantage of providing multiple velocity components in a full spatial field. This is extremely desirable in the flow field that is induced by the plasma actuator.

In the general operation of the PIV system, the flow is seeded with spherical, micron-sized particles. A cross-section of the flow is illuminated using a laser sheet that is pulsed on twice for a very short duration. The time between the laser sheet pulses is adjustable to distinguish the motion of the particles in the flow. The illuminated region is viewed and the light scattered from the particles is captured by a high-resolution camera(s) in two images corresponding to the two laser sheet pulses. A cross-correlation between the two images yields a velocity reconstruction of the flow field.

The PIV system used in this research was a TSI Ultra PIV Stereo System. A photograph of the system is shown in Figure 2.12. It used two Model Y120-15 New Wave Research Nd:Yag lasers that operated at 532 nm and had a user-defined variable pulse rate with an energy output of 120 mJ per pulse.

The system has two charged-coupled device (CCD) cameras with a 1K by 1K pixel resolution and frame rates of up to 30 frames per second. The camera lens that was used was a Nikon 25 mm with a 2x multiplier. This resulted in an image resolution of approximately 50 μm per pixel. The image sampling rate used in the experiments was 15 Hz.

The flow was seeded using a TSI atomizer based on a Lanskin Nozzle design. The working fluid for the atomizer was olive oil. The estimated diameters of the particle sizes produced by this system were from 0.1 to 1 micron.

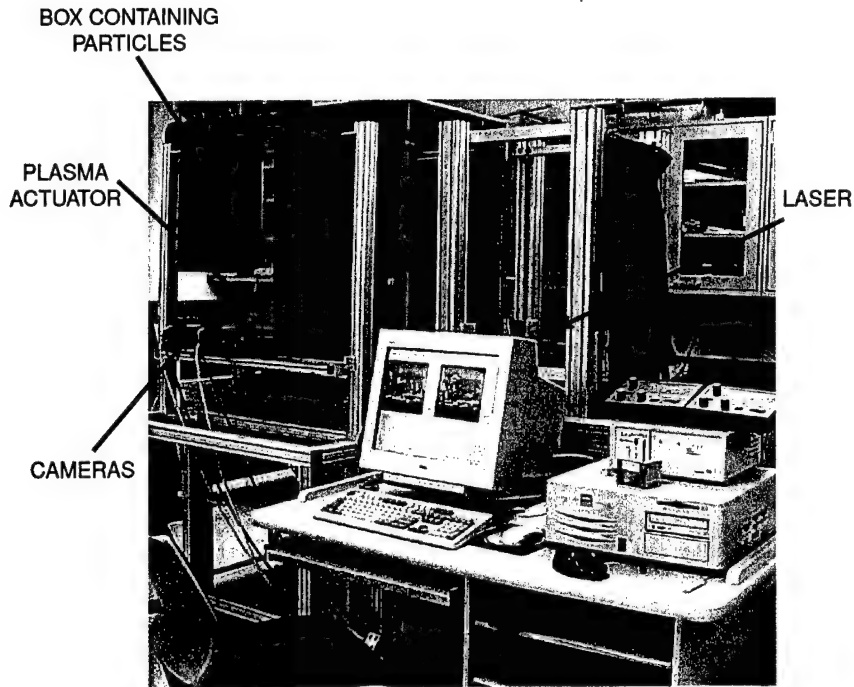


Figure 2.12. Photograph of the setup used for plasma actuator optimization.

The study was conducted inside a 1.2 m (4 ft) in length by 0.6 m (2 ft) in width by 0.91 m (3 ft) in height box. The box can be seen in the left background of the photograph in Figure 2.12. The front and two sides of the box were made from 1.27 cm (0.5 in) thick Plexiglas to allow for optical viewing and access for the laser sheet. The back side, and top and bottom was constructed of 1.9 cm (0.75 in) thick particle board for strength.

The ambient air within the box was shielded from air flow within the laboratory space. The atomized olive oil was introduced into the box by a small diameter hose that entered near the top of the box. The particles would stay suspended for many hours and were only replenished when needed.

The plasma actuators used in these experiments were generally constructed in the following manner. The electrodes were fabricated from 2-mil thick copper tape. The dielectric insulator was most typically made from 6-mil thick Kapton film tape. In most cases the 6-mil thickness was build up by three layers of 2-mil thick Kapton tape.

The width of the upper electrode is not a factor in the operation of the plasma actuator. However, the width of the lower electrode is important, and different widths were investigated. The range of widths of the lower electrodes varied from 4 mm to 24 mm. In the asymmetric arrangement, the overlap between the upper and lower electrodes was typically 1 mm.

The span of the electrodes was typically around 12.5 cm (4 to 5 inches). This was intended to eliminate end effects in the actuator and insure that the induced flow was as nearly as possible two-dimensional.

The voltage supplied to the electrodes was monitored by a LeCroy PPE-20kV high-voltage probe. The current was measured by a Pearson Model 2100 coil inductance current meter. Both signals were displayed and averaged on a LeCroy LT342 or LT264 oscilloscope.

2.2.2 Steady Actuator Measurements

For the experiments on steady operation, the single, asymmetric electrode was the most basic configuration. For this, the lower electrode was 16 mm in width. PIV data was taken at the mid-span location of the actuator.

Results in this section consider the maximum velocity output of the actuator while varying several parameters. The maximum velocity generated by the plasma actuator was determined from an ensemble average of 100 instant realizations. The a.c. input to the actuator was a 5 kHz triangle waveform in all cases, unless otherwise noted.

An example of the ensemble-averaged PIV velocity vectors are shown in Figure 2.13. The actuator is located at $x = 0$ mm and is designed to generate a body force in the positive x-direction. The velocity vectors indicate that the actuator induced a velocity field with motion toward the wall, and then as a wall-jet from left to right. The peak velocity occurs at approximately 10 mm from the actuator.

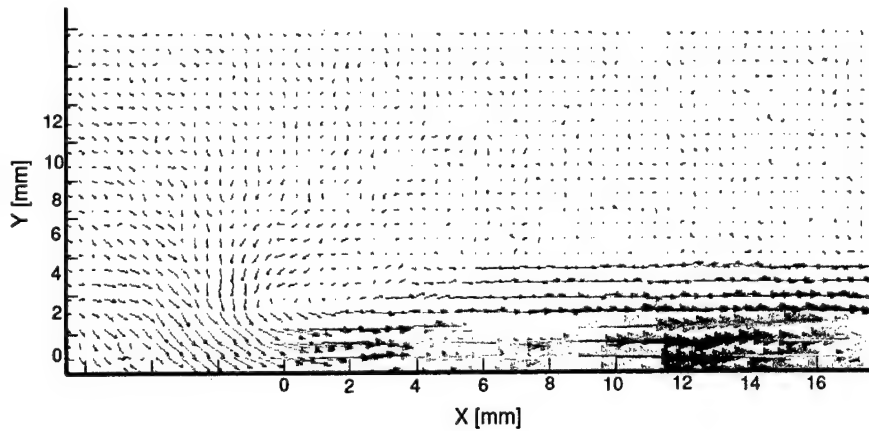


Figure 2.13. Ensemble average of 100 PIV images showing the average velocity vectors in the velocity field induced by a single plasma actuator under steady operation. Actuator is located at $x = 0$ mm.

2.2.2.1 Effect of Amplitude Input

The results presented here document the effect of the a.c. voltage amplitude on the maximum velocity output. For this the voltage was increased in 2 kV_{p-p} increments up to 16 kV_{p-p} . For each, the maximum velocity generated by the actuator was determined from 100 ensemble averages of the PIV acquired velocity field, similar to that shown in Figure 2.13.

The result of the effect of the output velocity on the a.c. voltage amplitude is shown in Figure 2.14. It represents multiple experiments. The error bars for each data point reflect the variation between the experiments.

Experiments performed by Enloe et al. [11, 12] indicated that the thrust produced by a single asymmetric plasma actuator varied as the voltage to the $7/2$ power, $V^{7/2}$. Given that thrust is the product of the mass flux and velocity, and assuming that the mass flux is fixed, the velocity, U , should then vary as the voltage, V , to the $7/2$ power. The solid curve in Figure 2.14 shows the least-squares fit of the function

$$U = 0.0018V^{7/2}. \quad (2.14)$$

This indicates that the $7/2$ power relation between the induced velocity and input voltage is a good representation of the input/output response of the actuator.

Also represented in Figure 2.14 as a dashed line is a best-fit of the data to $U \propto V^2$. This would be representative of the heating effect of the actuator. This relation does not represent well the behavior of the induced velocity with input voltage. In addition it indicates that at higher voltages, the effect of any heating becomes less significant.

Single Asymmetric Steady Actuator (Triangle Waveform, 5kHz)

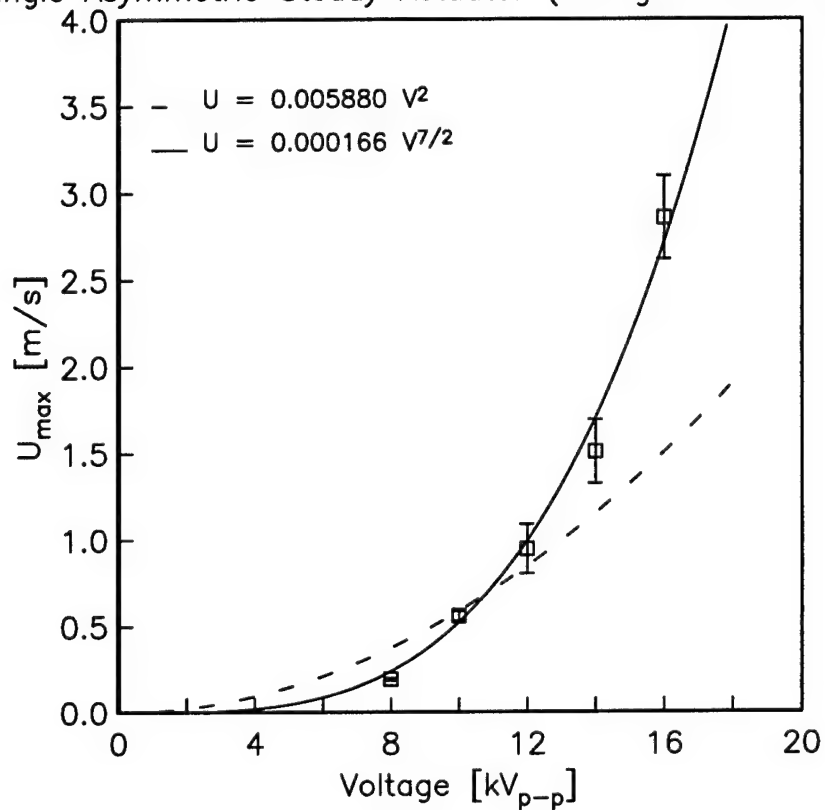


Figure 2.14. $U \propto V^{7/2}$ relationship between actuator voltage amplitude input and induced velocity output for a single steady actuator (Triangle Waveform, Operating frequency: 5 kHz).

2.2.2.2 Effect of Waveform Input

This part of the work was intended to investigate the effect different waveforms of the a.c. input would have on the maximum induced velocity. This stems from the understanding of how the single dielectric plasma is generated during the a.c. cycle, such as was illustrated in Figure 2.3.

In these studies, the a.c. frequency and amplitude were kept fixed at 5 kHz and 12 kV_{p-p}, respectively. Four different waveforms were examined. They were a square wave, triangle wave, and positive and negative slope sawtooth waves. Again multiple experiments were done, and error bars reflect the variation between experiments.

The results are shown in Figure 2.15. These results seem to indicate that the square wave and triangle wave are slightly better than the other waveforms. Enloe et al. [11] found a sawtooth waveform to generate more thrust than other waveforms. This is consistent with the fact that the plasma generation is less efficient over the half of the a.c. cycle where electrons are coming off of the dielectric. It is possible that some distortion was occurring in the input signals to the actuators due to capacitance effects. This may have reduced the difference in effect between the different waveforms. For example, the sawtooth wave could have appeared more like the triangle wave.

Since there might be some component dependence of the actuator operation, the triangle wave was used throughout the separation control experiments.

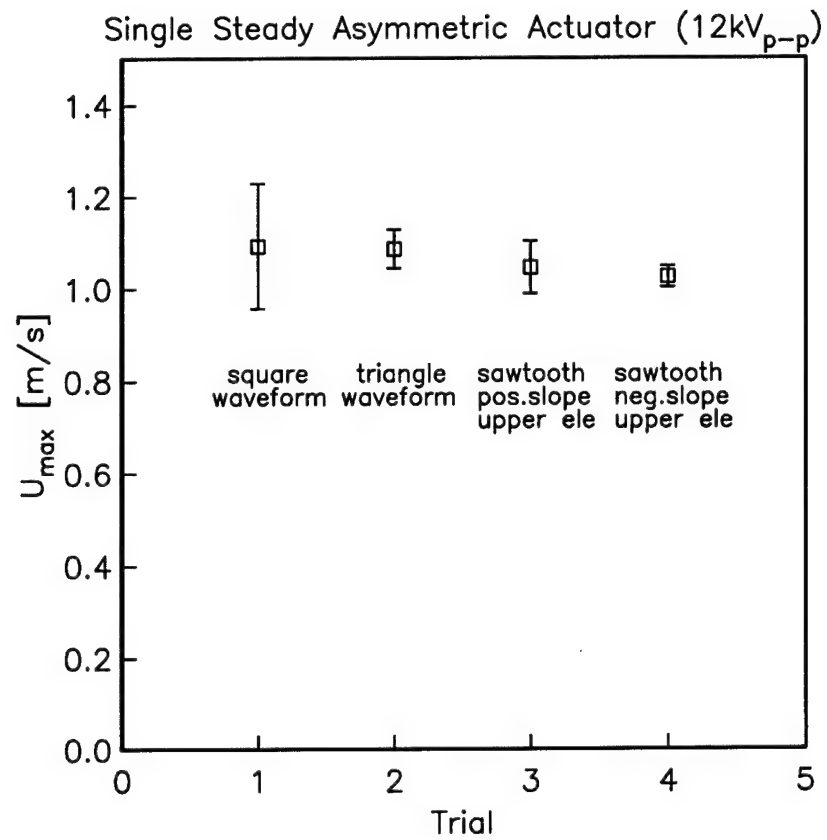


Figure 2.15. Comparison of maximum velocity output for various waveforms of the a.c. operating frequency.

2.2.2.3 Effect of Operating Frequency

The effect of the a.c. input frequency on the maximum induced velocity and power supplied by the a.c. power supply was investigated here. For this, the a.c. frequency was varied from 2 kHz to 10 kHz, in 1 kHz increments. The a.c. waveform was a triangle wave, and the amplitude was kept fixed at 12 kV_{p-p} . The power was determined by measuring the current from the d.c. power supply that powered the 10:1 amplifier stage that drove the 120:1 step-up transformer.

The results are illustrated in Figure 2.16. In this, the square symbols correspond to the maximum velocity, and the triangle symbols correspond to the measured power. Focusing first on the velocity, the maximum induced velocity was observed to increase with frequency and asymptote at approximately 6 kHz.

The a.c. supply power increased linearly with the a.c. frequency. This result is certainly component dependent. In particular it depends on the transistor characteristics in the a.c. power amplifier and the transformer/actuator equivalent circuit natural frequency. The latter can result in reflected power which makes operation at a particular frequency more or less efficient than at another frequency.

The results in Figure 2.16 should then only represent the particular setup used in these experiments. Based on this, the optimal frequency is one that is close to the frequency/velocity asymptote. For this reason, the 5 kHz a.c. frequency was chosen and used for all of the separation control experiments to follow.

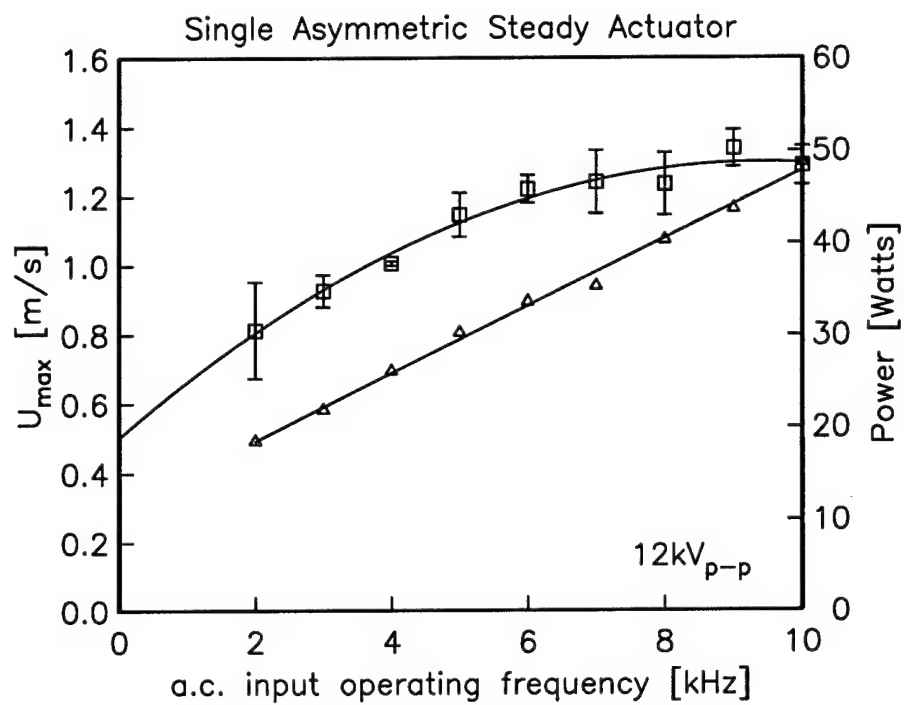


Figure 2.16. Comparison of velocity output (square symbols) and power (triangle symbols) for different a.c. input operating frequencies.

2.2.2.4 Effect of Width of Lower Electrode

This part of the work was intended to investigate the effect of width of the lower electrode on maximum induced velocity. For this, the a.c. input frequency was 5 kHz, and two different amplitudes of 12 kV_{p-p} and 16 kV_{p-p} were used. The upper electrode width was kept fixed at 2 mm. The lower electrode width was varied from 4 to 24 mm. The overlap between the upper and lower electrodes was kept fixed at 1 mm.

The results are presented in Figure 2.17. Focusing first on the 12 kV_{p-p} amplitude, the results indicate that there is a minimum required width of the lower electrode that is needed to reach the maximum possible induced velocity. This is consistent with the process of plasma generation of the actuator in that there needs to be sufficient area on the dielectric above the lower electrode to deposit electrons. Anything less than the minimum reduces the effectiveness of the actuator. Anything more provides no further gain.

The overall area of the lower electrode required to reach the maximum velocity depends on the input voltage amplitude. At the higher voltage of 16 kV_{p-p} in Figure 2.17, the maximum velocity was still not reached with a lower electrode width of 24 mm. Therefore in the design of the actuator, the voltage needed to achieve a desired velocity is first determined, such as by Figure 2.14. Then based on that voltage, the necessary width of the lower electrode is determined, such as from results like those in Figure 2.17.

In the experiments on separation control that follow, the width of the lower electrode was never less than 25 mm and was typically as large as 50 mm. Therefore this

width was sufficient for the largest a.c. voltages that were possible for the electronics setup.

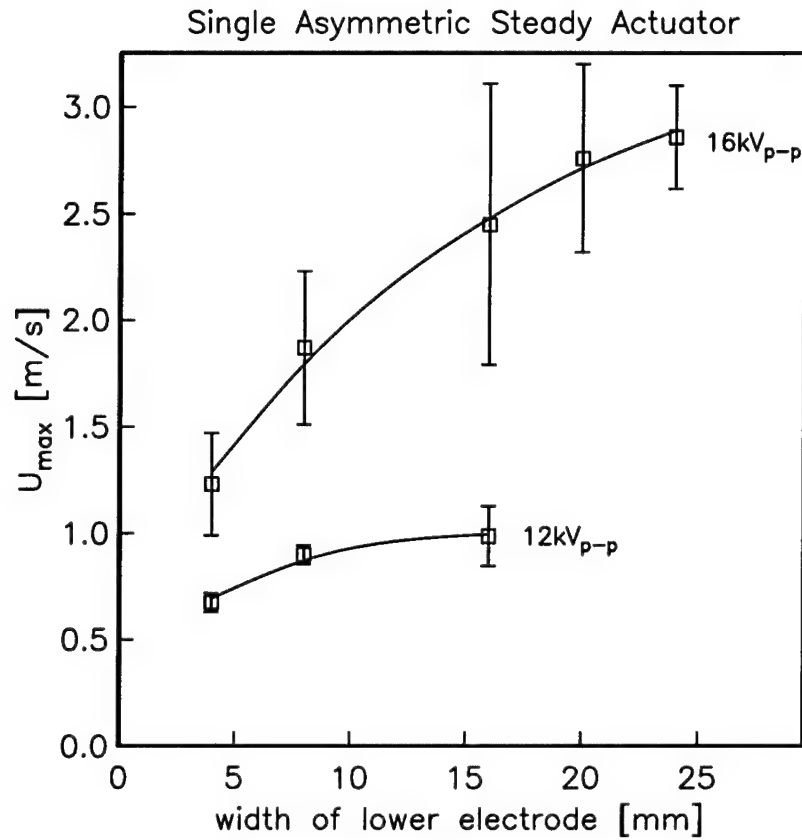


Figure 2.17. Maximum velocity versus width of lower electrode for two a.c. input voltages of 12 kV_{p-p} and 16 kV_{p-p}.

2.2.2.5 Effect of Multiple Steady Actuators

These results examine the effect of operating multiple asymmetric actuators simultaneously. In this case, two identical actuators were placed next to each other. For these, the width of the lower electrodes was 8 mm, and the width of the upper electrodes was 2 mm. The overlap between the upper and lower electrodes was 1 mm. The two actuators were spaced apart so that the distance between the lower electrodes was 4 mm.

Note that the total width of the lower electrodes (8 mm + 8 mm) was the same as the 16 mm wide lower electrode used in Figure 2.14. Therefore the results could be directly compared to the previous single actuator case.

The results for the two actuators are shown in Figure 2.18. The square symbols correspond to the single actuator case previously presented in Figure 2.17. The triangle symbols correspond to when the two actuators were operating. The dashed curve corresponds to a least-squares fit of $U = CV^{7/2}$ for this data. The fit indicates that the same $7/2$ power relation exists between the induced velocity and input voltage. However, the coefficient is twice that of the single actuator case, indicating that the two actuators are producing twice the effect of the single actuator.

Note that based on the previous section results on the effect of the lower electrode width, the 8 mm width used for the two actuator arrangement is not large enough for the 16 kV_{p-p} input. Therefore the velocity does not follow the trend of the lower voltage points.

Asymmetric Steady Actuator (Triangle Waveform, 5kHz)

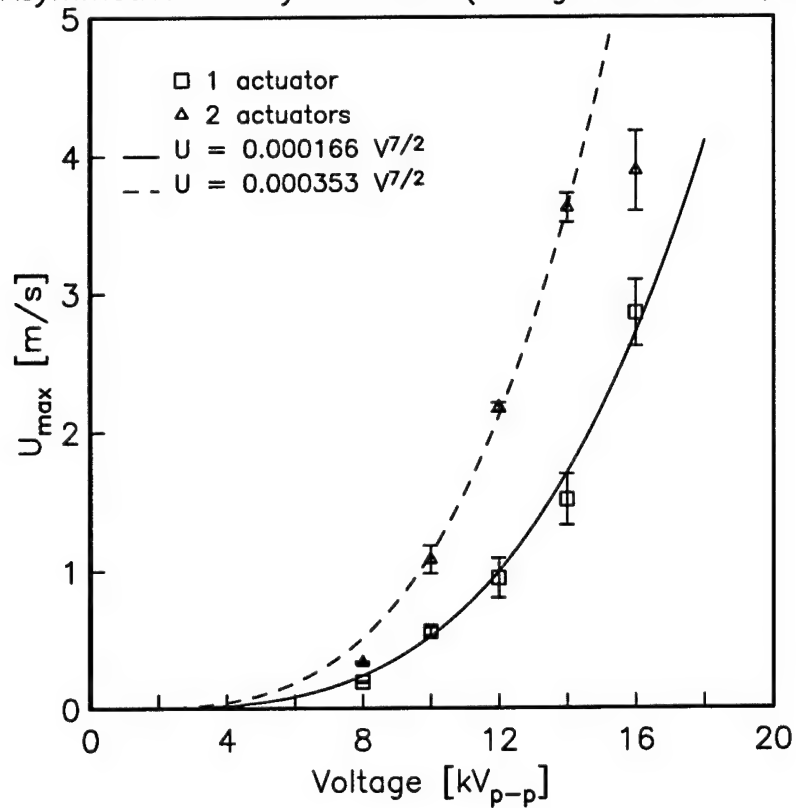


Figure 2.18. Relationship between actuator input amplitude voltage and velocity output for one and two steady actuators (Triangle Waveform, Operating frequency: 5 kHz).

2.2.3 Unsteady Actuator Measurements

The results in this section examine the dynamic response of the flow to a step-input of the a.c. voltage to the plasma actuator. This is important for the unsteady operation of the actuator that is used in the separation control experiments that follow.

The dynamic response experiments use a single asymmetric actuator that is identical to the one used for the results in Figure 2.14. The measurements consist of switching the actuator a.c. input on and off at a low frequency of 0.5 Hz. In this, the a.c. frequency is 5 kHz, and the waveform is a triangle wave. The amplitude was 10 kV_{p-p} .

The velocity data is obtained using the PIV system with the lasers triggered at a particular phase in the 0.5 Hz cycle. Multiple realizations at a given phase were then averaged together to give phased-averaged velocity vectors.

An example of the phase-averaged velocity vectors at different delay times from first turning on the actuator are shown in Figure 2.19. Each of the vector plots corresponds to an average of 100 realizations. The actuator is located at $x = 12 \text{ mm}$.

At the smallest delay time of 2 ms, the velocity vectors show the initial entrainment of air toward the actuator. At 12 ms the formation of a starting vortex is evident in the velocity vectors. This vortex is observed to convect from left to right as time increases. By 120 ms, the vortex has convected out of the measurement plane. Finally by 200 ms, the induced flow appears as a steady wall-jet.

Different phase-averaged velocity fields such as in Figure 2.19 were used to examine the response of the mean flow to the step input with different input voltages. The

Single, Asymmetric, Unsteady Plasma Actuator

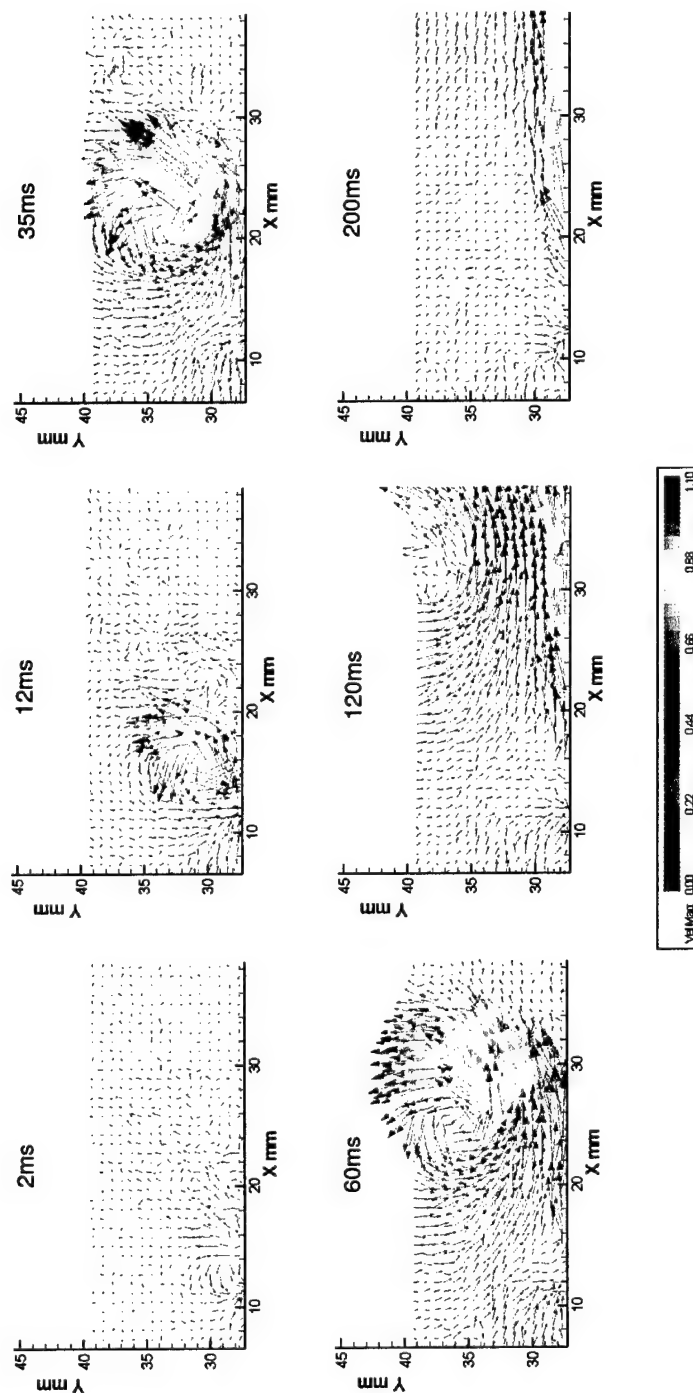


Figure 2.19. Phase-averaged velocity vectors at different phases of the 0.5 Hz unsteady plasma actuator cycle.

results are presented in Figure 2.20. The curves in the top plot represent the velocity measured at one selected spatial point. This point was determined to be representative of the maximum velocity produced by the single, steady actuator. The velocity was then measured at different time increments after the single, unsteady actuator was turned on. The curves represent the time evolution of the velocity induced by the actuator. The different curves represent three different input amplitudes. These are denoted by the symbols marking the last time sample.

The intention for the top plot in Figure 2.20 is to consider the curves to be the step response of a first-order system from which a time constant can be determined. To accomplish this, and account for the different input voltages, the measured velocities were normalized by their respective maximum velocities. Based on this, the time constant was determined to be the time needed to reach 63% of the maximum value. These time constants are shown by the star symbols in the top plot, with the accompanying time labeled.

The time constants have been plotted versus the input voltage in the bottom plot of Figure 2.20. This indicates that the time constant decreases approximately linearly with the actuator voltage. This result is important for the unsteady actuator control used in the flow separation control experiments to follow.

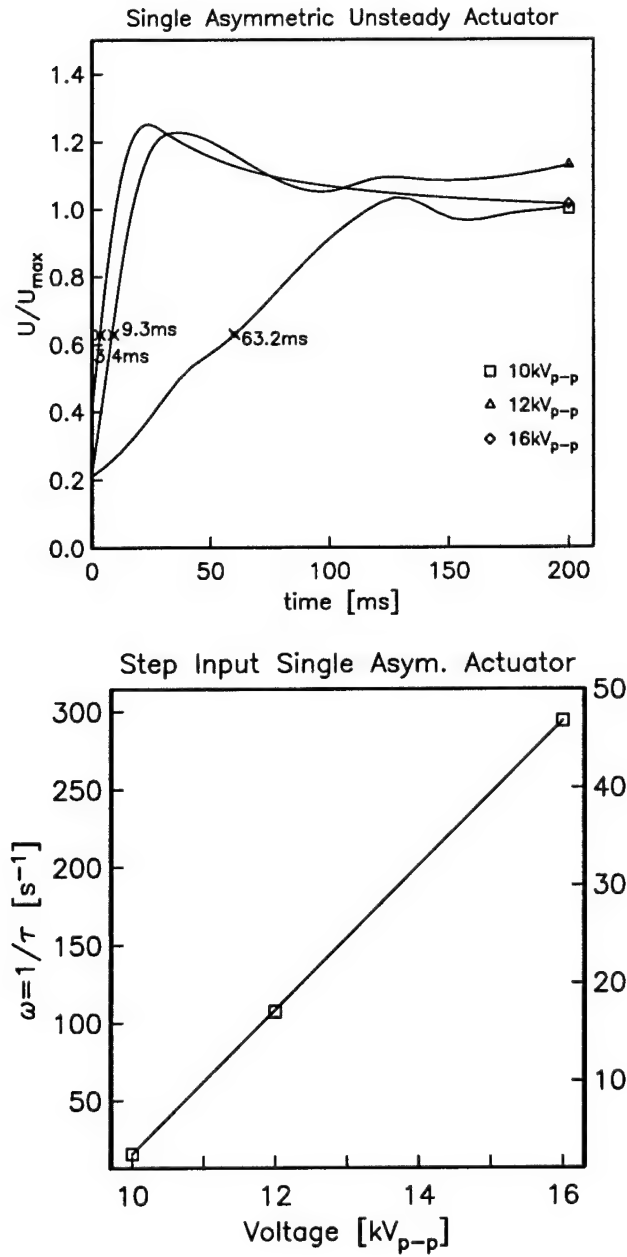


Figure 2.20. Top: Velocity time response due to a step input of the actuator voltage for different amplitudes of a single, unsteady plasma actuator. Bottom: Time constants for different input voltage amplitudes for a single, unsteady plasma actuator (Triangle Waveform, Operating frequency: 5 kHz).

2.2.4 Phased Actuator Measurements

The results in this section examine the response of the flow when operating in the phased actuation mode previously described in Section 2.1.2.3. This was illustrated in Figure 2.11 for an array of actuators. In these results however, only a single actuator was used. Two a.c. inputs were used. One was supplied to the lower electrode at frequency, f_1 . The other was supplied to the upper electrode at frequency, f_2 . As a result, the plasma turned on and off at the difference frequency, $f_1 - f_2$.

In order to obtain ensemble-averaged velocity data for the phased actuator, a circuit was built that could provide a signal that was phase locked with the difference frequency of the two a.c. inputs. This signal was used as a phase reference to trigger the lasers of the PIV system. A schematic of this circuit is shown in Figure 2.21.

As illustrated in Figure 2.21, the two a.c. signals were input into an analog multiplier to form a new time series with frequencies at the sum and difference frequencies, $f_1 + f_2$ and $f_1 - f_2$. This was then passed through a low-pass filter to remove the component at $f_1 + f_2$ and retain the component at $f_1 - f_2$. The time series corresponding to the difference frequency was then converted into a TTL pulse series, which was capable of triggering the PIV system.

The exact circuit design is shown in Figure 2.22. The MPY634 is the multiplier circuit. The output from that goes to the LM741 op-amp circuit which is a 4th-order, low-pass filter. The filter cut-off was set by the resistance and capacitance elements. In this case it was set to be approximately 200 Hz. The typical difference frequency was from 1 – 100 Hz.

The circuits using the LM322 timing chips were used to convert the filtered signal into a TTL pulse. The first stage is a zero crossing circuit. The second stage is used to control the width of the TTL pulse. Typically the width was made as narrow as possible but sufficient to trigger the lasers. The circuit using the CA3240 and LT1010 buffered the output signal.

A variable delay from the time of the trigger was set using PIV software. The velocity data was then acquired following the delay. Multiple realizations were then accumulated in order to obtain an ensemble average of the velocity at different times in the difference frequency cycle of the actuator.

Examples of the velocity field generated by the actuator in this phased actuation mode are shown in Figure 2.23. This corresponds to different phase delays for the actuator operating at a difference frequency of 1 Hz. The actuator is located at $x = -25$ mm. The delay time between different realizations corresponds to one-quarter of the 1 Hz cycle, or namely 0, 90, 180 and 270 degree phase locations.

The top plot shows the velocity field near the instant when the actuator is turning on. This illustrates the entrainment of the still, outer air toward the wall. The relatively rapid acceleration of the flow results in a starting vortex. This vortex is apparent in the velocity field at the next phase increment. The vortex grows in strength and convects to the right in subsequent phase realizations. The convection velocity of the vortex appears to be about constant since it is possible to fit a straight line through the vortex centers for the different realizations that are acquired at equal time increments.

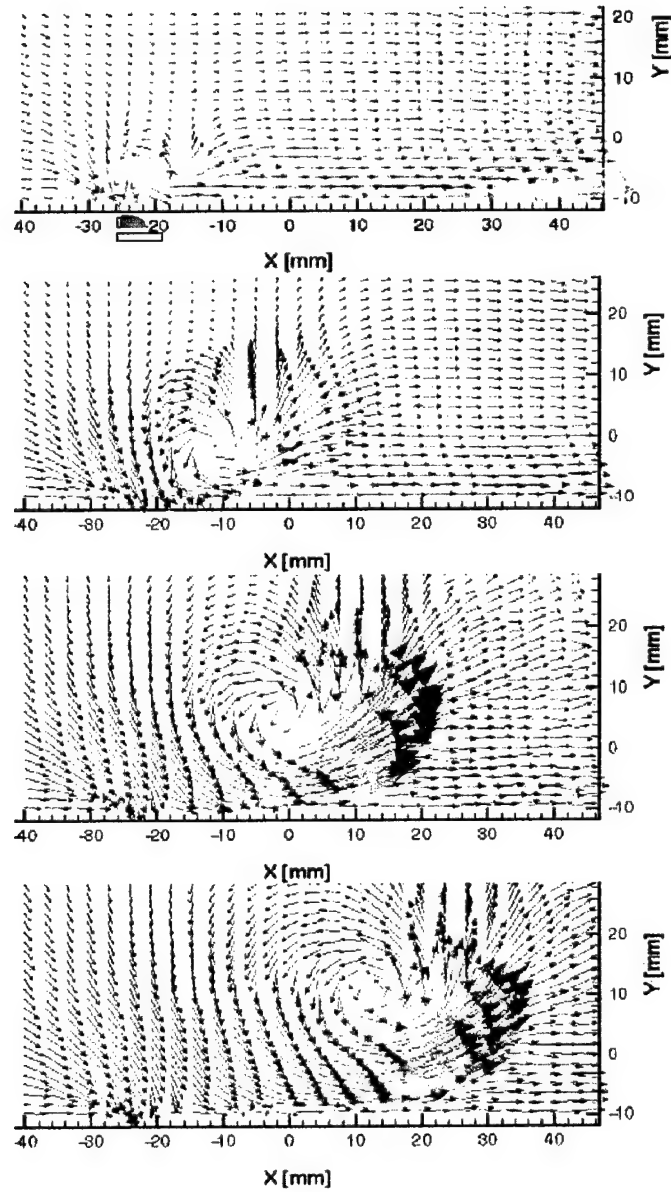


Figure 2.23. Phase-averaged velocity vectors at different time delays for an actuator difference frequency of 1 Hz.

The effect of different difference frequencies on the initial velocity field are presented in Figure 2.24. This shows the ensemble averaged velocity field at a fixed phase shift of 270 degrees for three difference frequencies of 1, 2, and 5 Hz. The first of these corresponds to the conditions in the previous figure.

The results show that as the difference frequency is increased, the starting vortex forms closer to the actuator location. In addition, the size of the vortex decreases as the frequency increases, and the wall-jet that is associated with the steady operation, such as was shown in Figure 2.13, is more quickly established. This is an important result depending on whether the actuator is intended to create an unsteady vortex, like in the unsteady operation in Section 2.1.2.2, or if it is intended to enhance the strength of the wall-jet, like in the steady operation in Section 2.1.2.1.

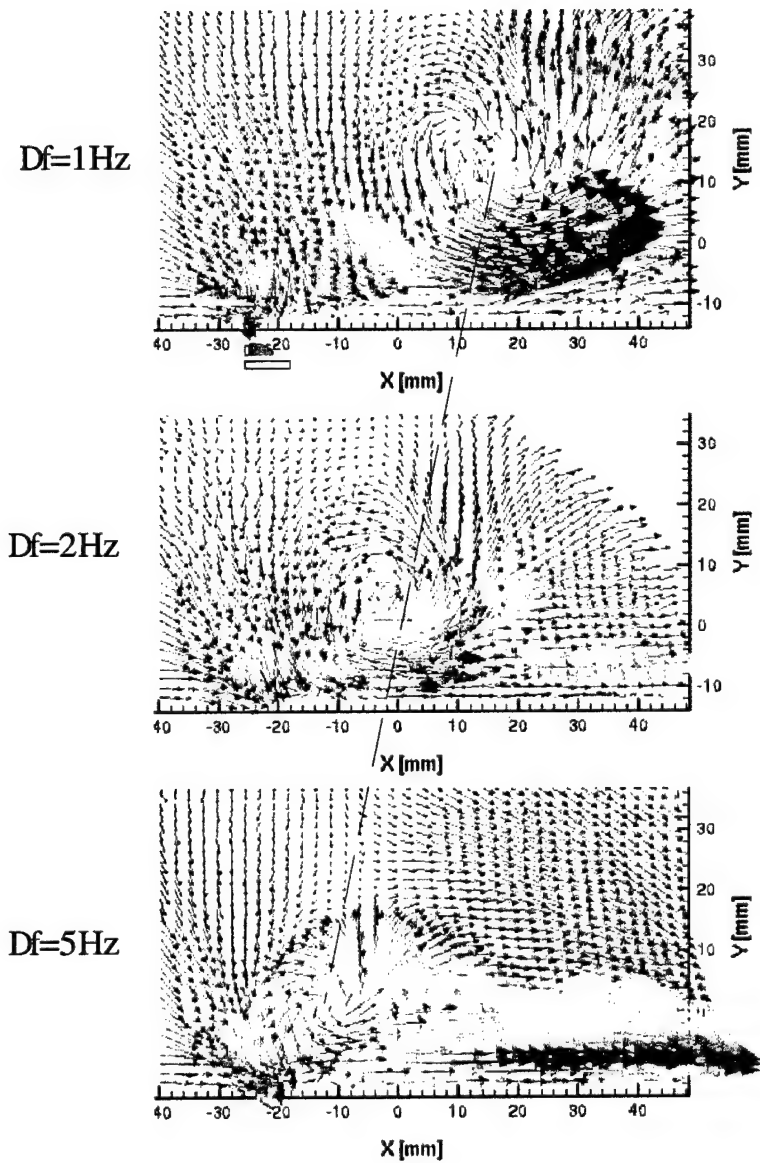


Figure 2.24. Phase-averaged velocity vectors at the same phase trigger, at different frequencies of the plasma actuator.

CHAPTER 3

EXPERIMENTAL SETUP

This chapter describes the experimental facilities and general experimental setup used in the research. The facilities are part of the Center for Flow Physics and Control (FlowPAC) in the Hessert Laboratory at the University of Notre Dame.

3.1 Experimental Facility

The experiments were conducted in an open-return wind tunnel with a 0.61 m by 0.61 m (2 ft square) by 1.8 m (6 ft) long test section. The freestream speed in the test section ranges from 1 to 35 m/s. The tunnel consists of a removable inlet having a series of 12 screens followed by an 18:1 contraction that attaches to the test section. The test section has a Plexiglas wall and a glass floor that allows optical access when flow visualization is performed. The back wall of the test section was used to mount the airfoil. Removable hatch doors in the back wall provided access into the test section. In addition, a slot in the test section ceiling provided access for a probe connected to a motorized traverse system. A schematic of the wind tunnel is shown in Figure 3.1, and a photograph of the facility is shown in Figure 3.2.

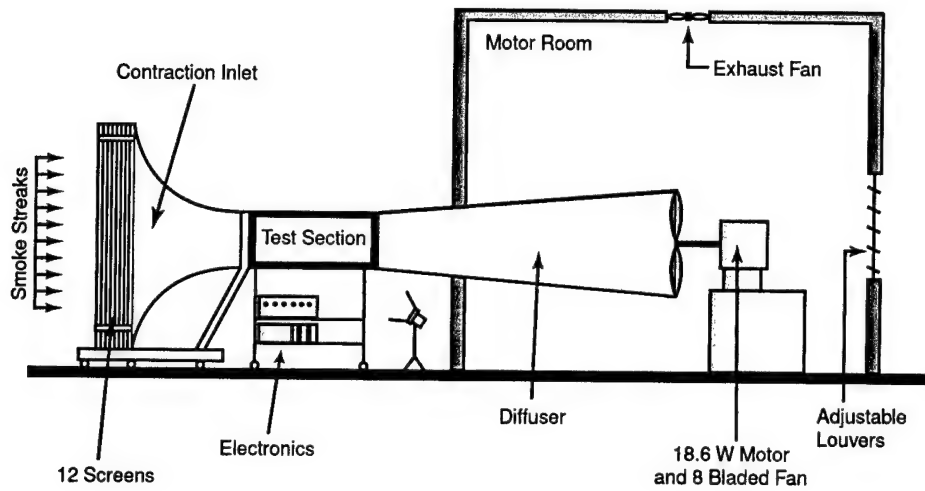


Figure 3.1. Schematic of the open-return wind tunnel at the Center for Flow Physics and Control.

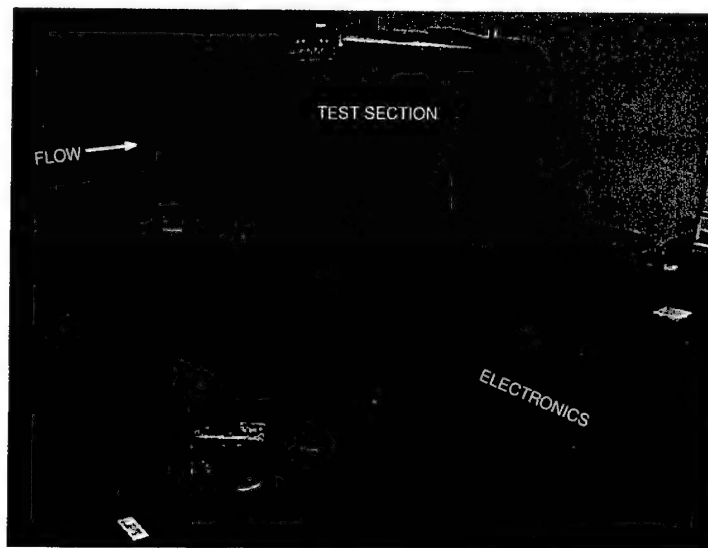


Figure 3.2. Photograph of the experimental facility.

3.2 Flow Visualization

Flow visualization was done by introducing continuous smoke streaklines upstream of the wind tunnel screens and contraction. The smoke generator was originally built by Brown in 1937 at the University of Notre Dame. A description is given by Mueller [46].

The smoke emanated from a rake of tubes as low-speed laminar jets. The tubes were aligned in the vertical direction and located at the spanwise centerline of the tunnel inlet. The smoke streaks were drawn into the tunnel inlet and converged into a closely spaced, vertically aligned group following the contraction. Figure 3.3 shows a photograph of the smoke generator and a close-up photograph of the smoke rake.

For the work with the stationary airfoil, the smoke streaks were illuminated by a steady, high-intensity light source located below the tunnel test section. For the work with the oscillating airfoil, a strobe light source was used. The strobe light was externally triggered from a signal that came from the motor encoder. This was used to obtain phase-conditioned visualization records at specific airfoil angles in the oscillating motion. With both light sources, the light entered through a slot that was masked in a glass window in the floor of the test section.

The flow visualization images were obtained using a Panasonic analog video camera. The video tape was digitized through a video capture card whereby individual frames were extracted. An example of a flow visualization image is shown in Figure 3.4. In this image, as well as others, the image has been inverted, with the light appearing to be coming from the top, to correspond to a positive angle of attack with lift vector directed upward.

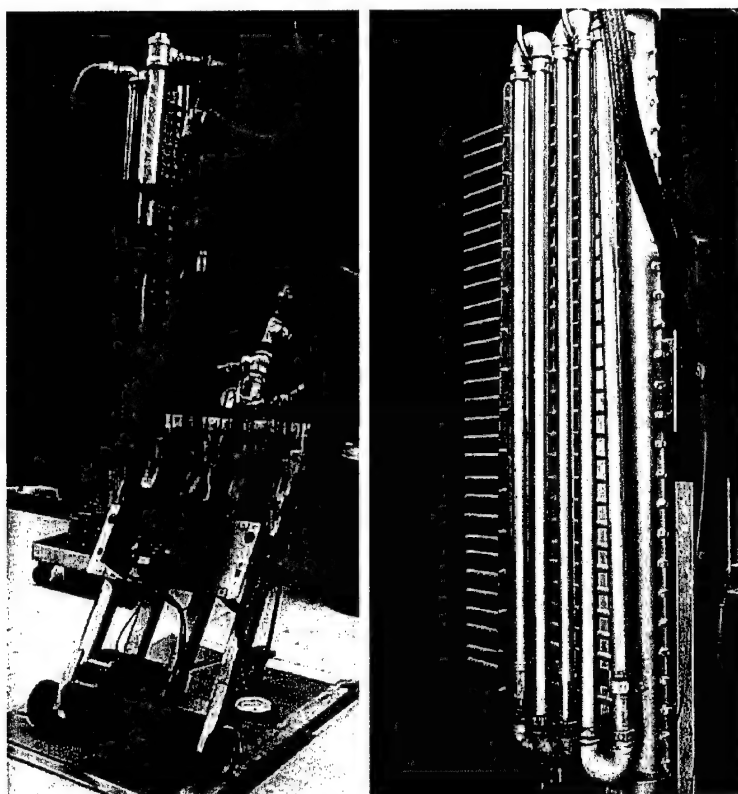


Figure 3.3. Photograph of the smoke generator and close-up of the smoke rake.

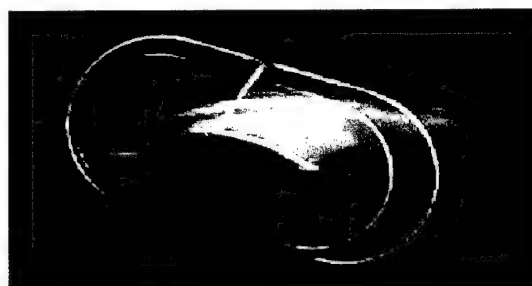


Figure 3.4. Sample flow visualization image for the NACA 66₃ – 018 airfoil at 16° angle of attack and a freestream velocity of 20 m/s (65.9 ft/s).

The maximum freestream speed where flow visualization could be performed was approximately 30 m/s. Above this, the density of smoke became low, and it was difficult to illuminate sufficiently to capture with the video camera.

3.3 Stationary Airfoil Setup

Two symmetric airfoils were used in the stationary airfoil studies: a NACA 66₃ – 018 and a NACA 0015. The shapes were chosen because the steady characteristics of these airfoils are well-known and documented in the literature [1], and at high angles of attack both exhibit leading-edge separation.

The NACA 66₃ – 018 was chosen because it had previously been used at Notre Dame for lift-drag measurements performed using a force balance. These allowed a direct comparison to benchmark lift and drag values that were based on airfoil surface pressure measurements and wake velocity profiles.

The NACA 0015 was chosen because it had commonly been used for helicopter rotor blades, and there are numerous experimental results using this airfoil in helicopter rotor simulations in the literature [1, 4, 22, 36, 40, 62]. This airfoil shape was used in the present research for both stationary and oscillating airfoil cases.

Both airfoils had a 12.7 cm (5 in) chord and a 25.4 cm (10 in) span. The size of the airfoils was set to minimize blockage effects, especially at the large angles of attack that were investigated. They were cast in an epoxy-based polymer in a two-piece aluminum mold. The mold used to cast the NACA 0015 airfoil is shown in Figure 3.5. It was precisely machined using a numerical-controlled milling machine. The

locations of surface pressure ports were drilled as holes in the surface of the mold. These accepted tubulations, 0.5 mm (0.02 in) I.D., that were cast into the airfoil and brought out through a hollow tube support on one end of the model. After the casting material had hardened, the airfoil was released from the mold and the pressure tubing projections were trimmed flush with the airfoil surface.

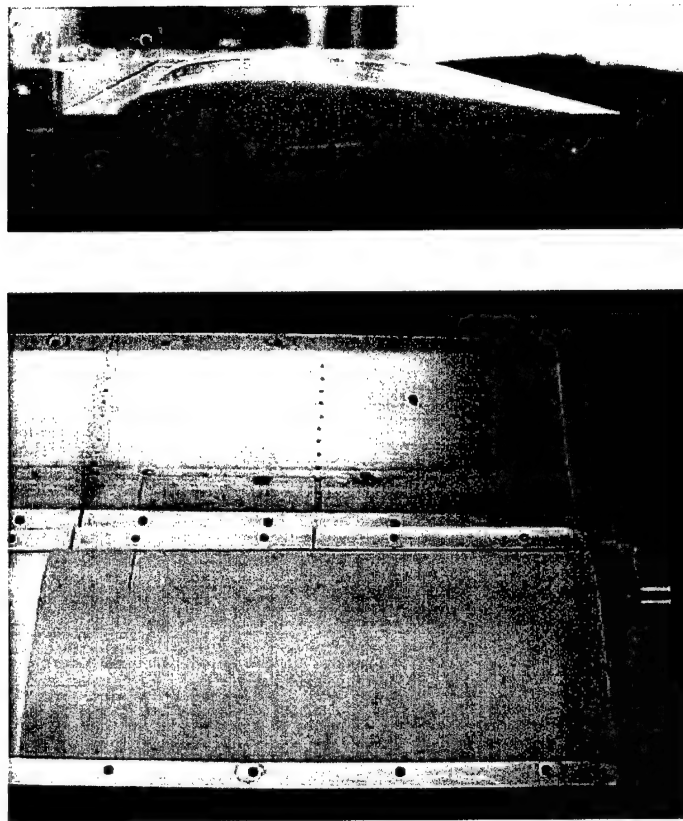


Figure 3.5. Aluminum mold used to cast the NACA 0015 airfoil.

End plates were used to minimize 3-D end effects on the airfoils. The end plates were constructed from clear Plexiglas to allow visual access for flow visualization. The end plates were 40.6 cm (16 in) by 20.2 cm (8 in), with a 10.2 cm (4 in) radius and were 3.2 mm (0.125 in) thick. A schematic drawing of the NACA 66₃-018 airfoil and a photograph outside the tunnel test section is shown in Figure 3.6.

The airfoils were mounted by passing the support tube through the back wall of the test section. The tube was held in place by a chuck that allowed angular motion for setting the angle of attack. The pressure tubes exited the tunnel through the support tube.

The plasma actuator consisted of two copper electrodes separated by a 5-mil thick Kapton film. The electrodes were made from 0.0254 mm thick copper foil tape, which was bonded directly to the surface of the airfoil. It filled a recess to produce a smooth, flush surface with the airfoil shape.

Two actuators were used on the NACA 66₃-018 airfoil. One was placed precisely at the leading edge ($x/c = 0$), and oriented to produce a velocity component toward the suction side of the airfoil. The other was placed near the maximum thickness location ($x/c = 0.5$), and oriented to produce a velocity component in the mean freestream direction.

A single actuator was used on the NACA 0015. It was placed at the leading edge ($x/c = 0$), and again oriented to produce a velocity component toward the suction side of the airfoil. The actuator placement on the two airfoils is illustrated schematically in Figure 3.7.

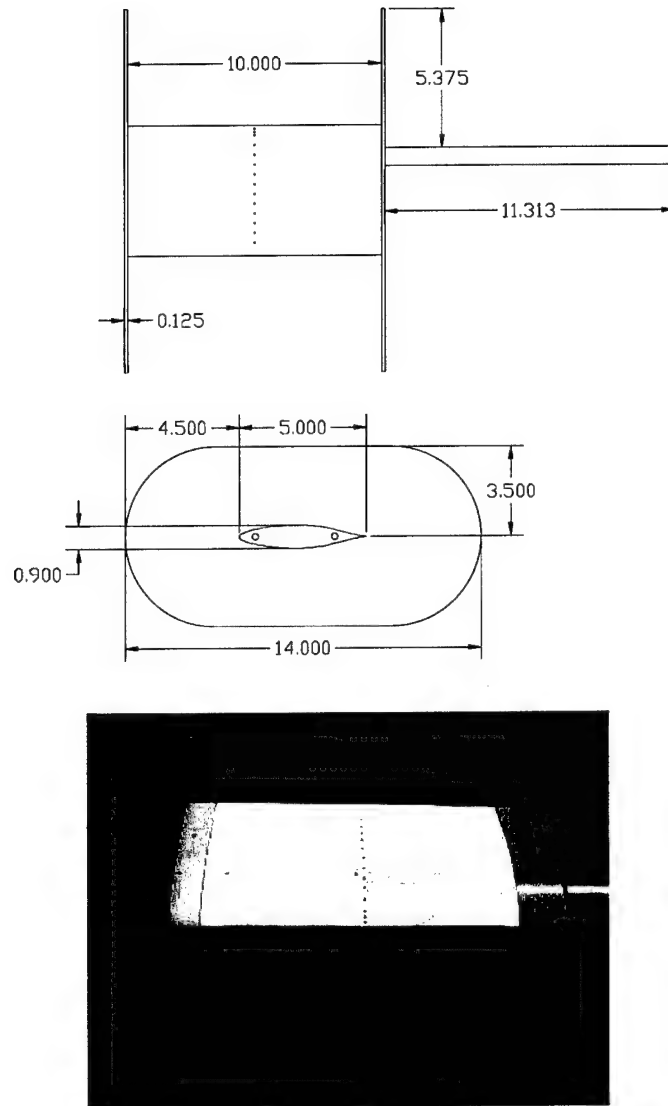


Figure 3.6. Schematic drawing and photograph the NACA 66₃-018 airfoil with end plates. Dimensions are in inches.

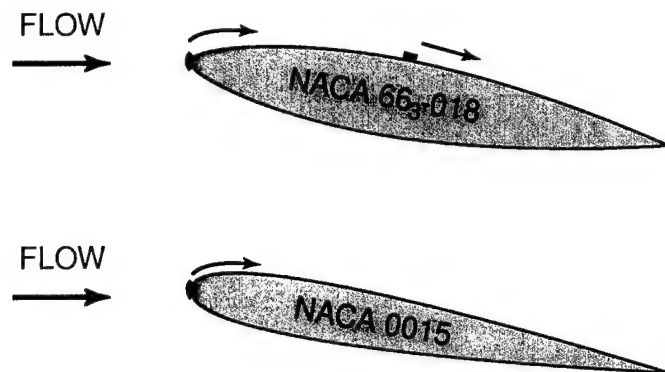


Figure 3.7. Schematic drawing showing the locations and orientations of plasma actuators used for separation control on the NACA 66₃ - 018 and NACA 0015.

Photographs of the NACA 66₃ - 018 airfoil with the electrodes and Kapton film in place are shown in Figure 3.8. The space that was allotted for the actuator on the airfoil was relatively large to accommodate a variety of configurations. In the top photograph, most of the area is passive and covered by Kapton film to bring the recessed area flush with the other airfoil surface. The active actuator regions are best seen in the lower photograph which shows the two lines of plasma that are weakly visible at the leading edge and mid-chord locations when viewed in a darkened lab. The actuator spanned most of the width of the airfoil. A narrow gap on the spanwise centerline where the pressure ports were located was left open without the actuator. However, the actuators on both sides of the line of pressure ports were electrically connected together.

The operating frequency of the a.c. voltage supplied to the electrodes was 5 kHz. The waveform was a triangle wave. Unless otherwise specified, the actuator a.c. amplitude was 11 kV_{p-p}.

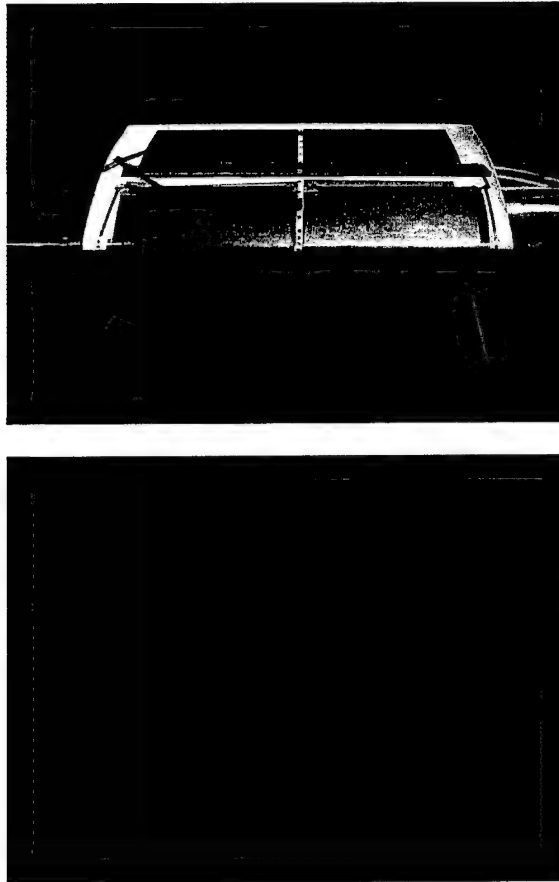


Figure 3.8. Photographs of the NACA 66₃ – 018 airfoil with plasma actuators at the leading edge and mid-chord locations (top) and lines of plasma when viewed in a darkened lab (bottom).

3.3.1 Pressure Data Acquisition

A total of 29 surface pressure ports, 0.5 mm (0.02 in) I.D., were aligned with the flow direction at the half-span location on the airfoil. Although they were spaced relatively uniformly around the airfoil, there was a slight increase in concentration of ports near the leading edge. Table 3.1 provides the positions of the surface pressure ports.

The pressure measurements were made using a Scanivalve Model J9 scanning pressure valve. A Validyne DP103 pressure transducer, with range up to 5.5 in. H₂O, and a Validyne CD23 carrier demodulator were used. This pressure transducer arrangement was selected because of its good sensitivity and stability. Also the use of a carrier frequency makes the transducer insensitive to electronic noise.

Static calibration was performed against a calibrated reference electronic manometer. Different pressures were supplied by a pitot probe located in the freestream of the tunnel test section. The test section velocities were varied in the range from 0 to 35 m/s. With the carrier demodulator set to provide a gain of 5, a static pressure calibration coefficient of 1.84 volts/ in. H₂O was obtained. The static calibration is presented in Figure 3.9. This indicates a linear relation between the transducer output voltage and pressure.

For the airfoil experiments, a pitot static probe was located in the freestream. This provided the reference static pressure for each pressure port. A second pitot static probe was mounted to a traversing mechanism. This was placed two chord lengths downstream of the airfoil at its spanwise centerline. Discrete points were sampled across the wake to construct the mean velocity profile.

TABLE 3.1. STATIC PRESSURE PORT LOCATIONS ON THE SURFACE OF THE AIRFOIL.

Port #	x/c	Port #	x/c
0	0.0	15/16	0.456
1/2	0.025	17/18	0.532
3/4	0.051	19/20	0.608
5/6	0.076	21/22	0.684
7/8	0.152	23/24	0.759
9/10	0.228	25/26	0.835
11/12	0.304	27/28	0.911
13/14	0.380		

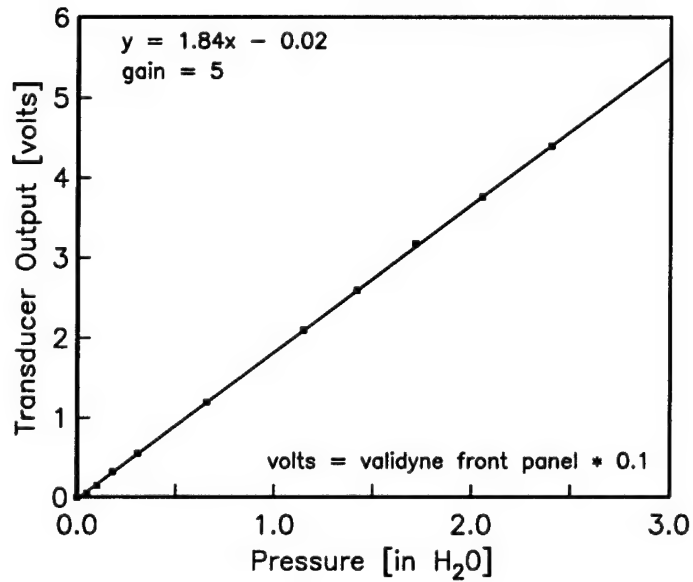


Figure 3.9. Static calibration curve for the Validyne pressure transducer.

On the surface of the airfoil, the coefficient of pressure, C_p , was calculated as

$$C_p = \frac{P_s - P_\infty}{\frac{1}{2}\rho U_\infty^2} = \frac{P_s - P_\infty}{P_0 - P_\infty} \quad (3.1)$$

where P_s is the static pressure at each port, P_∞ is the static pressure of the freestream, ρ is the density of the freestream air, U_∞ is the velocity of the freestream, and P_0 is the total pressure of the freestream.

The coefficient of lift, C_l , was found by integrating the C_p distribution around the airfoil. Since high angles of attack were investigated with the oscillating airfoil, the coefficient of lift was calculated using

$$C_l = C_n \cos \alpha - C_a \sin \alpha \quad (3.2)$$

where c_n is the normal force coefficient given by

$$C_n = \int_0^1 (C_p^L - C_p^U) d\left(\frac{x}{c}\right) \quad (3.3)$$

and c_a is the axial force coefficient given by

$$C_a = \int_0^1 \left(C_p^U \left(\frac{dy_U}{c} \right) - C_p^L \left(\frac{dy_L}{c} \right) \right) d\left(\frac{x}{c}\right), \quad (3.4)$$

where the subscripts and superscripts of U and L refer to the upper and lower surface of the airfoil, respectfully.

The drag coefficient, C_d , on the airfoil was determined from the mean velocity profiles taken in the wake. This is given as

$$C_d = \frac{4}{U_\infty^2} \int_0^1 U(y)(U_\infty - U(y)) d\left(\frac{y}{H}\right) \quad (3.5)$$

where $U(y)$ is the local mean streamwise velocity, and H is a distance which encompasses the full wake. The velocity profiles used to determine the drag were measured well downstream of any recirculation region that might exist in the separated flow at high angles of attack. This location was two chord lengths downstream of the trailing edge.

Data acquisition was performed using a LabView program. The surface pressure measurements were scanned separately at each port. Velocity profiles in the wake were scanned by starting at the bottom of the wake and traversing to the top of the wake in 0.3175 cm (0.125 in) increments. Data processing was done using Matlab. A program was written to calculate the coefficients of lift and drag using the previously given definitions.

3.4 Oscillating Airfoil

A NACA 0015 airfoil was used as the model for the oscillating airfoil measurements. It was chosen because its characteristics are well-known and documented in the literature, and because it was commonly used for helicopter rotor blade applications and experiments [1, 4, 22, 36, 40, 62].

The airfoil had a 12.7 cm (5 in) chord and a 25.4 cm (10 in) span. Like the other airfoil, it was cast in an epoxy-based polymer in a two-piece mold. The end plates for the oscillating airfoil were round, with a 40 cm (15.75 in) diameter. The thickness of the end plates was 3.2 mm (0.125 in). The center of the circular end plates was at the airfoil's pitching location, which corresponded to the quarter-chord location.

With this configuration, the end plates appeared stationary in the flow visualization results. A schematic drawing of the airfoil with circular endplates and a photograph inside the test section are shown in Figure 3.10.

The airfoil was mounted by passing its support tube through the back wall of the test section. In this case the support tube was connected to a servo motor that powered the oscillating motion. The pressure tubes exited the tunnel through the support tube, which was hollow.

The plasma actuator for the oscillating NACA 0015 had the same configuration as for the stationary NACA 0015 experiments, which was described in Section 3.3. As was illustrated schematically in Figure 3.7, it was placed at the leading edge ($x/c = 0$), and oriented to produce a velocity component toward the suction side of the airfoil when at an angle of attack.

3.4.1 Servo Motor

The oscillating motion of the airfoil was driven by a specially selected servo motor (SmartMotor SM3430 by Animatics). The motor had a 1000-count, quadrature digital optical encoder. A photograph of the servo motor is shown in Figure 3.11. The motor has a gear drive with a 10:1 gear ratio. With this, it can provide up to 11 N·m (96.8 lb-in) of continuous torque.

The motor has an internal processor that runs a controller program. The Smart-Motor Interface software was provided by the manufacturer. The motor controller program was modified so that the motor motion would follow an analog input voltage

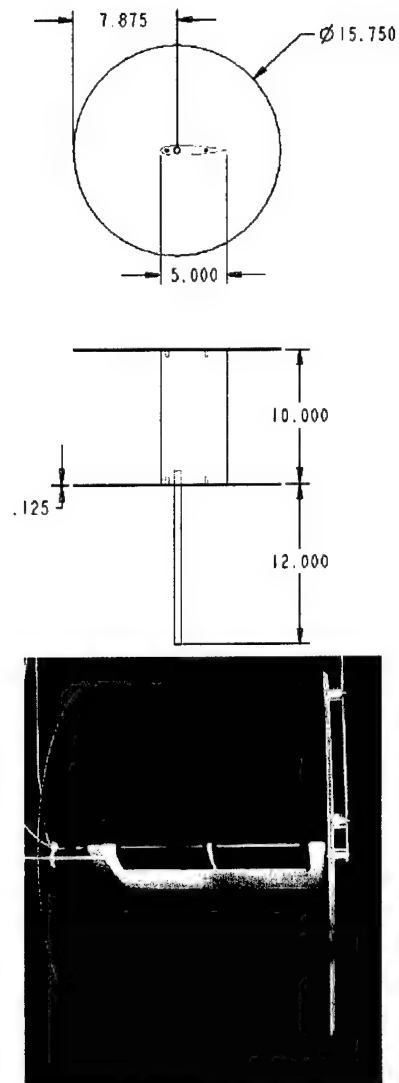


Figure 3.10. Schematic drawing and photograph of the NACA 0015 airfoil with circular end plates. Dimensions are in inches.

amplitude. The modified controller program is included in Appendix A.

A Stanford Research Systems DS335 3.1 MHz synthesized function generator was used to generate the voltage time series that oscillated the airfoil sinusoidally. The oscillatory airfoil motion was defined as

$$\alpha(t) = \alpha_{mean} + \alpha_{amp} \sin \omega t \quad (3.6)$$

where $\alpha(t)$ is the instantaneous angle of attack, α_{mean} is the mean angle of attack, α_{amp} is the amplitude of the oscillating motion, ω is the frequency of oscillation, and t is time.

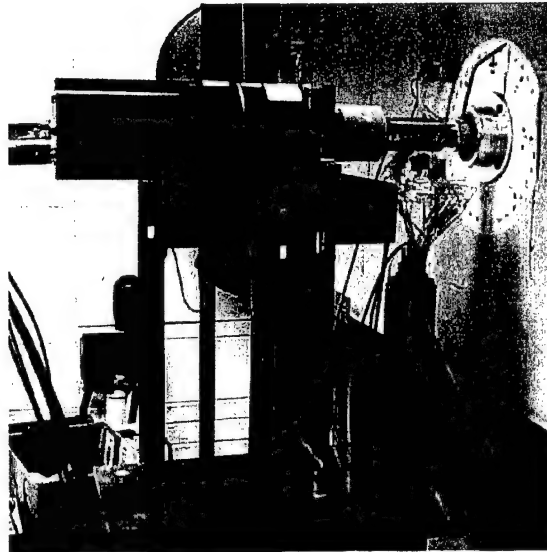


Figure 3.11. Photograph of the motor on the back wall of the test section.

3.4.2 Servo Motor Position and Direction Circuit

Feedback of the servo motor position came from two digital optical encoders that were part of the motor system. These were used to determine the instantaneous position and direction of the oscillating airfoil. For this, a circuit was designed and constructed that used the digital encoder signals to construct an analog voltage that was proportional to the airfoil's position.

A schematic of the circuit is shown in Figure 3.12, and a photograph of the actual circuit is shown in Figure 3.13. The main components and a description of their function are given in the following:

P85A: The P85A is a 1 MHz crystal signal generator. It was used to generate clock pulses for the circuit.

4017 and 4013: The 4017 and 4013 chips divide down the clock pulses by factors of ten and two, respectively.

HP2020: The HP2020 chip is a quadrature decoder. It used the two optical encoder output signals (A and B) as inputs, and generated a pulse and a logical direction value on every rising and falling edge.

4049: The 4049 is a hex inverter. It was used to invert some of the digital signals as needed.

LS191: The four LS191 chips are 4-bit up/down binary counters that increment (or decrement) with each pulse of the HP2020.

4047: The 4047 is a 1-shot pulse generator that resets the counters to zero. The MSB of the counter array is inverted in order to position the count at mid-range. The counters have been cascaded and are input to the LTC1597.

LTC1597: The LTC1597 is a 16-bit Digital-to-Analog (D/A) converter.

1112: The 1112 is a current to voltage op-amp. It converts the output of the D/A converter to a voltage that corresponds to the airfoil's position.

LT1236-10: The LT1236-10 regulates a precise 10 volts. It served as the reference for the LTC1597.

A comparison between the function generator input to the servo motor, and the output from the motor position and direction circuit is shown in Figure 3.14. The sine wave frequency was 4 Hz. The top trace is the function generator input to the motor. The bottom trace is the instantaneous position of the motor as determined from the motor encoder. Comparing the two traces, it is clear that the actual instantaneous motor position is sinusoidal, but lags in phase behind the function generator. For this reason, the output from the motor encoder was used to determine the instantaneous position and direction of the oscillating airfoil.

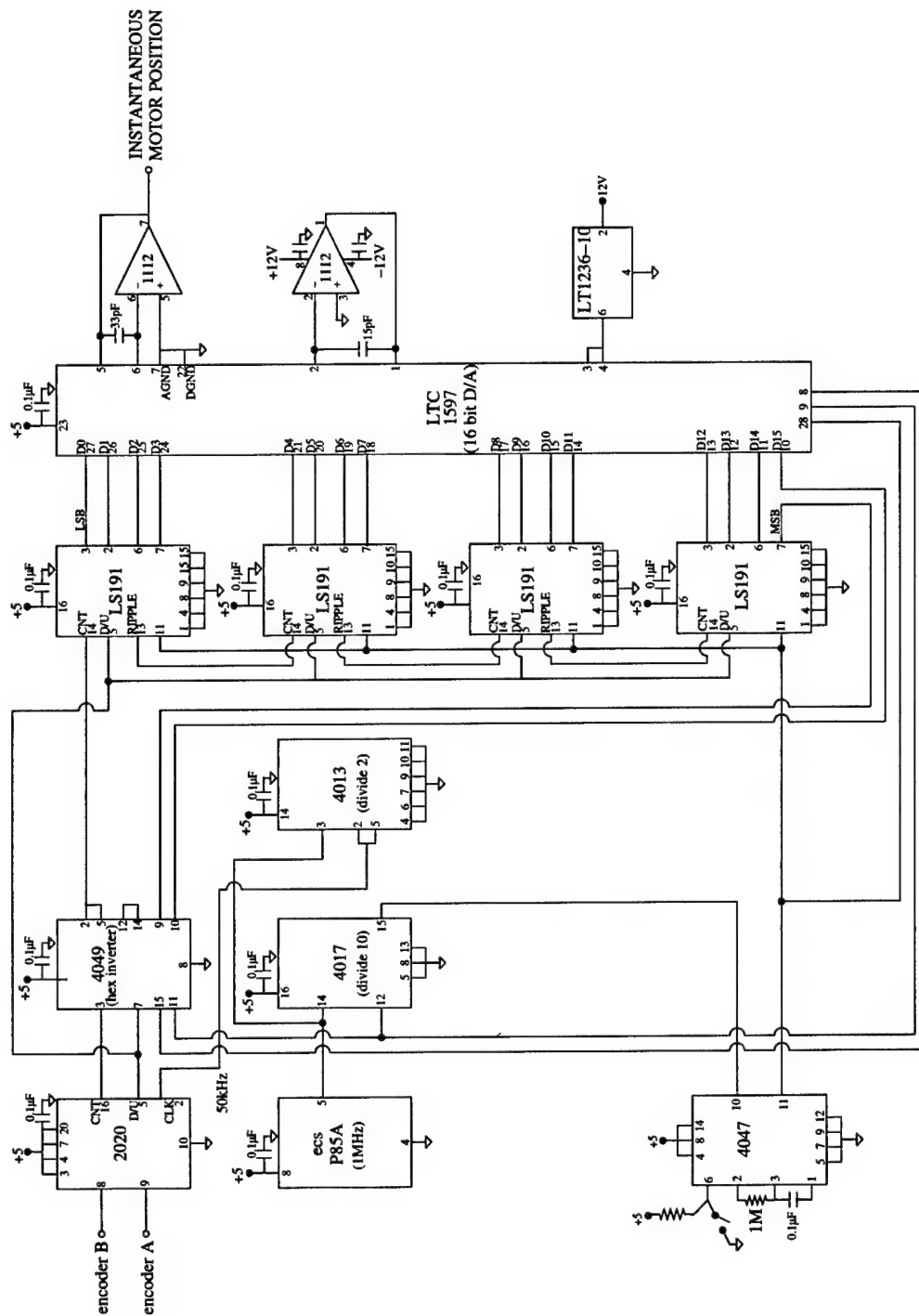


Figure 3.12. Schematic of the circuit that uses the motor encoder to determine the instantaneous airfoil position and direction.

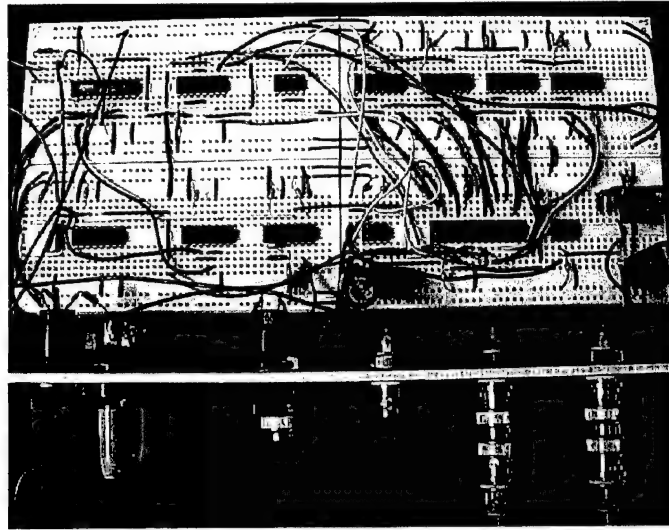


Figure 3.13. Photograph of the servo motor position and direction circuit.

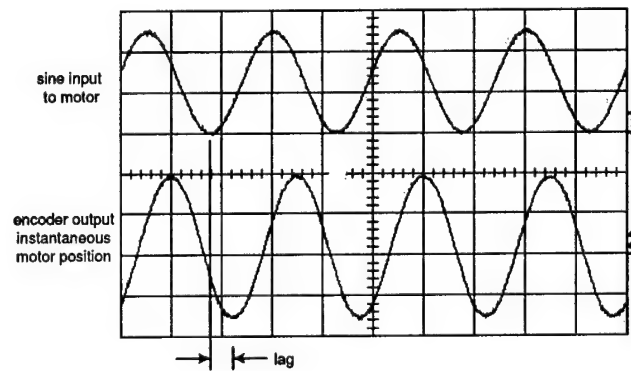


Figure 3.14. Oscilloscope trace of the sine input to the motor (top) and the actual position of the motor (bottom).

3.4.3 Angle of Attack Indicator Circuit

A circuit was built that could provide a voltage pulse at a specified angle of attack of the oscillating airfoil. This was used to trigger the strobe light for phase-conditioned flow visualization and to provide a reference pulse to be used to turn off and on the plasma actuator during "smart" actuator operation.

The angle of attack indicator circuit was designed to produce a square wave pulse centered about each integer angle of attack. A schematic of the circuit is shown in Figure 3.15, and a photograph of the actual circuit is shown in Figure 3.16.

The input to the circuit was the analog output of the motor position and direction circuit previously described in Section 3.4.2. The top circuit in Figure 3.15 consisted of a variable d.c. offset and gain that was applied to the motor position signal. The output from this part of the circuit went through a unity gain follower that acted as an output buffer.

The middle circuit was used to produce a d.c. reference voltage. Its output was also buffered with a unity gain follower. This d.c. reference voltage set the width of the square wave pulse that was centered about each integer angle of attack.

The bottom circuit in Figure 3.15 is one of twelve used. It was used to generate a square wave pulse whenever the airfoil was at an integer angle of attack. The inputs common to all twelve circuits were the outputs from the top two circuits, the conditioned motor position signal and the d.c. reference voltage.

A variable resistor on the left side of the circuit was used to set one voltage limit. Another limit was obtained by a difference amplifier, which subtracted the d.c.

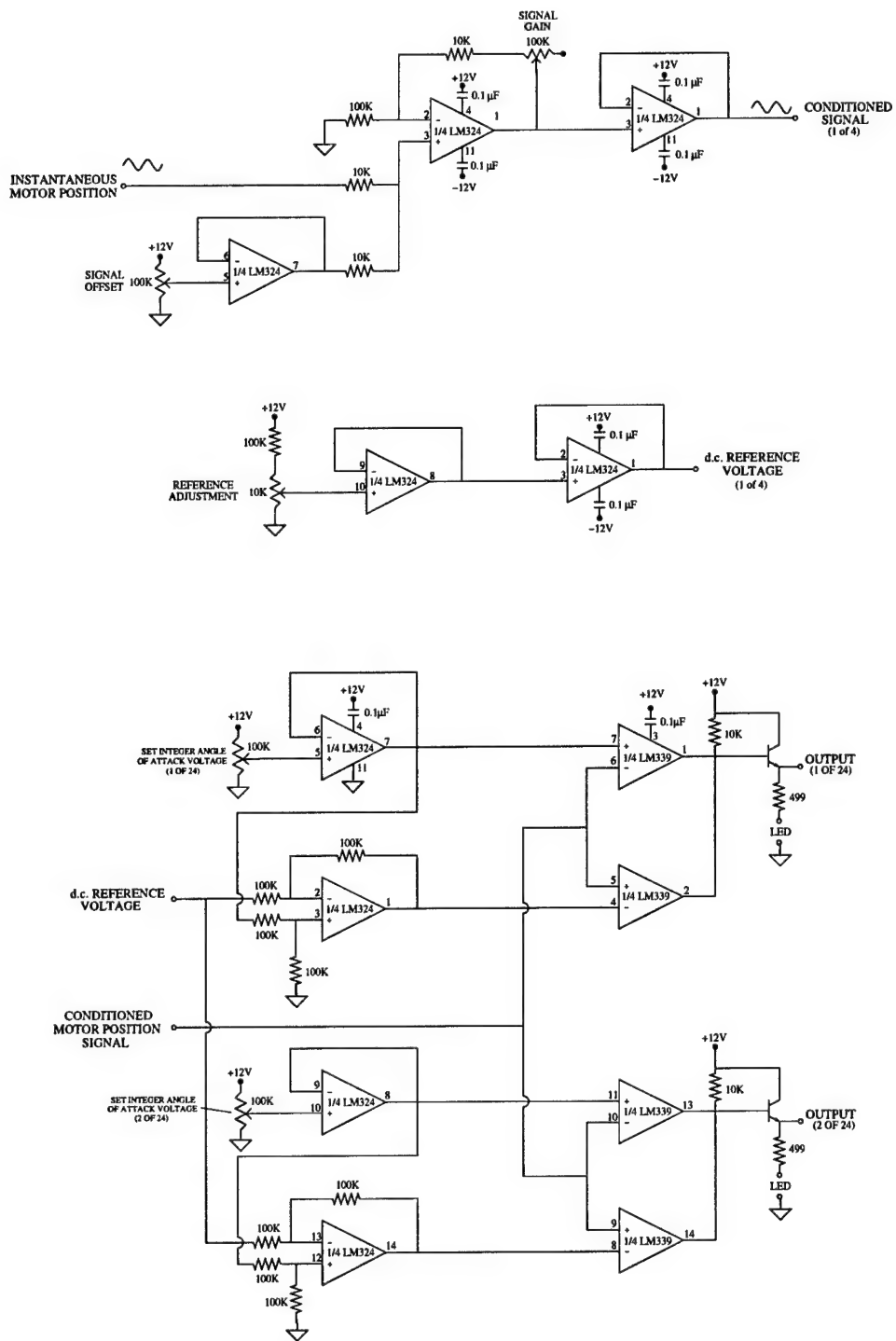


Figure 3.15. Schematic of the circuits that comprise the angle of attack indicator circuit.

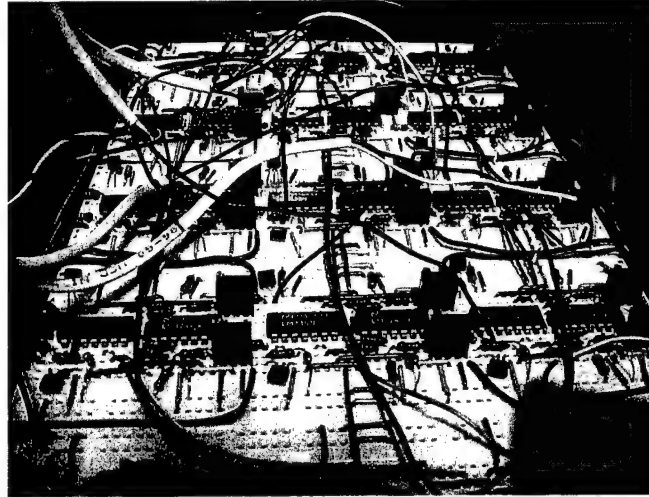


Figure 3.16. Photograph of the angle of attack indicator circuit.

reference voltage from the first limit. A window comparator on the right side of the circuit generated a square wave pulse whenever the motor position signal was between the two limits.

This square wave pulse was centered about each integer angle of attack. The procedure for doing this was to instruct the motor to move to a specified integer airfoil angle of attack. This produced a voltage proportional to the angle of attack from the analog signal from the motor position and direction circuit. The variable resistor was then adjusted so that the center of the square wave pulse was at the voltage proportional to the integer angle of attack.

Up to 24 comparator outputs could be used. For this experiment, the outputs were set at one degree increments in angle of attack. As a visual reference, the outputs were used to power a rainbow array of LEDs.

3.4.4 "Smart" Actuation Circuit

The "smart" actuation consisted of turning on the actuator only during portions of the oscillation cycle. This required the design of a special circuit whose schematic is shown in Figure 3.17. A photograph of the fabricated circuit is shown in Figure 3.18.

The circuit has three signal inputs. These are (1) the low-voltage a.c. signal that is used to drive the plasma actuator, (2) the up/down direction signal indicator from the motor position and direction circuit, and (3) the square wave pulse(s) from the angle of attack indicator circuit. The main components of the circuit and a description of their function are given in the following:

4050: The 4050 is a hex, non-inverting buffer and TTL driver. Signals from the angle of attack indicator circuit were buffered and conditioned to a 5 V TTL signal.

74LS08: The 74LS08 is a quad, two-input 'and' gate. The up/down direction signal from the motor position and direction circuit were used along with the angle of attack signals from the angle of attack indicator circuit as inputs to the 'and' gate.

74LS112: The 74LS112 is a flop-flop used to generate a signal 'high' between the 'ON' and 'OFF' voltage range. When a high signal was received on the 'ON' input, the output of the flip-flop was set high. When a high signal was received on the 'OFF' input, the output of the flip-flop was set low. When neither input was active, the output of the flip-flop would maintain its previous state.

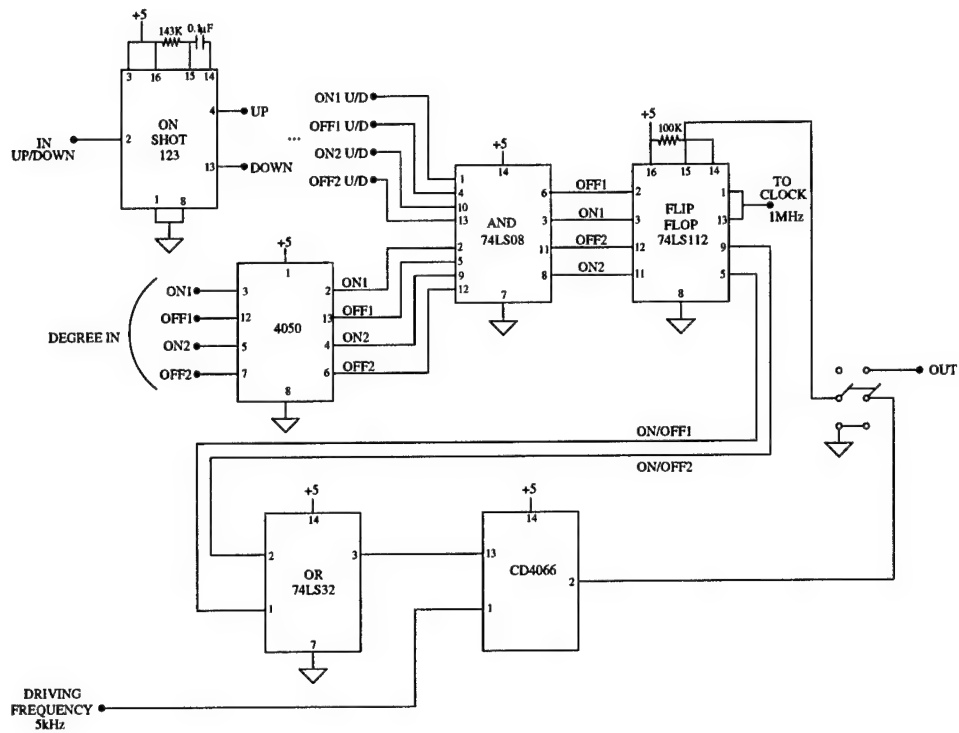


Figure 3.17. Schematic of the circuit that generates a signal for the “smart” actuation operation.

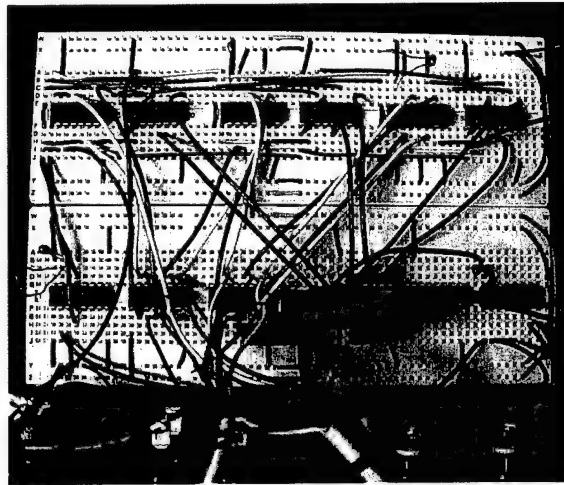


Figure 3.18. Photograph of the “smart” actuation circuit.

74LS32: The 74LS32 is a quad, dual-input 'or' gate. It was used to combine multiple on/off signals into a single signal.

CD4066: The CD4066 is a quad, bilateral switch that requires two inputs. The single output signal from the 74LS32 was used to drive the CD4066 to turn off or on the a.c. signal that was used to drive the plasma actuator.

An example of the time trace produced by the smart actuation circuit is shown in Figure 3.19. The top trace is the typical 5 kHz a.c. operating frequency signal that is sent to the actuator. The bottom trace illustrates how the "smart" actuation circuit only activates the 5 kHz a.c. signal in selected portions of the airfoil oscillation period. The actual portions of the period when the actuator was activated will be discussed in Chapter 5.

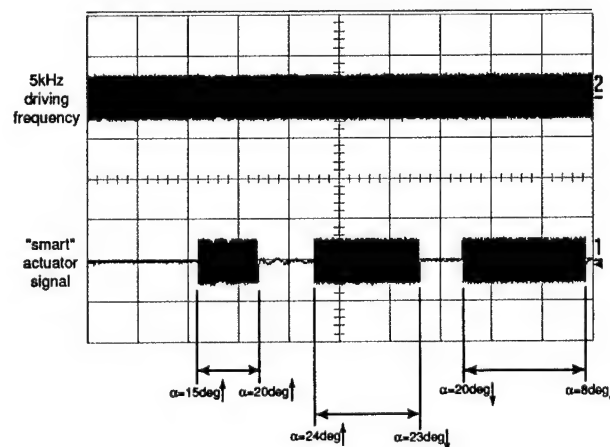


Figure 3.19. Oscilloscope trace of the 5 kHz used to generate the plasma (top) and the "smart" actuation trace (bottom).

3.4.5 Pressure Data Acquisition

The locations and number of pressure ports were the same as for the stationary airfoil. These were discussed in Section 3.3.1 and listed in Table 3.1. However, the pressure transducer used for the oscillating airfoil measurements was different. It was a Scanivalve PDCR24 differential pressure transducer that mounted inside the Model J9 Scanivalve. The pressure transducer range was ± 10 in. H₂O. The advantage of this transducer was that it minimized the length of pressure tubing, and thereby maximized the frequency response of the pressure measurement system.

A circuit to power the pressure transducer was designed and built. A schematic of the circuit is shown in Figure 3.20. A photograph of the actual circuit is shown in Figure 3.21. The transducer is represented as the Wheatstone Bridge at the top of the circuit diagram. The output of the transducer was amplified by a differential gain circuit [23]. A gain of 500 was set by the ratio of the $2\text{ M}\Omega$ feedback resistance and the $4\text{ k}\Omega$ resistance of the Wheatstone Bridge.

The signal from the transducer amplifier was low-pass filtered using a second-order Butterworth filter. The circuit schematic for this is shown in the middle circuit of Figure 3.20. The filter circuit was designed to have a cut-off frequency, f_c , of 200 Hz. This was 50 times larger than the highest oscillating frequency used in the experiments.

The cut-off frequency was set by the circuit components based on

$$f_c = \frac{1}{2\pi RC_1 \xi}, \quad (3.7)$$

where ξ is the damping factor which is defined as

$$\xi = \left(\frac{C}{C_1} \right)^{1/2} \quad (3.8)$$

A damping factor of approximately 0.68 gives a critically damped response that has minimizes amplitude overshoot. Therefore the capacitor values were selected so that

$$\xi = \left(\frac{0.0047}{0.01} \right)^{1/2} = 0.685. \quad (3.9)$$

For the desired cut-off frequency of 200 Hz, the values of the resistors were found from Equation 3.7. They were

$$R = \frac{1}{2\pi f_c \xi C_1} = \frac{1}{2\pi (0.685)(200)(0.01 \times 10^{-6})} = 116K \approx 120K. \quad (3.10)$$

The last stage of the pressure transducer circuit was a unity gain follower (depicted in the bottom circuit of Figure 3.20) that acted as an output buffer.

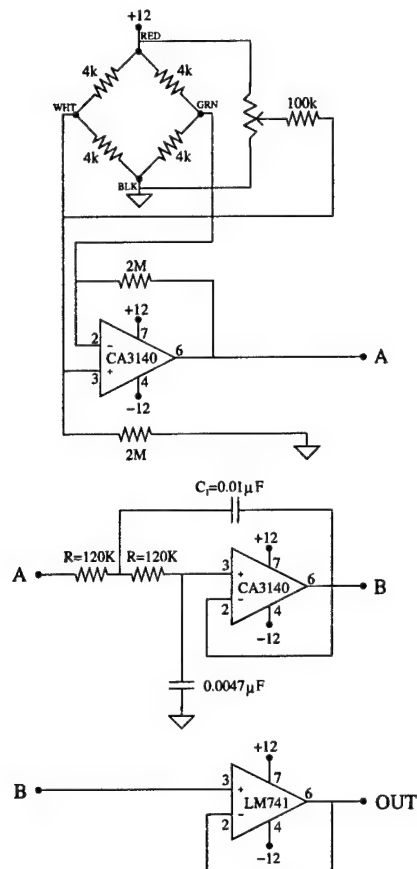


Figure 3.20. Schematic of the circuit used to condition the output signal from the Scani-valve pressure transducer.

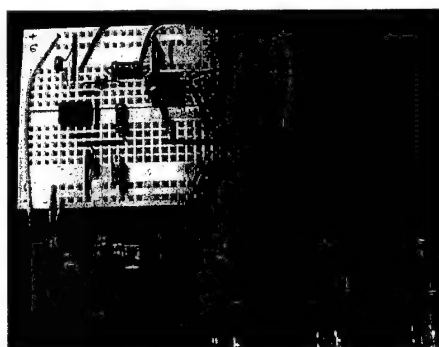


Figure 3.21. Photograph of the circuit used to condition the output signal from the Scani-valve pressure transducer.

A static calibration of the Scanivalve pressure transducer was performed in the same manner as the Validyne pressure transducer used in the stationary airfoil measurements. This was described in Section 3.3.1. The results of the calibration are presented in Figure 3.22. For this, a good linear static response is noted, with a calibration coefficient of 2.17 volts/in. H₂O.

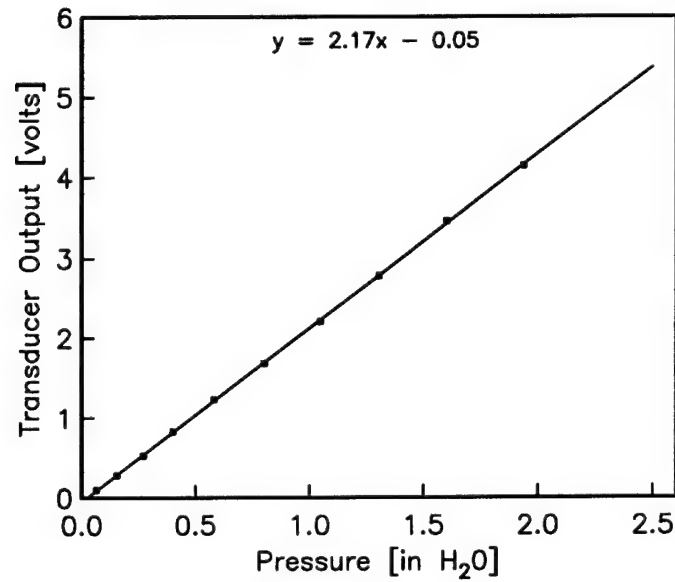


Figure 3.22. Static calibration curve for the Scanivalve PDCR24 pressure transducer.

The dynamic response of the pressure system was performed by introducing a constant amplitude, varying frequency sinusoidal pressure fluctuation through one port on the NACA 0015 airfoil. For this a Stanford Research Systems DS335 3.1 MHz Synthesized Function Generator was used to provide the input to a Crown D150A amplifier which drove a 0.127 m (5 in) speaker. A 0.127 m (5 in) diameter, 0.1651 m (6.5 in) length cylinder enclosure with a 0.003175 m (0.125 in) exit hole with an o-ring seal channeled the pressure fluctuations to the one pressure port on the model. An ACO microphone was used to monitor the fluctuations in the cylinder enclosure to ensure that the amplitude was constant for different frequencies.

The dynamic response measurements consisted of recording the r.m.s. amplitude and phase delay of the pressure transducer circuit output, for a range of frequencies. The phase delay used the microphone signal as a reference. The results are shown in Figures 3.23 and 3.24.

The amplitude response was found to be flat within 3 dB up to 150 Hz. The phase change was relatively small up to approximately 50 to 60 Hz. Given that the maximum oscillation frequency is only 4 Hz, it was not considered necessary to perform any amplitude or phase compensation to the dynamic pressure measurements on the oscillating airfoil.

As with the stationary airfoil, a pitot static probe located in the freestream provided the reference static pressure for each pressure port measurement. The downstream pitot probe that was traversed in the wake of the stationary airfoil was not used for the oscillating airfoil experiments.

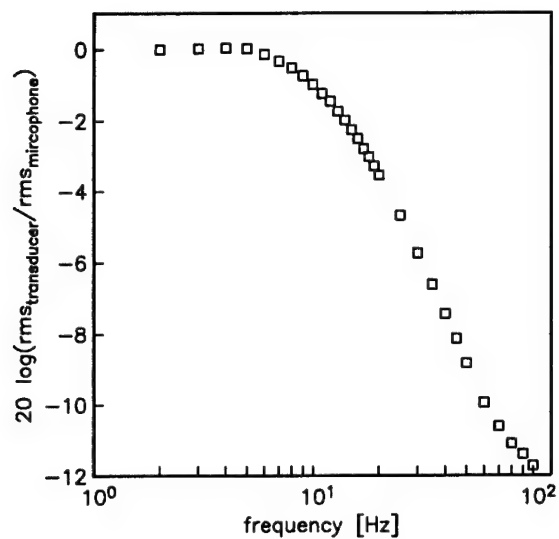


Figure 3.23. Dynamic calibration of the Scanivalve PDCR24 pressure transducer.

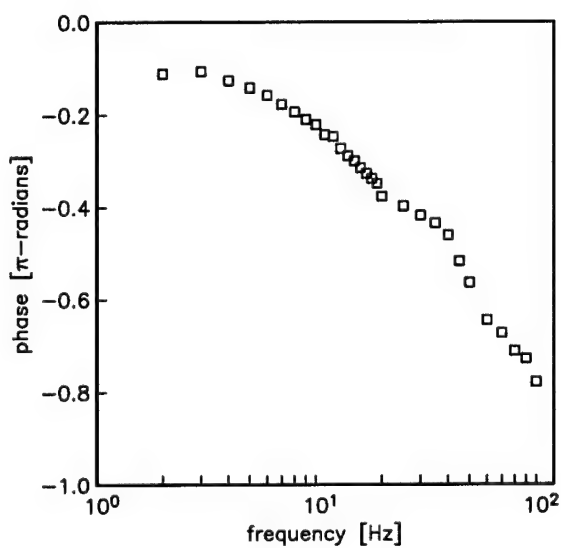


Figure 3.24. Phase lag of the Scanivalve PDCR24 pressure transducer.

Acquisition of the pressure ports on the oscillating airfoil was performed using a LabView program. This worked as follows:

1. a pressure port to be sampled was selected,
2. a time delay occurred to allow for the response of the Scanivalve to move,
3. instantaneous motor position and pressure time series were sampled at an acquisition rate of 1,000 Hz in a continuous record for a user-defined number of cycles (typically 20 oscillations),
4. the time-series record was stored,
5. oscillating-cycle ensemble averages and standard deviations were computed and stored for discrete angles, and
6. another pressure port was selected and the acquisition steps were repeated until all of the pressure ports had been sampled.

The pressure coefficient distribution on the oscillating airfoil was calculated in the same manner as with the stationary airfoil (Equation 3.1). Also as before, the coefficient of lift, C_l , was found by integrating the C_p distribution around the airfoil (Equation 3.2). In the case of the oscillating airfoil, the C_l cycled according to the oscillating airfoil period. The normal and axial force coefficients, C_n and C_a , were also calculated as before (Equations 3.3 and 3.4).

One additional coefficient that was calculated for the oscillating airfoil cases was the moment coefficient, C_m . The moment coefficient about the leading edge, $C_{m_{LE}}$, is defined as

$$C_{m_{LE}} = -\frac{1}{c^2} \int_0^1 (C_p^L - C_p^U) \frac{x}{c} d\left(\frac{x}{c}\right). \quad (3.11)$$

This was transferred to the quarter-chord location as

$$C_{m_{1/4}} = C_{m_{LE}} + \left(\frac{x}{c}\right) C_n. \quad (3.12)$$

All of the post acquisition processing of the pressure data was done using Matlab codes. These can be found in Appendix B.

CHAPTER 4

SEPARATION CONTROL ON STATIONARY AIRFOILS

This chapter presents results on the use of the plasma actuator for control of leading-edge separation on stationary airfoils at high angles of attack. Two airfoil shapes, a NACA 66₃ – 018 and a NACA 0015, were examined for a range of freestream speeds and chord Reynolds numbers. The NACA 0015 was also used for the oscillating airfoil experiments that appear in Chapter 5.

4.1 NACA 66₃ – 018 Experiments

4.1.1 Baseline Measurements

The object of the baseline measurements was to document the angle of attack characteristics of the airfoil before performing separation control. This involved measurement of the static pressures on the surface of the airfoil and mean velocity profiles in the airfoil wake. From these measurements lift and drag were derived, respectively.

An example of the C_p distribution around the airfoil at an angle of attack of 8 degrees at $Re_c = 75K$ is shown in Figure 4.1. This relatively low Reynolds number was chosen because it corresponded to conditions investigated by Jansen [25].

The C_p distributions, like this one, were integrated around the airfoil in order to determine the lift coefficient. A plot of the lift coefficient for a range of angles of attack at $Re_c = 75K$ is shown in Figure 4.2. Also plotted for reference are the C_l values from Jansen, which were derived using a force balance. The comparison is reasonably good, except at this low Reynolds number the linear C_l versus α region is not well defined.

A similar comparison is made at a higher Reynolds number of 200K in Figure 4.3. Here the linear regime of C_l versus α region is very clear. The two experiments agree reasonably well in this regime. However at higher angles of attack, Jansen measured a higher $C_{l_{max}}$ and stall angle, α_s . In our lift calculations, a more relaxed stall regime is observed, with stall occurring between 10 and 11 degrees.

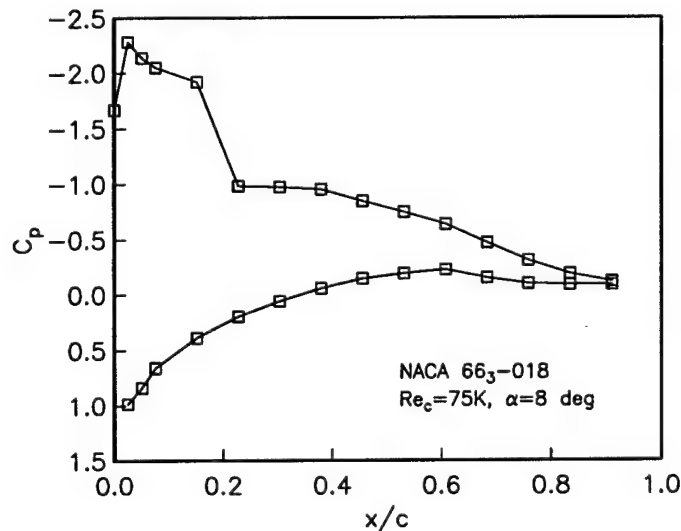


Figure 4.1. Sample C_p distribution around the NACA 663 - 018 airfoil for $\alpha = 8^\circ$ and $Re_c = 75K$.

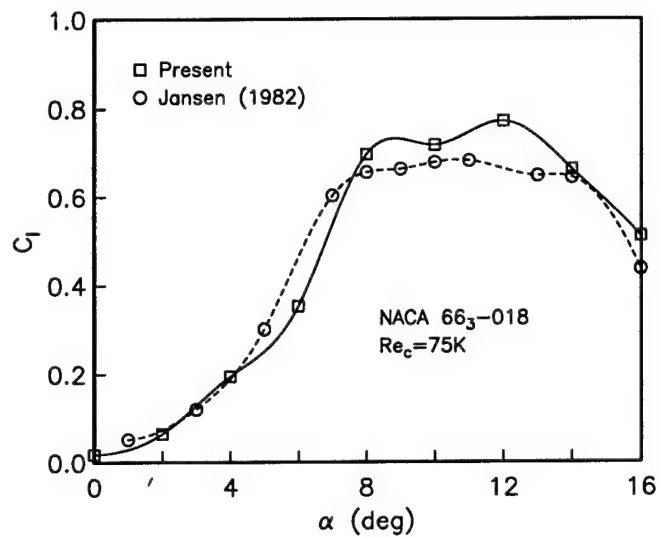


Figure 4.2. Comparison between calculated lift coefficient values for a NACA 66₃ - 018 airfoil found by integrating C_p distribution, and those of Jansen [25] using a lift-balance at $Re_c = 75K$.

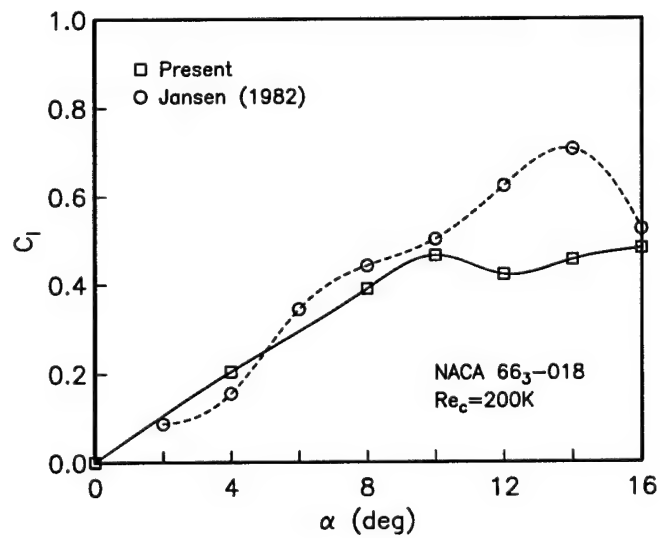


Figure 4.3. Comparison between calculate lift coefficient values for a NACA 66₃ - 018 airfoil found by integrating C_p distribution, and those of Jansen [25] using a lift-balance at $Re_c = 200K$.

4.1.2 Vortex Generators

As a precursor to the separation control using the plasma actuators, passive vortex generators were used to provide a reference condition. The vortex generators consisted of brass shim material that was bent in a 90° angle. A photograph of the vortex generators on the NACA 66₃ - 018 airfoil is shown in Figure 4.4. The part of the vortex generator that was above the surface of the airfoil was approximately 2 mm (0.08 in) square. This was estimated to extend past the edge of the boundary layer in the attached flow, but well within the separated flow region at large angles of attack. The flat face of the generators were oriented to 45° to the mean flow direction. The result was an array of co-rotating vortices.

The effect of the vortex generators were documented for two angles of attack; the first near $C_{l_{max}}$ and the other well past stall where the flow was separating at the leading edge. Figure 4.5 documents the results at $Re_c = 79K$, corresponding to $U_\infty = 10$ m/s for the 12.7 cm (5 in) chord airfoil. This shows the C_p distribution around the airfoil. The baseline condition corresponds to the two angles of attack prior to stall ($\alpha = 14^\circ$) and post-stall ($\alpha = 16^\circ$) without the vortex generators. At a post-stall angle of attack, a large decrease in the pressure on the suction side of the airfoil near the leading edge indicates leading-edge separation.

The dashed curves in Figure 4.5 show the C_p distributions with the vortex generators at two different location $x/c = 0.05$ and $x/c = 0.2$. At both locations, the vortex generators were able to cause the flow to reattach, which is signified by a recovery of the suction pressure near the leading edge. The vortex generators placed

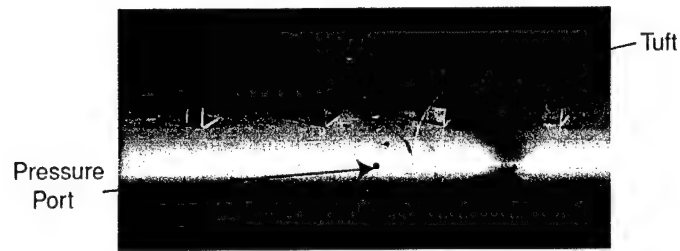


Figure 4.4. Photograph of vortex generators used as a baseline flow reattachment device on the NACA 66₃ - 018 airfoil.

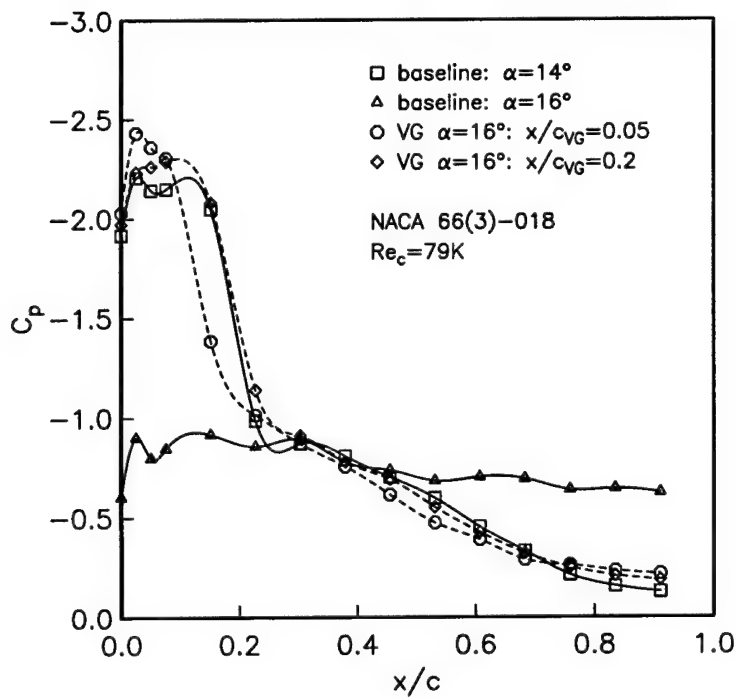


Figure 4.5. Comparison of C_p distributions on the NACA 66₃ - 018 airfoil at $Re_c = 79K$, without and with vortex generator tabs.

closer to the leading edge produced a higher $-C_p$ peak; however, those placed at $x/c = 0.2$ improved the suction pressure over a larger portion of the chord so that the integrated effect was larger. Other measurements at 30 m/s ($Re_c = 237K$) with the vortex generators showed similar results, although the vortex generators located closer to the leading edge were slightly more effective overall.

4.1.3 Steady Actuation

Two plasma actuators were applied on the surface of the NACA 66₃ - 018 airfoil. One was placed precisely at the leading edge ($x/c = 0$), and oriented to produce a velocity component toward the suction side of the airfoil when at an angle of attack. The other was placed near the maximum thickness location ($x/c = 0.5$), and oriented to produce a velocity component in the mean freestream direction. The actuators were operated in the steady mode at 5 kHz and at an amplitude of 11 kV_{p-p}. The actuator effectiveness was documented at two different Reynolds numbers, 79K and 158K.

The first results are at a Reynolds number of 79K, which is comparable to where the baseline vortex generator tabs were examined. A flow visualization photograph with the plasma actuator off and on is shown in Figure 4.6. Here, the symmetric airfoil is at a negative angle of attack so that the separated region is on the bottom where the light source below the test section can illuminate that region.

In Figure 4.6, $\alpha = 16^\circ$, which is approximately 4 degrees past stall at $Re_c = 79K$. With the actuator off, the flow separates at the leading edge of the airfoil and forms

a large recirculation region that extends beyond the trailing edge. With the actuator on, the flow is fully attached at the leading edge. The wake is also visibly narrower based on the number of smooth streak lines downstream of the airfoil.

Quantitative data is in the form of surface pressure measurements and velocity profiles in the wake. These were used to calculate lift and drag forces on the airfoil. The suction-side C_p distributions for the same conditions as in the flow visualization in Figure 4.6 ($Re_c = 79K$, $\alpha = 16^\circ$) are presented in Figure 4.7. The pressure distributions for the actuator off, the actuator on, and the $x/c = 0.2$ vortex generator tabs are all plotted. Based on the higher $-C_p$ peak near the leading edge, the plasma actuator appears to recover the suction pressure better than the vortex generators.

The mean velocity profiles in the wake of the airfoil are presented in Figure 4.8. With the plasma actuator on, there is a substantial reduction in the wake width and an increase in the centerline deficit velocity. Both of these characteristics are consistent with a decrease in the drag on the airfoil.

Complete sets of C_p distributions and mean velocity profiles in the wake were used to determine the lift and drag coefficients at different angles of attack up to 18° with the plasma actuator off and on. The results in terms of the lift-to-drag ratio (L/D) are compiled in Table 4.1. For the conditions in the flow visualization in Figure 4.6, the L/D ratio increased more than 4 times with the plasma actuator on to cause the flow to reattach.

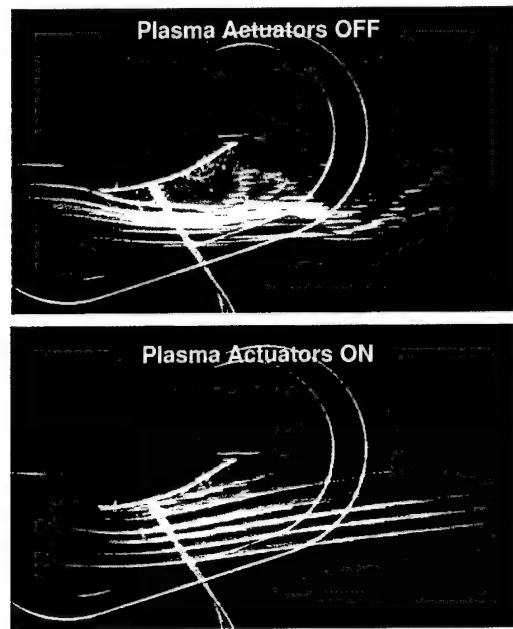


Figure 4.6. Photographs of visualized flow around the NACA 66₃-018 airfoil with plasma actuators off (top) and on (bottom) for $\alpha = 16^\circ$ and $Re_c = 79K$.

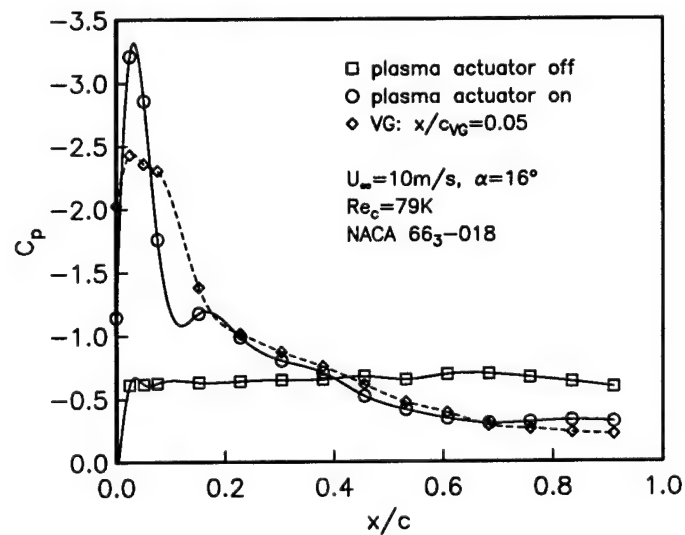


Figure 4.7. Suction-side C_p distribution on the NACA 66₃-018 airfoil with plasma actuator off and on and comparison to vortex generator for $\alpha = 16^\circ$ and $Re_c = 79K$.

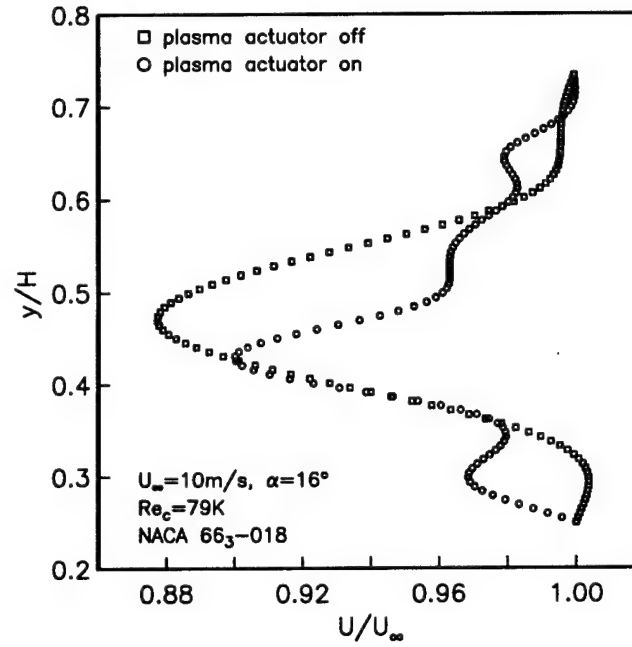


Figure 4.8. Wake mean velocity distribution of the NACA 66₃ – 018 airfoil with the plasma actuator off and on for $\alpha = 16^\circ$ and $Re_c = 79K$.

TABLE 4.1. COMPARISON OF L/D WITH PLASMA ACTUATORS ON THE NACA 66₃ – 018 AIRFOIL FOR $Re_c = 79K$.

Actuator	α ($^\circ$)	L/D
Off	16	14
On	16	60
Off	18	21
On	18	40

A higher Reynolds number of 158K was also investigated and found to produce similar results as the lower Reynolds number case. Flow visualization results are shown in Figure 4.9 for $\alpha = 16^\circ$, which is approximately 4° past the stall angle of attack. Again, the symmetric airfoil is at a negative angle so that the separated region is on the bottom where the light source below the test section can illuminate that region. When the actuator is off, the air flow exhibits full leading-edge separation. When the actuator is turned on, the flow fully reattaches and the wake is visibly narrower.

The pressure distribution on the suction side of the airfoil for $\alpha = 16^\circ$ is presented in Figure 4.10 for the cases with the actuator off and on. This data corresponds to the same conditions as in flow visualization record in Figure 4.9. With the actuator off, the pressure distribution is essentially flat across the chord, signifying that the flow is separated. With the actuator on, the large negative C_p at the leading edge indicates a full pressure recovery and flow reattachment.

Again the C_p distributions were integrated around the airfoil to obtain the lift coefficients at different angles of attack with the actuator off and on. The lift coefficients are shown in Figure 4.11 for post-stall angles of attack. With the actuator off, the C_l values are flat at a value of approximately 0.5. With the actuator on, the lift coefficient continues to increase with angle of attack even up to 20° , where $C_l \simeq 0.75$.

The mean velocity profiles in the wake of the airfoil at $\alpha = 16^\circ$ with the actuator off and on are presented in Figure 4.12. These show a dramatic reduction on the wake width and an increase in the minimum peak velocity with the actuator on.

Wake profiles like these were used to calculate the drag coefficient. The results are presented in Figure 4.13 for post-stall angles of attack. This shows an almost 4-times decrease in C_d at $\alpha = 16^\circ$. Although a reduction in drag occurred up to the highest angles of attack investigated with the actuator on, the margin of improvement decreased. In assessing this, it is important to note that the amplitude to the actuator was kept fixed. It is possible that higher amplitudes would have given further improvement at the higher angles. Therefore, the effect of the actuator amplitude was investigated and will be discussed in Section 4.1.4.

The lift and drag results for $Re_c = 158K$ are combined in the form of a drag polar that is shown in Figure 4.14. This demonstrates that the plasma actuator produced a significant widening of the drag bucket which resulted in a significant performance enhancement of the airfoil.

4.1.4 Sensitivity to Actuator Amplitude

All of the results to this point were based on a single actuator amplitude (V_{p-p}). The selection of the amplitude had primarily been based on a visual indication of flow reattachment using flow visualization. The following considers the sensitivity of the lift and drag on the actuator amplitude.

The effect of the plasma actuator amplitude on the C_p distributions on the suction side of the airfoil are presented in Figures 4.15. The amplitude designated as 100% corresponds to that used to obtain the previous results at $Re_c = 158K$, including the flow visualization in Figure 4.9. The C_p distributions indicate that an essentially full

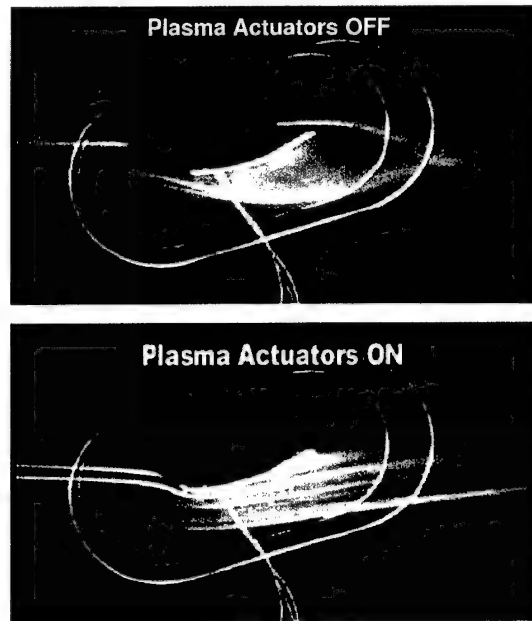


Figure 4.9. Photographs of visualized flow around the NACA 66₃ – 018 airfoil with plasma actuators off (top) and on (bottom) for $\alpha = 16^\circ$ and $Re_c = 158K$.

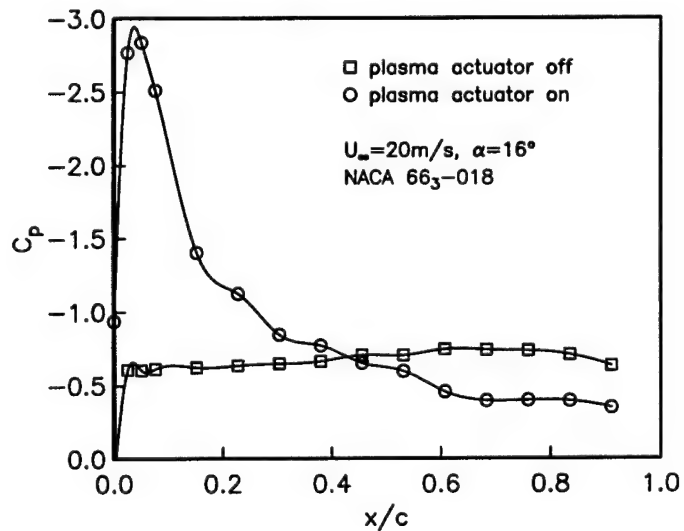


Figure 4.10. Suction-side C_p distribution on the NACA 66₃ – 018 airfoil with plasma actuator off and on, and comparison to vortex generator for $\alpha = 16^\circ$ and $Re_c = 158K$.

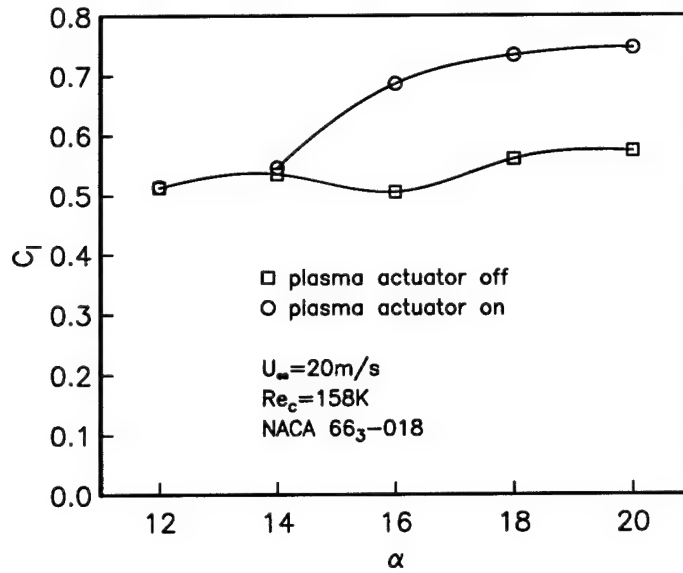


Figure 4.11. Comparison of lift coefficient versus angle of attack on the NACA 66₃ - 018 airfoil with the plasma actuator off and on at $Re_c = 158K$.

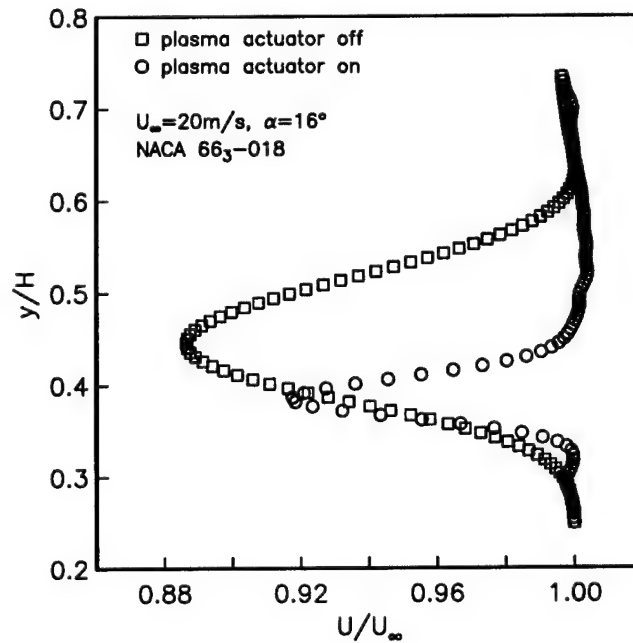


Figure 4.12. Wake mean velocity distribution of the NACA 66₃ - 018 airfoil with the plasma actuator off and on for $\alpha = 16^\circ$ and $Re_c = 158K$.

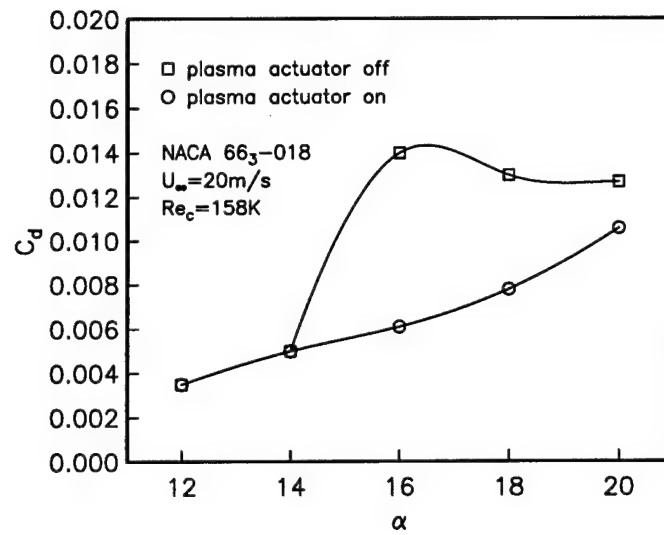


Figure 4.13. Comparison of drag coefficient versus angle of attack on the NACA 66₃ - 018 airfoil with the plasma actuator off and on at $Re_c = 158K$.

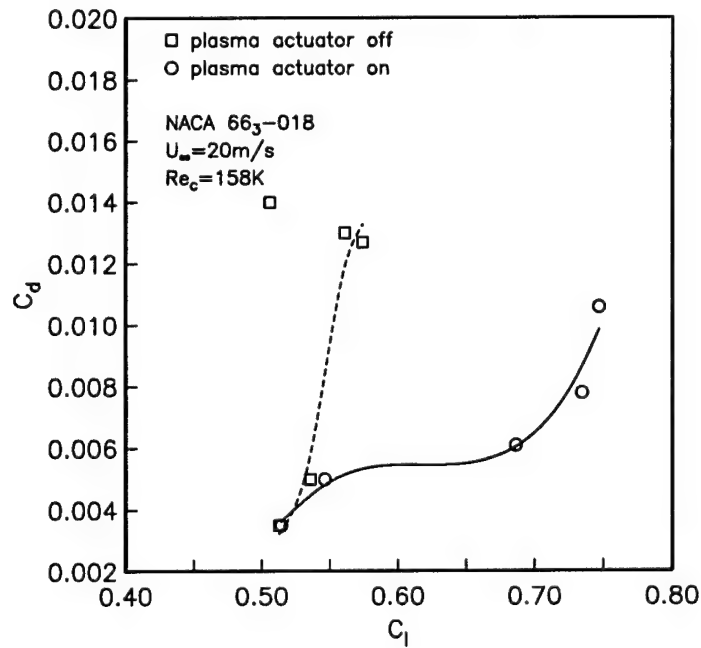


Figure 4.14. Comparison of drag polars of the NACA 66₃ - 018 airfoil with the plasma actuator off and on at $Re_c = 158K$.

pressure recovery occurred at 60% of the original amplitude, and that there were only minor improvement at higher amplitudes.

The corresponding mean velocity profiles in the airfoil wake are presented in Figure 4.16. In contrast to the C_p distributions, the wake profiles indicate a continual improvement (reduction in the wake width) in the drag with increasing actuator amplitude.

The C_p distributions and mean velocity profiles in the wake were used to determine the lift and drag coefficients for the different actuator amplitudes. These are plotted in Figure 4.17, where the circle symbols correspond to C_l which is read on the left axis, and the square symbols correspond to C_d which is read on the right axis. The results indicate that for the lift coefficient, once a threshold amplitude was reached (approximately 40% in this case), the flow reattached. Beyond this threshold, there was little more to be gained in lift with additional actuator amplitude. However, for the drag coefficient, there was an approximately linear decrease in the drag as the actuator amplitude increased, even after the lift value had saturated. As a consequence, the L/D ratio continued to increase as the actuator amplitude increased.

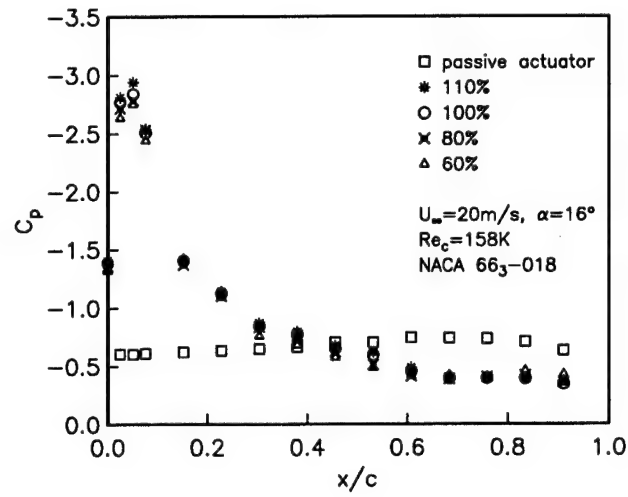


Figure 4.15. Suction-side C_p distributions for different plasma actuator amplitudes at $\alpha = 16^\circ$ and $Re_c = 158K$.

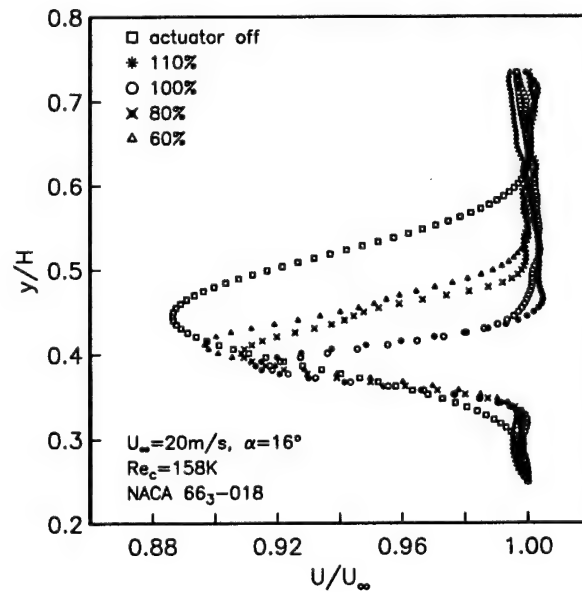


Figure 4.16. Wake mean velocity profiles for different plasma actuator amplitudes at $\alpha = 16^\circ$ and $Re_c = 158K$.

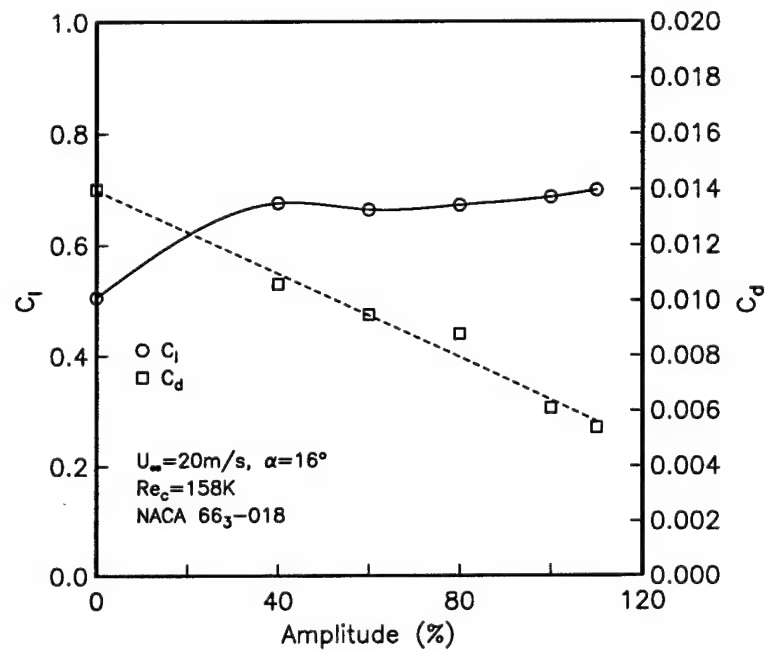


Figure 4.17. Lift and drag coefficients for different plasma actuator amplitudes at $\alpha = 16^\circ$ and $Re_c = 158K$.

4.2 NACA 0015 Experiments

Presented here are the results obtained with the NACA 0015 airfoil. A single, asymmetric plasma actuator was bonded on the surface of the airfoil at the leading edge. The arrangement of the actuator was illustrated in Figure 3.7 in Chapter 3. This was designed to produce a velocity component toward the suction side of the airfoil when at an angle of attack. The results in this section document the ability of the steady and unsteady plasma actuator to control leading-edge flow separation. As with the NACA 66₃ – 018 airfoil, the actuator a.c. frequency was 5 kHz and the amplitude was 11 kV_{*p-p*}. The freestream speed was 20 m/s, which gave a chord Reynolds number of 158K.

4.2.1 Steady Actuation

The flow visualization records presented in Figure 4.18 illustrate the effectiveness of the plasma actuator to control leading-edge separation on the airfoil at $\alpha = 16^\circ$. This angle is approximately 4 degrees past the static stall angle for these conditions. In the top photograph the plasma actuators are off. As with the NACA 66₃ – 018 airfoil, at such post-stall angles the flow separates from the leading edge and a large recirculation region covers the airfoil and extends beyond the trailing edge. The bottom photograph documents the flow with the plasma actuators on. In this case the flow remains fully attached at the leading edge and the wake region is narrower.

The C_p distributions for the conditions in the flow visualization photographs in Figure 4.18 ($Re_c = 158K$, and $\alpha = 16^\circ$) are shown in Figure 4.19. This illustrates

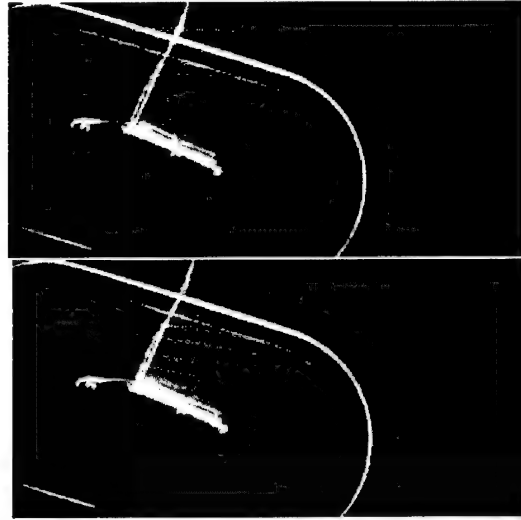


Figure 4.18. Photographs of visualized flow around the airfoil with the plasma actuator off (top) and on (bottom) for $\alpha = 16^\circ$ and $Re_c = 158K$.

the significant $-C_p$ peak that occurs when the actuator is on, which is quantitative evidence that the flow is reattached.

As with the other stationary airfoil cases, the C_p distributions around the airfoil were integrated to obtain the coefficient of lift, C_l . These are presented for the conditions with the actuator off and on in Figure 4.20. This demonstrates a substantially larger C_l with the actuator on compared to the original post-stall condition. As before, the improvement is less at the highest angles of attack; however, as with the other airfoil shape, the actuator amplitude was kept fixed and based on the $\alpha = 16^\circ$ condition.

Mean velocity profiles in the wake of the airfoil for the conditions in the flow visualization photographs in Figure 4.18, are presented in Figure 4.21. These profiles

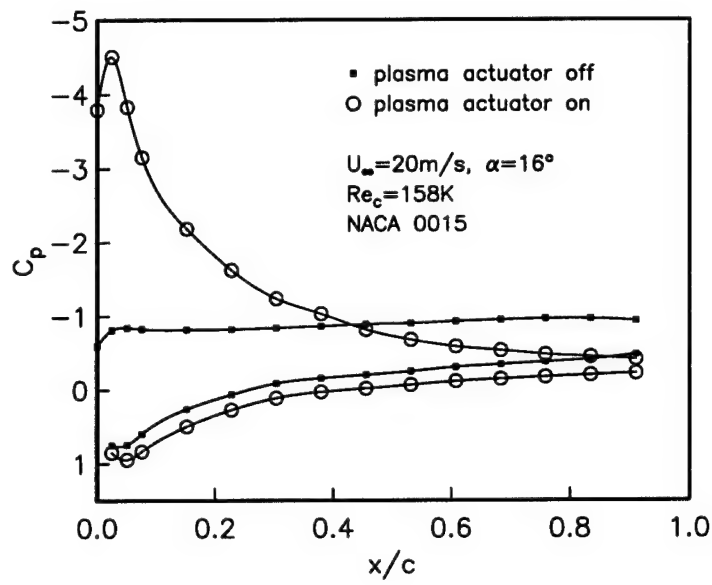


Figure 4.19. Coefficient of pressure distribution on the NACA 0015 airfoil with the plasma actuator off and on for $\alpha = 16^\circ$ and $Re_c = 158K$.

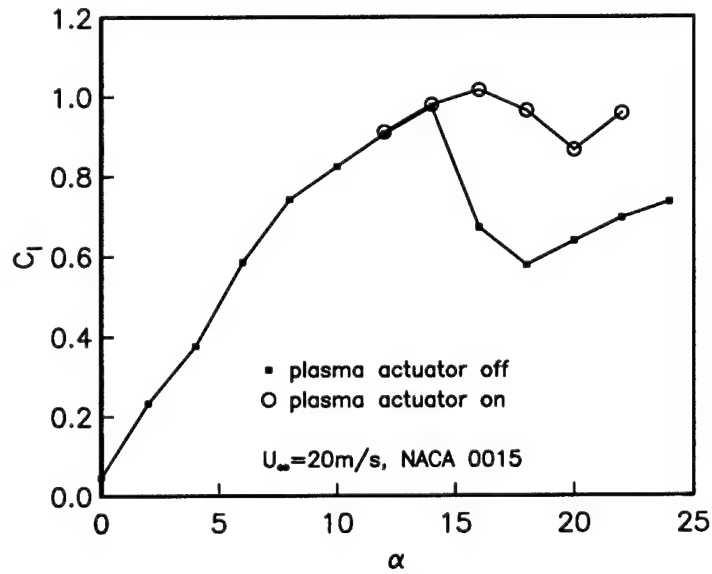


Figure 4.20. Comparison of lift coefficient versus angle of attack for the NACA 0015 airfoil with the steady plasma actuator off and on for $Re_c = 158K$.

were measured two chord lengths downstream of the airfoil, which was well downstream of the flow recirculation region that existed in the separated flow at high angles of attack. The profiles illustrate that with the plasma actuator on, the wake behind the airfoil is smaller. This is seen as a reduction of the mean velocity deficit ($U_\infty - U_{centerline}$), and a substantial reduction in the wake width compared to when the actuator was off.

The coefficient of drag, C_d , was determined by integrating the mean velocity profiles in the wake. The results for different angles of attack with the actuator on and off are shown in Figure 4.22. They demonstrate a substantial decrease in the drag coefficient at post-stall angles of attack with the actuator on.

When the lift and drag results are combined, the reattachment control that the plasma actuator provides results yields a better than 300% increase in the lift-to-drag ratio at post-stall angles of attack. These are comparable to the improvements found on the NACA 66₃ - 018 and would be expected to be the general outcome on airfoils undergoing leading-edge separation.

A composite of the flow visualization results for the NACA 0015 airfoil at angles of attack between 16° and 24° with the actuator off and on are shown in Figure 4.23. The photographs in the left column are with the actuator off, and those in the right column are with the actuator on. Comparing the flow visualization records with the actuator off and on at each angle of attack gives an indication of the effectiveness the actuator had in reattaching the flow. For example at $\alpha = 16^\circ$, the flow visualization indicates that the flow is completely attached at the leading edge. Even at the

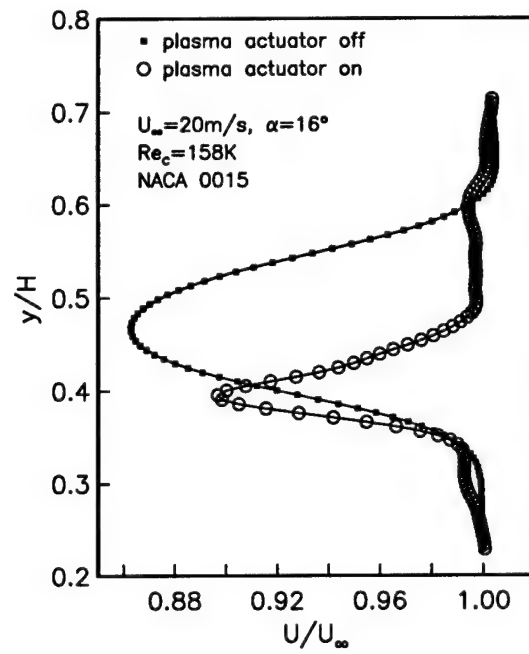


Figure 4.21. Wake mean velocity profiles for the NACA 0015 airfoil with the plasma actuator off and on at $\alpha = 16^\circ$ and $Re_c = 158K$.

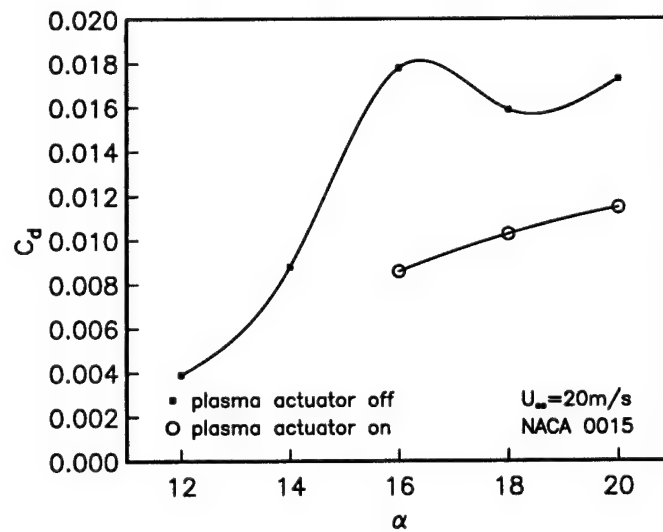


Figure 4.22. Comparison of drag coefficient versus angle of attack for the NACA 0015 airfoil with the plasma actuator off and on at $Re_c = 158K$.

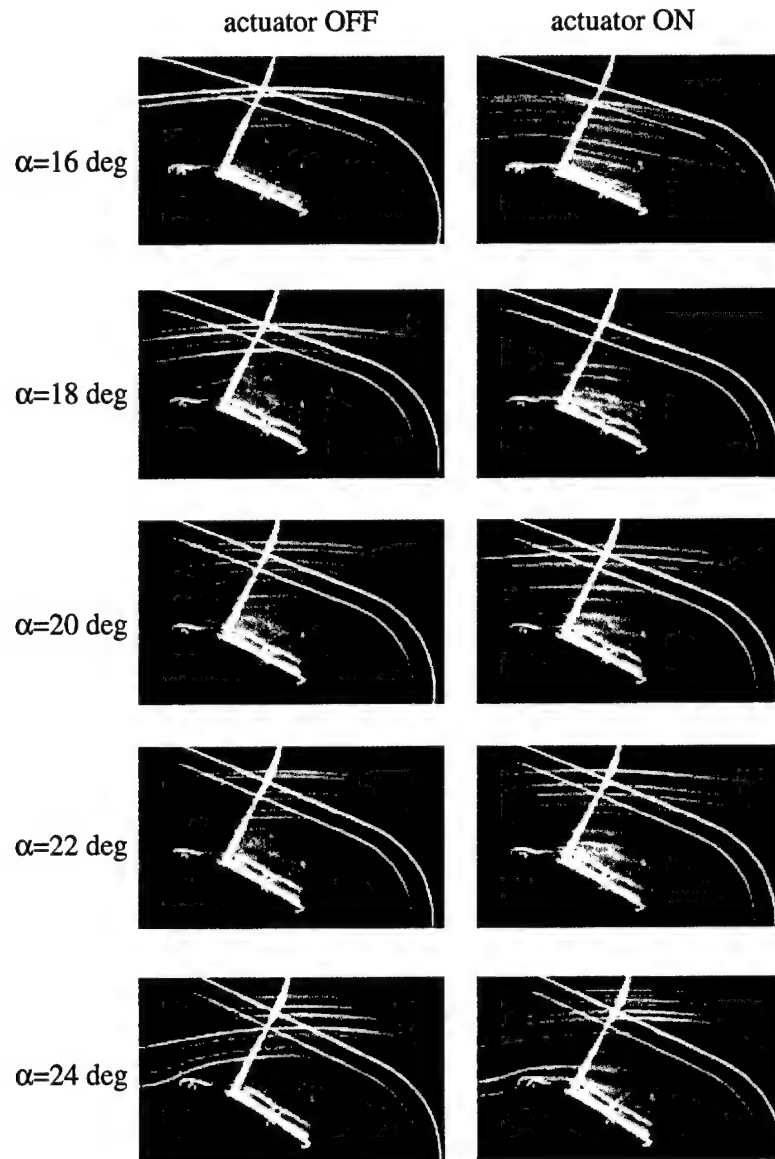


Figure 4.23. Photographs of visualized flow around the NACA 0015 airfoil with plasma actuators off (left) and on (right) at $Re_c = 158K$.

highest angle of attack, where the improvement in L/D was not as pronounced, the flow visualization indicates that the flow was at least partially attached as a result of the actuator.

4.2.2 Unsteady Actuation

Unsteady flow control has been shown in the literature [22, 61, 62, 63, 64] to be effective in separation control because the induced periodic disturbance could accelerate and regulate the generation of large coherent structures useful in preventing separation. This section examines the use of the plasma actuator to produce low frequency unsteady disturbances for leading-edge separation control on the NACA 0015 airfoil.

The forcing frequency for the unsteady disturbances is believed to be optimum when the Strouhal number, defined as

$$St = fc/U_{\infty} \quad (4.1)$$

is approximately 1, In the definition of the Strouhal number, f is the actuator forcing frequency, c is separation length which in the case of the full leading-edge separation is the airfoil chord length, and U_{∞} is the freestream velocity. For the results presented here, c is 12.7 cm (5 in) and U_{∞} is 20 m/s, so the optimum forcing frequency based on $St = 1$ is $f \simeq 160$ Hz.

The method for operating the unsteady actuator was presented in section 2.1.2.2 of Chapter 2. The a.c. (driving) frequency for the actuator was 5 kHz, and the amplitude was 11 kV_{p-p}, which were both the same as the case with the steady actuation presented in the previous section. The duty cycle for the unsteady actuator was only

10%. This meant that only 10 percent of the power was used compared to the steady actuation.

A comparison between the three cases of the actuator off, the steady actuator, and the unsteady actuator of the coefficient of lift versus angle of attack is presented in Figure 4.24. In this the unsteady actuator substantially increased the lift, even compared to the steady actuator cases. In particular it was capable of extending the lift curve for 12 degrees past the natural (no actuation) stall angle, which was the highest angle tested.

A comparison between the three cases of the coefficient of drag versus angle of attack is shown in Figure 4.25. This documents that the unsteady actuator substantially reduced the drag, and was even more effective than the steady actuator cases.

Finally these results are summarized in a plot of L/D versus angle of attack. This is shown in Figure 4.26. This illustrates the ability of the plasma actuator when operating in the unsteady mode to improve the performance of the airfoil compared to the steady operation. This is even more remarkable from a systems standpoint when one considers that the overall power input to the actuator was one-tenth that of steady operation.

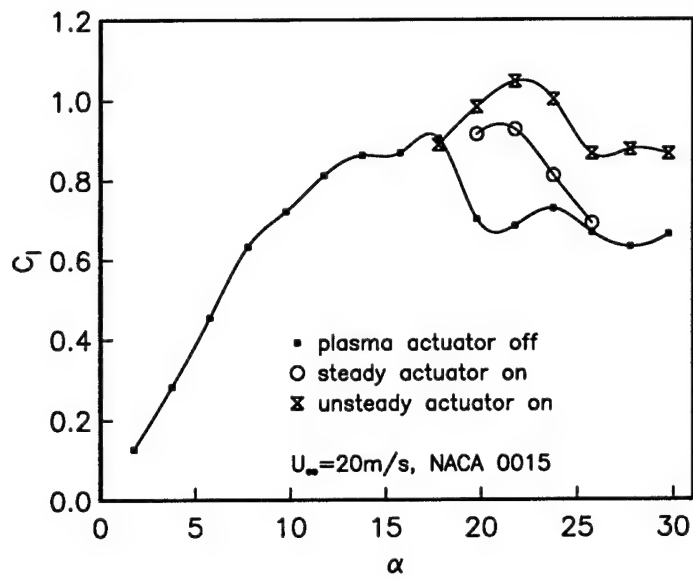


Figure 4.24. Comparison of lift coefficient versus angle of attack for the NACA 0015 airfoil with the actuator off, steady actuator, and 160 Hz unsteady actuator for $Re_c = 158K$.

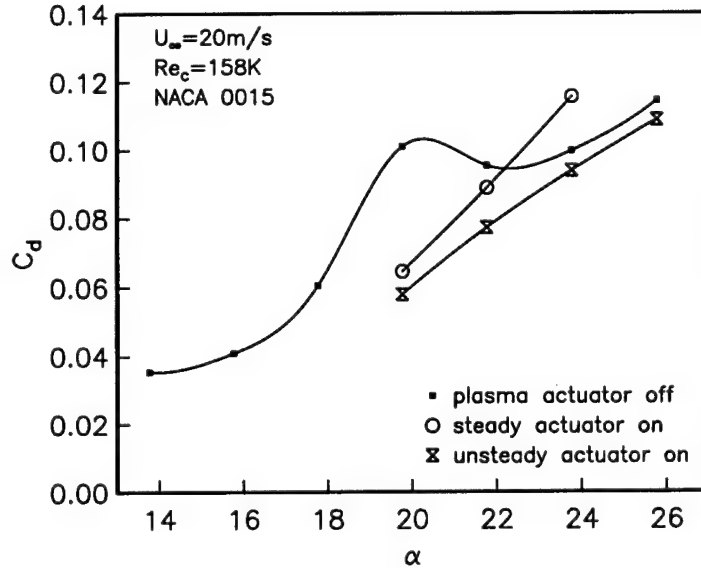


Figure 4.25. Comparison of drag coefficient versus angle of attack for the NACA 0015 airfoil with the actuator off, steady actuator, and 160 Hz unsteady actuator for $Re_c = 158K$.

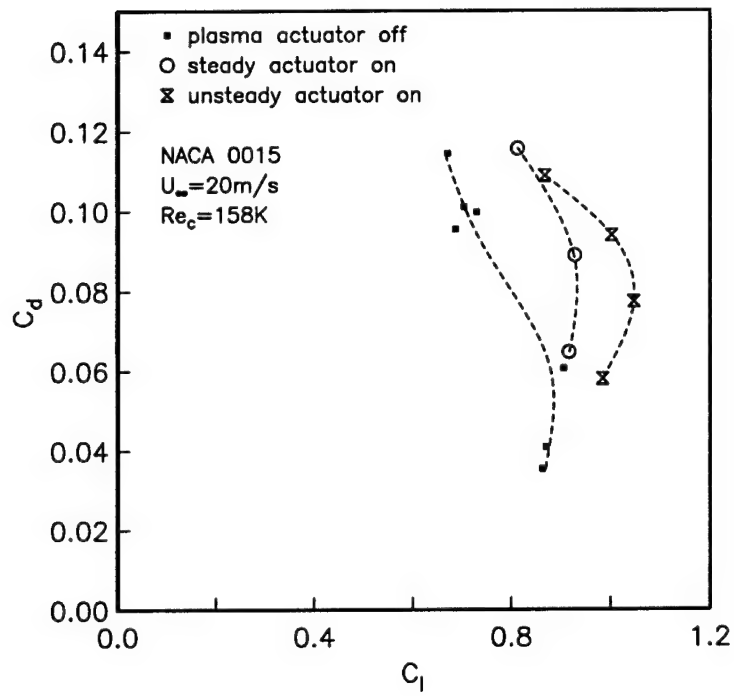


Figure 4.26. Comparison of drag polars for the NACA 0015 airfoil with the actuator off, steady actuator, and 160 Hz unsteady actuator at $Re_c = 158K$.

CHAPTER 5

SEPARATION CONTROL ON OSCILLATING AIRFOIL

This phase of the research relates to the problem of retreating blade stall on helicopter rotors. Dynamic stall has mostly been studied experimentally, using oscillating 2-D airfoils in wind tunnel experiments [34, 35, 40, 47]. This simulates the quasi-periodic first harmonic angle of attack vibrations that are found on helicopter rotors during forward flight. Here, the same NACA 0015 airfoil that was used in the stationary study was oscillated about its quarter-chord in a periodic cycle corresponding to $\alpha(t) = \alpha_{mean} + \alpha_{amp} \sin \omega t$.

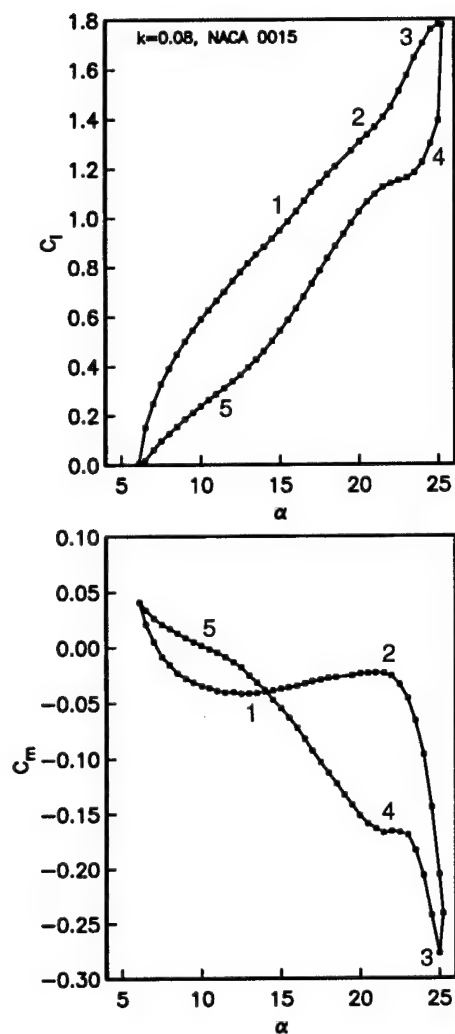
Dynamic stall on an airfoil occurs when the airfoil is pitched above its natural static stall angle. This investigation examined how the process of forming and shedding the leading-edge vortex results in lift-cycle hysteresis. The object of this work was to document the effect of the plasma actuators in controlling the oscillatory lift cycle and cycle hysteresis. For this, the plasma actuator was operated in both steady and unsteady modes, over the full, and selected portions of the oscillatory cycle. The experiment examined a large range of parameters including different α_{mean} , α_{amp} , and reduced frequencies, $k = \omega c / 2U_{\infty}$.

5.1 Baseline Measurements

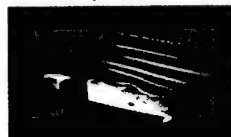
The baseline results were for the conditions of $\alpha(t) = 15^\circ + 10^\circ \sin \omega t$, with ω corresponding to a reduced frequency of $k = \omega c / 2U_\infty = 0.08$. The physical frequency was $f = 4$ Hz. The freestream speed was $U_\infty = 10$ m/s, which gave a chord Reynolds number of 76K. Even at this low Reynolds number, the flow physics was dominated by the dynamic stall mechanism.

The lift and moment coefficient cycles shown in Figure 5.1 are for the case with the actuator off. These were found to have the characteristic shape observed by others [37]. Flow visualization records corresponding to the dynamic stall process stages are also shown in the figure.

Different classical ‘stages’ in the oscillating flow cycle have been denoted in Figure 5.1. Stage 1 corresponds to an almost linear increase in the lift with increasing angle of attack. This extends up to $\alpha \simeq 22^\circ$. Stage 2 is denoted by the nonlinear increase in the lift coefficient that occurs at the higher angles of attack. This results from the formation of the DSV. The onset of dynamic stall is indicated by the rapid drop in the moment coefficient. In stage 3, the dynamic stall vortex provides additional lift on the airfoil as long as it stays over the airfoil’s surface. During stage 4, the flow progresses to a state of full separation, which is accompanied by a sudden loss of lift. The initial part of the pitch-down portion of the cycle shows the result of the remnant of the DSV with the sharp drop in lift past α_{max} , and the “lobe” in the lift cycle that persists to approximately $\alpha = 22^\circ$. Flow reattachment occurs once the angle of attack of the airfoil is low enough. This marks the beginning of stage 5.



STAGE 1: Airfoil exceeds static stall angle, flow reversals take place in boundary layer.



STAGE 2: Flow separation at the leading-edge and formation of a vortex. Moment stall.



STAGE 3: Vortex convects over chord, inducing extra lift.



STAGE 4: After vortex reaches trailing edge, flow progresses to a state of full separation.



STAGE 5: When angle of attack becomes low enough, flow reattaches from front to back.



Figure 5.1. Baseline lift and moment coefficients for the NACA 0015 oscillatory airfoil where $\alpha(t) = 15^\circ + 10^\circ \sin \omega t$ and $k = 0.08$.

5.2 Effects of Different Oscillation Conditions on Dynamic Stall

This section presents a parametric look at the effects of different oscillation conditions. This includes the effect of the mean angle of attack, oscillation amplitude, freestream velocity, and reduced frequency. These were found to influence the different stages of the dynamics stall process in the lift and moment cycles by affecting the flow separation, leading-edge vortex formation and shedding, and flow reattachment.

Varying one parameter, while holding others constant, can help to understand better the physics of dynamic stall. A few examples showing the variation of the dynamic stall process caused by varying the mean angle of attack, the freestream velocity, and the reduced frequency will now be described.

5.2.1 Effect of Mean Angle of Attack

Four different mean angles of attack were investigated to document its effect on the lift and moment cycle of the oscillating airfoil. These corresponded to $\alpha_{mean} = 10^\circ$, 15° , 18° , and 20° . For all of these, the amplitude of the oscillation was 10° and the reduced frequency was $k = 0.08$, which were the same conditions as the baseline conditions.

The effect of the different mean angles of attack on the lift and moment coefficient cycles is presented in Figure 5.2. The top row corresponds to the lowest mean angle of attack of 10° . These conditions are just sufficient to cause minor flow separation from the airfoil. The dynamic stall here is particularly weak compared to the baseline case. This is evident by the lack of the sharp increase (Stage 2-3) and subsequent

sharp decrease (Stage 4) in the lift associated with the dynamic stall vortex. As a result, there is very little hysteresis in the lift cycle. The moment stall occurs late in the cycle, near the peak angle of attack. The moment cycle forms a clockwise loop, which represents negative damping.

The second row of plots in Figure 5.2 corresponds to the baseline mean angle of attack of 15° . This mean angle of attack is high enough to cause a stronger leading-edge vortex shedding typical of light stall. The maximum lift coefficient is significantly higher than in the previous case. However, there is a dramatic loss in lift (Stage 4) directly after the maximum angle of attack, and a noticeable lift-cycle hysteresis. The moment stall is more dramatic and occurs earlier in the cycle compared to the previous case. The moment cycle still forms a clockwise loop, signifying negative damping.

The lower two rows of plots in Figure 5.2 correspond to the two highest mean angles of attack of 18 degrees and 20 degrees. These result in what is categorized as strong dynamic stall. The leading-edge vortex formation and shedding significantly contributes to the high lift, although the peak lift coefficient is not larger than in the previous case. Because of the higher mean angle of attack, a larger part of the oscillation cycle involves partly or fully separated flow. This results in larger lift-cycle hysteresis. The large open shape of the lift cycle indicates that relatively long time scales are required for the flow to reorganize after the strong dynamic stall has occurred. The moment stall for these large mean angle of attack oscillation cases is earlier in the cycle, and the negative pitching moment is much larger.

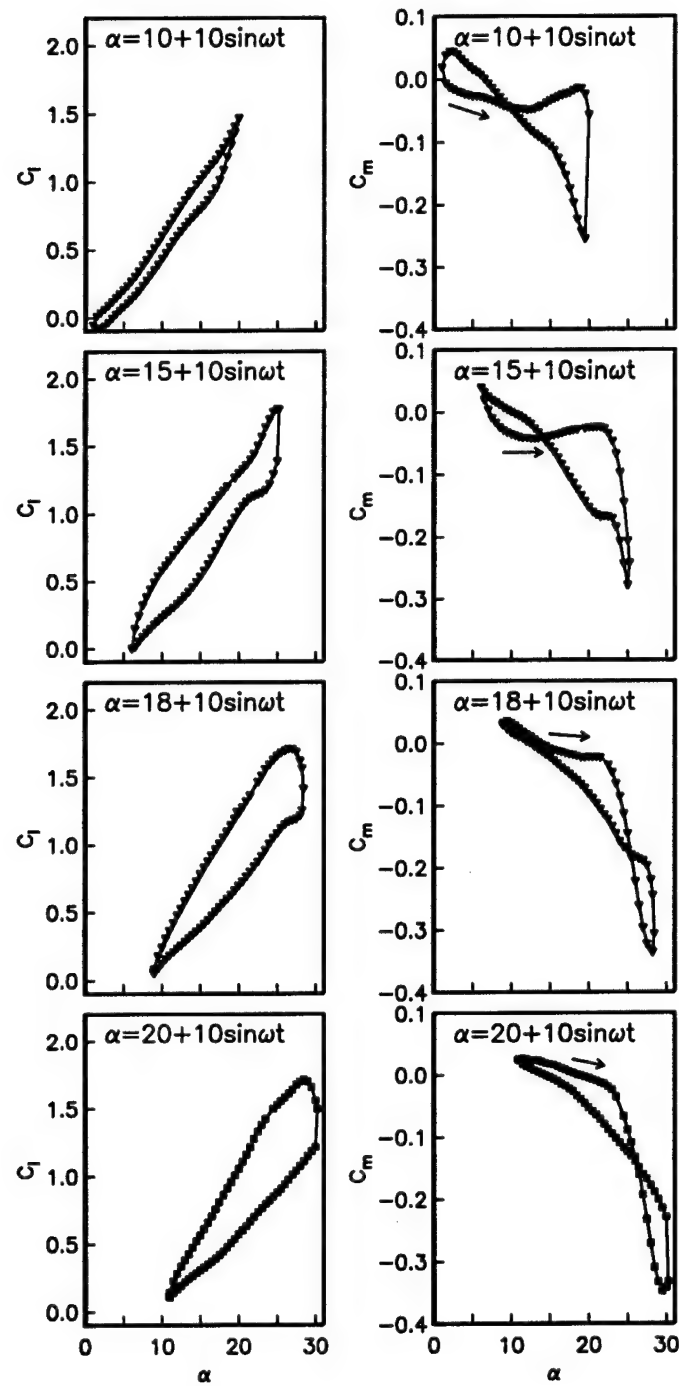


Figure 5.2. Effect of varying the mean angle of attack on the lift coefficient (left) and moment coefficient (right), while the amplitude of oscillation is 10 degrees and $k = 0.08$.

5.2.2 Effect of Freestream Velocity

This section investigates the effect of the freestream speed for the baseline conditions consisting of $\alpha_{mean} = 15^\circ$, $\alpha_{amp} = 10^\circ$, and $k = 0.08$. Two freestream velocities of 5 and 10 m/s were investigated.

The effect of the two freestream velocities on the lift and moment coefficient cycles is shown in Figure 5.3. The two plots in the top row correspond to the lower velocity of 5 m/s, while the two plots in the bottom row correspond to a velocity of 10 m/s. The lower velocity results in a lower peak lift. In addition, there is more hysteresis in the lift cycle, which is evident by the larger area inside the loop of the lift cycle curve.

The lower velocity also results in an earlier moment stall. This indicates that the leading-edge flow disturbances developed and propagated downstream earlier in the dynamic stall process than at the higher freestream speed.

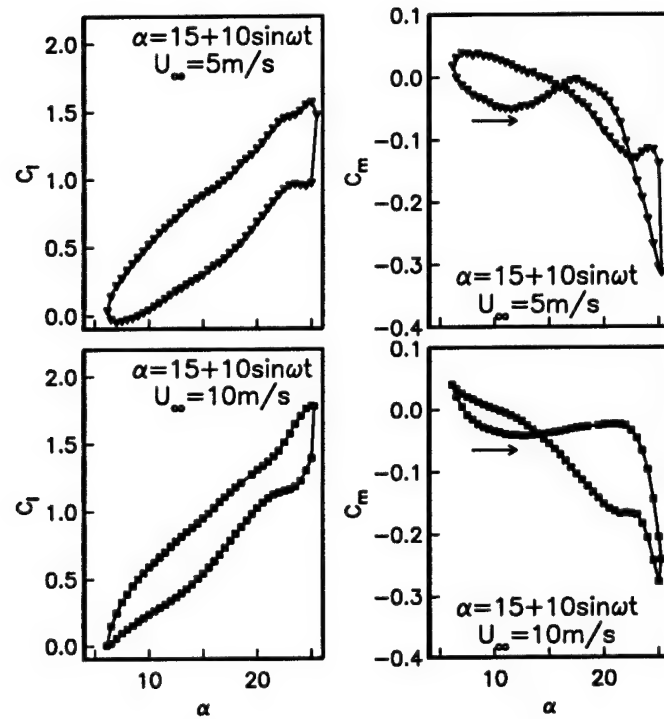


Figure 5.3. Effect of varying the freestream velocity on the lift coefficient (left) and moment coefficient (right) for $\alpha(t) = 15^\circ + 10^\circ \sin \omega t$ and $k = 0.08$.

5.2.3 Effect of Reduced Frequency

This section investigates the effect of the reduced frequency, k , on the lift and moment coefficient cycles. For this, $\alpha_{mean} = 15^\circ$, $\alpha_{amp} = 10^\circ$ were the same as the baseline conditions. The reduced frequency was then varied by changing the physical oscillation frequency for two values of the freestream velocity, $U_\infty = 5 \text{ m/s}$ and $U_\infty = 10 \text{ m/s}$.

Given the limitations on the maximum physical frequency, the lowest reduced frequencies corresponded to the higher freestream speed. The lift and moment coefficient cycles for four reduced frequencies of 0.05, 0.06, 0.07 and 0.08 at 10 m/s are presented in Figure 5.4. As a general trend, as the reduced frequency was increased, the peak lift coefficient increased, and the lift-cycle hysteresis decreased. The moment cycles reveal that the moment stall and vortex shedding, that are evident by the sharp negative-going C_m , occur later in the cycle with increasing reduced frequency.

The lift and moment coefficient cycles for the four reduced frequencies of 0.08, 0.10, 0.12 and 0.14 that were obtained at 5 m/s are presented in Figure 5.5. The trend for these is consistent with the higher velocity cases, with a decrease in the amount of hysteresis occurring with increasing reduced frequency. At the highest reduced frequency of 0.14, the dynamic stall, normally evident by the sharp drop in C_l past the maximum angle of attack, is virtually nonexistent. This represents an almost ideal condition that could be a goal to achieve at the lower reduced frequencies more common to helicopter rotors.

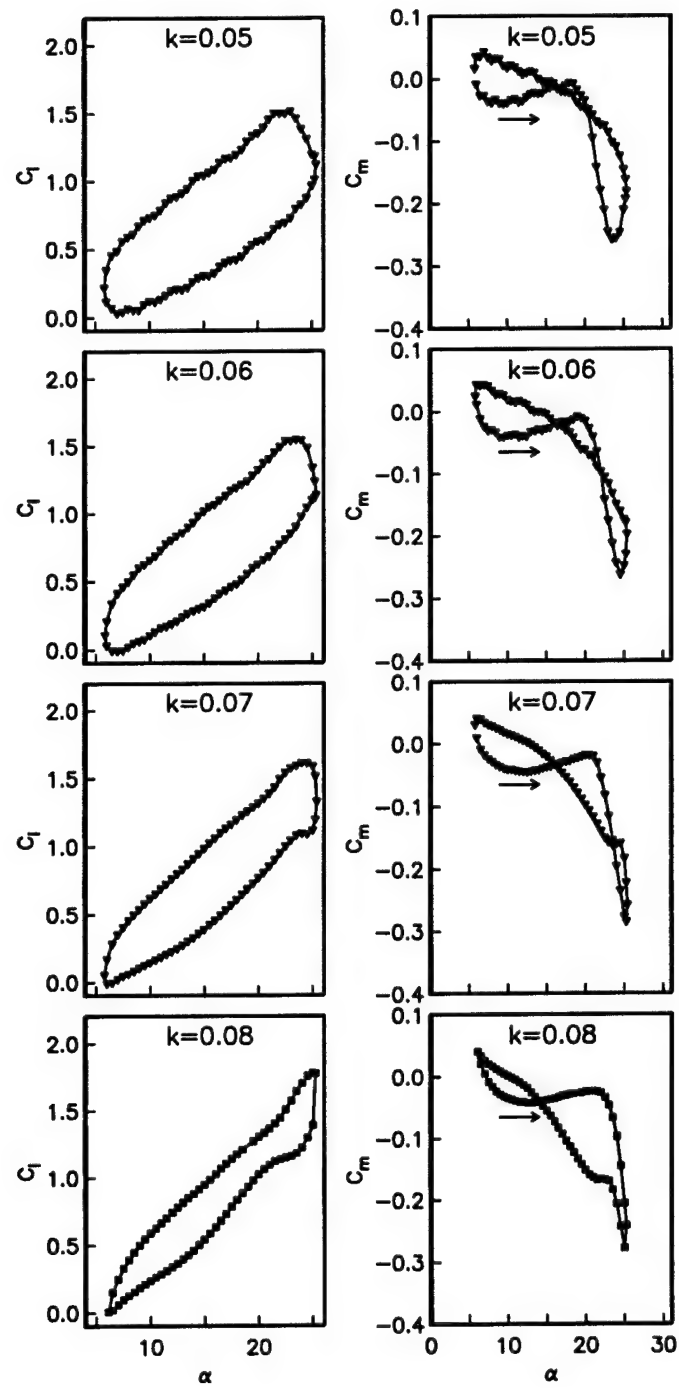


Figure 5.4. Effect of varying the reduced frequency on the lift coefficient (left) and moment coefficient (right) for $\alpha(t) = 15^\circ + 10^\circ \sin \omega t$ and $U_\infty = 10 \text{ m/s}$.

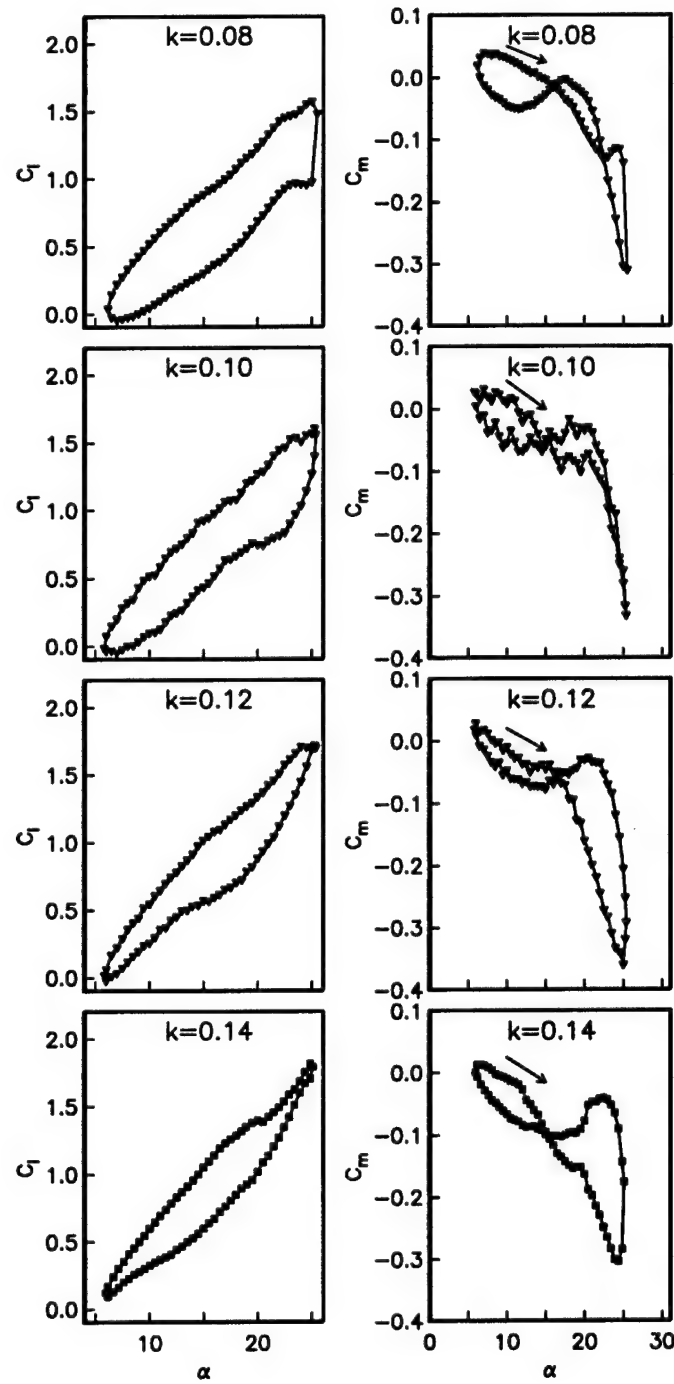


Figure 5.5. Effect of varying the reduced frequency on the lift coefficient (left) and moment coefficient (right) for $\alpha(t) = 15^\circ + 10^\circ \sin \omega t$ and $U_\infty = 5\text{m/s}$.

5.3 Steady Actuation

This section documents the ability of the plasma actuator with steady actuation to improve the lift and reduce the cycle hysteresis of the oscillating airfoil. For this, a single plasma actuator placed at the leading-edge of the airfoil was used.

An example of the effect of the actuator is first presented for the baseline conditions with $\alpha_{mean} = 15^\circ$, $\alpha_{amp} = 10^\circ$, $k = 0.08$, and $U_\infty = 10$ m/s. This is initially shown in terms of the pressure coefficient distributions on the upper (suction) surface of the airfoil during the pitch-up motion (from 7° to 25° in 2° increments) in Figure 5.6. The left plot corresponds to the natural condition with the actuator off. In this case the C_p values peak at $\alpha = 21^\circ$, with a maximum $C_p \simeq -4$. As the pitch cycle continues, the $-C_p$ diminishes, and a broad “bulge” in the C_p distribution appears. This “bulge” is a characteristic of the dynamic stall vortex. Subsequent angles in the pitching cycle show the movement of the bulge toward the trailing edge that marks the downstream convection of the vortex.

The corresponding pressure coefficient distributions with the steady actuator on are shown in the right plot of Figure 5.6. In this case, the $-C_p$ peak is larger, approximately -5.75. In addition, the steady plasma actuator has suppressed the formation of the dynamic stall vortex. This is evident by the lack of the characteristic “bulge” in the C_p distributions at the higher angles of attack.

Flow visualization records that are phased-locked with the oscillatory motion are used to obtain a better understanding of the flow phenomena. The flow visualization results in Figure 5.7 focus on angles of attack on either side of where the $-C_p$ peak

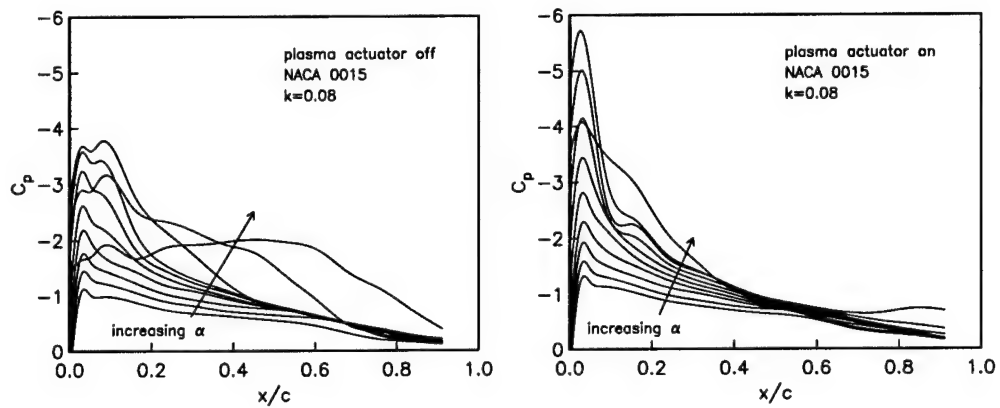


Figure 5.6. Coefficient of pressures with the plasma actuator off (left) and on (right) for the upper surface of the airfoil during the pitch-up part of the cycle for $\alpha = 7^\circ$ to 25° in 2° increments for $\alpha(t) = 15^\circ + 10^\circ \sin \omega t$ and $k = 0.08$.

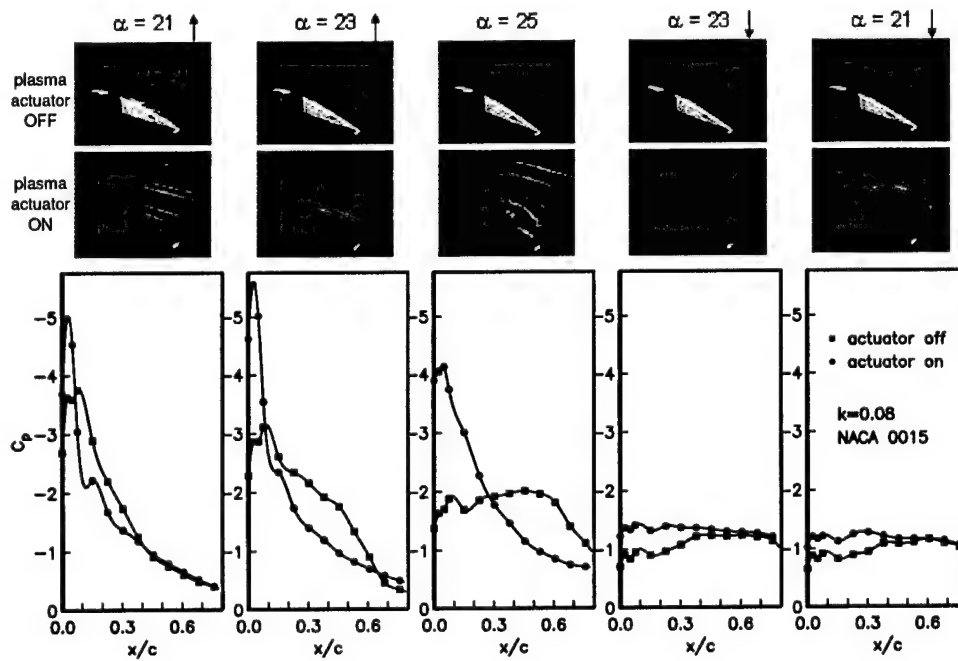


Figure 5.7. Flow visualization and pressure coefficient records for angles of attack near and at the peak of the oscillatory cycle for $\alpha(t) = 15^\circ + 10^\circ \sin \omega t$ and $k = 0.08$.

occurs. These are presented with the corresponding pressure coefficient distributions at the respective angles in the oscillation cycle. The left two visualization records and plots correspond to $\alpha = 21^\circ$ and 23° , as the airfoil pitches up. The middle flow visualization record and plot correspond to the maximum positive angle of attack, $\alpha = 25^\circ$. Finally the right two visualization records and plots correspond to $\alpha = 23^\circ$ and 21° , as the airfoil pitches down.

The top row of photographs in Figure 5.7 shows the visualized flow with the actuator off. The C_p distribution with the actuator off is shown by the curve with the closed-square symbols. The second row of photographs correspond to the flow when the actuator is on, and the corresponding C_p distribution is shown by the curve with the open-circle symbols.

With the actuator off, in the pitch-up portion of the cycle at $\alpha = 21^\circ$, the $-C_p$ peak at the leading edge reaches its maximum level. The accompanying flow visualization reveals small disturbances on the upper surface of the airfoil, possibly originating from the leading edge. As the cycle continues to $\alpha = 23^\circ$, the flow is now visibly separated at the leading edge, and the peak $-C_p$ level has dropped. The dynamic stall vortex is also clearly visible at the mid-chord location of the airfoil. This coincides with the location of the "bulge" in the C_p distribution.

At the maximum angle of attack in the cycle, $\alpha = 25^\circ$, the leading edge C_p value continues to drop. In addition, the location of the pressure "bulge" is observed to move downstream. The flow visualization indicates that the outer edge of the flow is fully separated. However, the more mixed smoke closer to the airfoil surface appears

to show a coherent feature that is at the right location and has the proper size to correspond to the dynamic vortex.

As the cycle continues and the airfoil begins to pitch down, the leading-edge pressure peak drops further, and the pressure "bulge" convects to the downstream edge of the airfoil. The flow visualization reveals that the outer edge of the flow remains fully separated.

The second row of photographs contrast the natural behavior of the flow over the oscillating airfoil to that where the plasma actuator is operating in a steady manner over the full cycle. At $\alpha = 21^\circ$ and $\alpha = 23^\circ$ during the pitch-up, the actuator maintains an attached flow at the leading edge. This results in a larger C_p peak of approximately -5. In addition at $\alpha = 23^\circ$, the C_p distribution does not show the "bulge" that marks the formation of the dynamic vortex.

At the maximum angle of attack, $\alpha = 25^\circ$, the complete lack of the pressure "bulge" is very evident. The flow visualization reveals that a small separation bubble exists with the actuator on, compared to the large separation without the actuator. As a result, the pressure peak is still quite strong at the leading edge, and still even exceeds the maximum C_p value for the case without the actuator on.

The flow eventually separates as the airfoil pitches down, but the flow visualization indicates that it is not separated as much compared to the case with the actuator off. As a result, the C_p distributions are more uniform over the airfoil, with higher (more negative) values within the first one-third chord.

Flow visualization results for the complete $\alpha(t) = 15^\circ + 10^\circ \sin \omega t$ cycle with the plasma actuator off are shown in Figure 5.8. The complete cycle with the plasma actuator on is shown in Figure 5.9.

With the actuator off, the flow visualization shows that the flow disturbances that lead to separation begin at $\alpha = 21^\circ$. With the actuator on, the flow remains completely attached up to the peak angle of attack of $\alpha = 25^\circ$. In addition, past the maximum angle, the recirculation region over the airfoil is smaller. The flow also reattaches at the leading edge earlier in the pitch-down motion with the actuator on, namely at approximately $\alpha = 9^\circ$ versus $\alpha = 5^\circ$ (with the actuator off).

A comparison of the lift and moment coefficient cycle with the actuator off and on are shown in Figure 5.10. With the actuator on, an improvement over most of the cycle is evident. During the pitch-up motion of the cycle, there is a higher lift coefficient at all angles below $\alpha = 20^\circ$. Since the plasma actuator has suppressed the dynamic stall vortex (evident in the flow visualization records in Figure 5.7), the lift associated with the vortex is also suppressed. This is a negative aspect of the control. However, by suppressing the vortex, the dynamic stall that normally occurs past the maximum angle of attack, is also suppressed. This has the benefit of eliminating the large unsteady loading that is associated with the rapid drop-off in lift. The remainder of the pitch-down portion of the cycle with the actuator off and on are fairly comparable in terms of the lift coefficient. However, the moment coefficient does reveal differences in the pitch-down portion that are due to the actuator.

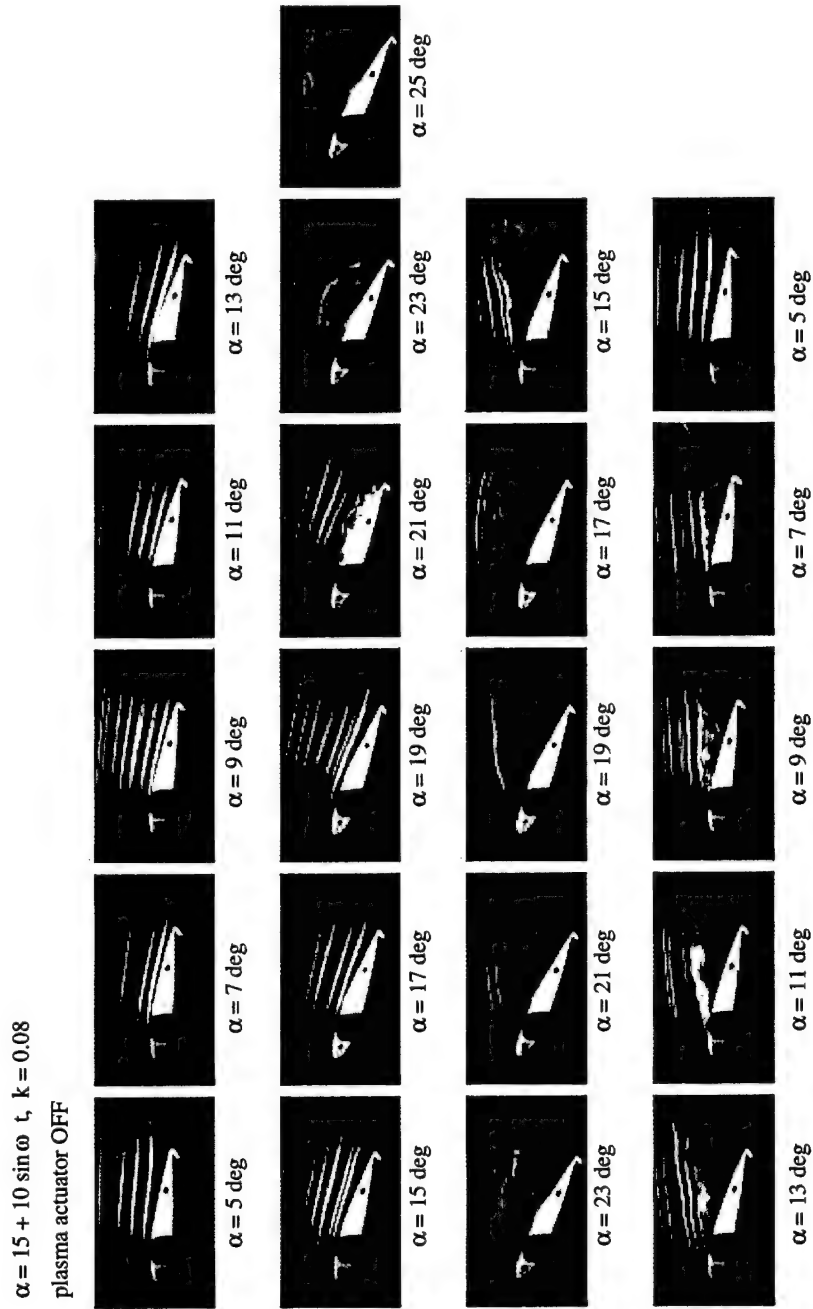


Figure 5.8. Flow visualization records with the plasma actuator off at $\alpha(t) = 15^\circ + 10^\circ \sin \omega t$ and $k = 0.08$.

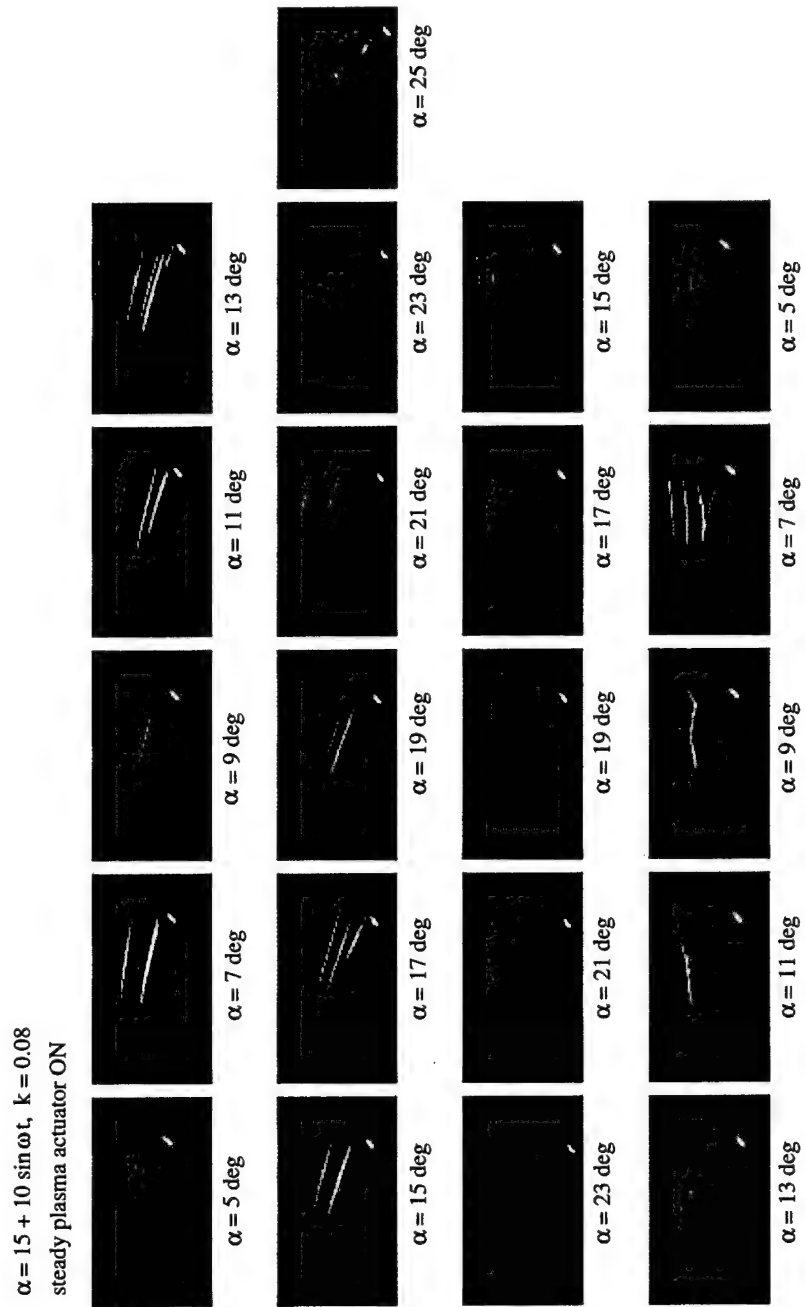


Figure 5.9. Flow visualization records with the steady plasma actuator on at $\alpha(t) = 15^\circ + 10^\circ \sin \omega t$ and $k = 0.08$.

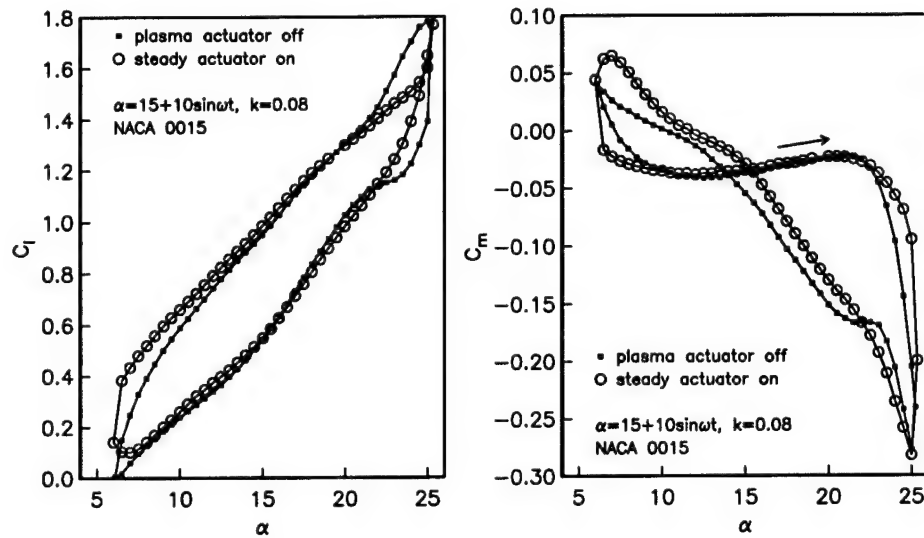


Figure 5.10. Comparison of lift coefficient (left) and moment coefficient (right) versus angle of attack with the plasma actuator off and on for the case of steady actuation at $\alpha(t) = 15^\circ + 10^\circ \sin \omega t$ and $k = 0.08$.

5.3.1 Effect of Different Oscillation Conditions

This section documents the ability of the steady plasma actuator in controlling the lift cycles for the oscillating airfoil with different mean angles of attack and oscillation amplitudes. The cases that were examined consist of:

α_{mean} [deg]	α_{alt} [deg]
10	5
10	10
12	8
15	5
15	10
18	10
20	10

For each case, the reduced frequency was kept fixed at $k = 0.08$. The freestream speed was always 10 m/s. The results compare the effect of having the actuator off and on. As a convention in the plots, the closed-square symbols correspond to when the actuator was off, and the open-circle symbols correspond to when the actuator was on.

Case 1: $\alpha(t) = 10^\circ + 5^\circ \sin \omega t$, $k = 0.08$

The oscillating lift cycles for the case of $\alpha(t) = 10^\circ + 5^\circ \sin \omega t$ and $k = 0.08$ are shown in Figure 5.11. It was the lowest mean angle of attack and the lowest amplitude of oscillation investigated. This case exhibits a light dynamic stall, meaning there is not a substantial drop in lift near the peak angle of attack. There is some lift-cycle hysteresis, which is most evident at the lower angles of attack in the cycle.

With the steady plasma actuator on, there is an increase in the lift over most of the cycle. In addition, the lift-cycle hysteresis is almost completely eliminated.

The flow visualization for this case with the actuator off and on are shown in Figures 5.12 and 5.13. With the actuator off, the oscillation conditions are just sufficient to cause a minor flow separation in the pitch-down just past the maximum angle of attack in the cycle. Compared to other cases with higher mean angles of attack and pitching angles, this is a relatively mild separation.

With the actuator on, the flow visualization results in Figure 5.13 indicate that the flow separation is completely suppressed over the entire cycle. This, of course, led to the elimination of the lift cycle hysteresis.

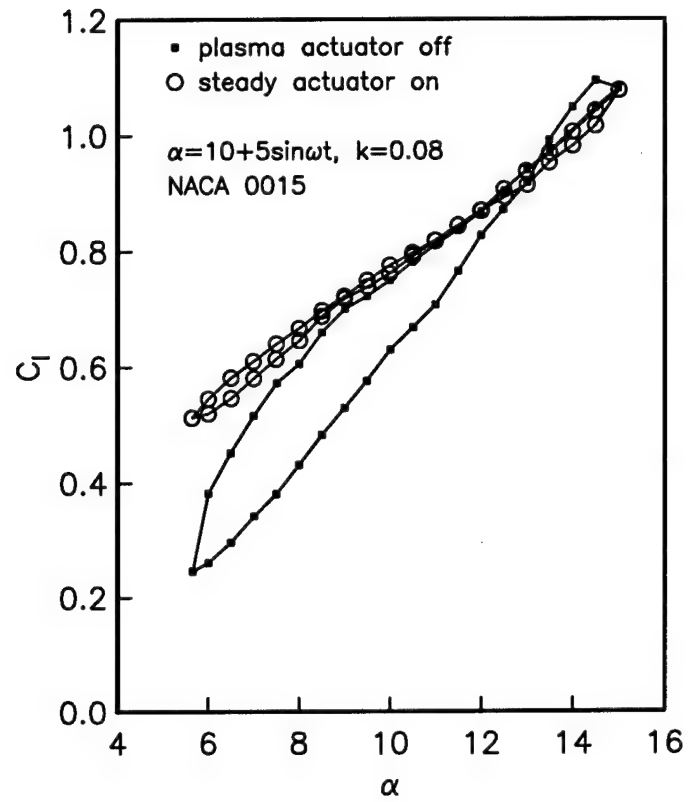


Figure 5.11. Comparison of coefficient of lift versus angle of attack with the plasma actuator off and on for the case of steady actuation at $\alpha(t) = 10^\circ + 5^\circ \sin \omega t$ and $k = 0.08$.

$\alpha = 10 + 5 \sin \omega t$, $k = 0.08$
 plasma actuator OFF

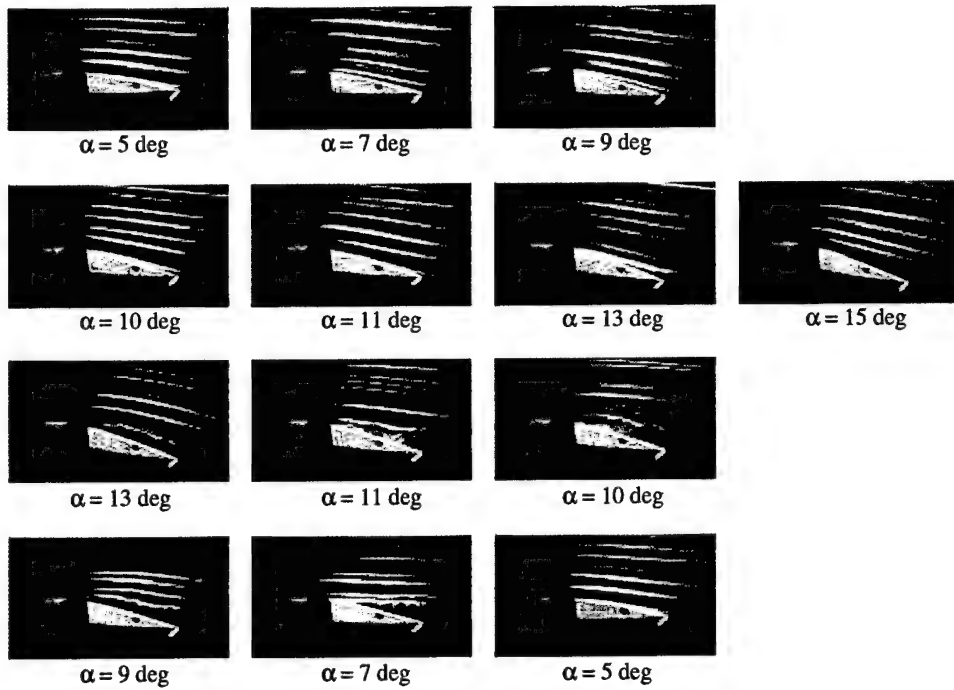


Figure 5.12. Flow visualization records with the plasma actuator off for the case of $\alpha(t) = 10^\circ + 5^\circ \sin \omega t$ and $k = 0.08$.

$\alpha = 10 + 5 \sin \omega t$, $k = 0.08$
 steady plasma actuator ON

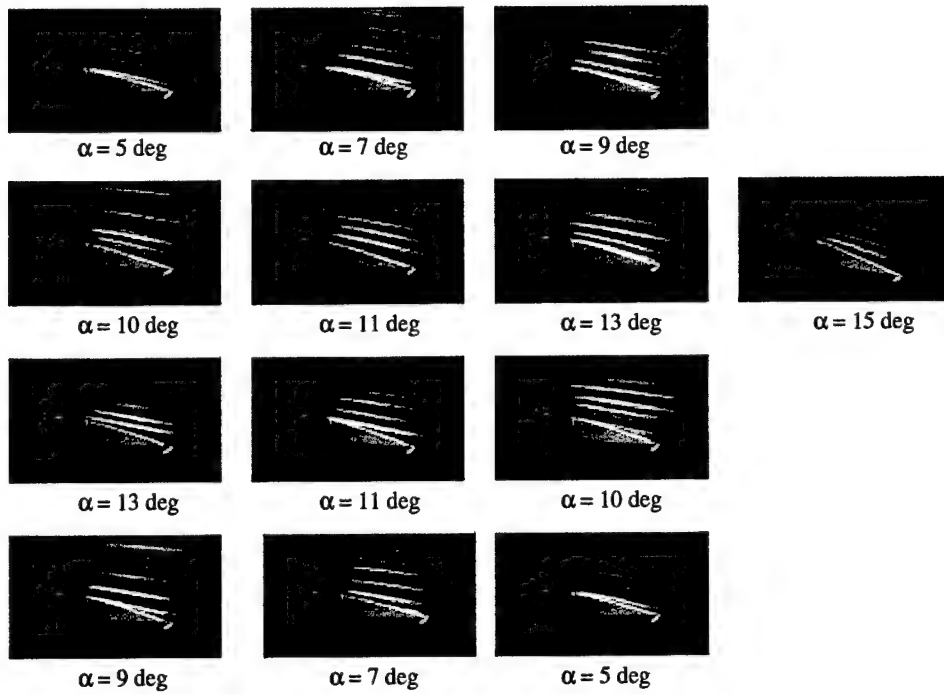


Figure 5.13. Flow visualization records with the plasma actuator on for the case of steady actuation at $\alpha(t) = 10^\circ + 5^\circ \sin \omega t$ and $k = 0.08$.

Case 2: $\alpha(t) = 10^\circ + 10^\circ \sin \omega t$, $k = 0.08$

The oscillatory lift cycles for $\alpha(t) = 10^\circ + 10^\circ \sin \omega t$ for the actuators on and off are presented in Figure 5.14. For this, the conditions are the same as the previous case with the exception of having twice the oscillation amplitude.

With the plasma actuator off, the conditions again lead to a light dynamic stall. The lift-cycle hysteresis is more pronounced compared to the previous case, with a lower lift occurring over the total pitch-down portion of the cycle. In contrast to this, with the plasma actuator on, the lift-cycle hysteresis is substantially eliminated. In addition, the cycle-integrated lift is improved with the actuator.

The flow visualization for this case with the actuator off and on are shown in Figures 5.15 and 5.16. With the actuator off, the flow at the leading edge separates at the maximum angle of attack of 20 degrees. It remains separated throughout the pitch-down portion of the cycle until the airfoil reaches approximately $\alpha = 7^\circ$. This leads to the loss of lift and lift-cycle hysteresis that was documented for this case in Figure 5.14.

With the actuator on, the flow visualization results in Figure 5.16 indicate that the flow separation is completely suppressed up to and just past the maximum angle of attack. Further during the pitch-down portion of the cycle, the flow separation that occurs is substantially smaller. The leading-edge flow appears to reattach much earlier in the pitch-down part of the cycle, at approximately $\alpha = 15^\circ$ compared to $\alpha = 7^\circ$ when the actuator is off. This result substantially reduced the lift-cycle hysteresis.

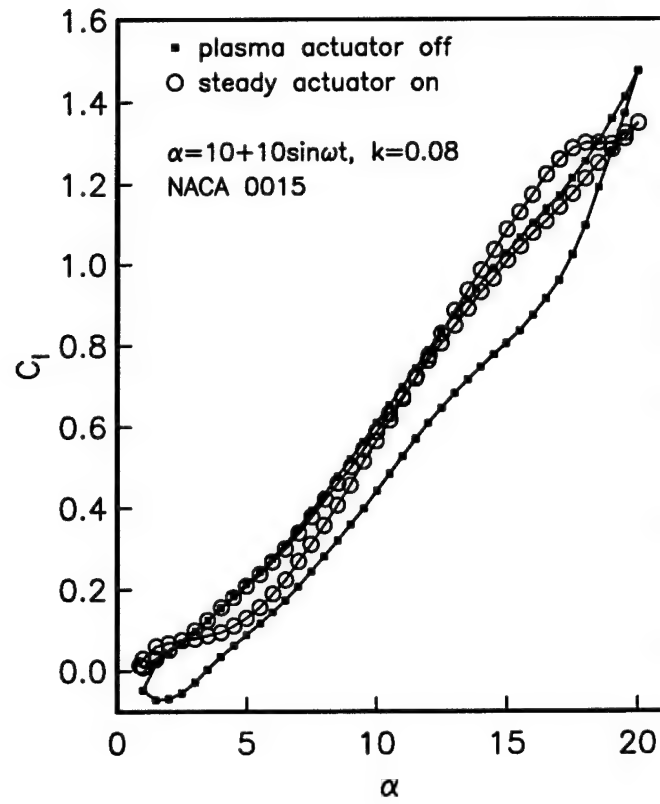


Figure 5.14. Comparison of coefficient of lift versus angle of attack with the plasma actuator off and on for the case of steady actuation at $\alpha(t) = 10^\circ + 10^\circ \sin \omega t$ and $k = 0.08$.

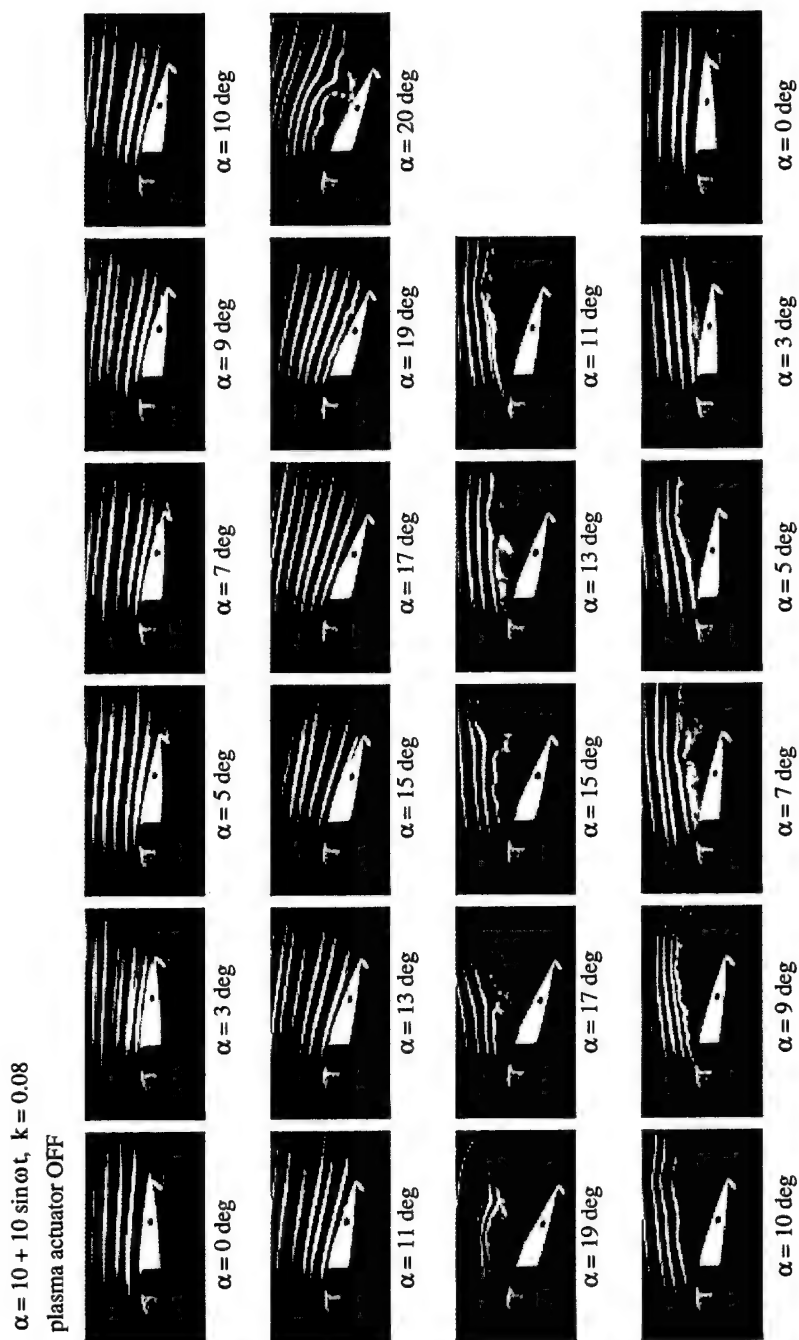


Figure 5.15. Flow visualization records with the plasma actuator off for the case of steady actuation at $\alpha(t) = 10^\circ + 10^\circ \sin \omega t$ and $k = 0.08$.

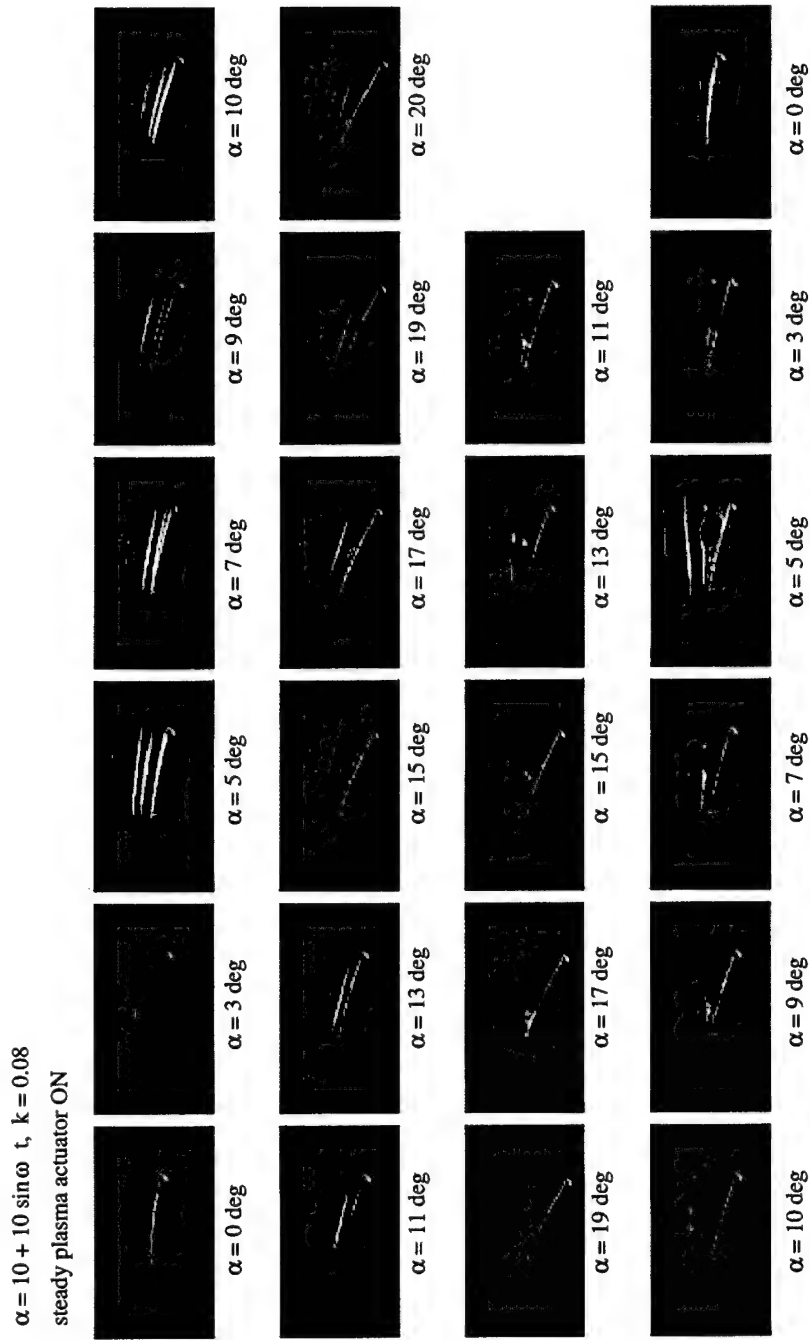


Figure 5.16. Flow visualization records with the plasma actuator on for the case of steady actuation at $\alpha(t) = 10^\circ + 10^\circ \sin \omega t$ and $k = 0.08$.

Case 3: $\alpha(t) = 12^\circ + 8^\circ \sin \omega t$, $k = 0.08$

The oscillation lift cycle for the cases with $\alpha(t) = 12^\circ + 8^\circ \sin \omega t$ are shown in Figure 5.17. For these, the mean angle of attack is larger, and the oscillation amplitude is in between that of the previous two cases. The result of the higher mean angle of attack is an increase in the lift coefficients during the pitch-up 'stage 1,' compared to the other two cases. The peak lift coefficient falls in between the previous two cases, which is expected given that the pitching amplitude is also in between the other cases.

With the plasma actuator on, there is a lift increase over the entire pitch-down portion of the cycle, and at the lower angles of attack. A slight reduction in the peak lift probably results from the suppression of the dynamic stall vortex.

The flow visualization for this case with the actuator off and on are shown in Figures 5.18 and 5.19. With the actuator off, the leading-edge flow separates at the peak angle of attack of 20 degrees. Disturbances on the surface of the airfoil keep the flow from completely reattaching until the minimum angle of attack of 4 degrees.

With the actuator on, the flow visualization results indicate that the flow at the leading edge never separates. Separation occurs past the maximum thickness point in the initial stage of the pitch-down portion of the cycle. It then appears that the flow becomes turbulent until the minimum angle angle is reached. The lack of the flow separation in the pitch-down portion of the cycle accounts for its larger lift with the actuator on.

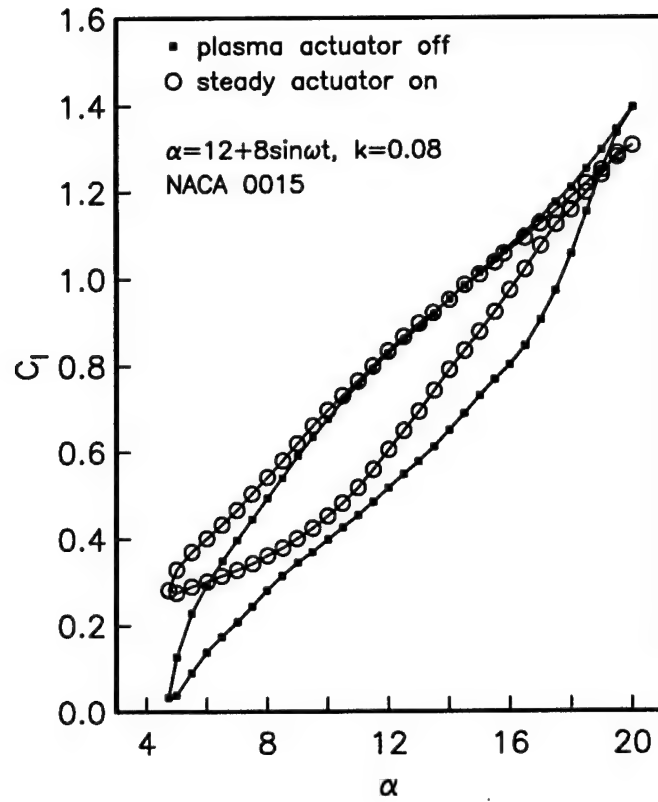


Figure 5.17. Comparison of coefficient of lift versus angle of attack with the plasma actuator off and on for the case of steady actuation at $\alpha(t) = 12^\circ + 8^\circ \sin \omega t$ and $k = 0.08$.

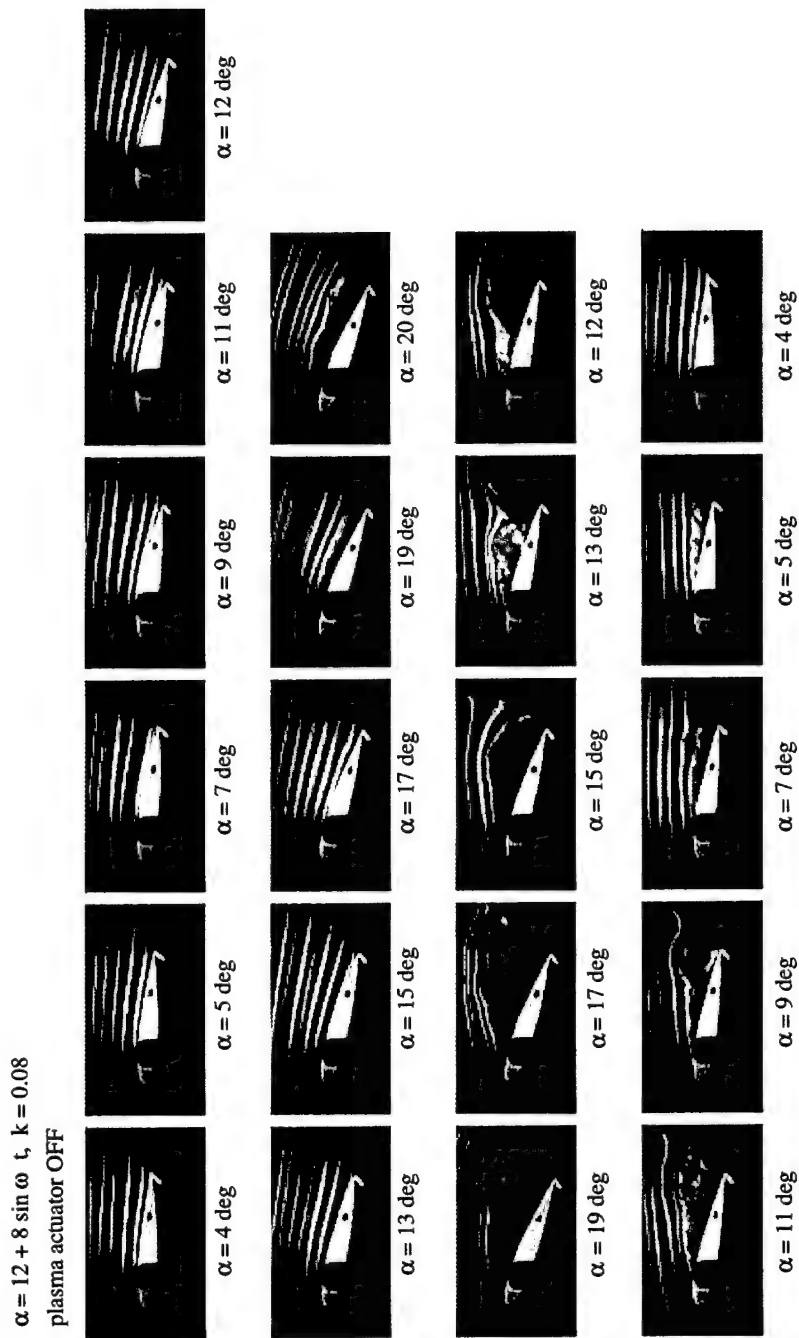


Figure 5.18. Flow visualization records with the plasma actuator off for the case of steady actuation at $\alpha(t) = 12^\circ + 8^\circ \sin \omega t$ and $k = 0.08$.

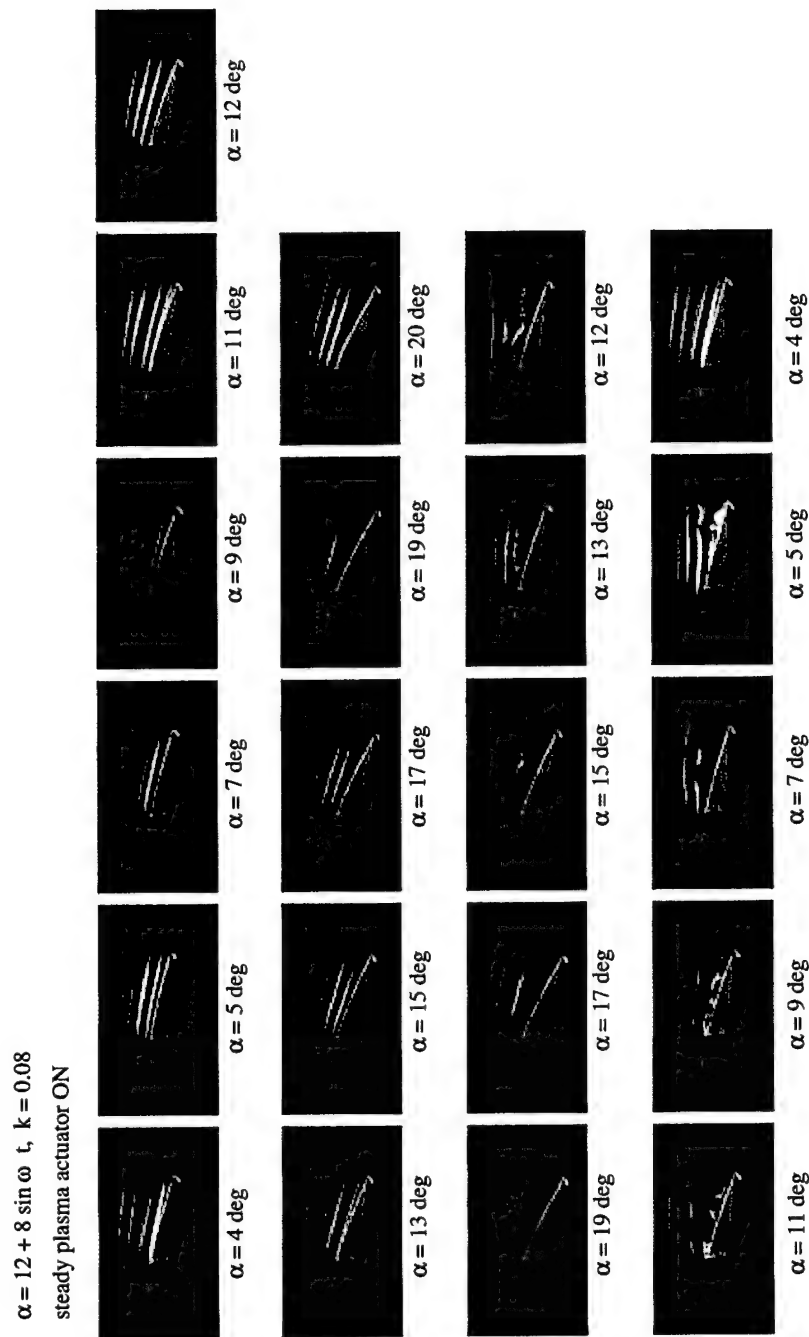


Figure 5.19. Flow visualization records with the plasma actuator on for the case of steady actuation at $\alpha(t) = 12^\circ + 8^\circ \sin \omega t$ and $k = 0.08$.

Case 4: $\alpha(t) = 15^\circ + 5^\circ \sin \omega t$, $k = 0.08$

The oscillatory lift cycle for the case with $\alpha(t) = 15^\circ + 5^\circ \sin \omega t$ is shown in Figure 5.20. The mean angle of attack is the same as the baseline case, but the amplitude is half as large. The peak angle of attack of 20 degrees in this case is the same as that in Cases 2 and 3. However, in this case there is a sharp drop in the lift (dynamic stall) that was not found with the others. The cause for this is the larger mean angle of attack, which for the static airfoil, is beyond the angle at which the airfoil stalls due to separation at the leading edge.

The effect of the actuator on the lift-cycle is extremely dramatic in this case. First, there is a significant increase in the lift over every part of the cycle except the peak angle. Secondly, the dynamic stall is completely suppressed so that there is no hysteresis near the peak angles in the cycle.

The flow visualization for this case with the actuator off and on are shown in Figures 5.21 and 5.22. With the actuator off, the flow is actually separated over most of the cycle. The only angles of attack that it remains attached are from $\alpha = 13^\circ$ to $\alpha = 17^\circ$ in the pitch-up portion of the cycle.

With the actuator on, the portion of the cycle that the leading-edge flow remains attached is greatly increased. In particular the flow at the leading edge is only separated in a small part of the pitch-down portion between $19^\circ \leq \alpha \leq 15^\circ$. The fact that the actuator keeps the flow attached over most of the cycle explains the dramatic shift in the lift coefficient over when the actuator was off.

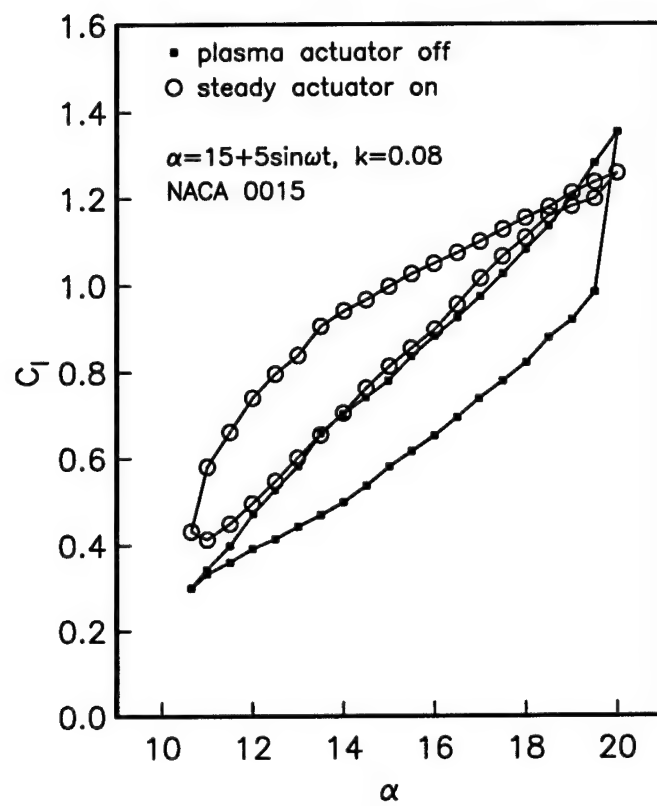


Figure 5.20. Comparison of coefficient of lift versus angle of attack with the plasma actuator off and on for the case of steady actuation at $\alpha(t) = 15^\circ + 5^\circ \sin \omega t$ and $k = 0.08$.

$$\alpha = 15 + 5 \sin \omega t, \quad k = 0.08$$

plasma actuator OFF

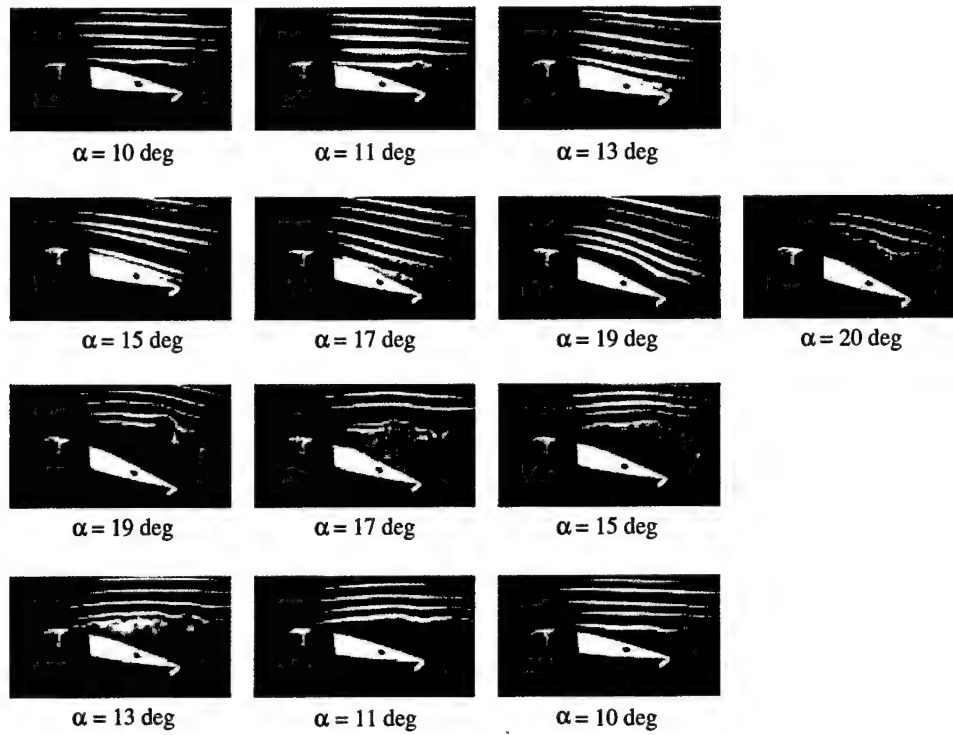


Figure 5.21. Flow visualization records with the plasma actuator off for the case of steady actuation at $\alpha(t) = 15^\circ + 5^\circ \sin \omega t$ and $k = 0.08$.

$\alpha = 15 + 5 \sin \omega t$, $k = 0.08$
steady actuator ON

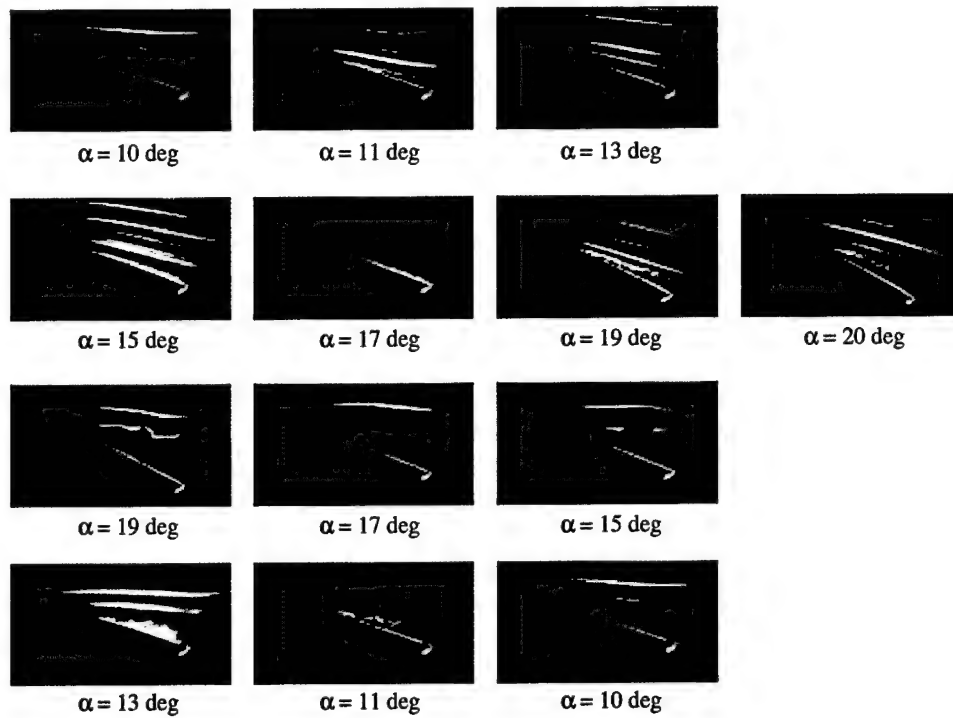


Figure 5.22. Flow visualization records with the plasma actuator on for the case of steady actuation at $\alpha(t) = 15^\circ + 5^\circ \sin \omega t$ and $k = 0.08$.

Case 5: $\alpha(t) = 18^\circ + 10^\circ \sin \omega t$, $k = 0.08$

The oscillatory lift cycles for $\alpha(t) = 18^\circ + 10^\circ \sin \omega t$ are presented in Figure 5.23. In this case, the mean angle of attack and the peak angle are even higher than the previous cases. As a result, with the actuator off, the peak lift is higher than in the previous cases, but there is also a large amount of lift-cycle hysteresis.

With the actuator on, there is a significant improvement in the peak lift, which almost reaches $C_l = 2.0$. However in contrast to the previous cases, there is not a significant reduction in the lift-cycle hysteresis. This would suggest that the dynamic stall vortex was not suppressed in the manner of the baseline case.

The flow visualization for this case with the actuator off and on are shown in Figures 5.24 and 5.25. With the actuator off, a separation bubble first appears at $\alpha = 18^\circ$ and grows to its maximum size at $\alpha = 27^\circ$, which is just prior to reaching the peak angle. At the peak angle, the flow is fully separated, which is the source of the fast drop in lift (dynamic stall). The flow remains fully separated during the entire pitch-down portion of the cycle.

With the actuator on, the leading-edge flow is fully attached during pitch-up through $\alpha = 25^\circ$. The leading-edge vortex forms just before the peak angle is reached, but it is short-lived because the airfoil fully separates at the peak angle. This accounts for the dynamic stall and rapid drop-off in lift that was found for this case, even with the actuator. The flow begins to reattach at the leading edge in the pitch-down at $\alpha = 19^\circ$, which is nearly 10 degrees sooner than with the actuator off. Full reattachment occurs at the minimum angle of attack in the cycle.

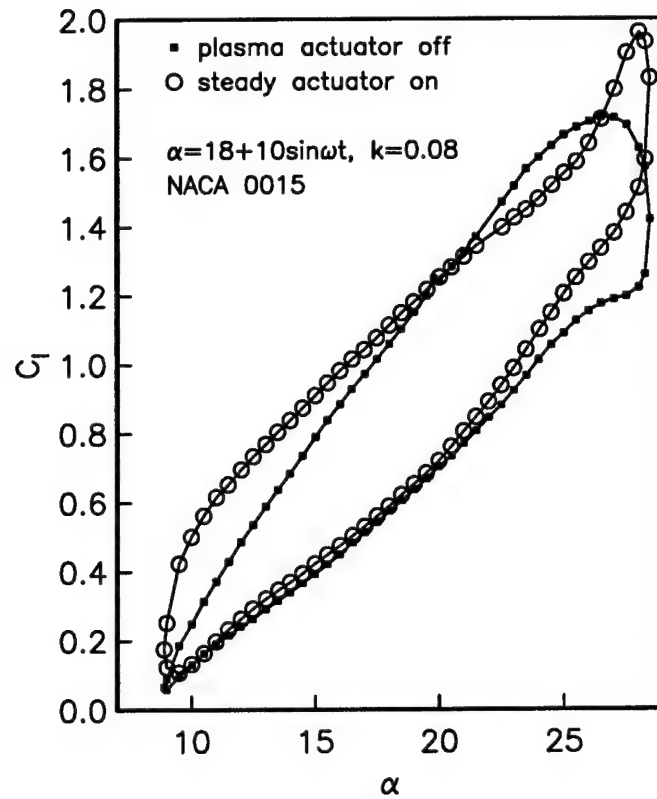


Figure 5.23. Comparison of coefficient of lift versus angle of attack with the plasma actuator off and on for the case of steady actuation at $\alpha(t) = 18^\circ + 10^\circ \sin \omega t$ and $k = 0.08$.

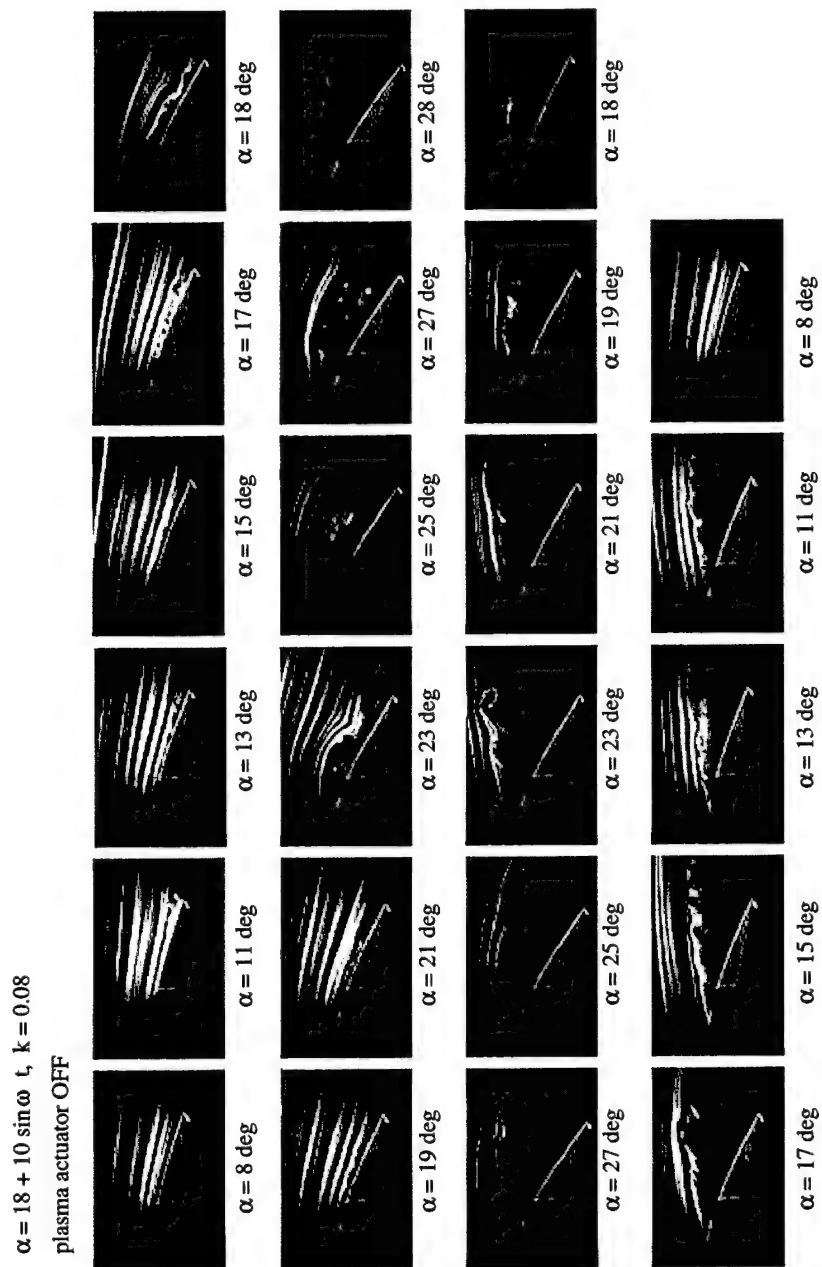


Figure 5.24. Flow visualization records with the plasma actuator off for the case of steady actuation at $\alpha(t) = 18^\circ + 10^\circ \sin \omega t$ and $k = 0.08$.

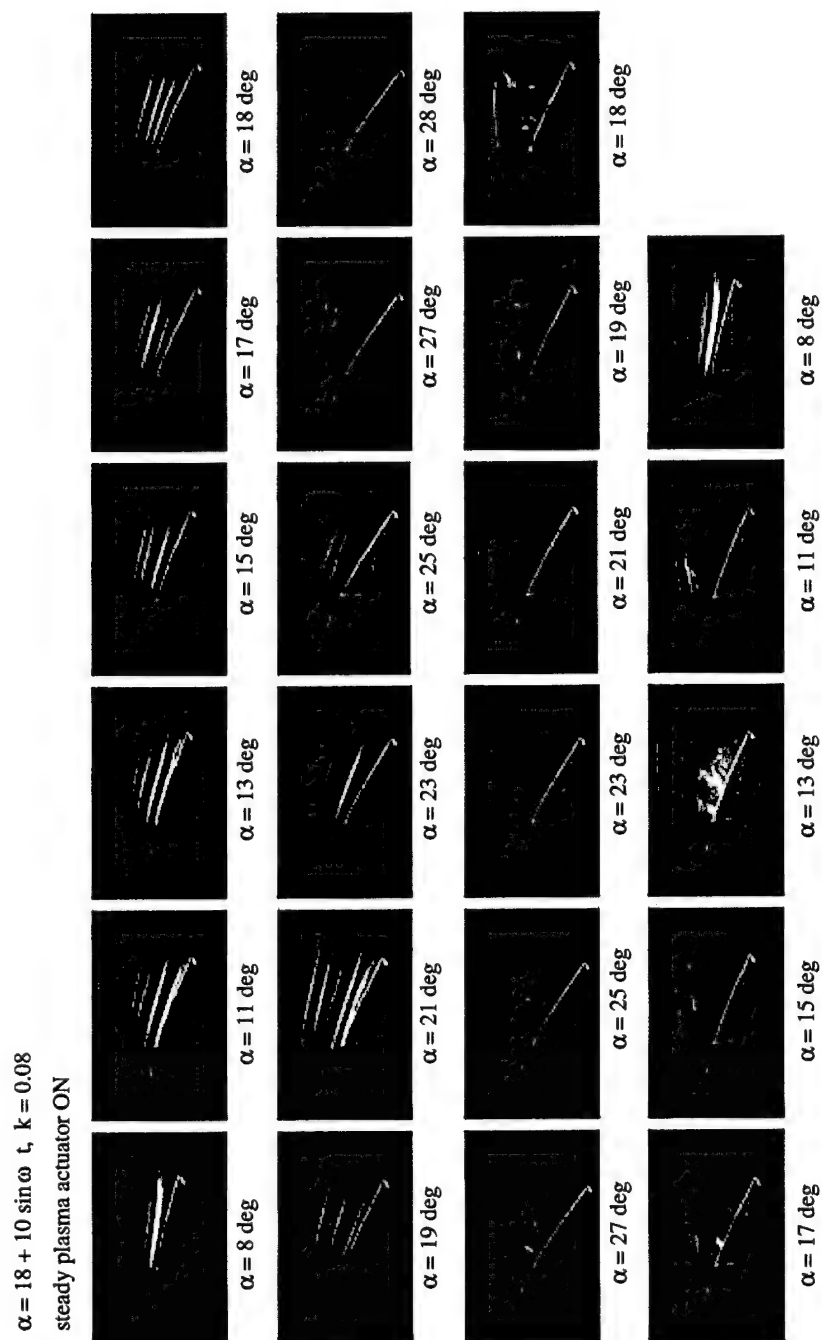


Figure 5.25. Flow visualization records with the plasma actuator on for the case of steady actuation at $\alpha(t) = 18^\circ + 10^\circ \sin \omega t$ and $k = 0.08$.

Case 6: $\alpha(t) = 20^\circ + 10^\circ \sin \omega t$, $k = 0.08$

The oscillation lift cycles for $\alpha(t) = 20^\circ + 10^\circ \sin \omega t$ are shown in Figure 5.26. In this case, the mean angle of attack and the peak angle are the highest of all the cases examined. With the actuator off, the lift cycle is not significantly different from the previous case, although the peak lift is slightly lower. Like the previous case there is a large amount of lift-cycle hysteresis.

With the actuator on, there is a significant improvement in the peak lift, which now exceeds $C_l = 2.0$. However as with the previous case, there is a sharp drop following the peak lift, and only a small reduction in the lift-cycle hysteresis. This would again suggest that the dynamic stall vortex was not suppressed in the manner of the baseline case.

The flow visualization for this case with the actuator off and on are shown in Figures 5.27 and 5.28. With the actuator off, a separation bubble first appears at $\alpha = 20^\circ$ and grows to its maximum size at $\alpha = 25^\circ$, which is now 5 degrees before reaching the peak angle. Above $\alpha = 25^\circ$ on the pitch-up, the flow is fully separated, which is likely the reason for the rounding off of the lift at the top of the cycle. The flow remains fully separated during the entire pitch-down portion of the cycle and does not fully reattach until $\alpha = 13^\circ$ in the pitch-up portion of the cycle.

With the actuator on, the flow is attached at the start of the pitch-up cycle. The formation of the separation bubble occurs later in the cycle, at $\alpha = 25^\circ$ versus $\alpha = 20^\circ$ with the actuator off. The angle at which the flow fully separates is also shifted by 5 degrees which is the reason for the significant increase in the maximum

lift at the peak angle. When the flow does separate, it prompts a rapid drop-off in lift like the previous case with the actuator on. It remains separated until the minimum angle of attack in the cycle is reached. This is approximately 3 degrees before the flow reattaches with the actuator off.

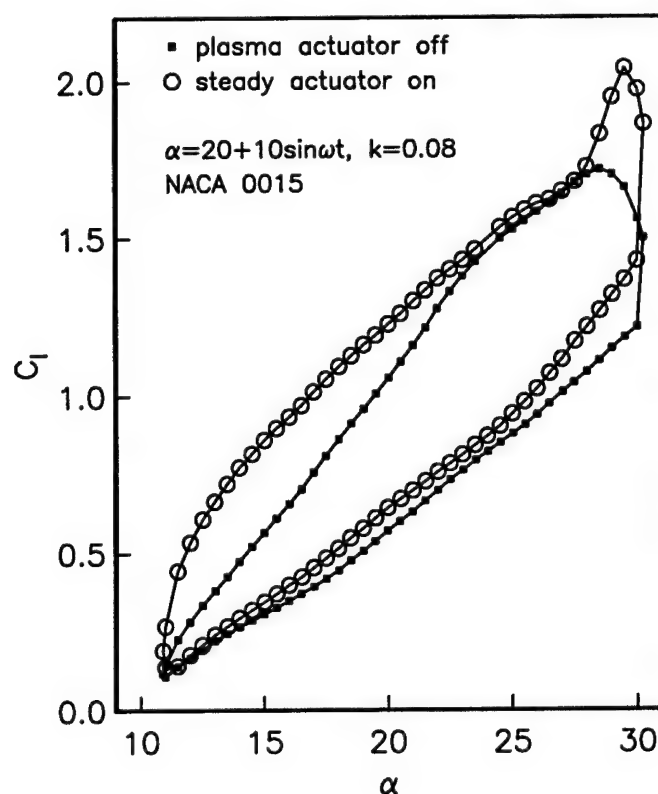


Figure 5.26. Comparison of coefficient of lift versus angle of attack with the plasma actuator off and on for the case of steady actuation at $\alpha(t) = 20^\circ + 10^\circ \sin \omega t$ and $k = 0.08$.

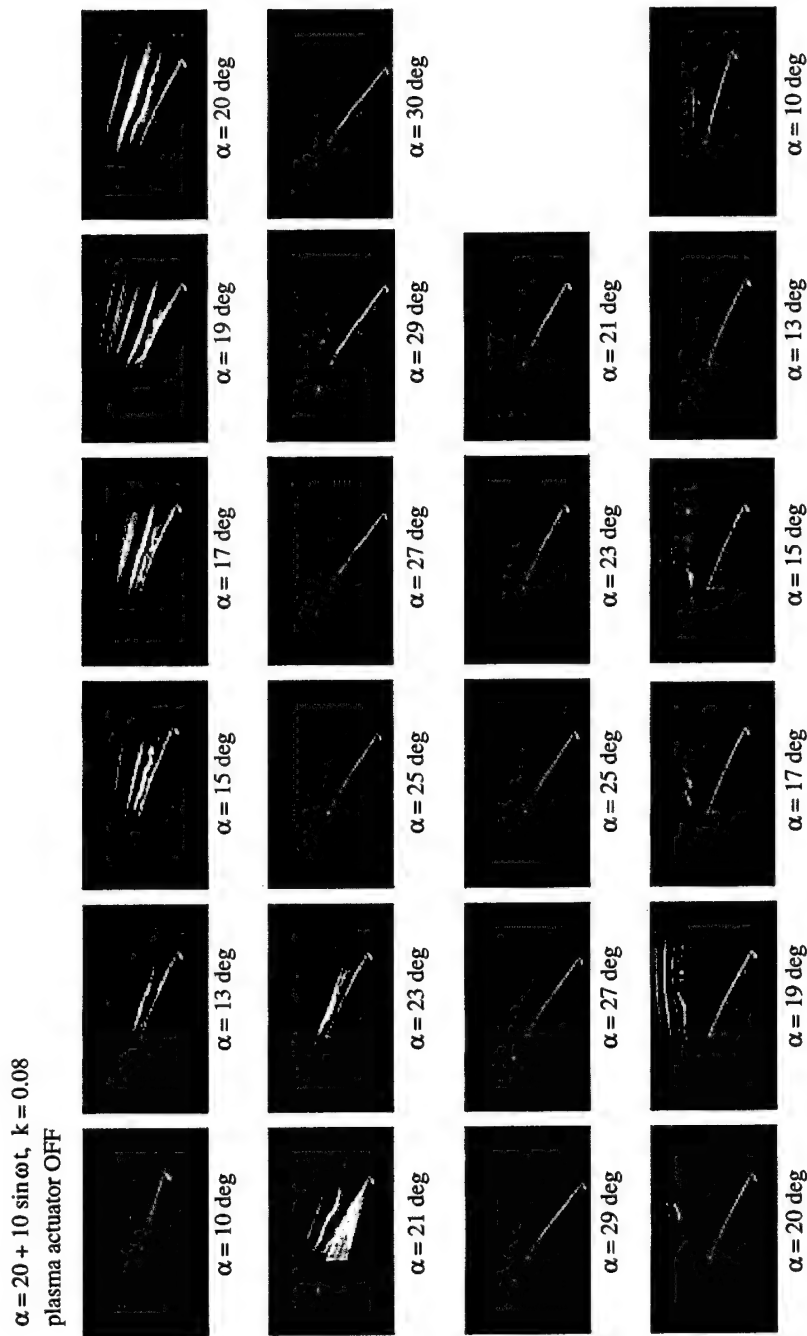


Figure 5.27. Flow visualization records with the plasma actuator off for the case of steady actuation at $\alpha(t) = 20^\circ + 10^\circ \sin \omega t$ and $k = 0.08$.

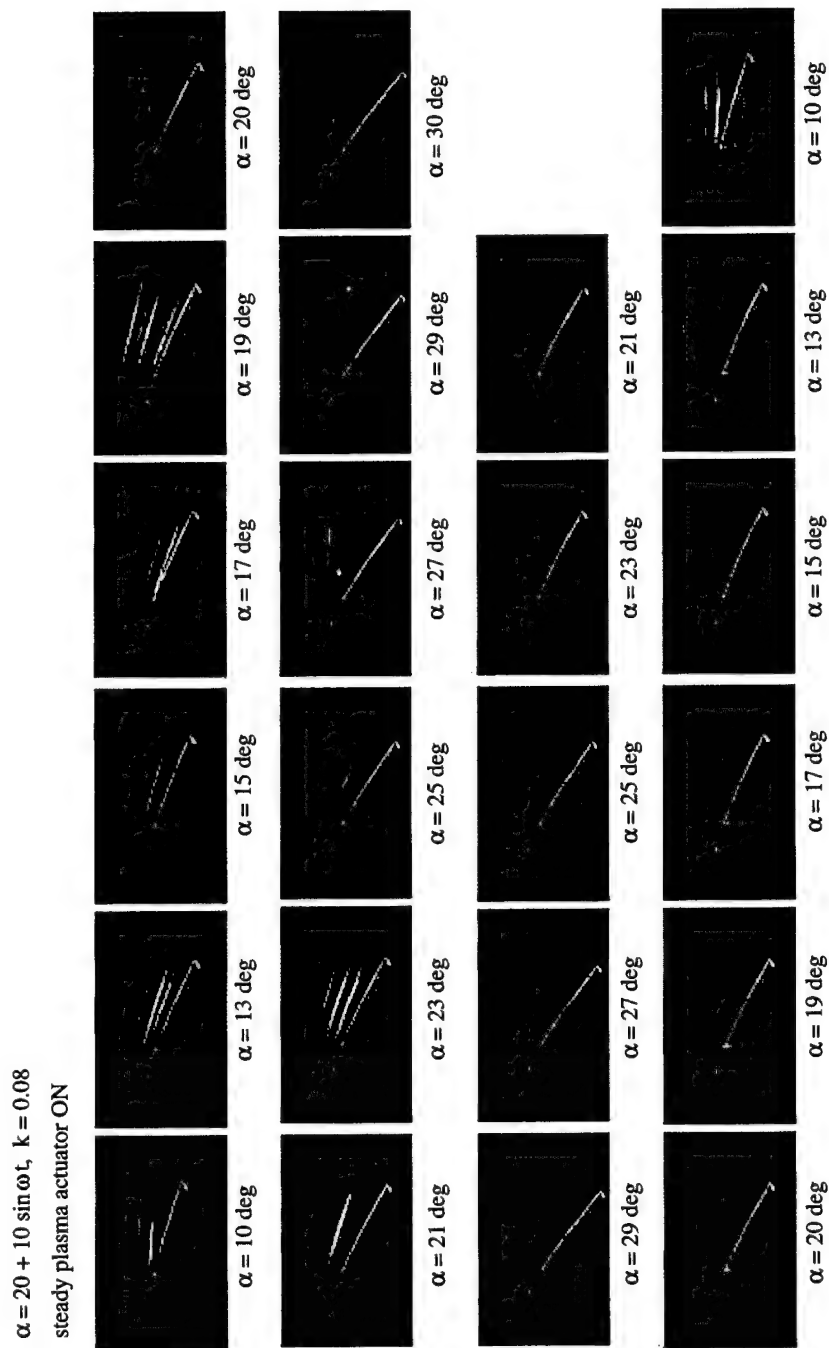


Figure 5.28. Flow visualization records with the plasma actuator on for the case of steady actuation at $\alpha(t) = 20^\circ + 10^\circ \sin \omega t$ and $k = 0.08$.

5.4 Unsteady Plasma Actuation

It has been shown in the literature that the introduction of unsteady disturbances near the separation location can cause the generation of large coherent vortical structures that could reattach the flow. These structures are thought to intermittently bring high momentum fluid to the surface, enabling the flow to withstand the adverse pressure gradient without separating. Periodic excitation by oscillatory blowing for use in flow separation control has been documented extensively by Seifert et al. [61, 62, 63, 64] and in the review by Greenblatt and Wygnanski [22].

The forcing frequency for the unsteady disturbances is believed to be optimum when the Strouhal number, $St = fc/U_\infty$, is near unity. Here f is the actuator forcing frequency, c is separation length which in the case of the full leading-edge separation is the airfoil chord length, and U_∞ is the freestream velocity. For the results presented here, $c = 12.7$ cm (5 in) and $U_\infty = 10$ m/s. Therefore the optimum forcing frequency is expected to be $f = 80$ Hz. For completeness, other frequencies of 40, 20 and 10 Hz, were also investigated. The choice of other frequencies is promoted by the uncertainty in the appropriate convection speed over the oscillating airfoil.

Figure 5.29 presents the lift and moment coefficient cycles produced when operating the actuator at an unsteady forcing frequency of 80 Hz. This involved using the same 5 kHz a.c. frequency to generate the plasma, while periodically switching the actuator on and off at the 80 Hz frequency (see illustration in Figure 2.9). With this, the duty cycle of the 80 Hz cycle was only 10%. This meant that the power supplied to the actuator was only ten percent of that used during steady actuation. Note that

the unsteady actuation used here was not phased with the airfoil oscillatory cycle.

Comparing the lift cycle with the 80 Hz actuation (open-circle symbols in Figure 5.29) to that without actuation (closed-square symbols), and the steady actuation (Figure 5.10), illustrates interesting differences. In particular, the 80 Hz forcing increased the lift at the lower angles of attack in the pitch-down portion of the cycle. However, at the beginning of the pitch-down phase, the lift is somewhat lower compared to either the no actuation or steady actuation cases. In addition, the unsteady actuation at 80 Hz left the undesirable large C_l drop past the maximum angle of attack.

To contrast the results with the 80 Hz actuator frequency, the lift cycle with a four-times lower actuator frequency of 20 Hz was examined. Note that 20 Hz is still five times the physical oscillatory frequency. The result is shown in Figure 5.30. This shows some key differences compared to the 80 Hz and steady actuator cases. In particular, a higher lift over the entire pitch-down portion of the cycle is evident. This is most noticeable in the range from $25^\circ \geq \alpha \geq 13^\circ$. In addition, the airfoil maintains a higher lift at the bottom of the pitch-down phase that persists for the first half of the pitch-up phase. All of these are positive effects toward increasing the lift. There is however a slight reduction in the peak lift at the maximum angle of attack that was not evident in the steady or 80 Hz actuator cases. The negative pitching moment of the 80 Hz actuator is less than the negative pitching moment of the 20 Hz actuator. This is desirable because large cyclic pitching moments put dangerously high stresses and loading on rotors.

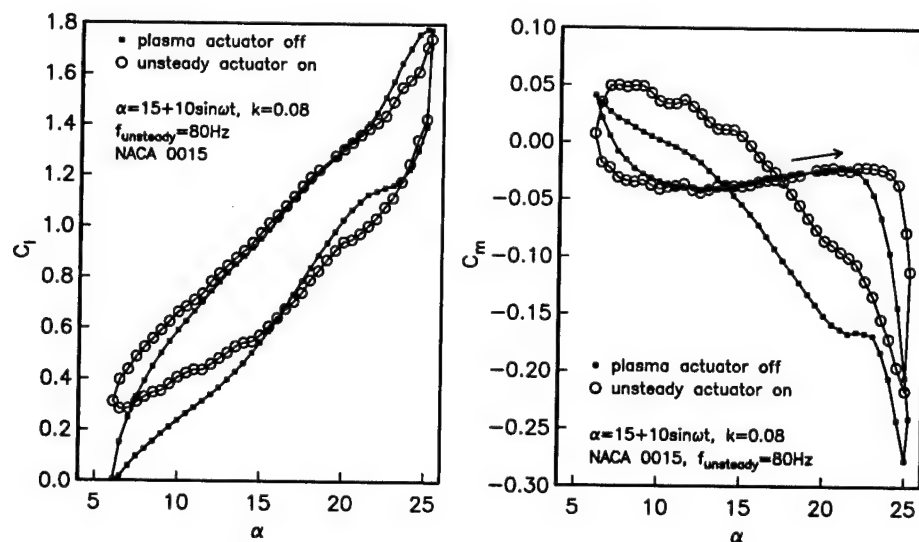


Figure 5.29. Comparison of lift coefficient (left) and moment coefficient (right) versus angle of attack with the plasma actuator off and on for the case of 80 Hz unsteady plasma actuation at $\alpha(t) = 15^\circ + 10^\circ \sin \omega t$ and $k = 0.08$.

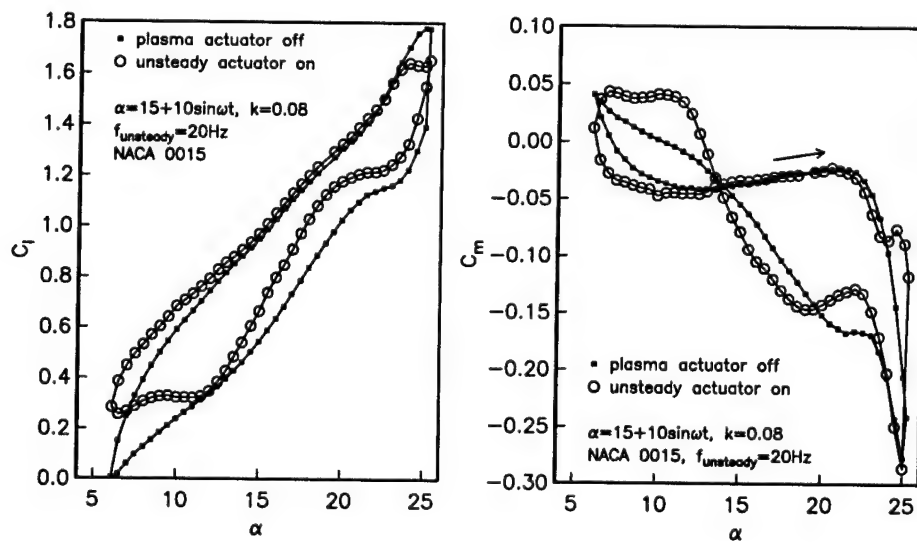


Figure 5.30. Comparison of lift coefficient (left) and moment coefficient (right) versus angle of attack with the plasma actuator off and on for the case of 20 Hz unsteady plasma actuation at $\alpha(t) = 15^\circ \pm 10^\circ \sin \omega t$ and $k = 0.08$.

To obtain a better understanding of the how the unsteady actuator might affect the flow over the pitching airfoil, flow visualization was examined. Figure 5.31 shows three angles in the cycle, $\alpha = 17^\circ$ and $\alpha = 23^\circ$ in the pitch-up phase of the cycle, and at $\alpha = 7^\circ$ in the pitch-down phase of the cycle, with no actuation (in the left column) and the 20 Hz unsteady actuation (in the right column). All of the images for the unsteady actuated case show what appears to be a train of periodic vortex-shaped structures on the upper surface. This regular pattern of vortices produced by the unsteady actuation is well defined, and there appears to be three structures per chord length. At $\alpha = 7^\circ$, the unsteady actuation results in a faster reattachment as indicated visually in Figure 5.31 and by the added lift documented in that portion of the cycle as illustrated in Figure 5.30.

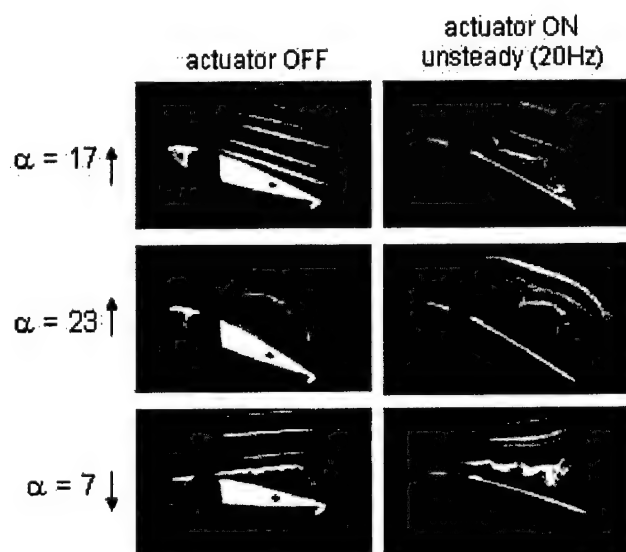


Figure 5.31. Flow visualization records for the unsteady plasma actuator at 20 Hz.

Flow visualization results for the complete $\alpha(t) = 15^\circ + 10^\circ \sin \omega t$ cycle with the 20 Hz unsteady plasma actuation are presented in Figure 5.32. These can be compared to those with no actuation in Figure 5.8 and with steady actuation in Figure 5.9. The flow phenomena over the suction surface of the airfoil with the unsteady actuation is quite different than that with steady actuation, or the actuator off. Regular coherent structures are visible at several different angles of attack. There also appear to be multiple larger structures shed from the leading edge over the oscillation cycle. These are particularly visible in the pitch-up part of the cycle at $\alpha = 23^\circ$, and when the airfoil is pitching down at $\alpha = 13^\circ$. These angles correspond to the location of the “lobes” in the lift and moment coefficients in Figure 5.30.

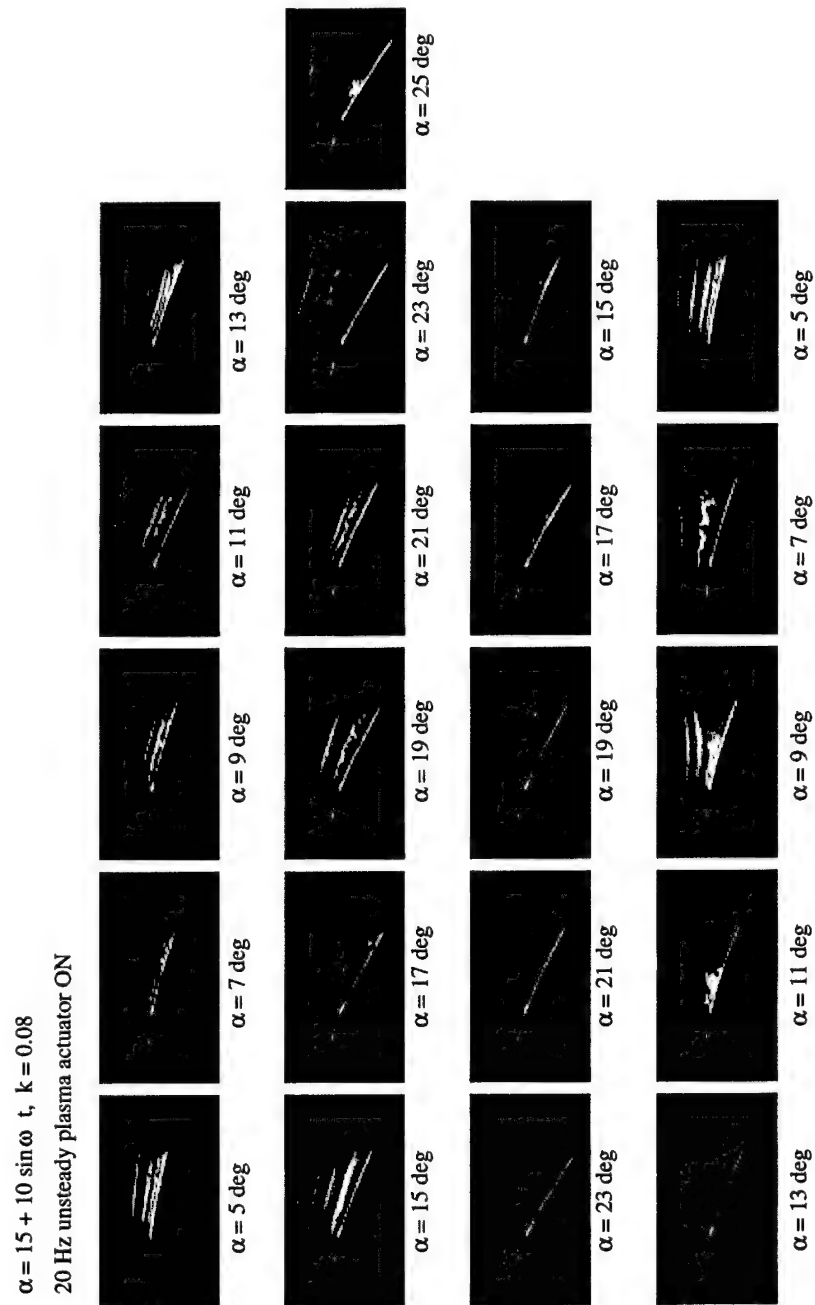


Figure 5.32. Flow visualization records with the unsteady plasma actuator at 20 Hz. for the airfoil with $\alpha(t) = 15^\circ + 10^\circ \sin \omega t$ and $k = 0.08$.

5.5 “Smart” Plasma Actuation

Based on observing the effect that the steady and unsteady plasma actuators had on controlling the lift cycle and correlating this with what was observed in the flow visualization, a “smart” actuator approach was designed that would turn on the actuator only during **portions** of the airfoil oscillatory cycle. These portions were defined as ranges of angles of attack where actuation was expected to produce an improvement in the lift cycle.

To accomplish this, a circuit was built that took the airfoil angle of attack information from the motor encoder as input, and selectively turned the actuator on or off in predetermined parts of the oscillatory cycle. During the “on” time, the actuator was operating in either the steady or unsteady mode. The results that follow only correspond to the steady actuator mode.

The “smart” actuation was applied to the baseline conditions, with $\alpha_{mean} = 15^\circ$, $\alpha_{amp} = 10^\circ$, $k = 0.08$ and $U_\infty = 10$ m/s. The actuator was operated with an a.c. frequency of 5 kHz and an amplitude of 11 kV_{p-p}.

The range of angles in the periodic cycle when the actuator was set to be on were:

1. $15^\circ \geq \alpha \geq 20^\circ$ during the pitch-up phase,
2. $24^\circ \geq \alpha \geq 23^\circ$ during the pitch-up phase, through the peak angle of attack,
3. $20^\circ \leq \alpha \leq 8^\circ$ during the pitch-down phase.

The rationale for operating the actuator between $15^\circ \geq \alpha \geq 20^\circ$ was to keep the flow attached during the high angles of attack of the pitch-up portion of the cycle. It was subsequently turned off from $21^\circ \geq \alpha \geq 23^\circ$ during pitch-up in order to allow the dynamic vortex to form. Previous cases showed that if the actuator suppressed the formation of the vortex, the maximum lift at the peak angle of attack would be less.

The actuator is turned back on just before the peak angle is reached, between $\alpha = 24^\circ$ in the pitch-up and $\alpha = 23^\circ$ in the pitch down. This rationale for this was to reduce the dynamic stall and thereby eliminate the sharp drop in lift that normally occurs as the cycle passes the maximum angle of attack.

In the pitch-down portion, the actuator is turned off at $\alpha = 22^\circ$, but turned on again at $\alpha = 20^\circ$, where it remains on until the angle of attack is near the minimum. The reason for this is to reattach the flow as soon as possible in the pitch-down which has the effect of reducing the lift-cycle hysteresis.

The effect of the "smart" actuation on the lift and moment coefficient cycle is shown in Figure 5.33. Also shown is the case with the actuator off. The "smart" actuation can also be compared to the lift cycle for the steady actuation that was shown in Figure 5.10.

With the “smart” actuation, there was an increase in the lift over the complete cycle. In particular there was a significant improvement in the lift during the pitch-down portion of the cycle, especially at the lower angles of attack. In addition, compared to the other steady actuator cases, the maximum lift was not lost at the higher angles of attack during the pitch-up. Also past the maximum angle of attack in the pitch-down portion of the cycle, the sharp stall that gave the lift cycle the “lobed” shape, has been replaced with a more desirable smooth lift decrease with less hysteresis.

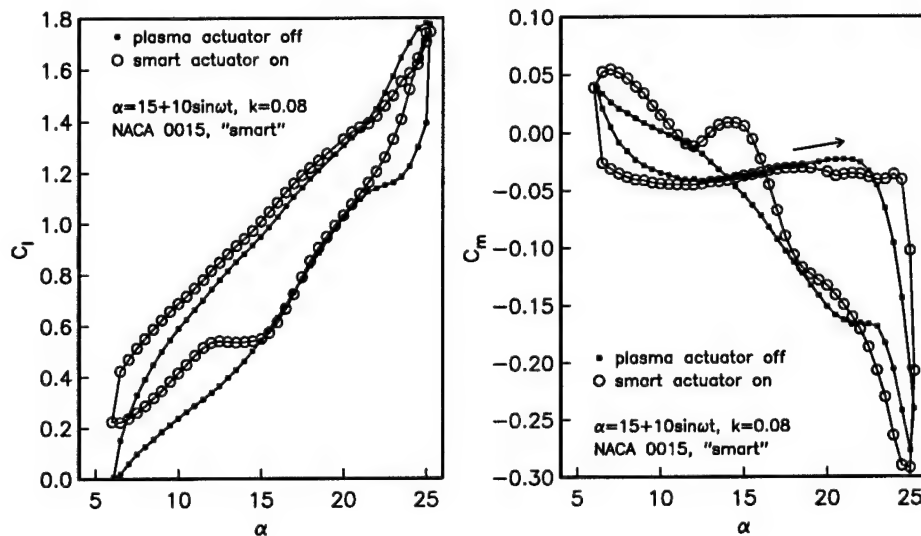


Figure 5.33. Comparison of lift coefficient (left) and moment coefficient (right) versus angle of attack with the plasma actuator off and on for the case of “smart” plasma actuation at $\alpha = 15^\circ + 10^\circ \sin \omega t$ and $k = 0.08$.

The flow visualization results for the complete $\alpha(t) = 15^\circ + 10^\circ \sin \omega t$ cycle with the “smart” plasma actuator on are presented in Figure 5.34. These can be compared with the flow visualization records with no actuation in Figure 5.8, with the steady actuation in Figure 5.9, and with the 20 Hz unsteady actuation in Figure 5.32. In general the visualized flow is consistent with the lift cycle results and the strategy of the “smart” operation. In particular, the flow remains attached up to $\alpha = 20^\circ$, where the actuator is then turned off. With the actuator off, the dynamic vortex is allowed to form, which is evident between $23^\circ \leq \alpha \leq 25^\circ$ in the pitch-up part of the cycle. Then with the actuator turned on again at $\alpha = 20^\circ$ in the pitch-down part of the cycle, the flow reattaches at the leading edge, and remains so throughout the rest of the cycle.

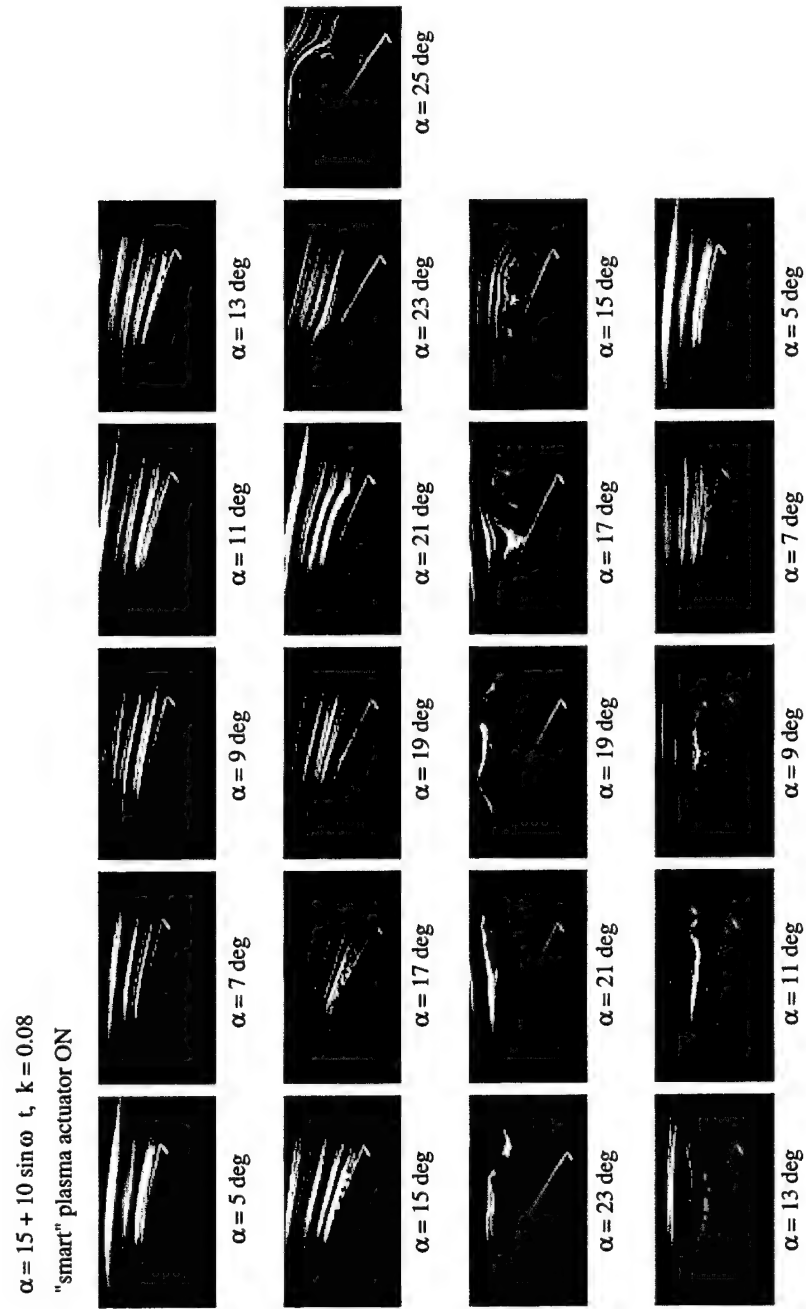


Figure 5.34. Flow visualization records with the "smart" plasma actuator on at $\alpha(t) = 15^\circ + 10^\circ \sin \omega t$ and $k = 0.08$.

5.6 Comparison Between Plasma Actuation Approaches

The flow visualization records in Figure 5.35 have been compiled to illustrate some of the differences in the flow field produced by the different plasma actuator operation. It represents three angles of attack in the cycle during pitch-down at $\alpha = 15^\circ$, $\alpha = 11^\circ$, and $\alpha = 7^\circ$ for four actuator conditions consisting of no actuation, steady actuation, unsteady actuation at 20 Hz, and “smart” actuation. These angles in the pitch-down portion of the cycle were chosen to be highlighted because they displayed some of the most dramatic differences between the cases.

The flow visualization shows that all four approaches are able to reattach the flow at the leading edge by $\alpha = 7^\circ$. However, the “smart” control is the best, with a visible reattachment occurring at $\alpha = 15^\circ$, which is the earliest of the four. As has been pointed out, achieving reattachment as soon as possible in the pitch-down portion of the cycle is extremely important in reducing the lift hysteresis. The “smart” control achieves this the best.

The lift and moment coefficient cycles for the four cases of no actuation, unsteady actuation at two frequencies, and “smart” actuation are directly compared in Figure 5.36. These demonstrate that “smart” actuation maintained the peak lift coefficient of the no actuation case and eliminated the dynamic stall that caused the rapid drop in the lift past the maximum angle of attack. Because the “smart” actuation was able to reattach the flow the earliest in the pitch-down portion of the cycle, it produced a significantly higher lift in the bottom part of the cycle from $5^\circ \leq \alpha \leq 15^\circ$.

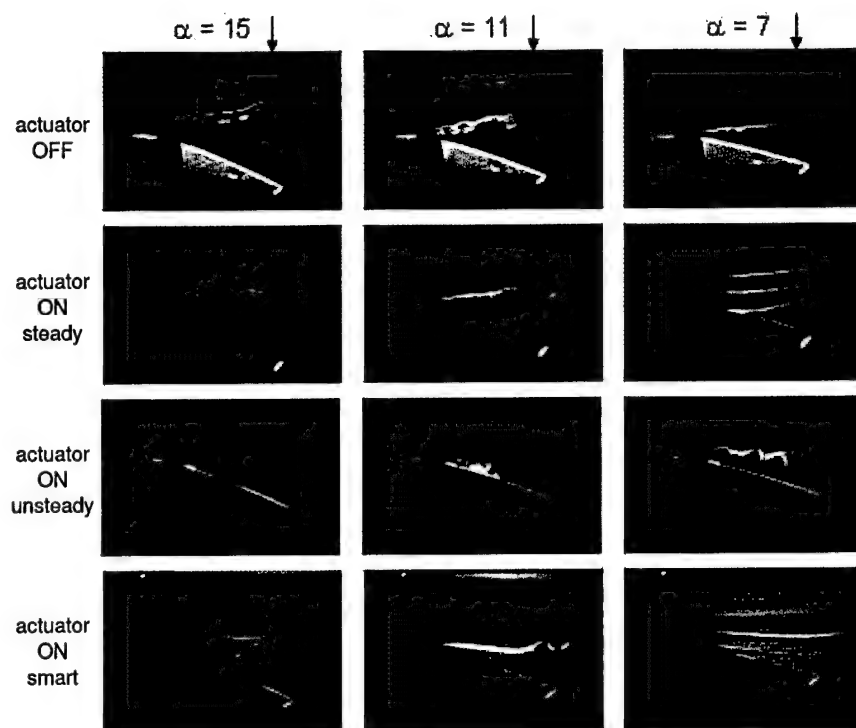


Figure 5.35. Flow visualization records at $\alpha = 15^\circ$, $\alpha = 11^\circ$, and $\alpha = 7^\circ$ while the airfoil is pitching down for no actuation, steady plasma actuation, unsteady plasma actuation, and "smart" actuation.

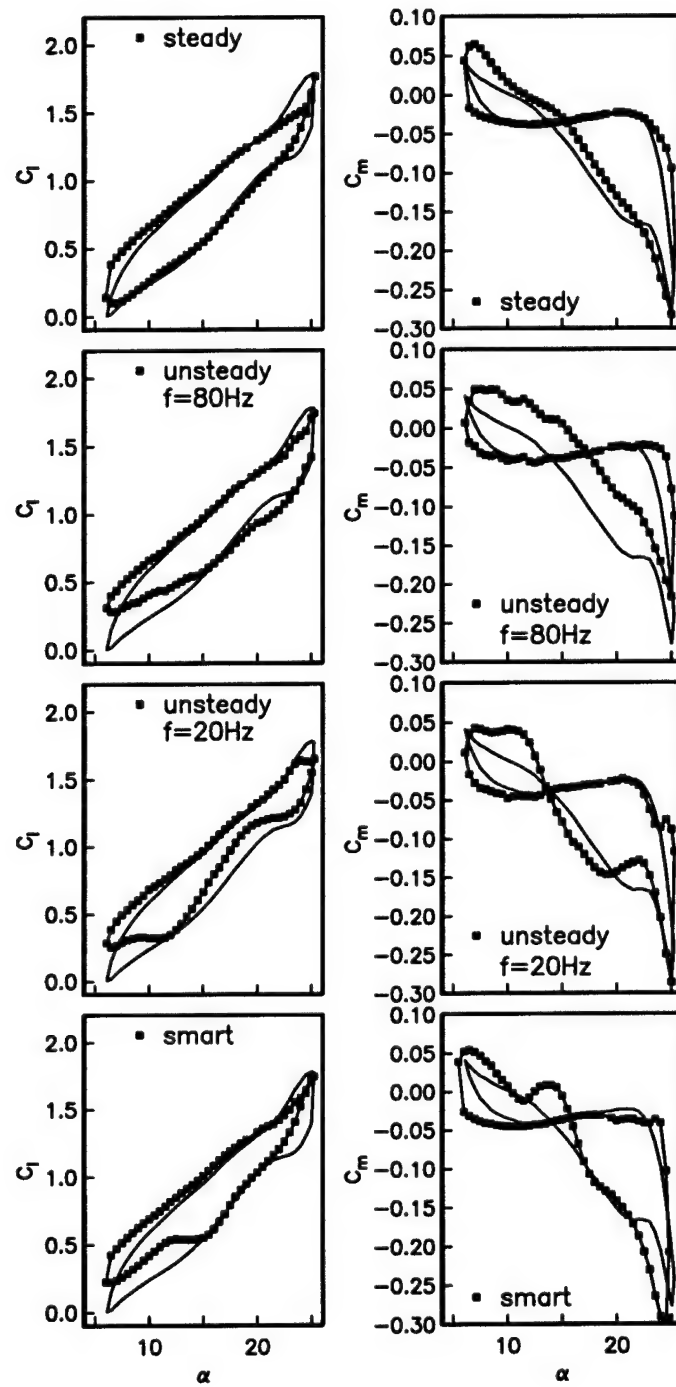


Figure 5.36. Effect of steady, unsteady, and “smart” actuation on the lift coefficient (left) and moment coefficient (right) for $\alpha(t) = 15^\circ + 10^\circ \sin \omega t$ and $k = 0.08$.

A comparison of the amount of lift improvement that was obtained for each of the cases with actuation is shown in Figure 5.37. The improvement was determined by integrating under the total lift cycle curve for each case and dividing by the integrated lift of the no actuation case. The results show that the "smart" control provided the largest lift improvement of approximately 13% compared to no control. The second best at approximately 10% improvement was the 20 Hz unsteady case. The steady case was the third best with about a 6% improvement, followed by the unsteady 80 Hz case which showed an approximately 5% increase in the lift. Any of these is a significant improvement. From a systems standpoint, the "smart" control and 20 Hz unsteady actuation are particularly attractive because of the actuator is not operating over all the cycle for the "smart" actuation and operating at only a 10% duty for the unsteady actuation. Therefore, the total power is reduced to the actuator which further improves a system energy balance.

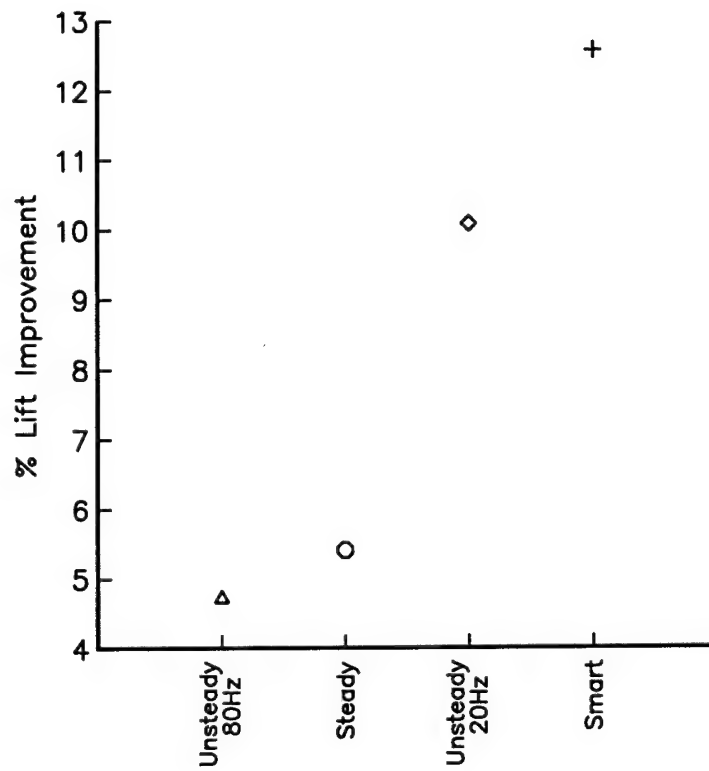


Figure 5.37. Percent lift improvement for plasma controlled cases.

5.6.1 Comparison of C_p Distributions

This section focuses on comparisons between the different actuator cases of the C_p distributions on the suction side of the oscillating airfoil. The purpose of this is to help to define a strategy for “smart” control that uses pressure information on the airfoil, instead of from the angle of attack information from the motor.

The ensemble-averaged C_p values over one cycle of the airfoil oscillation at different pressure port location on the suction side are shown in Figure 5.38. The two conditions shown are no actuation and steady actuation. Port 0 is at the leading edge. The increasing port numbers correspond to increasing x/c locations. The exact locations are given in Table 3.1 in Chapter 3.

For each port location, the steady actuation case is shown as the dashed line. The solid line corresponds to the case with no actuation. It is evident from Figure 5.38 that there is little difference between the C_p values with the actuator off and on at locations beyond Port 15 which corresponds to $x/c > 0.456$. This means that the effect of the plasma actuator is primarily upstream of this location. It indicates that from a control approach that is based on pressure measurements on the airfoil, the sensor locations need to be upstream of the 45% chord position.

The magnitude of the differences between the C_p values depends on the x/c location on the airfoil, and the part of the oscillating cycle. For example, at the leading edge (Port 0), the differences in C_p are noticeable in the part of the cycle near

the maximum angle of attack. As the measurement position moves aft, the part of the cycle where the difference between control and no control is most evident shifts toward the pitch-down.

An local indication of the effectiveness of the control approach could be the difference between C_p values at a port location without and with actuation. An example of this is given in Figure 5.39, which shows the difference between the ensemble averaged values over one cycle at the different port positions from Figure 5.38. The difference is taken as $C_{pC} - C_{pNC}$, where subscript C refers to the case with control and NC refers to the case with no control. If the difference is negative, indicated above the horizontal line at $C_p = 0$, it represents an improvement over the no control case.

The figure reveals that the largest improvements are primarily made near the leading edge. At the very leading edge (Port 0), the improvement is felt over the complete cycle, and it is a maximum in the pitch-up portion to the peak angle of attack.

With the steady control, the previous results have indicated a negative result of completely suppressing the formation of the dynamic vortex. The signature of this is evident in the C_p -difference as the dip that is seen in Ports 3 - 13 at the high angles of attack in the pitch-up part of the cycle. This is precisely the portion of the cycle where the dynamic vortex first forms.

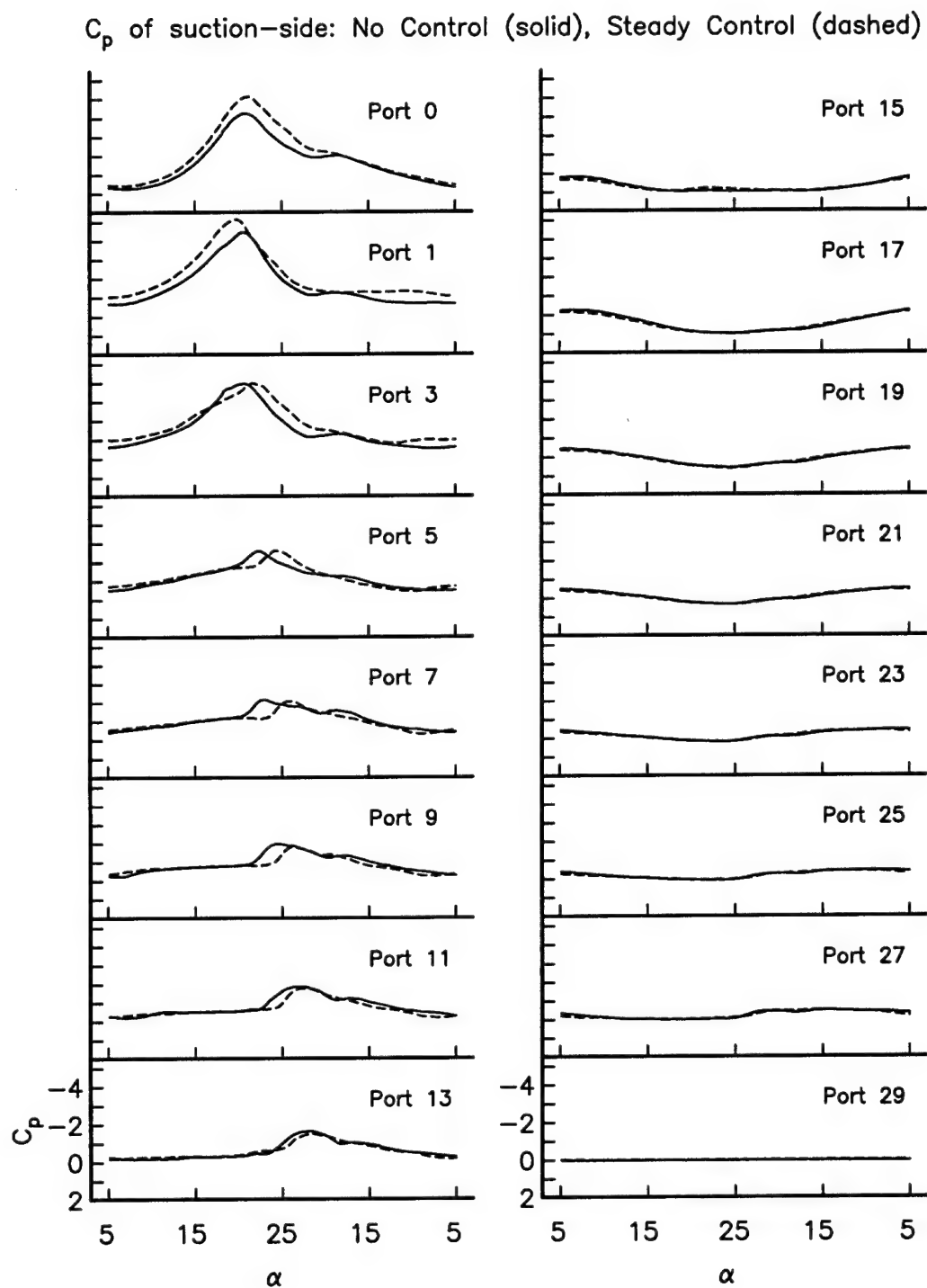


Figure 5.38. Comparing the coefficient of pressure on the suction-side of the airfoil for the no actuation and steady actuation cases.

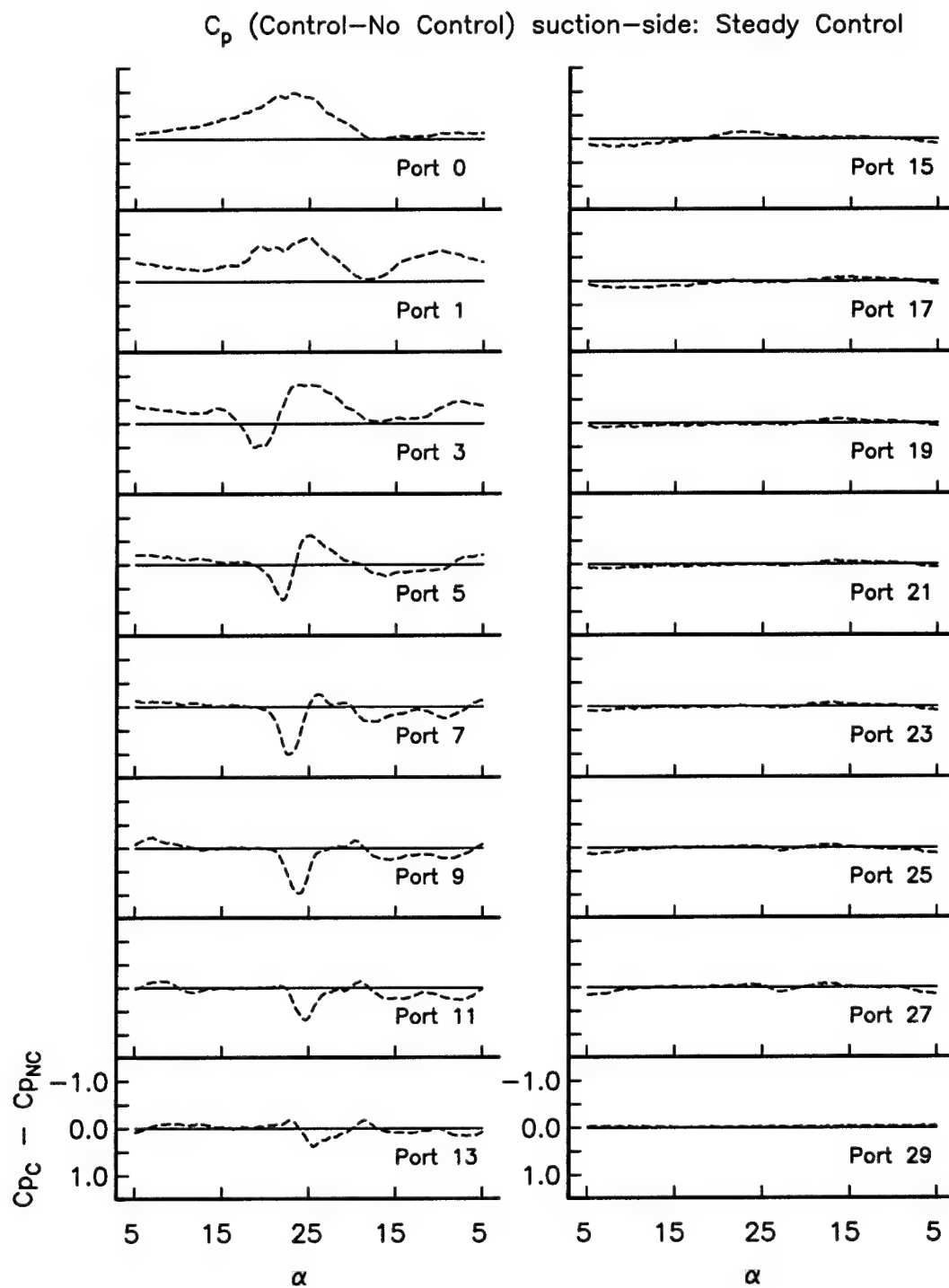


Figure 5.39. Difference between the coefficient of pressure for the no actuation and steady actuation cases.

A comparison between the two unsteady actuation cases and the no actuation case are made in Figure 5.40. Note that based on the integrated lift, the 20 Hz was better than the 80 Hz unsteady case. When the ensemble-averaged C_p distributions are compared it is evident where the improvement comes.

Given that some of the improvement for the unsteady cases is coming at the peak angles of attack in the pitch-up and pitch-down parts of the cycle, it is noted that very near the leading edge (Ports 0 - 3), the 80 Hz unsteady control results in the highest $-C_p$ values. This indicates that the 80 Hz unsteady actuation was better in keeping the leading-edge flow attached than the 20 Hz unsteady actuation. However, further back from the leading edge (Ports 7 - 13), the 20 Hz unsteady control produces larger $-C_p$ values. These improvements also appear primarily in the pitch-down part of the cycle, indicating that the 20 Hz unsteady actuation is better in reattaching the flow at that location.

These differences between the two unsteady actuation cases become even more apparent in Figure 5.41. This clearly illustrates that there is no single optimum unsteady actuator frequency. And that in fact, another "smart" scheme might be to change the unsteady frequency during the oscillating cycle. For example, the 80 Hz frequency could be used in the pitch-up portion and the 20 Hz frequency used during the pitch-down portion to use the advantages of each scheme. The results indicate that this may be more optimal than using either 20 Hz, 80 Hz, or another single frequency alone.

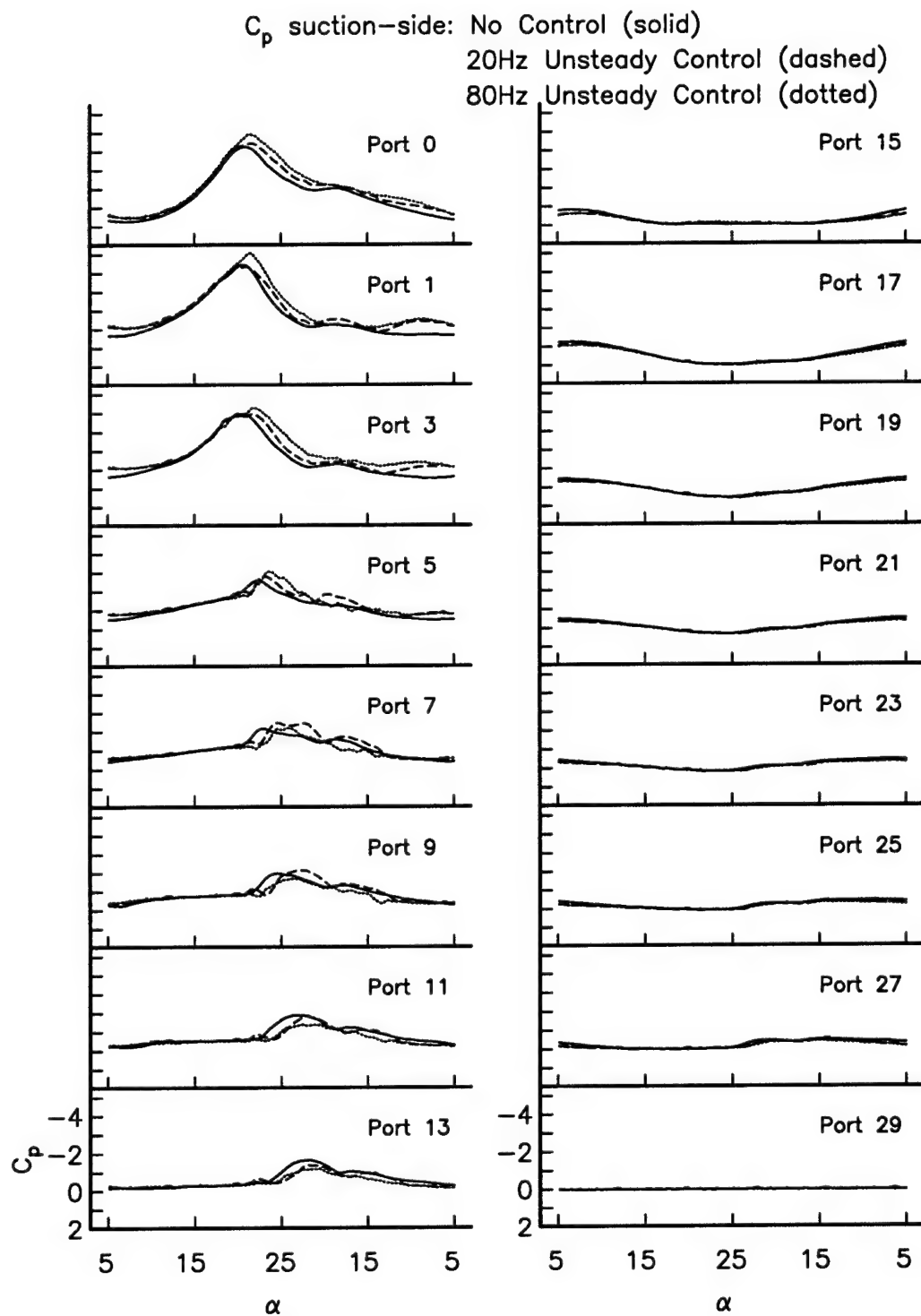


Figure 5.40. Comparing the coefficient of pressure on the suction-side of the airfoil for the no actuation, 20 Hz unsteady, and 80 Hz unsteady actuation cases.

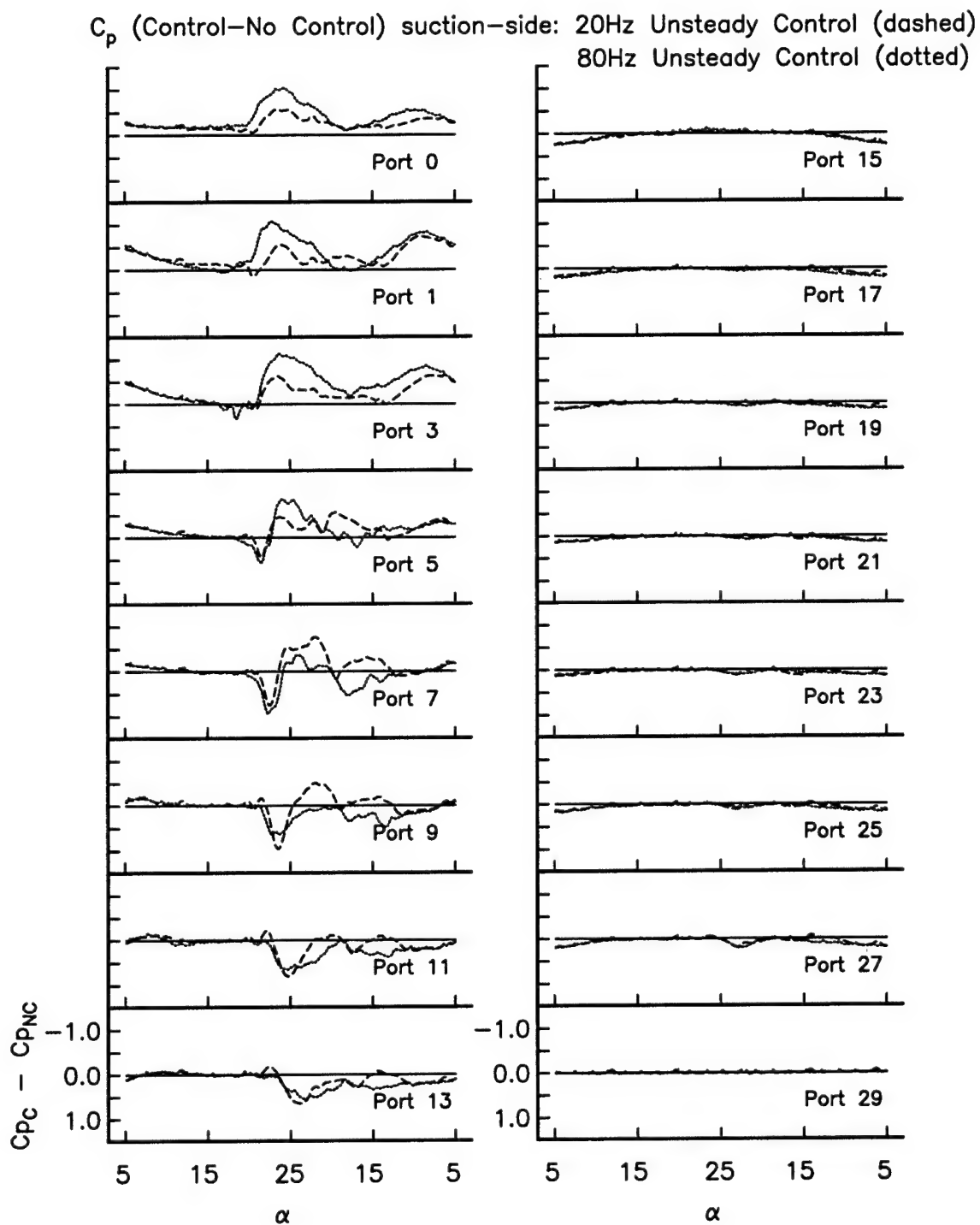


Figure 5.41. Difference between the coefficient of pressure for the no actuation and unsteady actuation cases.

A comparison of the ensemble averaged C_p distributions at the different locations on the airfoil for the "smart" actuation is shown in Figure 5.42. The vertical lines in the plots indicate the angle of attack range that the plasma actuator was on in the case of the "smart" actuation. The differences between the C_p distributions of the "smart" and no actuation conditions are shown in Figure 5.43. These reveal effects that are similar to the other actuator cases, namely an improvement at the higher angles of attack in the pitch-up and pitch-down portions of the cycle.

It has been shown that overall, the "smart" actuation produced more lift than the other approaches. To break down where this improvement came from, the differences between the C_p distributions of the "smart," 20 Hz unsteady, and steady conditions are presented in Figure 5.44.

Near the leading edge (Ports 0 and 1), the "smart" and steady actuation produce a comparable improvement during pitch-up. However, also based on these port locations, the "smart" actuation produces a larger $-C_p$ at the lower angles of attack during pitch-down. This would signify that the "smart" actuation is reattaching the flow sooner.

The 20 Hz unsteady actuation provides a better improvement somewhat more downstream of the airfoil's leading edge (Ports 7 and 9) at the high angles of attack during pitch-down. However, the magnitude of those improvements are smaller than those obtained elsewhere with the "smart" actuation, so that averaging over the whole cycle, the "smart" actuation produces the largest lift improvement.

Exercises like this are useful in pinpointing how the different actuation approaches affect the lift cycle. More importantly, they can lead to other, more effective “smart” control approaches that can produce to even larger overall performance improvement.

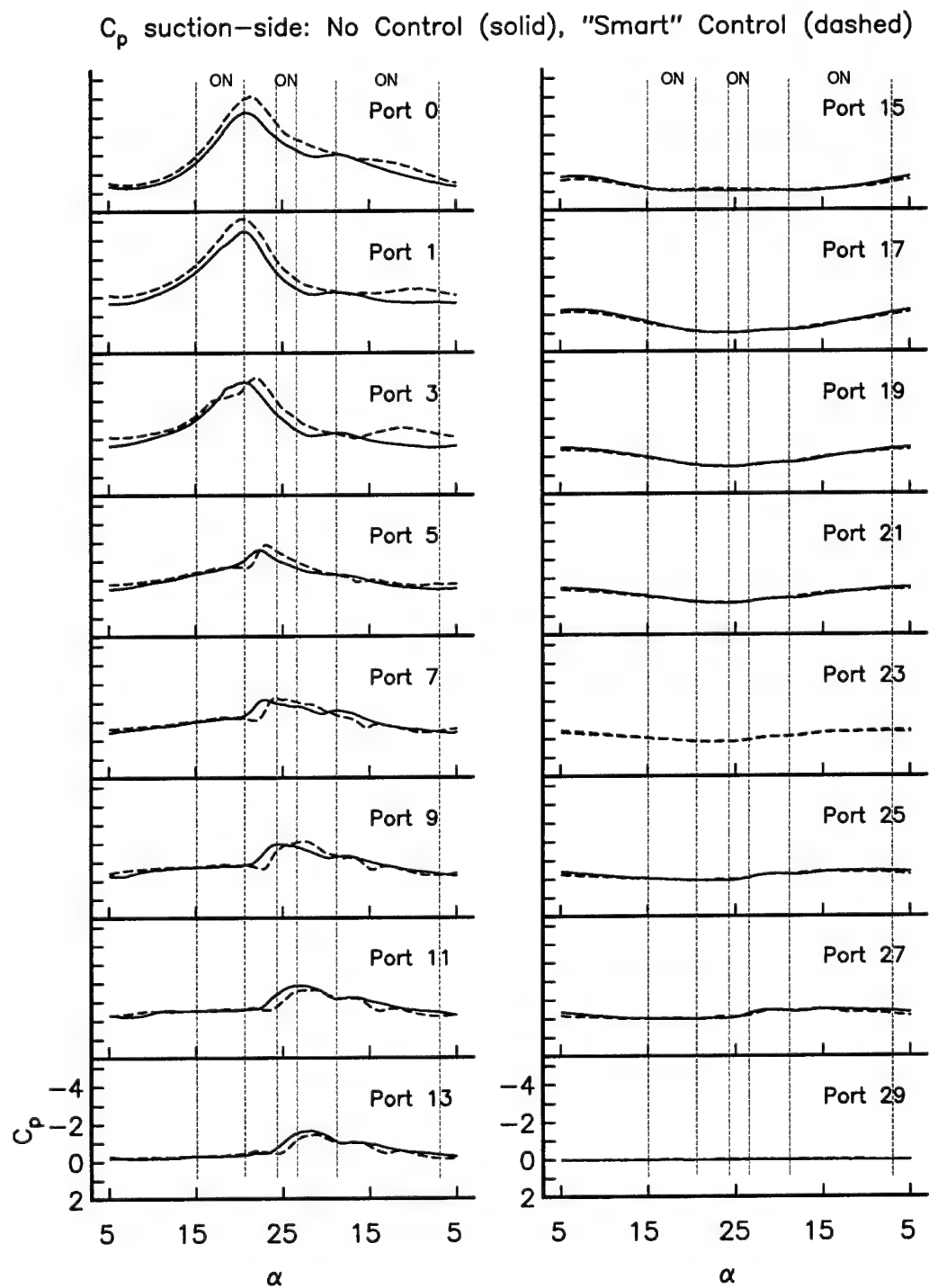


Figure 5.42. Comparing the coefficient of pressure on the suction-side of the airfoil for the no actuation and "smart" actuation cases.

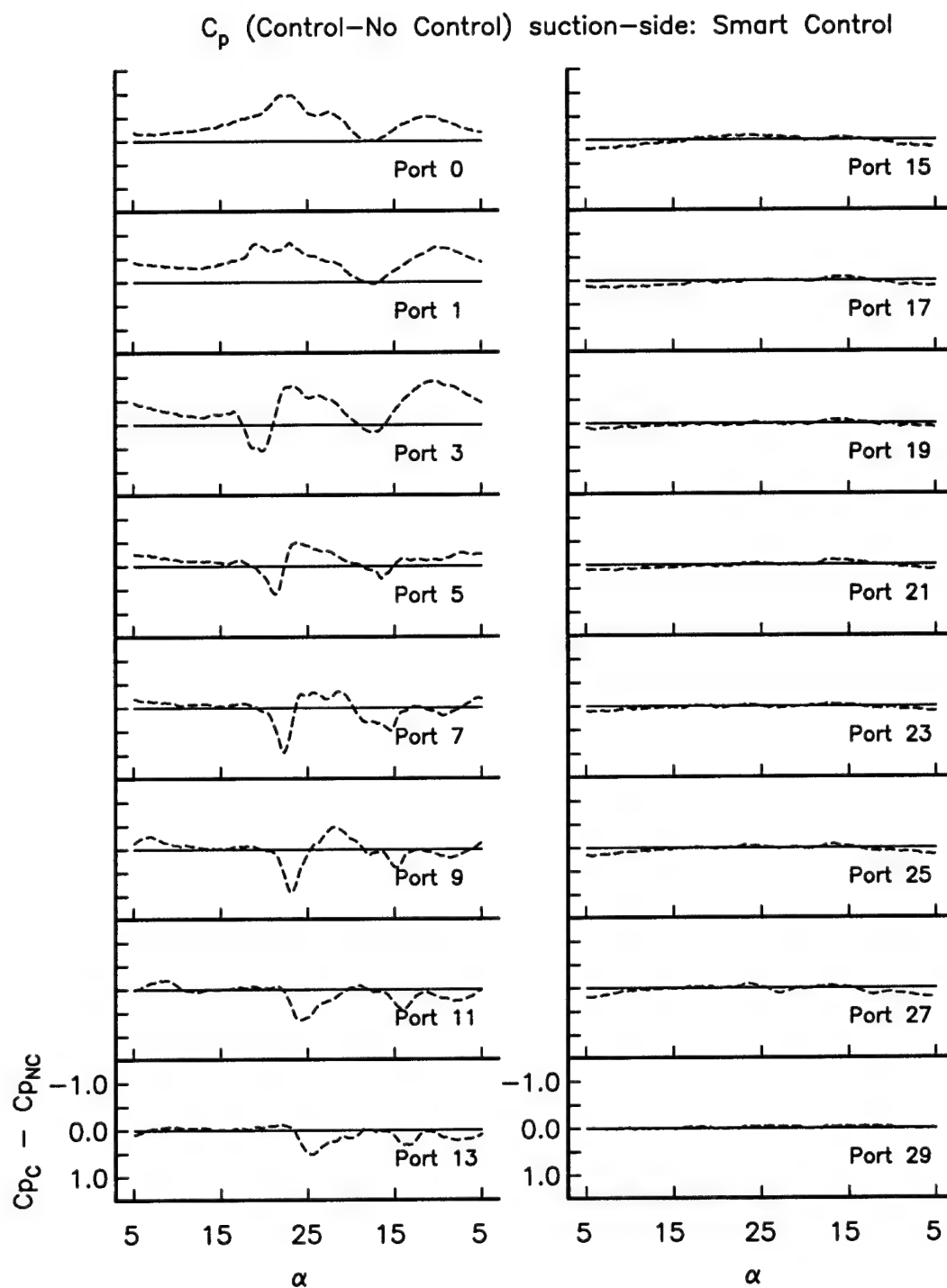


Figure 5.43. Difference between the coefficient of pressure for the no actuation and "smart" actuation cases.

Steady(solid); 20Hz Unsteady(dashed); "Smart"(dotted) Control

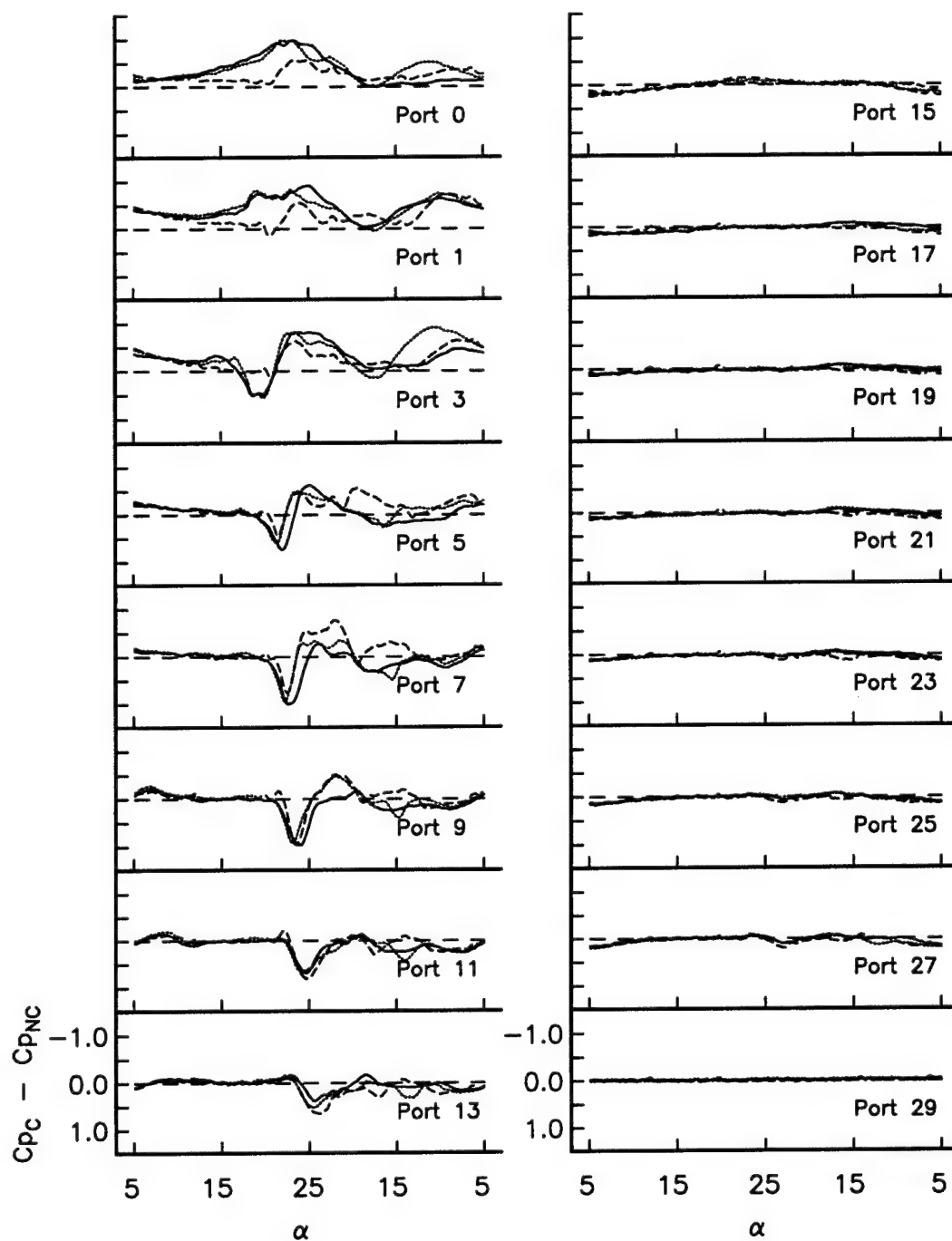


Figure 5.44. Difference between the coefficient of pressure for the no actuation, 20 Hz unsteady actuation, and "smart" actuation cases.

CHAPTER 6

CONCLUSIONS & RECOMMENDATIONS

This chapter presents conclusions related to the experiments on separation control with stationary and oscillating airfoils using the plasma actuator. In addition it summarizes the results of experiments designed to optimize the performance of the actuator. Finally it makes recommendations for future work toward the principle application of helicopter retreating blade stall.

6.1 Conclusions

This section presents conclusions on the optimization of the plasma actuator and its effectiveness for leading-edge separation control on stationary and oscillating airfoils.

6.1.1 Plasma Actuator Optimization

The operation of the plasma actuator was fully characterized through a systematic set of experiments. The focus was on different physical actuator configurations, determining the amplitude and frequency input/output relations, comparing steady versus unsteady operation, and determining the important time scales associated with the fluid response to the actuator. These experiments were fundamental in optimizing the actuator for the separation control experiments.

PIV was used to measure the response of the flow induced by the plasma actuator. The electrode configuration was an asymmetric design that was intended to draw air toward the wall and then accelerate it in a manner that was similar to a wall jet. The maximum mean velocity produced of the actuator was measured while varying several parameters. One of these parameters was the a.c. input voltage amplitude. The mean input/output response of the actuator was found to be $U \propto V^{7/2}$. This agreed with experimental results by Enloe et al. for the thrust produced by a plasma actuator [11]. The impact of this result is that the nonlinear static response makes the actuator more effective as the input voltage increases and that velocities appropriate to flow control at flight conditions are within the capability of the actuator.

The a.c. input frequency was varied to determine its effect on the maximum induced mean velocity and power requirements for the actuator. The exact frequency dependence will be a function of the properties of the driving electronics and of the plasma actuator design. These can be simulated as an inductor-resistor-capacitor network. In our setup, the maximum induced velocity was found to increase with frequency until it asymptoted at approximately 6 kHz. The a.c. supply power increased linearly with the a.c. frequency. The optimum driving frequency for the plasma was chosen to be 5 kHz, which was close to the frequency/velocity asymptote.

The effect of the width of the lower electrode on the maximum induced mean velocity was also investigated. The results indicated that there was a minimum electrode width (or area) that was required to reach the maximum attainable velocity. The minimum width was a function of the amplitude of the input voltage. This

was consistent with the process of the plasma generation whereby there needs to be sufficient area on the dielectric above the lower electrode for electrons to be deposited.

Multiple steady actuators placed next to each other were found to follow the same $U \propto V^{7/2}$ relation as a single actuator. However, the constant of proportionality was twice that of a single actuator. This indicated the effect of multiple actuators was linear with the number of actuators. This result is consistent with the physics of the actuator, in which it acts as a body force in the fluid momentum equation.

The dynamic response of the unsteady actuator was determined by measuring the response of the ambient air to a step input of the actuator voltage. For this the actuator was switched on and off while a phase-locked trigger signal was used to capture PIV velocity data at different times in the on-off cycle. The response to the step input was captured and found to be similar to a first-order response. Based on this, a time constant was found. The results showed that the time constant varied linearly with the actuator voltage.

6.1.2 Separation Control on Stationary Airfoils

Plasma actuators were documented to reattach the leading-edge flow separation over stationary NACA 66₃ – 018 and NACA 0015 airfoils. Each actuator consisted of a pair of electrodes that were separated by a dielectric layer. The electrodes were in an asymmetric configuration which produced a body force vector that would induce the flow in one direction. The plasma actuator was designed to produce a 2-D wall

jet in the flow direction, thereby adding momentum to the boundary layer to combat separation.

Baseline measurements on the NACA 66₃ - 018 were conducted to document the angle of attack characteristics of the airfoil and to benchmark the lift coefficient measurements. The lift was found by integrating the surface C_p distribution around the airfoil. This approach was found to agree well with measurements made with a force balance by Jansen [25]. The drag was found by calculating the momentum deficit in the wake based on measurements of the mean streamwise velocity profile.

As a precursor to the separation control using the plasma actuators, the use of vortex generators on the NACA 66₃ - 018 was investigated. Two different locations for the tab vortex generators were used: $x/c = 0.05$ and $x/c = 0.2$. At both locations, the vortex generators are able to recover the pressure near the leading edge of the suction surface. The vortex generators at $x/c = 0.05$ produced a higher $-C_p$ peak, however those placed at $x/c = 0.2$ improved the suction pressure over a larger portion of the chord so that the integrated effect was larger.

For the NACA 66₃ - 018, two plasma actuators operated in the steady mode were used. One actuator was placed at the leading edge ($x/c = 0$) and the other at the maximum thickness point on the airfoil ($x/c = 0.5$). Both were arranged to induce a downstream oriented body force parallel with the freestream.

The flow reattachment on the NACA 66₃ - 018 produced by the steady plasma actuator was documented at $Re_c = 79K$ and $Re_c = 158K$. In both cases there was a pressure recovery at the leading edge at angles of attack higher than the natural

static stall angle. The velocity profile in the wake showed a substantial narrowing of the wake and an increase in the minimum peak velocity. At $Re_c = 79K$, the actuator led to a significant suction pressure recovery and drag reduction that yielded as much as a 400 percent increase in the L/D ratio.

At $Re_c = 158K$, there was an increase in lift and a decrease in drag for all of the angles of attack investigated, which was to 6 degrees beyond the static stall angle. With the actuators, there was a widening of the drag bucket. The estimated power to achieve this was approximately 20 watts per foot span.

An investigation on actuator amplitude on the NACA 66₃ - 018 indicated that once a threshold amplitude was reached, the flow reattached, and there was little more to be gained in lift with additional actuator amplitude. The threshold amplitude was found to be approximately 40% of the power used for the bulk of the results. However, for the drag coefficient, there was an approximately linear decrease in the drag as the actuator amplitude increased, even after the lift value had saturated. As a consequence, the L/D ratio continued to increase as the actuator amplitude increased.

In terms of the pressure recovery on the NACA 66₃ - 018, slightly better, yet comparable results were found to that of vortex generator tabs. The advantage of the plasma actuators is that they can be operated only when needed, and when not in use, they produce no parasitic effects. From this experiment, it was determined that the most effective actuator location to reattach the leading-edge flow separation was directly at the leading edge.

For the NACA 0015 stationary airfoil, a single plasma actuator at the leading edge was operated in either the steady or unsteady mode. The steady actuator was able to reattach the flow for angles of attack up to 22° , which was 8° past the normal stall angle. Under these conditions, the lift-to-drag ratio increased by as much as 300%.

These results motivated additional work which extended the potential of the plasma actuator from inducing a steady body force to generating an unsteady body force. The idea behind generating an unsteady body force was that: (1) unsteady plasma generation had the ability to generate coherent structures beneficial for separation control, and (2) energy expenditure of unsteady flow control systems are usually more efficient than steady control systems.

For the unsteady operation, the plasma actuator was impulsively turned off and on at 160 Hz. This frequency was the estimated optimum frequency based on $St = fc/U_\infty \approx 1$ for the conditions tested. The unsteady actuator performed even better than the steady actuator. Only a 10% duty cycle was found to be needed so that the power consumption was one-tenth that used for steady operation. This result is expected to be the general outcome for leading-edge separation control on airfoils using the plasma actuator.

6.1.3 Separation Control on Oscillating Airfoil

The use of plasma actuators for leading-edge separation control on an oscillating NACA 0015 airfoil was investigated for the application of retreating blade stall for a helicopter. Their effectiveness was based on a combination of flow visualization records and pressure measurements on the surface of the airfoil. The majority of the data was taken for $\alpha(t) = 15^\circ + 10^\circ \sin \omega t$ and a reduced frequency of $k = 0.08$, although the effect of the mean angle of attack, oscillating amplitude, and reduced frequency were all investigated.

Three cases with the plasma actuator were documented here: steady plasma actuation, unsteady plasma actuation, and “smart” plasma actuation in which the actuator was operated in a steady mode over selected parts of the oscillatory cycle.

All of the actuator cases were found to improve the lift cycle to some degree. The steady plasma actuation increased the lift over most of the cycle, except at the peak angle of attack where it was found to suppress the dynamic stall vortex. The principle advantage of this was that it eliminated the sharp drop in the lift coefficient at the start of the pitch-down that is associated with the dynamic stall.

The unsteady plasma actuation produced significant improvements in the lift coefficient during the pitch-down phase of the cycle, especially near the minimum angle of attack. Two actuator frequencies were investigated in detail, 80 Hz and 20 Hz. The lowest of these is still approximately five times the airfoil oscillation frequency. The 80 Hz was based on $St = fc/U_\infty \approx 1$. Overall, the 20 Hz produced the larger cycle-integrated lift. However, a detailed analysis of the lift improvement over the

cycle indicated that the 80 Hz was better during the pitch-up portion of the cycle while the 20 Hz was better during the pitch-down portion. The former is important in keeping the flow attached as long as possible before reaching the maximum angle of attack. The latter is important in reattaching the flow as soon as possible past the peak angle of attack.

Based on observing the effect that the steady and unsteady plasma actuators had on controlling the lift cycle, and correlating this with what was observed in the flow visualization, a “smart” actuator approach was designed that would turn on the actuator only during **portions** of the airfoil oscillatory cycle. These portions were defined as ranges of angles of attack where actuation was expected to produce an improvement in the lift cycle.

The range of angles in the periodic cycle when the actuator was set to be on were:

1. $15^\circ \geq \alpha \geq 20^\circ$ during the pitch-up phase,
2. $24^\circ \geq \alpha \geq 23^\circ$ during the pitch-up phase, through the peak angle of attack,
3. $20^\circ \leq \alpha \leq 8^\circ$ during the pitch-down phase.

The rationale for operating the actuator between $15^\circ \geq \alpha \geq 20^\circ$ was to keep the flow attached during the high angles of attack of the pitch-up portion of the cycle. It was subsequently turned off from $21^\circ \geq \alpha \geq 23^\circ$ during pitch-up in order to allow the dynamic vortex to form. Previous cases showed that if the actuator suppressed the formation of the vortex, the maximum lift at the peak angle of attack would be less.

The actuator is turned back on just before the peak angle is reached, between $\alpha = 24^\circ$ in the pitch-up and $\alpha = 23^\circ$ in the pitch down. This rational for this was to reduce the dynamic stall and thereby eliminate the sharp drop in lift that normally occurs as the cycle passes the maximum angle of attack.

In the pitch-down portion, the actuator is turned off at $\alpha = 22^\circ$, but turned on again at $\alpha = 20^\circ$, where it remains on until the angle of attack is near the minimum. The reason for this is to reattach the flow as soon as possible in the pitch-down which has the effect of reducing the lift-cycle hysteresis.

With the “smart” actuation, there was an increase in the lift over the complete cycle. In particular there was a significant improvement in the lift during the pitch-down portion of the cycle, especially at the lower angles of attack. In addition, compared to the other steady actuator cases, the maximum lift was not lost at the higher angles of attack during the pitch-up. Also past the maximum angle of attack in the pitch-down portion of the cycle, the sharp stall that gave the lift cycle the “lobed” shape, has been replaced with a more desirable smooth lift decrease with less hysteresis.

A comparison of the amount of lift improvement that was obtained for each of the cases with actuation was done. The improvement was determined by integrating under the total lift cycle curve for each case and dividing by the integrated lift of the no actuation case. The results showed that the “smart” control provided the largest lift improvement of approximately 13% compared to no control. The second best at approximately 10% improvement was the 20 Hz unsteady case. The steady case was

the third best with about a 6% improvement, followed by the unsteady 80 Hz case which showed an approximately 5% increase in the lift. Any of these is a significant improvement. From a systems standpoint, the "smart" control and 20 Hz unsteady actuation are particularly attractive because of the actuator is not operating over all the cycle on the former and operating at only a 10% duty in the latter. Therefore the total power is reduced to the actuator which further improves a system energy balance.

It is possible that the "smart" actuation could be optimized further. However, in this first approach, the results are extremely promising for improving helicopter rotor performance.

6.2 Recommendations

Based on these results, it appears that this flow control technique may only be limited by the ability to generate adequate forcing conditions at the higher Mach numbers required for helicopters. Additional testing at higher velocities are needed to determine if the plasma actuator is feasible for a helicopter rotor flow control device. Further work can be directed toward improving the actuator design to increase the maximum velocity it can produce.

As stated before, the work presented here represents a first approach for the "smart" actuator. This showed a benefit to operating the actuator only during selected portions of the oscillation cycle. The choice of the portions was prompted by the different flow physics that were identified in different parts of the cycle. A recom-

mendation for future work is to seek further improvements in the "smart" actuation. This may involve the use of unsteady actuation instead of the steady actuation. In addition, it might involve different frequencies of unsteady actuation over different portions of the cycle.

The implementation of the "smart" actuation used specific angles of attack as an indicator of when to turn the plasma actuator on and off. Future work should look at making use of the surface pressure information as an indicator. This is likely to produce even greater improvements since it will be able to adapt to different conditions such as changes in the oscillation conditions that change the flow physics.

It is also important to point out that while much of what is known about dynamic stall has been obtained from experiments on 2-D airfoils, it is important to recognize that when dynamic stall occurs on an actual rotor there is more of a 3-D character. Therefore, testing on a finite aspect ratio oscillating airfoil, and eventually on a rotating airfoil would be necessary steps that are needed to transition this work to actual helicopter applications.

APPENDIX A

SMARTMOTOR PROGRAM

This program was used by the servo motor through the Smartmotor Interface Software to oscillate the airfoil. For different physical oscillation frequencies, the motor's velocity and acceleration was modified using this program. The range of angles of attack was also controlled by this program by scaling the analog input accordingly. The motor had a 1000-count, quadrature digital optical encoder, and the motor had a 10:1 gear drive. This resulted in $4,000 \times 10 = 40,000$ encoder counts per rotation. Each rotation was 360 degrees, giving $111.\bar{1}$ encoder counts per physical degree.

```
'Notre Dame Wing Flapper Program
'Scale factor:  1 deg = 111.111111111 counts
'Calculate the distance and round off to the nearest integer.
'Set up Limit inputs/Home Complete output
    LIMD  'Directional Limits
    LIMH  'Set limit active high
'Set up tuning values
```

```

KP=250      'Proportional gain
KI=350      'Integral gain
KD=2200     'Differential gain
KL=100      'Integral limit
KS=1        'Sample speed
KV=500      'Velocity feed-forward
KA=250      'Acceleration feed-forward
KG=0        'Gravity gain
F           'Set values
F=8         'Improve settling time
E=1000      'Following error limit
RUN?        'Wait for run command
O=0         'Set origin to current position
'Read analog input (0-5VDC = -10-10 deg on gearhead shaft)
'Allow motion to match analog input
UGI         'Set up pin G as analog input
'A=4500     'Acceleration necessary for 5Hz
'V=580000   'Velocity necessary for 5Hz
A=2880      'for 4Hz
V=464000    'for 4Hz
'A=2205     'for 3.5Hz
'V=406000   'for 3.5Hz
'A=1630     'for 3Hz
'V=348000   'for 3Hz
'A=1125     'for 2.5Hz
'V=290000   'for 2.5Hz
'A=720      'for 1-2Hz
'V=232000   'for 1-2Hz
'A=6480
'V=696000
WHILE 1      'Infinite loop
g=UGA       'Read analog input
           'For 20 deg (+/-10) degree range
g=g*800000  'Start scaling of analog input
g=409200000-g 'Finish scaling of analog input
'g=g*400000 'For 10 deg (+/-5) degree range
'g=204600000-g 'For 10 deg (+/-5) degree range
'g=g*640000 'For 16 deg (+/-8) degree range
'g=327360000-g 'For 16 deg (+/-8) degree range
g=g/368280
P=g         'Set new position
G          'Start motion
LOOP
END

```


APPENDIX B

MATLAB PROGRAMS

```
*****
% This Matlab program loads the data,
% calculates the coefficient of drag
% and plots the result for the stationary airfoil.
*****

clear
datafile = load('vp14actoff.dat');
variable=0.99;
n = length(datafile);

% constants
% converting to lbm
mu = 3.7373*10^-7*32.2;
rho = 0.073;

% 10 in -> 10/12 ft
c = 5/12;
% calib_constant=0.463;

% traverse setup
% interval of traverse movement converted to ft
% offset value dependent upon which point is first
%q = 1;

y = datafile(:,2)/.3048;
x = datafile(:,1);

% Find number of points around the freestream
total = 0;
for i = 1:n
    total = total + y(i);
    meanV = total/i;
```

```

        if i>10
            yperc = y(i)/meanV;
            if yperc < variable
                break
            end
        end
    end
end
stopv = y(i);

% Set up points for integration
freeV = meanV;
m = 0;
for j = i:n
    m = m+1;
    wakev(m) = y(j);
    wake(m) = y(j)*(freeV-y(j));
    if y(j) > stopv
        break
    end
end

% Trapezoidal rule
n = length(wake);
isum = 0;
for i = 1:n-1
    isum = isum + (y(i) + y(i+1))*(x(i+1) - x(i))/2;
end

D = rho*isum
freeV
plot(wakev)
Re = rho*freeV*c/mu
Cd = D/.5/rho/(freeV*freeV)*c*32.2

```

```

*****
% This Matlab program loads the data and
% calculates the coefficient of lift and moment
% for the oscillating airfoil.
% It also plots the results
% and saves calculated values to a data file.
*****

clear all
figure(1)
clf
hold on

% Modify these parameters for each case
run_date = 120203;
vel = 10;
freq = 4;
angle_range = '15pm10';
run_num = 9;
angleset = 1;
act = '_ACTON';

% Loads data and rearranges
direct = ['D: Data data_wind_tunnel tunneldata_2003oct '
    num2str(run_date) act ' ' num2str(vel) 'ms' num2str(freq) 'hz '
    angle_range ' run' num2str(run_num) ' angleset'
    num2str(angleset,'%02d')' '];
data = dir([direct 'xc_run' num2str(run_num,'%03d')
    '_set' num2str(angleset,'%02d') '_angle-*']);

% initializes parameter
flip_num = 0;
for n = 1:size(data,1)
    filename = data(n).name;
    B(:, :, n) = load([direct filename]);

    % determines angle from filename
    angleB(n) = str2num(filename(24:24+end-28));

    % determines direction (a=ascending, d=descending)
    adB(n) = filename(23);
    if (adB(n) == 'd') & (flip_num == 0)
        % locates 1st descending point
        flip_num = n;
    end
end

```

```

end

% A = (all rows, all columns, ascending points)
A = B(:, :, 1:flip_num-1);

% tells where to start in A
% (all rows, all columns, descending points)
% then flips and inserts descending points
A(:, :, flip_num:size(B,3)) = flipdim(B(:, :, flip_num:end), 3);

% repeat same procedure for angles
angle = angleB(1:flip_num-1);
angle(flip_num:size(B,3)) = fliplr(angleB(flip_num:end));
ad = adB(1:flip_num-1);
ad(flip_num:size(B,3)) = fliplr(adB(flip_num:end));

J1 = subplot(1,2,1);
J2 = subplot(1,2,2);

% c=color, hsv=hue-saturation-value color map
% for plots in 100 divisions
c = hsv(100);
maxa = max(angle);
mina = min(angle);

% counters
o1 = 1;
o2 = 1;

for n = 1:size(A,3)
    % builds legends
    if ad(n) == 'a'
        subplot(1,2,1)
        adtext = 'Increasing';
        leg1(o1,:) = [num2str(angle(n), '%02.0f') ' ' adtext];
        o1 = o1 + 1;
    else
        subplot(1,2,2)
        adtext = 'Decreasing';
        leg2(o2,:) = [num2str(angle(n), '%02.0f') ' ' adtext];
        o2 = o2 + 1;
    end
end
hold on

% plots data
x = [flipud(A(1:15,1,n)); A(16:end,1,n)];
cp = [flipud(A(1:15,2,n)); A(16:end,2,n)];

```

```

J = plot(x,cp,'k.-');
set(J,'Color',c(floor((angle(n)-mina)/(maxa-mina)*80+1),:))

% Coefficient of Lift Calculation
% puts 1's on either side of the x array
% to account for trailing edge
x = [1;x;1];

% calculates y using profile equation
y = 0.15./2.*(0.29690.*sqrt(x)+x.*(-0.1260+x.*
(-0.3516+x.*(0.2843-0.1015.*x))));

% defines upper and lower airfoil surfaces
y = [y(1:16);-y(17:end)];

% calculates slope at each pressure port
dydx = (y(3:end)-y(1:end-2))./(x(3:end)-x(1:end-2));

% slope at LE is infinity, so reset to 0
dydx(15) = 0;

% distance between each pressure port
dx = (x(3:end)-x(1:end-2))/2;

% calculates TE distance
dx(1) = dx(1)+((x(2)-x(1))/2);

% calculates TE distance
dx(end) = dx(end)+(x(end)-x(end-1))/2;

% redefines x without TE points
x = x(2:end-1);

% redefines y without TE points
y = y(2:end-1);

% coefficient of force normal to chord
cn(n) = sum(dx.*cp);

% coefficient of force aligned with chord
ca(n) = sum(dx.*cp.*dydx)+cp(15)*(y(14)-y(16))/2;

% coefficient of lift
cl(n) = cn(n)*cos(angle(n)*pi/180)-ca(n)*sin(angle(n)*pi/180);
cmm(n) = -sum(dx.*cp.*x);

% coefficient of moment
cm(n) = cmm(n) + 0.25*cn(n);

end

% Formats for Cp

```

```

subplot(1,2,1)
axis([0 1 -7 1.5])
set(J1,'YDir','Reverse')
legend(leg1)
xlabel('x/c')
ylabel('C_p')

subplot(1,2,2)
axis([0 1 -7 1.5])
set(J2,'YDir','Reverse')
legend(leg2)
xlabel('x/c')
ylabel('C_p')

% Plots Coefficient of Lift
figure(5)
clf
hold on
plot(angle(1:flip_num-1),cl(1:flip_num-1),'k^')
plot(angle(flip_num:end),cl(flip_num:end),'kv')
plot(angle,cn,'k.')
AX = axis;
axis([mina-2 maxa+2 AX(3) AX(4)]);
xlabel(' alpha [deg]')
ylabel('C_l')
legend('Ascending','Descending',4)

figure(6)
clf
hold on
plot(angle,cm)

for n = 1:length(ad)
    if ad(n) == 'a'
        ad01(n) = 1;
    else
        ad01(n) = 0;
    end
end

outfile = [angle' cl' ad01'];
filename = [direct 'cl_' num2str(run_date) act '_' num2str(vel) 'ms'
            num2str(freq) 'hz_' angle_range '_run' num2str(run_num) '_angleset'
            num2str(angleset,'%02d') '.dat'];

```

```

eval(['save ' char(39) filename char(39) ' outfile -ASCII -TABS'])
filename = ['D: Data data_wind_tunnel tunneldata_2003oct C1 cl_'
    num2str(run_date) act '_' num2str(vel) 'ms' num2str(freq) 'hz_'
    angle_range ' _run' num2str(run_num) '_angleset'
    num2str(angleset,'%02d') '.dat']
eval(['save ' char(39) filename char(39) ' outfile -ASCII -TABS'])

outfile = [angle' cm' ad01'];
filename = [direct 'cm_' num2str(run_date) act '_' num2str(vel) 'ms'
    num2str(freq) 'hz_' angle_range ' _run' num2str(run_num) '_angleset'
    num2str(angleset,'%02d') '.dat'];
eval(['save ' char(39) filename char(39) ' outfile -ASCII -TABS'])
filename = ['D: Data data_wind_tunnel tunneldata_2003oct Cm cm_'
    num2str(run_date) act '_' num2str(vel) 'ms' num2str(freq) 'hz_'
    angle_range ' _run' num2str(run_num) '_angleset'
    num2str(angleset,'%02d') '.dat']
eval(['save ' char(39) filename char(39) ' outfile -ASCII -TABS'])

disp('complete')

```

APPENDIX C

ERROR ANALYSIS

Experimental uncertainty analysis involves the identification of errors that arise during all stages of the experiment and the propagation of these errors into the overall uncertainty of a desired result. It is the result of both systematic (bias) and random (precision) errors. The systematic error is a resolution error associated with a particular measurement. The random error considers the repeatability of data, independent of the measurement tools. Systematic error is relatively easy to quantify, while random error depends on statistics to quantify.

Most experiments can be categorized either as timewise or sample-to-sample [10]. The work here was exclusively sample-to-sample experimentation. In a sample-to-sample experiment, the random error comes from both measurement system variability and variations due to small, uncontrollable factors during the measurement.

Sources of error in this experiment include the uncertainty in the voltage measurement, error in the calibration fit for voltage/pressure, and the calculation of the lift, drag and moment coefficients using a finite integral technique. A schematic of how these errors propagate to the final desired result is shown in Figure C.1.

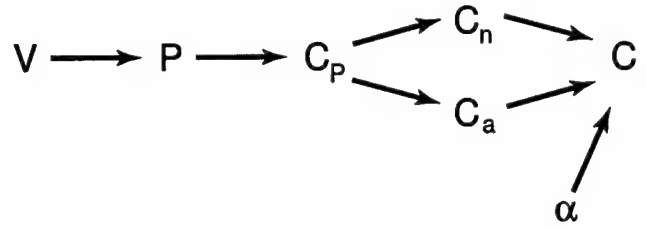


Figure C.1. Sources of error and their propagation.

Uncertainty in Voltage

The uncertainty in voltage is derived from both bias and random error. The published error of the Scanivalve pressure transducer was 0.3% full scale. Since the full scale output of the pressure transducer is ± 10 V, the absolute bias error of the transducer is

$$u_a = 20 \text{ V}(0.003) = 0.06 \text{ V.} \quad (\text{C.1})$$

Error associated with the A/D converter is the absolute quantization error of the A/D converter. The resolution, Q , of a 12-bit converter with a full scale range of -10 V to 10 V is given by

$$Q = \frac{E_{FSR}}{2^{12}} = \frac{20}{4096} = 0.00488 \text{ V/bit} \quad (\text{C.2})$$

where E_{FSR} is the full scale range of the voltage. Therefore, the quantization error per bit, e_Q , is

$$e_Q = \frac{1}{2}Q = 0.00244 \text{ V.} \quad (\text{C.3})$$

Random uncertainty can be characterized by the standard deviation, S_r , of an ensemble of data where the input to the measurement device is constant. The random uncertainty, u_{r_V} , in the average voltage, \bar{V} , is given by

$$u_{r_{\bar{V}}} = t_{\nu_{r_V}, C} \cdot S_{r_V}, \quad (\text{C.4})$$

where $t_{\nu_{r_V}, C}$ is the Student's t variable, ν_{r_V} is the number of degrees of freedom, and C is the confidence level. The number of degrees of freedom is

$$\nu = N - c, \quad (\text{C.5})$$

where N is the number of samples and c is the number of independent constraints. The standard confidence assumption is 95%.

The standard deviation of the measurement was calculated during data acquisition. When computing the standard deviation, the value of the mean is required, so there is one constraint so $c = 1$. With $N = 20$ and $c = 1$, the corresponding $t_{\nu_{r_V}, C}$ is ± 2.093 [10]. This means that there is a 95% probability that a sample value will be within ± 2.093 sample standard deviations of the sample mean. The random uncertainty for the voltage measurement for the oscillating airfoil is

$$u_{r_{\bar{V}}} = \pm 2.093(0.02) = 0.042 \text{ V} \quad (\text{C.6})$$

The total uncertainty of the voltage measurement is

$$u_V = (u_a^2 + e_Q^2 + u_{r_{\bar{V}}}^2)^{1/2} = (0.06^2 + 0.00244^2 + 0.042^2)^{1/2} = 0.073 \text{ V} \quad (\text{C.7})$$

Uncertainty in Pressure

The sources for the uncertainty in pressure are the propagation of the error in voltage and the error in the calibration curve for the voltage/pressure relationship. A Matlab code by Dunn [10] calculates the error in the pressure, p , from the calibration of voltage versus pressure to be 1.66%. Therefore, the uncertainty in the pressure measurement is

$$u_P = P_s(0.0166) = 0.245(0.0166) = 0.004 \text{ in. H}_2\text{O}. \quad (\text{C.8})$$

Uncertainty in Pressure Coefficient

The coefficient of pressure is defined as

$$C_p = \frac{P_s - P_\infty}{\frac{1}{2}\rho U^2} = \frac{P_s - P_\infty}{P_o - P_\infty} = \frac{\Delta P_s}{\Delta P_o}. \quad (\text{C.9})$$

Using the method of Kline and McClintock, the uncertainty in the coefficient of pressure is

$$u_{C_p} = \left[\left(\frac{\partial C_p}{\partial P_s} u_{\Delta P_s} \right) + \left(\frac{\partial C_p}{\partial P_o} u_{\Delta P_o} \right) \right]^{\frac{1}{2}} = \left[\left(\frac{1}{\Delta P_o} u_{\Delta P_s} \right) + \left(\frac{\Delta P_s}{\Delta P_o^2} u_{\Delta P_o} \right) \right]^{\frac{1}{2}} \quad (\text{C.10})$$

Since $u_P = u_{\Delta P_s} = u_{\Delta P_o}$ and $P_s = P_o = 0.245 \text{ in. H}_2\text{O}$ at freestream conditions, a typical error in C_p is

$$u_{C_p} = \left[\frac{1}{\Delta P_o^2} + \frac{\Delta P_s^2}{\Delta P_o^4} \right]^{1/2} u_P = \left[\frac{1}{0.245^2} + \frac{0.245^2}{0.245^4} \right]^{1/2} u_P = 4.1 u_P. \quad (\text{C.11})$$

Using the uncertainty in the pressure, the calculated uncertainty in the pressure coefficient is

$$u_{C_p} = 4.1 u_P = 4.1(0.004) = 0.017. \quad (\text{C.12})$$

Uncertainty in Angle of Attack

The total uncertainty in the angle of attack, u_α , can be determined by

$$u_\alpha = \left(u_{\alpha_s}^2 + u_{\alpha_R}^2 + u_{\alpha_{A/D}}^2 + u_{\alpha_{St}}^2 \right)^{\frac{1}{2}}, \quad (C.13)$$

where u_{α_s} is the uncertainty due to setting the initial angle of attack, u_{α_R} is the uncertainty due to the resolution of the motor, $u_{\alpha_{A/D}}$ is the uncertainty due to the A/D converter, and $u_{\alpha_{St}}$ is the uncertainty due to the random error in the measurement.

The initial angle of attack at $\alpha = 0^\circ$ was set using a ruler, setting the distance from the airfoil leading edge to the test section floor, h_0 , equal to the distance from the airfoil trailing edge to the test section floor h_1 . This results in the geometric relationship shown in Figure C.2, where Δh , would occur if $h_0 \neq h_1$ and c is the airfoil chord. This geometric relationship can be expressed as

$$\alpha = \tan^{-1} \frac{\Delta h}{c}. \quad (C.14)$$

The uncertainty due to setting the initial angle of attack is

$$u_{\alpha_s} = \left(\frac{\partial \alpha}{\partial (\Delta h)} \right) u_{\Delta h} = \left(\frac{c}{c^2 + \Delta h^2} \right) u_{\Delta h}, \quad (C.15)$$

where $u_{\Delta h}$ is the uncertainty of the measurement ruler, which was assumed to be only the result of the ruler's finite resolution. Assuming $\Delta h = 0$, then

$$u_{\alpha_s} = \left(\frac{5 \text{ in}}{(5 \text{ in})^2 + 0} \right) 0.0156 \times \frac{360}{2\pi} = 0.1788 \text{ deg}. \quad (C.16)$$

The uncertainty due to the resolution of the motor is

$$u_{\alpha_R} = \frac{1}{2} \frac{1}{\text{resolution}} = \left(\frac{1}{2} \right) \frac{1 \text{ deg}}{111.111 \text{ encoder counts}} = 0.0045 \text{ deg}. \quad (C.17)$$

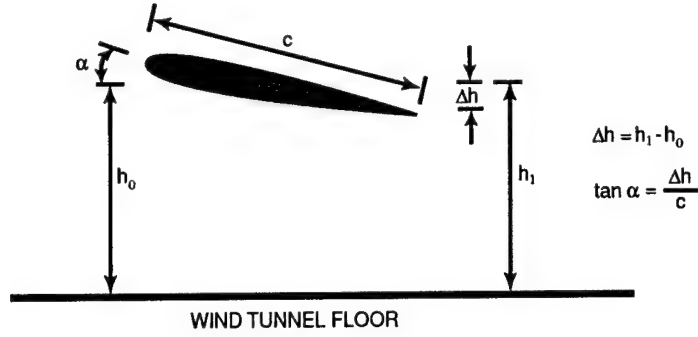


Figure C.2. Geometric relationship between airfoil and the test section floor.

The resolution, Q , of the 12-bit A/D converter with a 20 volt full scale range is

$$Q = \frac{E_{FSR}}{2^{12}} = \frac{20}{4096} = 0.00488 \text{ V/bit.} \quad (\text{C.18})$$

This results in the quantization error of the A/D converter to be

$$u_{\alpha_{A/D}} = \frac{1}{2}(0.00488) \frac{10 \text{ deg}}{3.41 \text{ V}} = 0.0072 \text{ deg.} \quad (\text{C.19})$$

The uncertainty due to the random error in the standard deviation in the measurement is given as

$$u_{\alpha_{St}} t_{\nu_{P_{u_{\alpha_{St}}}}, C} \cdot S_{P_{u_{\alpha_{St}}}} = (2.093)0.165 = 0.345. \quad (\text{C.20})$$

The total angle of attack uncertainty is

$$u_{\alpha} = (0.1788^2 + 0.0045^2 + 0.0072^2 + 0.345^2)^{\frac{1}{2}} = 0.39 \text{ deg.} \quad (\text{C.21})$$

Uncertainty in Lift Coefficient

The coefficient of lift, C_l , is defined as

$$C_l = C_n \cos \alpha - C_a \sin \alpha \quad (\text{C.22})$$

where C_n is the normal force coefficient given by

$$C_n = \frac{1}{c} \int_{-c}^c (C_p) dx \quad (\text{C.23})$$

and C_a is the axial force coefficient given by

$$C_a = \frac{1}{c} \int_{-c}^c \left(C_p \frac{dy}{dx} \right) dx. \quad (\text{C.24})$$

Using the method of Kline and McClintock, the uncertainty in C_l is

$$u_{C_l} = \left[\left(\frac{\partial C_l}{\partial C_n} u_{C_n} \right)^2 + \left(\frac{\partial C_l}{\partial C_a} u_{C_a} \right)^2 + \left(\frac{\partial C_l}{\partial C_\alpha} u_{C_\alpha} \right)^2 \right]^{1/2}. \quad (\text{C.25})$$

The total uncertainty in the normal force coefficient comes from two sources

$$u_{C_n} = (u_{C_{nC_p}}^2 + u_{C_{nD}}^2)^{1/2}, \quad (\text{C.26})$$

where $u_{C_{nC_p}}$ is the uncertainty associated with the coefficient of pressure and C_{nD} is the discretization error from using a finite integral technique. The uncertainty associated with the coefficient of pressure is

$$u_{C_{nC_p}} = \left(\frac{\partial C_n}{\partial C_p} u_{C_p} \right) = 1 u_{C_p} = 1(0.017) = 0.017. \quad (\text{C.27})$$

The discretization error for the normal force coefficient is

$$C_{nD} = \frac{(b-a)}{24N} \left\{ \sum_{i=1}^N [f(x_{i+1}) - 2f(x_i) + f(x_{i-1}))^2] \right\}^{1/2} \quad (\text{C.28})$$

where a and b are the limits of integration and N is the number of points. This is estimated as

$$C_{n_D} = 0.008. \quad (C.29)$$

Therefore, the total uncertainty in the normal force coefficient is

$$u_{C_n} = (u_{C_{nC_p}}^2 + u_{C_{n_D}}^2)^{1/2} = (0.017^2 + 0.008^2) = 0.019. \quad (C.30)$$

Likewise, the total uncertainty for the axial force coefficient is

$$u_{C_a} = (u_{C_{aC_p}}^2 + u_{C_{a_D}}^2)^{1/2}, \quad (C.31)$$

where $u_{C_{aC_p}}$ is the uncertainty associated with the coefficient of pressure and C_{a_D} is the discretization error. The uncertainty associated with the coefficient of pressure is

$$u_{C_{aC_p}} = \left(\frac{\partial C_a}{\partial C_p} u_{C_p} \right) = \left(\frac{dy}{dx} \right)_{avg} u_{C_p} = 0.2(0.017) = 0.0034. \quad (C.32)$$

The discretization error for the axial force coefficient is found in a similar manner as the normal force coefficient. This is estimated as

$$C_{a_D} = 0.0012. \quad (C.33)$$

Therefore, the total uncertainty in the axial force coefficient is

$$u_{C_a} = (u_{C_{aC_p}}^2 + u_{C_{a_D}}^2)^{1/2} = (0.0034^2 + 0.0012^2) = 0.0034. \quad (C.34)$$

Recall that the coefficient of lift is

$$C_l = C_n \cos \alpha - C_a \sin \alpha. \quad (C.35)$$

Therefore total uncertainty in the coefficient of lift is

$$u_{C_l} = \left[\left(\frac{\partial C_l}{\partial C_n} u_{C_n} \right)^2 + \left(\frac{\partial C_l}{\partial C_a} u_{C_a} \right)^2 + \left(\frac{\partial C_l}{\partial C_\alpha} u_{C_\alpha} \right)^2 \right]^{1/2} \quad (C.36)$$

this simplifies to

$$u_{C_l} = [((\cos \alpha) u_{C_n})^2 + ((\sin \alpha) u_{C_a})^2 + ((C_n \sin \alpha + C_a \cos \alpha) u_\alpha)^2]^{1/2}. \quad (C.37)$$

Solving for the uncertainty at for a typical angle of attack ($\alpha = 15^\circ$) gives

$$u_{C_l} = 0.0215. \quad (C.38)$$

Uncertainty in Moment Coefficient

The moment coefficient at the leading edge $C_{m_{LE}}$ is

$$C_{m_{LE}} = -\frac{1}{c^2} \int C_p x dx \quad (C.39)$$

The uncertainty in the moment coefficient at the leading edge is

$$u_{C_{m_{LE}}} = (u_{C_{m_{LE}C_p}}^2 + u_{C_{m_{LE}D}}^2)^{1/2} \quad (C.40)$$

where $u_{C_{m_{LE}C_p}}$ is the uncertainty associated with the coefficient of pressure and $C_{m_{LE}D}$

is the discretization error. The error associated with the coefficient of pressure is

$$u_{C_{m_{LE}C_p}} = \frac{\partial C_m}{\partial C_p} u_{C_p} = x u_{C_p} = 0.5(0.017) = 0.0085 \quad (C.41)$$

The discretization error in $C_{m_{LE}}$ is

$$C_{m_{LE}D} = \frac{(b-a)}{24N} \left\{ \sum_{i=1}^N [f(x_{i+1}) - 2f(x_i) + f(x_{i-1}))^2] \right\}^{1/2}. \quad (C.42)$$

This is estimated as

$$C_{m_{LE_D}} = \frac{2}{24 \cdot 29} (0.011)^{1/2} = 0.0003. \quad (C.43)$$

This results in the total uncertainty of the moment coefficient at the leading edge to be

$$u_{C_{m_{LE}}} = (u_{C_{m_{LE_{C_p}}}}^2 + u_{C_{m_{LE_D}}}^2)^{1/2} = (0.0085^2 + 0.0003^2)^{1/2} = 0.0085. \quad (C.44)$$

The moment coefficient at the quarter chord $C_{m_{1/4}}$ is

$$C_{m_{1/4}} = C_{m_{LE}} + 0.25C_n. \quad (C.45)$$

Because the moment coefficient approaches zero, it is necessary to calculate its error as a percentage error. The uncertainty is

$$u_{C_{m_{1/4}}} = C_{m_{1/4}} \left[\left(\frac{\partial C_{m_{1/4}}}{\partial C_{m_{LE}}} \frac{u_{C_{m_{LE}}}}{C_{m_{LE}}} \right)^2 + \left(\frac{\partial C_{m_{1/4}}}{\partial C_n} \frac{u_{C_n}}{C_n} \right)^2 \right]^{1/2} \quad (C.46)$$

$$u_{C_{m_{1/4}}} = C_{m_{1/4}} \left[\left(1 \frac{u_{C_{m_{LE}}}}{C_{m_{LE}}} \right)^2 + \left(0.25 \frac{u_{C_n}}{C_n} \right)^2 \right]^{1/2} \quad (C.47)$$

$$u_{C_{m_{1/4}}} = 0.037 \left[\left(\frac{0.0085}{0.285} \right)^2 + \left(0.25 \frac{0.019}{0.9918} \right)^2 \right]^{1/2} = 0.0011 \quad (C.48)$$

Uncertainty in Drag Coefficient

The coefficient of drag was calculated using

$$C_d = \frac{4}{U_\infty^2} \int_0^1 U(y)(U_\infty - U(y))d\left(\frac{y}{H}\right). \quad (\text{C.49})$$

The total uncertainty in the drag coefficient is

$$u_{C_d} = (u_{C_{dU}}^2 + U_{C_{dD}}^2)^{1/2} \quad (\text{C.50})$$

To determine C_{dU} , start with Bernoulli's equation

$$U = \sqrt{\frac{2\Delta P}{\rho}} \quad (\text{C.51})$$

where U is the velocity and ρ is the density of the fluid. Therefore the uncertainty associated with the velocity is

$$u_U = \frac{\partial U}{\partial P} u_P = \frac{1}{\sqrt{2\Delta P\rho}} u_P. \quad (\text{C.52})$$

For $\Delta P = 0.245$ in. H_2O ,

$$u_U = 0.2737 \text{ ft/s} = 0.0824 \text{ m/s}. \quad (\text{C.53})$$

This error is for a single velocity measurement. The velocity used in the drag calculation was the mean of 1000 samples. Therefore, the error in the mean is

$$u_{\bar{U}} = \frac{u_U}{\sqrt{N}} = \frac{u_U}{\sqrt{1000}} = 0.003 \text{ m/s}. \quad (\text{C.54})$$

Recall, that the coefficient of drag was calculated using

$$C_d = \frac{4}{U_\infty^2} \int_0^1 U(y)dUd\left(\frac{y}{H}\right) \quad (\text{C.55})$$

letting $dU = U_\infty - U$. Then the uncertainty in dU is

$$u_{dU} = \left[\left(\frac{\partial dU}{\partial U_\infty} \right)^2 - \left(\frac{\partial dU}{\partial U} u_{\bar{u}} \right)^2 \right]^{1/2}. \quad (\text{C.56})$$

Since

$$u_{\bar{U}} = u_{U_\infty} \text{ and } \frac{\partial dU}{\partial u_\infty} = \frac{\partial U}{\partial U} = 1, \quad (\text{C.57})$$

it follows that

$$u_{\bar{dU}} = \sqrt{2} u_{\bar{U}} = \sqrt{2}(0.003) = 0.0036 \text{ m/s}. \quad (\text{C.58})$$

Then the uncertainty of Equation C.55

$$u_{C_{dU}} = \left[\left(\frac{\partial C_d}{\partial U} u_{\bar{U}} \right)^2 + \left(\frac{\partial C_d}{\partial dU} u_{\bar{dU}} \right)^2 \right]^{1/2} = \left[\left(\frac{4}{U_\infty^2} dU u_{\bar{U}} \right)^2 + \left(\frac{4U}{U_\infty^2} u_{\bar{dU}} \right)^2 \right]^{1/2}. \quad (\text{C.59})$$

Substituting in $U_\infty = 20 \text{ m/s}$ and $U = 19 \text{ m/s}$ yields $dU = 1 \text{ m/s}$ and

$$u_{C_{dU}} = \left[\left(\frac{4}{20^2} (1) 0.003 \right)^2 + \left(\frac{4(19)}{20^2} 0.0036 \right)^2 \right]^{1/2} = 0.0007. \quad (\text{C.60})$$

The discretization error is

$$u_{C_{dD}} = \frac{(b-a)}{24N} \left\{ \sum_{i=1}^N [f(x_{i+1}) - 2f(x_i) + f(x_{i-1}))^2] \right\}^{1/2}, \quad (\text{C.61})$$

which simplifies to

$$u_{C_{dD}} = \frac{1}{24 \cdot 94} (4.62)^{1/2} = 0.0013. \quad (\text{C.62})$$

Combining this result gives the total uncertainty in the drag coefficient as

$$u_{C_d} = (u_{C_{dU}}^2 + u_{C_{dD}}^2)^{1/2} = (0.0007^2 + 0.0013^2)^{1/2} = 0.0014. \quad (\text{C.63})$$

Summary of Uncertainty

A summary of the quantities and their associated uncertainties for this experiment are presented in Table C.1.

TABLE C.1. SUMMARY OF THE UNCERTAINTY IN THE EXPERIMENT.

Quantity	Uncertainty	Percent Uncertainty
Voltage	0.0073 V	1.6
Pressure	0.004 in. H ₂ O	1.6
Coefficient of Pressure	0.017	1.7
Normal Force Coefficient	0.019	1.9
Axial Force Coefficient	0.0036	7
Angle of Attack	0.39°	2
Coefficient of Lift	0.0215	2.1
Coefficient of Moment	0.0011	2.2
Coefficient of Drag	0.0014	9

BIBLIOGRAPHY

- [1] Abbott, I.H. and A.E. Von Doenhoff. 1959. "Theory of Wing Sections." Dover Publications, Inc.; New York.
- [2] Anderson Jr., J.D. 1989. "Introduction to Flight." McGraw-Hill, Inc.; New York.
- [3] Anderson Jr., J.D. 2001. "Fundamentals of Aerodynamics." McGraw-Hill, Inc.; New York.
- [4] Bragg, M.B. and G.M. Gregorek. 1987. "Experimental Study of Airfoil Performance with Vortex Generators." *J. Aircraft*, Volume 24, Number 5, pg. 305-309.
- [5] Chang, P.K. 1976. "Control of Flow Separation." Hemisphere Publishing Corporation; Washington.
- [6] Corke, T.C. 2002. "Design of Aircraft." Prentice-Hall Publishers; New York.
- [7] Corke, T., D. Cavalieri, and E. Matlis. 2001. "Boundary layer instability on a sharp cone at Mach 3.5 with controlled input." *AIAA Journal*, Volume 40, Number 5, pg. 1015.
- [8] Corke, T., E. Jumper, M. Post, D. Orlov, and T. McLaughlin. 2002. "Application of weakly-ionized plasmas as wing flow-control devices." *AIAA Paper 2002-0350*, *AIAA Journal*, in review.
- [9] Corke, T. C. and E. Matlis. 2000. "Phased Plasma Arrays for Unsteady Flow Control." *AIAA 2000-2323*.
- [10] Dunn, P.F. 2005. "Measurement and Data Analysis for Engineering and Science." McGraw-Hill; New York.
- [11] Enloe, L., T. McLaughlin, R. VanDyken, Kachner, E., Jumper, and T. Corke. 2004. "Mechanisms and Response of a Single Dielectric Barrier Plasma Actuator: Plasma Morphology." *AIAA Journal*, Volume 42, Number 3, pg. 589-594.
- [12] Enloe, L., T. McLaughlin, R. VanDyken, Kachner, E., Jumper, T. Corke, M. Post, O. Haddad. 2004. "Mechanisms and Response of a Single Dielectric Barrier Plasma Actuator: Geometric Effects." *AIAA Journal*, Volume 42, Number 3, pg. 595-604.
- [13] Enloe, L., T. McLaughlin, and R. VanDyken. 2004. "Plasma Structure in the Aerodynamic Plasma Actuator." *AIAA 2004-0844*.

- [14] Eppler, R. 1999. "Airfoils with boundary layer suction, design and off-design cases." *Aerospace Science Technology*, Volume 3, pg. 403-415.
- [15] Fink, D. and D. Christiansen. 1982. "Electronics Engineers' Handbook." McGraw-Hill Book Company: New York.
- [16] Gad-el-Hak, M. 2000. "Flow Control: Passive, Active, and Reactive Flow Management." Cambridge University Press; New York.
- [17] Gad-el-Hak, M. and D. Bushnell. 1991. "Separation Control: Review." *Journal of Fluids Engineering*, Volume 115, pg. 5-30.
- [18] Gadri, R. and J.R. Roth. 1998. "Glow discharge-like characteristics of a OAUGDP revealed by computer modeling." 25th IEEE International Conference on Plasma Science.
- [19] Glauert, M.B. 1956. "The Wall Jet." *Journal of Fluid Mechanics*, Volume 1, pg. 625.
- [20] Glezer, A., M.G. Allen, D.J. Coe, S.L. Barton, M.A. Trautman, and J.W. Wiltse. 1998. "Synthetic Jet Actuator and Applications Thereof." U.S. Patent 5,758,823.
- [21] Goldstein, R.J. (Editor) and T. Mueller (Chapter 6: Flow Visualization by Direct Injection). 1996. "Fluid Mechanics Measurements." Taylor and Francis: Washington D.C.
- [22] Greenblatt, D. and I. Wygnanski. 2000. "The control of separation by period excitation." *Progress in Aerospace Sciences*, Volume 36, pg. 487-545.
- [23] Graeme, J., G. Tobey, and L. Huelsman. 1971. "Operational Amplifiers: Design and Applications." Burr-Brown. McGraw-Hill Book Company, New York.
- [24] Huang, J., T. Corke, and F. Thomas. 2003. "Plasma actuators for separation control of low pressure turbine blades." *AIAA 2003-1027*.
- [25] Jansen, 1982. "Experimental studies of the effect of the laminar separation bubble on the performance of a NACA 66₃ - 018 airfoil at low Reynolds numbers." M.S. Thesis, University of Notre Dame.
- [26] Jumper, E., S. Schreck, and R. Dimmick. 1987. "Lift-curve Characteristics for an Airfoil Pitching at Constant Rate." *Journal of Aircraft*, Volume 25, Number 10, pg. 680-687.
- [27] Jumper, E., W. Dardis III, and E. Stephen. 1988. "Toward an Unsteady-Flow Airplane." *AIAA 1988-0752*.
- [28] Jumper, E. R. Dimmick, and A. Allaire. 1989. "The Effect of Pitch Location on Dynamic Stall." *Journal of Fluids Engineering*, Volume 111, pg. 256-262.
- [29] Kakuta, S., T. Kamata, and T. Makabe. 1995. "Study of surface charges on dielectric electrodes in a radio-frequency." *Journal of Applied Physics*, Volume 77, Number 3, pg. 985-991.

- [30] Karim, M.A. and M. Acharya. 1993. "Control of the Dynamic Stall Vortex over a Pitching Airfoil by Leading Edge Suction." *AIAA 1993-3267*.
- [31] Kawthar-Ali, M., and M. Acharya. 1996. "Artificial Neural Networks for Suppression of the Dynamic-Stall Vortex over Pitching Airfoils." *AIAA 1996-0540*.
- [32] Kerho, M, S. Hutcherson, R.F. Blackwelder, and R.H. Liebeck. 1993. "Vortex generators used to control laminar separation bubbles." *Journal of Aircraft*, Volume 30, Number 3, pg. 315-319.
- [33] Khorrami, M.R., M. Choudhari, B.A. Singer, D.P. Lockard, and C.L. Streett. 2003. "In search of the physics: The interplay of experiment and computation in slat aeroacoustics." *AIAA 2003-0980*.
- [34] Kiedaisch, J., and M. Acharya. 1997. "Investigation of Incipient Dynamic Stall Over Pitching Airfoils using Hot-Film Sensors." *AIAA 1997-0656*.
- [35] Kiedaisch, J., and M. Acharya. 1998. "Investigation of Unsteady Separation Over Pitching Airfoils at High Reynolds Numbers." *AIAA 1998-2975*.
- [36] Lachmann, G.V. (Editor) 1961. "Boundary Layer and Flow Control: Volume I and Volume II." Pergamon Press; New York.
- [37] Leishman, J. Gordon. 2000. "Principles of Helicopter Aerodynamics." Cambridge University Press, New York.
- [38] Lin, J.C., S.K. Robinson, and R.J. McGhee. 1994. "Separation control on high-lift airfoils via micro-vortex generators." *Journal of Aircraft*, Volume 31, Number 6, pg. 1317-1323.
- [39] Lin, J.C. 2002. "Review of research on low-profile vortex generators to control boundary-layer separation." *Progress in Aerospace Sciences*, Volume 38, pg. 389-420.
- [40] Lord P., D. McCormick, T. Anderson, B. Wake, and D. MacMartin. 2000. "Rotorcraft Retreating Blade Stall Control." *AIAA 2000-2475*.
- [41] Malik, M., L. Weinstein, and M. Hussaini. 1983. "Ion Wind Drag Reduction." In the Proceedings of the AIAA 21st Aerospace Sciences Meeting.
- [42] Massines, F., A. Rabehi, P. Decomps, R. Gadri, P. Segur, & C. Mayoux. 1998. "Experimental and Theoretical Study of a Glow Discharge at Atmospheric Pressure Controlled by a Dielectric Barrier." *Journal of Applied Physics*, Volume 83, Number 6, pg. 2950-2957.
- [43] Matlis, E. 2004. "Controlled Experiments on Instabilities and Transition to Turbulence on a Sharp Cone at Mach 3.5." PhD Dissertation, University of Notre Dame.
- [44] McCormick, D. 2000. "Boundary Layer Separation Control with Directed Synthetic Jets." *AIAA 2000-0519*.

- [45] Mendoza, J.M., T.F. Brooks, and W.H. Humphreys, Jr. 2002. "Aeroacoustic Measurements of a Wing/Slat Model." *AIAA 2002-2604*.
- [46] Mueller, T.J. 1980. "On the historical development of apparatus and techniques for smoke visualization of subsonic and supersonic flows." *AIAA Paper 80-0420-CP*.
- [47] Nagib, H., J. Kiedaisch, D. Greenblatt, I. Wygnanski, and A. Hassen. 2001. "Effective flow control for rotorcraft applications at flight Mach numbers." *AIAA 2001-2974*.
- [48] Olson, S. 2003. "Slat Tonal Noise Mechanisms in a Two-Dimensional Multi-Element Airfoil Configuration." PhD Dissertation, University of Notre Dame.
- [49] Orlov, D., E. Erturk, M. Post, and T. Corke. 2001. "DNS Modeling of Plasma Array Flow Actuators." Bulletin of the American Physical Society Fluid Dynamics Division, Annual Meeting.
- [50] Orlov, D., T. Corke, and M. Post. 2002. "DNS Modeling of plasma array flow actuators." Bulletin of the American Physical Society Fluid Dynamics Division, Annual Meeting.
- [51] Orlov, D., T. Corke, and O. Haddad. 2003. "DNS Modeling of plasma actuators." Bulletin of the American Physical Society Fluid Dynamics Division, Annual Meeting.
- [52] Post, M.L. 2001. "Phased plasma actuators for unsteady flow control." M.S. Thesis, University of Notre Dame.
- [53] Post, M. and T. Corke. 2002. "Separation control using plasma actuators." Bulletin of the American Physical Society Fluid Dynamics Division, Annual Meeting.
- [54] Post, M. and T. Corke. 2003. "Separation control on high angle of attack airfoil using plasma actuators." *AIAA Paper 2003-1024*.
- [55] Post, M. and T. Corke. 2003. "Airfoil Leading-edge Separation Control using Plasma Actuators." Bulletin of the American Physical Society Fluid Dynamics Division, Annual Meeting.
- [56] Post, M. and T. Corke. 2004. "Separation control using Plasma Actuators - Stationary and Oscillating Airfoils." *AIAA Paper 2004-0841*.
- [57] Roth, J.R., M. Laroussi, and C. Liu. 1992. "Experimental Generation of a steady-state Glow Discharge at Atmospheric Pressure." In the Proceedings of the 19th IEEE International Conference on Plasma Science.
- [58] Roth, J.R. 1995. "Industrial Plasma Engineering." Institute of Physics Publishing.
- [59] Roth, J.R., D. Sherman, and S. Wilkinson. 1998. "Boundary Layer Flow Control with One Atmosphere Uniform Glow Discharge Surface Plasma." *AIAA 1998-0238*.

- [60] Schlichting, H. 1960. "Boundary Layer Theory." McGraw-Hill Book Company, Inc.; New York.
- [61] Seifert, A., T. Bachar, D. Moss, M. Shepshelovich, and I. Wygnanski. 1993. "Oscillatory Blowing: A Tool to Delay Boundary-Layer Separation." *AIAA Journal*, Volume 11, Number 31, pg. 2052-2060.
- [62] Seifert, A., A. Darabi, and I. Wygnanski. 1996. "Delay of Airfoil Stall by Periodic Excitation." *Journal of Aircraft*, Volume 33, Number 4, pg. 691-698.
- [63] Seifert, A., S. Eliahu, and D. Greenblatt. 1998. "Use of piezoelectric actuators for airfoil separation control." *AIAA Journal*, Volume 36, Number 8, pg. 1535-1537.
- [64] Seifert, A., and L. Pack. "Oscillatory Excitation of Unsteady Compressible Flows over Airfoils at Flight Reynolds Numbers." *AIAA 99-0925*.
- [65] Schubauer, G.B. and W.G. Spangenberg. 1960. "Forced mixing in boundary layers." *Journal of Fluid Mechanics*, Volume 8, pg. 10-32.
- [66] Smith, B.L. and A. Glezer. 1998. "The formation and evolution of synthetic jets." *Physics of Fluids*, Volume 10, Number 9, pg. 2281-2297.
- [67] Taylor, H.D. 1947. "The elimination of diffuser separation by vortex generators." United Aircraft Corporation Report No. R-4012-3. [22].
- [68] Yu, Y.H., K.W. McAlister, C. Tung, and C.M. Wang. 1995. "Dynamic Stall Control for Advanced Rotorcraft Application." *AIAA Journal*, Volume 33, Number 2.